2018

Flow Structure of Vortex-Wing Interaction

Christopher Kyle McKenna
Lehigh University

FLOW STRUCTURE OF VORTEX-WING INTERACTION

by

Christopher K. McKenna

Presented to the Graduate and Research Committee

of Lehigh University

in Candidacy for the Degree of

Doctor of Philosophy

In

Mechanical Engineering

Lehigh University

January, 2018

DISSERTATION SIGNATURE SHEET

Approved and recommended for acceptance as a dissertation draft.

_____

Date

_____

Professor Donald Rockwell

Dissertation Director

_____

Accepted Date

Committee Members:

_____

Professor D. O. Rockwell

_____

Professor A. R. Banerjee

_____

Professor K. W. Moored

_____

Professor H. D. Ou-Yang

ACKNOWLEDGMENTS

While this dissertation would not be possible without any of the people mentioned below, the impact that Dr. Donald Rockwell had was immense. Both in offering advice in every step of the dissertation development and expanding my understanding of fluid dynamics, it is impossible to overstate his contribution.

I would also like to acknowledge Dr. Arindam Banerjee, Dr. Keith Moored, and Dr. Daniel Ou-Yang who comprised my doctorial committee. Their insight, advice, and time made this work possible.

Mr. Richard Towne, Mr. James Bunderla, Mr. Bill Maroun, and Mr. Eli Towne all contributed to this dissertation, both in manufacturing the experimental setup and providing more assistance than I could ever thank them for.

I would never have been in a place to create this dissertation if it were not for the diligent help of Mrs. JoAnn Casciano, Mrs. Jennifer R. Smith and Mrs. Barbara McGuire. I would also like to thank Mr. Naazer Ashraf and Mr. Tim Nixon for fixing countless computer issues, Dr. Matthew Bross, Dr. Ahmet Burak Tuna, Dr. Maxwell Wolfinger, and Mr. Daniel Tudball for giving valuable advice and direction during the inception of this work, and Mr. Gregory Fishman for both his keen insights and friendship.

Dr. Garmann, Dr. Barnes, and Dr. Visbal from the AFOSR also helped immensely with this work by generating fascinating simulations of the vortex-wing interaction. They were also kind enough to allow me to use their computations in my own work.

Finally I would like to thank my friends and family. Without their support none of this would have been possible.

TABLE OF CONTENTS

Pages

LIST OF FIGURES

Pages

NOMENCLATURE

b	Span
BL	Bifurcation line
C	Chord
c_τ	Centroid constant
D_v	Vortex diameter
d_p	Particle diameter
d_r	Pixel pitch
d_τ	Particle image diameter
e_r	Error ratio
f	Frequency
F	Focus
$f^\#$	F-stop
L/D	Lift to drag ratio
M_0	Image magnification
N	Nodal line
Q	Q-criterion
q	Swirl Ratio
r	Radius
$r_{0.5}$	Radius at which the axial deficit is half the maximum
r_v	Vortex radius based on azimuthal velocity
r^*	Vortex radius based on circulation
Re	Reynolds number
Re_v	Vortex Reynolds number
SP	Saddle point
St	Strouhal number
t	Time
	Plate thickness
T	Turbulent Kinetic Energy
T^*	Adjusted inplane turbulent kinetic energy
Δt	Time between image captures
u	Streamwise velocity
u_r	Radial velocity
u_{rms}	rms of streamwise velocity
u_θ	Azimuthal velocity
Δu	Velocity deficit
$\partial u_r/\partial x$	Derivative of radial velocity in streamwise direction
U_∞	Freestream velocity
v	Spanwise velocity
w'	Fluctuations in spanwise velocity
w	Vertical velocity
w'	Fluctuations in vertical velocity
w_w	Vertical velocity of wing
x	Coordinate in streamwise direction

x'	Distance upstream of the leading edge of the trailer wing
Δx	Streamwise distance between the two wings
y	Coordinate in spanwise direction
Δy_0	Spanwise location of leader wing which leads to aligned interaction
Δy	Spanwise distance of vortex impingement to wing tip
z	Coordinate in vertical direction
z_w	Vertical location of wing
z_0	Distance from object plane to lens
Z_0	Distance from image plane to lens
Δz_0	Vertical location of leader wing which leads to aligned interaction
Δz	Vertical distance of vortex impingement to wing tip

Greek Symbols

α	Angle of attack of the leader wing
β	Angle of attack of the trailer wing
Γ	Circulation
δz	Depth of field
λ	Wavelength
ν	Kinematic viscosity
σ	Smoothing kernel
σ_u	rms random velocity error
$\sigma_{\Delta X}$	R.M.S. random in-plane displacement error
ϕ	Phase angle
ϕ_L	Phase lag
ω_x	Streamwise vorticity
$(\omega_x)_{rms}$	R.M.S. of streamwise vorticity
ω_y	Spanwise vorticity
ω_z	Vertical vorticity
ω_θ	Azimuthal vorticity

Acronyms

CCD	Charge-Coupled Device
LDV	Laser Doppler Velocimetry
MPIV	Monoscopic Particle Image Velocimetry
RMS	Root Mean Square
SPIV	Stereoscopic Particle Image Velocimetry

ABSTRACT

Impingement of a streamwise-oriented vortex upon a fin, tail, blade or wing represents a fundamental class of flow-structure interaction that extends across a range of applications. This interaction can give rise to time-averaged loading, as well as unsteady loading known as buffeting. The loading is sensitive to parameters of the incident vortex as well as the location of vortex impingement on the downstream aerodynamic surface, generically designated as a wing. Particle image velocimetry is employed to determine patterns of velocity, vorticity, swirl ratio, and streamlines on successive cross-flow planes upstream of and along the wing, which lead to volume representations and thereby characterization of the interaction.

At locations upstream of the leading edge of the wing, the evolution of the incident vortex is affected by the presence of the wing, and is highly dependent on the spanwise location of vortex impingement. Even at spanwise locations of impingement well outboard of the wing tip, a substantial influence on the structure of the incident vortex at locations significantly upstream of the leading edge of the wing was observed. For spanwise locations close to or intersecting the vortex core, the effects of upstream influence of the wing on the vortex are to: decrease the swirl ratio; increase the streamwise velocity deficit; decrease the streamwise vorticity; increase the azimuthal vorticity; increase the upwash; decrease the downwash; and increase the root-mean-square fluctuations of both streamwise velocity and vorticity. The interrelationship between these effects is addressed, including the rapid attenuation of axial vorticity in presence of an enhanced defect of axial velocity in the central region of the vortex.

Moreover, when the incident vortex is aligned with, or inboard of, the tip of the wing, the swirl ratio decreases to values associated with instability of the vortex, giving rise to enhanced values of azimuthal vorticity relative to the streamwise (axial) vorticity, as well as relatively large root-mean-square values of streamwise velocity and vorticity.

Along the chord of the wing, the vortex interaction gives rise to distinct modes, which may involve either enhancement or suppression of the vortex generated at the tip of the wing. These modes are classified and interpreted in conjunction with computed modes at the Air Force Research Laboratory. Occurrence of a given mode of interaction is predominantly determined by the dimensionless location of the incident vortex relative to the tip of the wing and is generally insensitive to the Reynolds number and dimensionless circulation of the incident vortex. The genesis of the basic modes of interaction is clarified using streamline topology with associated critical points. Whereas formation of an enhanced tip vortex involves a region of large upwash in conjunction with localized flow separation, complete suppression of the tip vortex is associated with a small-scale separation–attachment bubble bounded by downwash at the wing tip.

Oscillation of the wing at an amplitude and velocity nearly two orders of magnitude smaller than the wing chord and free stream velocity respectively can give rise to distinctive patterns of upwash, downwash, and shed vorticity, which are dependent on the outboard displacement of the incident vortex relative to the wing tip. Moreover, these patterns are a strong function of the phase of the wing motion during its oscillation cycle. At a given value of phase, the wing oscillation induces upwash that is reinforced by the upwash of the incident vortex, giving a maximum value of net upwash. Conversely, when

these two origins of upwash counteract, rather than reinforce, one another during the oscillation cycle, the net upwash has its minimum value. Analogous interpretations hold for regions of maximum and minimum net downwash located outboard of the regions of upwash.

During the oscillation cycle of the wing, the magnitude and scale of the vorticity shed from the tip of the wing are directly correlated with the net upwash, which takes different forms related to the outboard displacement of the incident vortex. As the location of the incident vortex is displaced towards the wing tip, both the maximum upwash and the maximum vorticity of the tip vortex initially increase, then decrease. For the limiting case where the incident vortex impinges directly upon the tip of the wing, there is no tip vortex or induced region of upwash. Furthermore, at small values of vortex displacement from the wing tip, the position of the incident vortex varies significantly from its nominal position during the oscillation cycle. For all locations of the incident vortex, it is shown that, despite the small amplitude of the wing motion, the flow topology is fundamentally different at maximum positive and negative values of the wing velocity, that is, they are not symmetric.

CHAPTER 1

INTRODUCTION

1.1 MOTIVATION

Interest in vortex-wing interactions has risen in recent years due to a variety of applications, which include; the tip vortex from a leading aircraft or biological flier impinging on its downstream counterpart; vortices shed from the tips of preceding blades of a helicopter rotor incident upon a downstream blade; vortices shed from the forebody or canard of an aircraft impinging on a downstream tail or fin; and vortices generated from rotor blades interacting with downstream stator blades in turbomachinery. While such interactions can lead to positive consequences, such as in formation flight, they are generally undesirable, and can cause unsteady loading of the aerodynamic component.

1.2 APPLICATIONS

1.2.1 Biological Formation Flight

Biological formation flight, represented in the photo of Figure 1.1 from Portugal et al. (2014) occurs for a variety of reasons, including protection, navigation, feeding, and most relevant to the present investigation, flight power reduction. This reduction occurs when a downstream flier is located in a region of upwash created by the flight of the leader. The existence of this power reduction, and the magnitude of the reduction, was an open question well into the start of the twentieth century. Hummel (1983) includes an

excellent overview of earlier works which attempted to analyze this question. In his own work, Hummel (1983, 1995) calculated the aerodynamic advantages for flocks of birds. This was performed by simplifying the wing and its wake as a line vortex, which was represented by a vertical velocity field in the crossflow plane. The vertical velocity was defined by upwash outside of the wing tips, and downwash inside the tips. By properly locating the follower wing in this wake, it is possible to achieve a significant increase in the lift to drag ratio, as well as a decrease of drag.

This type of analysis is used to find the energy savings of several types of geese formations in Hainsworth (1987). A median power savings of 36% was found, which was approximately half of the predicted savings for optimum wing tip spacing. The observed wing tip spacing varied considerably on both a bird to bird and formation to formation basis. Beyond these conclusions, it was also shown that formation leaders experienced lower savings. The author did note however that the model used did not take into account the flapping motions of the wings, which would most likely change the optimum spacing of the wing tips.

Weimerskirch et al. (2001) performed an in-depth study of pelicans flying in formation utilizing both heart rate monitors and cameras. They found that the largest benefit of formation flight was that it allowed individuals to spend a larger portion of their time gliding rather than flapping, with most of the calculated total energy savings of 11.4-14% being due to increased gliding time. Figure 1.2 shows the strain placed on the birds for a variety of flight conditions.

Portugal et al. (2014) found that some bird formations take advantage of more sophisticated aerodynamics than was previously believed. It was shown that northern bald ibises flying in V formation not only positioned themselves in the optimum aerodynamic location, but also utilized synchronized flapping to gain the most advantage at every phase during each flap cycle, which can be seen in Figure 1.3. An additional study of inline flight showed that the follower bird flapped 180° out of phase with the leader bird in order to decrease the losses due to flying in the downwash created by the leader.

1.2.2 Aircraft Formation Flight

Even though traditional aircraft do not mimic the wing motion of birds, flying in formation can still lead to achievable savings. Several different aircraft formation flight configurations are shown in Figure 1.4 from Bangash et al. (2006), furthermore Figure 1.5, Thomas 2001, shows a smoke visualization of the interaction between a tip vortex and a wing. An initial examination of aircraft formation flight, performed by Schlichting (1951), utilized horseshoe vortices to represent the aircraft in formation, and found that some benefits could be achieved. A theoretical treatment of aircraft formation flight was performed in Maskew (1977) in which the vortex lattice method was used to identify possible increases of range for aircraft in formation. This analysis took into account complicating factors such as trimming and different formation arrangements. It was found that two arrangements, V and double row, both showed increases in potential range between 46% and 67%. However, these arrangements did not give equal savings to all aircraft, with leading aircraft receiving little advantage during flight.

Wagner et al. (2002) showed experimentally the advantage of formation flight, with 9% fuel savings being achieved in the optimum arrangement. They also touched on some of the problems of aircraft formation flight, which include: difficulty maintaining position; inability to predict tip vortex position; and unsteadiness caused by the incident vortex.

Aircraft formation flight is not limited to a small number of aircraft and wings of large or moderate scale, but extends to a large number of very small-scale of micro air vehicles in a swarm or flock that may be deployed for atmospheric surveillance (Kroo, 2004).

1.2.3 Tail and Fin Buffeting

Vortices shed from the forebody or canard of an aircraft have the potential to interact with downstream features on the aircraft, most notably tails and fins. This can cause unsteady loading and potentially vibration. Wentz (1987) investigated this interaction, and showed that the position of downstream fins can cause tip vortices to burst well upstream of the obstruction. When bursting occurs, a dominant frequency may occur. In the investigation of Wentz (1987), it corresponded to a value of Strouhal number St=0.7, thereby giving rise to a coherent loading component of the fin. In essence, these experiments showed the possibility of excitation of natural frequencies of the structural components of the aircraft due to vortex bursting. Figure 1.6 features an image from Moses (1997) that shows how a vortex shed from the forebody can burst upstream of a fin, the wake created by this engulfs the fin causing unsteady loading.

Moses (1997) used active control to reduce the root mean square values of root strain in the fin by 19%.

1.2.4 Helicopter Rotors

A helicopter rotor blade can rotates through the wakes and trailing vortices generated by preceding rotor blades. This interaction generates increased noise, which is undesirable in both military and civilian applications. Unsurprisingly, the first investigations into the interaction between tip vortices and helicopter rotors were performed in an attempt to reduce this noise. Figure 1.7 shows an image from Raffel (2001) that illustrates these interactions, where the rotor blades can be seen to cut through the flow structures shed from the preceding blades. Windall (1970) considered the noise generated by a blade which interacts with, but does not cut through, a tip vortex. At low Mach number, good agreement was found between the calculated and actual noise generated by the vortex-blade interaction, but this agreement was not expected to extend to higher Mach numbers.

In more recent years, investigations have moved from pure analysis of the phenomenon towards study of possible methods for alleviating it. A review of these methods is provided by Yu et al. (1997), which found that while noise reduction was possible, it was not yet practical. These techniques included higher harmonic pitch control, individual blade control, and smart rotor control. While these methods did reduce vibration, they came at the cost of decreased power, increased weight, and increased complexity.

1.2.5 Turbomachinery

Similar to the case of a helicopter rotor, vortex-blade interaction causes undesirable vibrations in the blade rows of turbomachinery. Simulations performed by Dawes (1994) showed that a vortex created from overtip leakage could adversely affect the performance of subsequent blade rows. This vortex was shown to have an unsteady effect on the blade near the casing, reducing the performance at that location by nearly a third.

In experiments performed by Schlienger et al. (2005) a streamwise-oriented vortex created by the rotor hub passage, indicated in Figure 1.8, impinges on a blade. The flow field was found to be highly unsteady, and created large levels of time-averaged turbulence on the surface of the blade.

1.3 PHYSICS OF VORTEX-WING INTERACTIONS

1.3.1 Steady Vortex-Wing Interaction

Steady vortex-wing interaction is the baseline case that must be understood as a basis for pursuing the interaction of an unsteady vortex with a wing or, conversely, the interaction of a steady vortex with an oscillating wing. The early investigation of Patel and Hancock (1974) studied this case, specifically in reference to helicopter blades. They employed qualitative visualization to examine the interaction between a streamwise-oriented vortex and both an airfoil and a flat plate. They showed that the incident vortex

exhibited breakdown upstream of the plate and tended to re-form on its underside, and that this complex flow interaction caused a load distribution that was too complex for theoretical treatment.

This investigation into the physics of vortex interactions with helicopter blades was later continued by Raffel et al. (1998), Wittmer and Devenport (1999), and Kao et al. (2013). Raffel et al. (1998) defined, on the basis of quantitative experiments, the overall pattern of generation of a tip vortex and its interaction with a given rotor. Wittmer and Devenport (1999) showed that a vortex passing close to the surface of a rotor blade was not initially affected, but downstream of the blade it decayed more quickly than usual. Kao et al (2013) defined quantitative patterns of the interaction of vortices with a given rotor blade; such vortices are generated from the tips of preceding rotors.

Steady vortex-wing interaction can also be seen in the impingement of tip vortices on the downstream feature of an aircraft, such as a fin or tail. Quantitative interpretation of the interaction of a broken down vortex with a fin/tail is provided by Wolf et al (1995), including the effects of a time-averaged, apparent partitioning of the vortex on either side of the fin/tail and the consequences for surface pressure fluctuations. Gordnier and Visbal (1999) revealed, via computations, basic physics of the vortex breakdown-plate interaction, including interpretation of the spectral content of the surface pressure fluctuations in terms of the spiral mode of breakdown.

Investigations into vortex-wing interaction as it applies to formation flight has been undertaken in order to identify any possible aerodynamic advantages. To analytically investigate formation flight, Hummel (1983, 1995) used a series of line

vortices to calculate the lift and drag experienced by wings in formation. These line vortices were represented by upwash outside of the wing tips, and downwash inside the tips. By properly locating the follower wing in this wake, a significant increase in the lift to drag ratio, as well as a decrease of drag occurred. Blake and Gingras (2004) compare formation flight experiments, which utilize delta wings, to calculations using a vortex lattice method. It was determined that the vortex lattice method well predicted increases in lift, pitching, and rolling moment except when the aircraft overlapped in the spanwise direction. In this case the induced drag was less than predicted; this difference is presumed to be caused by flow separation on the trailer wing. Bangash et al. (2006) performed experiments that examined several different configurations of formation flight, including echelon, chevron, and in-line. An increase in the lift-to-drag ratio was found for both the echelon and chevron arrangements, with the amount of increase dependent on the spatial offset and the angle of attack of the leader wing.

Ning et al. (2011) assess the advantages of extended formation flight, which they define as a streamwise distance between aircraft of at least 10 spans. It is shown that many of the effects seen in close formation flight, such as increased lift to drag ratio and rolling moment, are also present in extended formation flight. Inasawa et al (2012) experimentally determined the lift and drag acting on the follower wing, relative to the leader wing, and interpreted these forces in relation to representative cuts of streamwise vorticity. Kless et al. (2013) performed an inviscid computational study of extended formation flight, with an assessment of different locations of vortex impingement as well as different trim arrangements. They show that optimal location for vortex impingement is approximately 10% of the span inboard of the wing tip. This location resulted in the

largest reduction of induced drag. Slotnick et al. (2014) model the entire airplane in their computations of extended formation flight. They found that, for the optimum formation flight configuration, a reduction in total drag of approximately 20% could be achieved.

Recent advances in both high-performance computing and numerical flow solvers have allowed numerical investigation into the complete flow field surrounding the vortex-wing interaction. Gordnier and Visbal (1999) showed that a vortex, created from a delta wing, will exhibit spiral vortex breakdown over the delta wing due to impingement upon a plate. The location of this breakdown was shown to be dependent on the degree of obstruction created by the plate. More recent computations that feature steady interactions are: Garmann & Visbal (2014a, 2015a), in which the effects of spanwise impingement location are investigated for a flat plate; Garman & Visbal (2015b), which features the interaction between an incident vortex and a NACA 0012 airfoil; Barnes, Visbal & Gordnier (2014b), where a flexible wing is used; and Barnes, Visbal & Gordnier (2014a), in which an upstream wing, used to generate the incident vortex, is included in the computation. These computations are complemented by the experiments of McKenna & Rockwell (2017), which showed good agreement with the computations.

Generally speaking, the incident vortex alters the flow pattern along the plate or wing, and can potentially invoke either enhancement or onset of a secondary vortex having a sense opposite to that of the incident vortex. The concept of onset of a secondary vortex has been well explored for a vortex incident upon a wall of infinite extent, as reviewed by Doligalski, Smith and Walker (1994), but has received relatively little attention for the case of an incident vortex at or near the tip of a wing. It is expected

that the mechanism of onset or enhancement of a secondary vortex will be substantially altered and, in some cases, attenuated, in the vicinity of the tip of a wing relative to the case of an infinite wall.

For the foregoing aspects of vortex-wing interaction, Q-Criterion iso-surfaces (iso-Q) of the incident vortex along the wing were characterized in conjunction with the altered vortex of opposite signed vorticity from the tip of the follower wing, separation phenomena along the wing, and the overall loading on the wing. Most relevant to our present considerations is the work of Garmann & Visbal (2014a & 2015a), which demonstrates that when the incident vortex is located inboard of the tip of the wing, iso-Q patterns indicate both detectable distortion and vertical inclination upstream of the leading edge.

For these cases, a spiral distortion, which twists in the opposite sense of rotation as the vortex, is present in the iso-surfaces of Q-criterion. As the vortex approaches the leading edge, it is reoriented from streamwise to plate normal, at which point it alternates between the top and bottom of the plate. Moreover, Barnes *et al.* (2014a & 2015b) examined effects of the swirl ratio q, where $q = \Gamma/(2\pi r \Delta u) \approx 1.567\ u_\theta/\Delta u$ according to Jacquin & Pantano (2002), in which Γ is circulation, r is the vortex radius, Δu is the velocity deficit in the core, and u_θ is the maximum azimuthal velocity. They showed that the swirl ratio of the impinging vortex is affected by the follower wing; furthermore, the dependence of swirl ratio on the spanwise impingement location of the incident vortex relative to the tip of the wing is shown by Garmann & Visbal (2015a). It was possible to attain low values of swirl ratio lying below the stability criterion of $q \geq \sqrt{2}$

corresponding to amplification of small-wavelength perturbations defined by Leibovich & Stewartson (1983). Barnes *et al.* (2014a & 2015b) show that these changes in swirl ratio are due to changes in the axial pressure gradient. Barnes *et al.* (2014a & 2015b) revealed that directly upstream of the leading edge, an adverse pressure gradient is present, but outside of the wing tip, Garmann & Visbal (2015a) showed that the pressure gradient is favorable. The extent of the upstream influence of the follower wing on the incident vortex is addressed in Barnes *et al.* (2014a & 2015b), which states that the axial velocity deficit is enhanced due to the presence of an adverse pressure gradient; it extends approximately one chord upstream of the leading edge of the follower wing.

The theoretical work of Batchelor (1964) provides the interrelationship between the azimuthal and axial components of velocity and the pressure gradient. A decrease in azimuthal velocity leads to an adverse axial pressure gradient, which in turn causes an increase in axial velocity deficit. To date, interpretation of the internal structure of the vortex on this basis has not been addressed using experiments or computations.

1.3.2 Unsteady Vortex Formation

A vortex that is created from a non-stationary airfoil has time-dependent variations of its properties, relative to a steady vortex shed from a stationary airfoil. Unsteady vortex formation involves: changes of effective angle of attack and disruption of the boundary layer on the wing and, in some cases, changes in the geometry of the wing due to flexing. The unsteady nature of this type of vortex formation has been difficult to characterize, but recent advances in both quantitative measurement techniques and visualization, as well as computational techniques, have led to new insight.

An early experiment on this topic was performed by Ramaprian and Zheng (1998), who examined a NACA 0015 wing oscillating sinusoidally in pitch using laser Doppler velocimetry. They showed that in the near wake there is little change in the vortex trajectory, but there are substantial oscillations in maximum circulation, as well as length and circulation scales. A similar investigation by Chang and Park (2000), featuring a larger amplitude of pitching oscillation, with variations of angle of attack from 0° to 30°, showed that larger oscillations created larger regions of flow separation during each cycle. This allowed the tip-vortex rollup to be analyzed, and it was shown that it caused a more disturbed and irregular tip vortex to form during this part of the oscillation. Birch and Lee (2005) employed a pitching airfoil and showed that if deep-stall occurs during the oscillation, hysteresis occurs between the pitch-up and pitch-down motions. Furthermore they showed that tangential velocity, circulation and lift-induced drag were larger during pitch-up than pitch-down.

Garmann and Visbal (2016a & 2016b) examined high-frequency, low-amplitude oscillation of a wing using high-fidelity, large-eddy simulation. These investigations employed a wing whose angle of attack remained constant, i.e., a heaving motion. This type of oscillation was found to create a tip vortex with varying core size. Moreover, it induced vortex motion as much as quintuple the initial oscillation amplitude of the wing. Further downstream, this induced motion changed from purely vertical to orbital. These vortex trajectories increased in amplitude with higher frequencies and amplitudes.

Fishman et al. (2016) used stereo particle image velocimetry to investigate the structure of a trailing vortex from a wing undergoing small amplitude heaving motion.

Large fluctuations of vortex circulation and axial velocity deficit occurred over the course of the oscillation cycle. Pronounced azimuthal vorticity arose in conjunction with increased axial velocity deficit as a result of decreased swirl ratio, which lay beneath the theoretical threshold for the amplification of azimuthal modes. This process involved the rapid amplification, then disruption, of axial vorticity fluctuation.

1.3.3 Unsteady Vortex-Wing Interaction

Interaction of a vortex undergoing either periodic oscillations or transient motion represents a particular challenging problem. Alternately, a steady incident vortex may impinge upon an oscillating wing. Both of these classes of unsteady vortex-wing interaction generate interesting physics.

An investigation of the effects of an oscillating fin on the breakdown of a vortex shed from a delta wing was performed by Gursul and Xie (2001). They found that while the breakdown location was dependent on spanwise location, it could also vary with oscillation frequency. Interestingly this variation was only present if the oscillation frequency was below a cutoff frequency; any frequency higher than the cutoff did not change the position of vortex breakdown.

Garmann & Visbal (2014b) considered a spanwise-wandering incident vortex that impinged upon a stationary wing. Immediately upstream of the wing, the spanwise motion diminished in amplitude, and a small vertical oscillation motion began. A vortex with this type of spanwise motion does not feature a spiraling instability upstream of the leading edge at any phase of its motion, implying that flow structures seen in the steady

interaction are not necessarily present in the unsteady interaction. Garmann & Visbal (2015c) investigated the transient interaction of a vortex and a wing which underwent steady spanwise motion. This transient encounter involved several different flow regimes that were originally seen in Garmann and Visbal (2014a), where the regimes represented steady interaction cases for different spanwise positions of vortex impingement. A spiral instability was present in this interaction once the wing tip had moved sufficiently close to the incident vortex. Additionally the lift, pitching moment, and rolling moment were analyzed, and it was found that all of these properties scaled proportionally to the side slip speed of the wing.

Barnes et al (2015) examined how bending oscillations of a wing affected the vortex-wing interaction, specifically for an interaction position inboard of the tip. Little change in the interaction was seen for the low frequency case unless the bending amplitude was large. It was shown that the bending motion inhibited the formation of the spiral instability upstream of the leading edge, previously noted as associated with this type of interaction. Closer to the leading edge, this instability could still form, with the oscillation frequency of the wing shifting the frequency of the instability if the two were sufficiently close.

1.4 UNRESOLVED ISSUES

The aforementioned studies provide significant insight into the interaction between a streamwise-oriented vortex and a wing. These previous investigations have not, however, addressed the following aspects of the flow physics:

The relationship between the streamwise development of the axial velocity, the axial component of vorticity, and the circulation and the radius of the impinging vortex. As the incident vortex approaches the follower wing it is distorted; this distortion has not yet been addressed.

The degree of dominance of the upwash and downwash of the incident vortex in relation to the upwash induced by the follower wing in absence of the incident vortex. The incident vortex creates a region of upwash and downwash on either side of its center. As the incident vortex approaches the follower wing, these regions of vertical velocity interact with both the upwash induced by the follower wing and are influenced by the upstream blockage that the wing creates. This concept has not been pursued.

The unsteady nature of the incident vortex upstream of the follower wing in relation to the degree of time-averaged distortion of the vortex. No quantitative insight is available on the unsteady characteristics of the incident vortex in relation to the spanwise location of the incident vortex relative to the tip of the wing, and thereby the degree of distortion of the vortex as it approaches the wing.

The sensitivity of the foregoing aspects of the vortex-wing interaction to both spanwise and vertical displacements of the centerline of the incident vortex relative to the tip of the wing. Possible distortion and loss of coherence of the incident vortex, as well as either

enhancement or attenuation of the pre-existing tip vortex on the wing in relation to position of the incident vortex have not been pursued..

The definition of new patterns of streamline topology of the vortex wing interaction based on critical point theory. The aforementioned physics of the vortex-wing interaction, including enhancement or attenuation of the tip vortex, has not yet been interpreted in terms of sectional streamline topology, which allows a comprehensive definition of key features of the flow structure.

1.5 RESEARCH OBJECTIVES

This investigation focuses on an in-depth understanding of the physics of interaction between a streamwise-oriented vortex and a wing. The explicit objectives of this investigation are as follows.

(1) *Design and implement a unique experimental system to examine the interaction between a streamwise oriented vortex and a wing.* This system will allow use of both monoscopic and stereoscopic particle image velocimetry (MPIV and SPIV). It will provide the possibility for two wings to be displaced independently of one another so that different vortex impingement locations can be analyzed and for the trailer wing to be subjected to vibrations of prescribed amplitude and frequency.

(2) *Determine the flow structure of the vortex-wing interaction upstream of the wing.* Of interest will be how the blockage of the downstream wing influences streamwise

development of the structure of the approaching vortex, especially near the leading edge of the trailer wing.

(3) *Characterize the flow structure of the vortex-wing interaction along the chord and downstream of the trailer wing*. Of primary interest will be the effect that the incident vortex has on the tip vortex formed on the trailer wing, particularly its enhancement or attenuation, and the possible distortion or disintegration of the incident vortex as it encounters and moves along the follower wing.

(4) *Reveal the basic physics of vortex-oscillating wing interaction*. For the case of a steady streamwise vortex impinging upon, or adjacent to, the tip region of a wing subjected to prescribed amplitude and frequency of oscillation, determine new types of patterns of vortex interaction and distortion.

Common to all of the foregoing objectives are the following experimental and post-processing techniques. MPIV and SPIV will lead to representations of the flow structure that include iso-surfaces, section slices, streamlines, and contours on cross-sectional cuts. Components of velocity and vorticity, root-mean-square of streamwise velocity deficit, and streamwise vorticity, will be determined in relation to swirl ratio, and streamline patterns. Experimental findings will be interpreted in conjunction with theoretical concepts regarding the structure and stability of a columnar vortex.

Figure 1.1: A group of northern bald ibises flying in formation. Portugal et al. (2014)

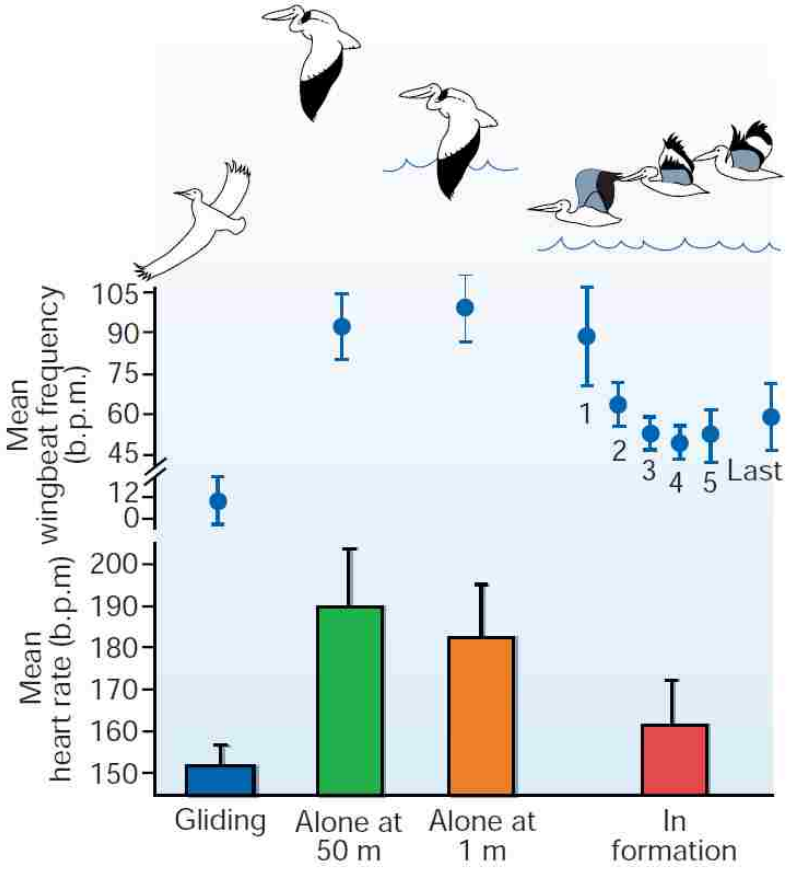

Figure 1.2: Heart rates and wingbeat frequencies for gliding of pelicans: alone at 50m above water; alone at 1m above water; and in formation. Weimerskirch et al. (2001)

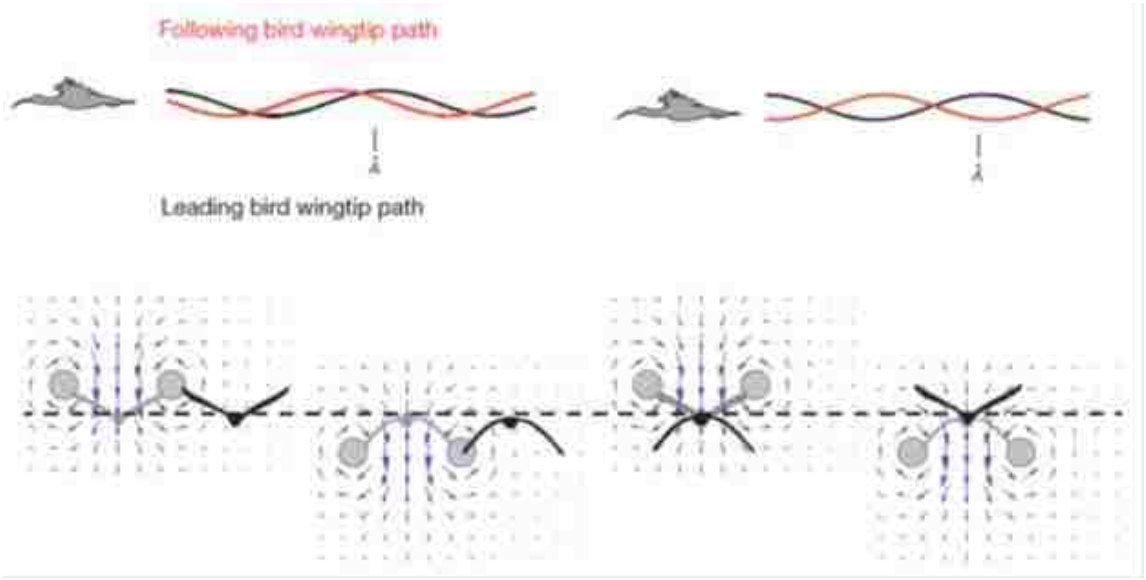

Figure 1.3: The top set of images shows the difference between the leading bird wingtip path (black) and the following bird wingtip path (red) for formation flight (left) and inline flight (right). The bottom set of images shows how the following bird (black) positions its wings in the airflow created by the leading bird (grey). Portugal et al. (2014)

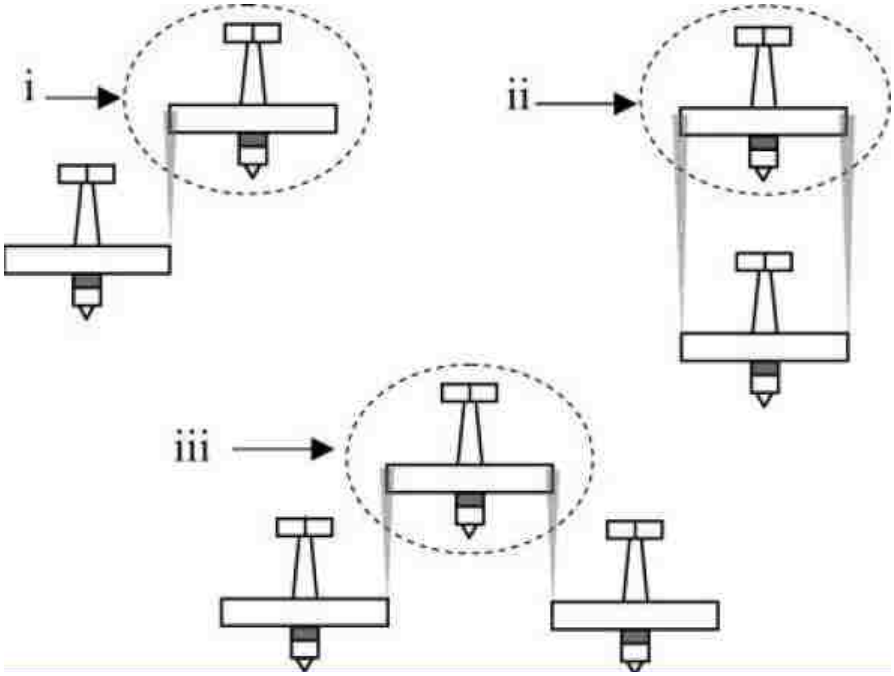

Figure 1.4: Three possible arrangements for formation flight: (i.) echelon, (ii.) inline, (iii.) chevron. Bangash et al. (2006)

Figure 1.5: Smoke visualization of the impingement of a tip vortex shed from a leading aircraft onto the wing of a downstream aircraft. This image was taken as a part of NASA Dryden's Autonomous Formation Flight Project and features a pair of F/A-18s. Thomas (2001)

Figure 1.6: Smoke visualization of a vortex shed from the forebody of an aircraft. Vortex bursts upstream of the fin. Moses (1997)

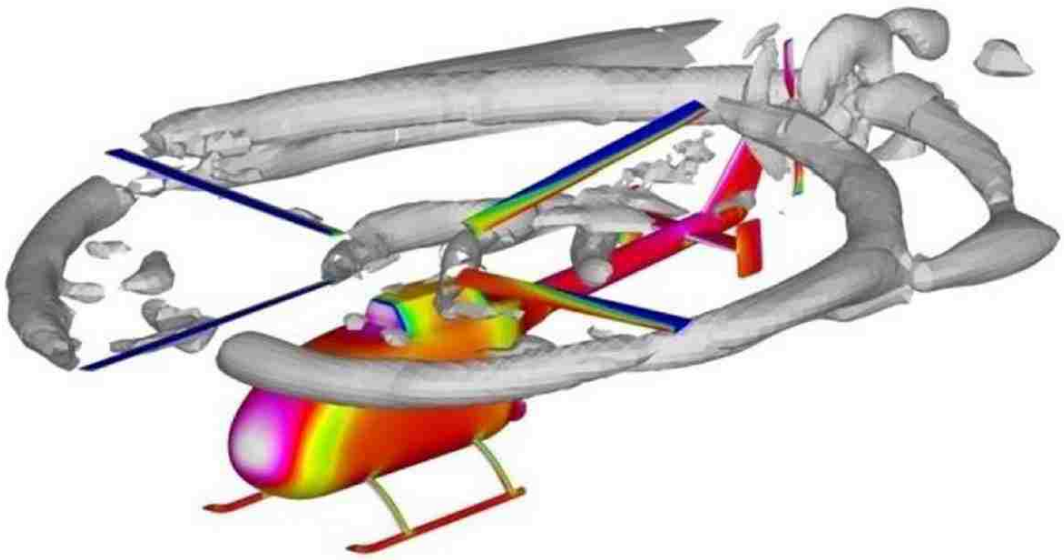

Figure 1.7: Iso-surfaces that show the complexity of vortex-wing interaction for helicopter rotor blades. Raffel (2000)

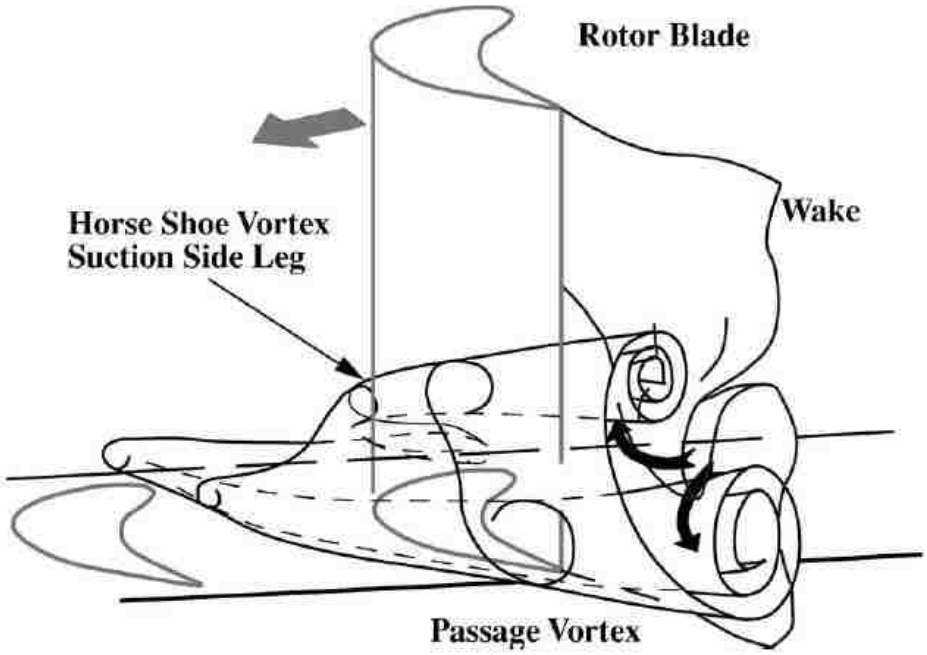

Figure 1.8: Schematic of the roll-up mechanism of the wake into vortices on a turbomachinery blade. Schlienger et al. (2005)

CHAPTER 2

EXPERIMENTAL SYSTEMS AND TECHNIQUES

This chapter provides an overview of the experimental systems and visualization techniques used in this investigation of vortex-wing interactions. The systems included a water channel, an experimental setup with wing configurations at arbitrary position and spacing, and motion control. The quantitative visualization techniques involved both monoscopic and stereoscopic particle image velocimetry.

2.1 WATER CHANNEL

The free-surface water channel, shown in Figure 2.1, located in Packard Lab room 174, was used for experiments. This water channel has a test section length of 4877 mm, a width of 927 mm, and a depth of 610 mm. Flow conditioning for this water channel includes a distributor attached to the entrance of the inflow reservoir, two successive sections of honeycomb, five screens, and a 2:1 contraction which results in a turbulence intensity below 0.5%. The freestream velocity used in all experiments was U = 158 mm/s in the test section, which corresponded to a Reynolds number Re = 8000 based on wing chord. The test section is made of Plexiglas, which allowed implementation of the visualization techniques described below.

2.2 EXPERIMENTAL SYSTEMS

The experimental setup used in these experiments featured two wings, which were positioned such that the vortex-wing interaction could be examined. To allow full control over this arrangement, the leader wing has the capability of independent motion along three axes, and the angle of attack of both wings can be adjusted. Additionally, the leader wing extends upwards through the free surface; therefore only the lower wing tip creates a tip vortex. Figure 2.2 shows this setup.

Two different configurations of this setup were utilized, with one featuring a stationary follower wing and the other an oscillating follower wing. The leader wing is a NACA 0012 airfoil which has chord C = 50.8 mm, angle of attack α = 16° and is oriented vertically. The stationary follower wing is a clear acrylic flat plate with chord C = 50.8 mm, thickness t = 1.5875 mm, span b = 203.2 mm, and angle of attack β = 4°. The spanwise distance between the two wings is Δx = 152.4 mm. For the case of the oscillating follower wing, shown in Figure 2.3, the leader wing is the same as the aforementioned, but the angle of attack α = 8°. The follower wing is a clear acrylic flat plate with chord C = 50.8 mm, thickness t = 3.175 mm, span b = 203.2 mm, and angle of attack β = 0°. The spanwise distance between the two wings is Δx = 254 mm.

2.3 MOTION CONTROL

To allow precise movement of the wings in these experiments, motion control was used. This system utilized two Compumotor stepper motors controlled by a National

Instruments P70530 micro-stepper drives, a National Instruments PCI-7344 4-card, and a UMI-7764 indexer box.

Two forms of motion control were used in these experiments. Motion control was used to accurately move the experimental system in the streamwise direction through the laser plane; this allowed volume reconstruction. Motion control was also used for the oscillation of the vertical position of the follower wing. This was achieved by applying a constant rotation to a wheel which had an off-center hole connected to the follower wing via an arm. This connection translated the rotational motion of the wheel into sinusoidal motion in the vertical direction; the specifics of that motion are available in Figure 2.4.

2.4 QUANTITATIVE IMAGING TECHNIQUES

In order to quantitatively analyze the flows under consideration in these experiments, particle image velocimetry (PIV) was used. This technique utilizes a dual-pulsed Nd-YAG laser to illuminate a plane of the flow, which was created by transmitting the laser through two 25 mm cylindrical lenses and a 1000 mm spherical lens. This plane was then turned to the desired orientation using a mirror. The frequency of this laser illumination had different values during the experiments: f = 14.29 Hz for the stationary follower wing; and f = 4 Hz and 10 Hz for the oscillating follower wing. The flow was seeded with 11 μm hollow metallic coated plastic spheres which have a specific density of 1.96 g/cc. As the laser pulses, the particles in the laser plane are illuminated, allowing them to be captured by TSI PowerView Plus cameras with a CCD array of 1600

x 1200 pixels. Two different PIV techniques were used in these experiments: monoscopic; and stereoscopic.

2.4.1 Camera Arrangements

Monoscopic PIV uses one camera to capture the field of view, resulting in a vector field composed of the two in-plane components of velocity. This technique was used along the chord of the trailer wing in order to collect data near the surface of the wing, which is difficult with other techniques. To allow the camera to have the most effective view, a mirror was inserted downstream of the wing at an angle of 45°; this gave the camera a direction of view normal to the laser plane without affecting the vortex development and interaction incident upon, and along, the wing. In Appendix A the mirror was shown to be located sufficiently far downstream such that it did not influence the flow around the trailer wing.

Stereoscopic PIV utilizes two cameras to capture all three velocity vectors in a field of interest. This technique was used upstream of the trailer wing, with each camera at a 40° angle. To eliminate refraction, prisms were constructed of 9.52 mm thick Plexiglas and filled with distilled water. They were designed such that the face of the prism closest to the camera was normal to the line of sight through the camera lens. Figure 2.5 shows a plan view of the arrangement of the cameras and the liquid prisms for both SPIV and MPIV. Details of the experimental test section together with components for the MPIV and SPIV systems are illustrated in Figure 2.6.

2.4.2 Image Analysis

To generate the quantitative vector fields from the particle images, several different steps must be taken. Before the data are acquired, the PIV system must be calibrated. This procedure defines the relative positions and angles of the camera(s) to the plane of the laser sheet, and also, in the case of SPIV, to each other. This calibration is performed by aligning a calibration plate with the laser sheet; the calibration plate used for this work had a 10 mm grid defined on the y-z plane, where every second point is on a raised surface offset 1mm from the base plane. After the calibration plate is aligned with the laser sheet the cameras are focused on the surface of the plate.

For MPIV, this process simply involves orienting the mirror at an angle of 45° with respect to the plate, arranging the camera perpendicular to the direction of flow, and focusing the camera on the plate. The calibration process for SPIV begins with orienting the cameras at 40° with respect to the plate on opposite sides of the water channel, and focusing them on the laser plate. To account for the varying distance between the camera and the calibration plate, the angle between the CCD array within the camera and the lens of the camera must be adjusted. The goal of this adjustment is to have the image, object, and lens planes all intersect at a line, which allows the entire object plane to be in focus. After the camera(s) has been properly focused on the calibration plane, images are taken. These images of the calibration plate are analyzed using Insight 4G, which generates a calibration file defining the relative positions between the camera(s) and the laser sheet.

2.4.3 Image Processing

During data capture the camera acquires a pair of images, designated as A and B, which are combined to create the vector fields. Images A and B are taken at times t_0 and

$t_0 + \Delta t$ respectively, where t_0 is some instant in time and Δt is a small time later. Δt is selected such that the particles image will not move more than one-third of the width of the interrogation window between the two frames. The interrogation window is the region of the pattern of particle images used to define each velocity vector. If, however, there is a substantial out of plane velocity component, such as occurs when the laser sheet intersects the axis of a trailing vortex, an additional criterion must be satisfied: the time delay Δt must be such that the distance the particle travels through the laser sheet is less than one-fourth the sheet thickness.

The first step of evaluation of the patterns of particle images is pre-processing, which enhances the pattern of particle images to ensure that subsequent processing creates the most accurate velocity vectors from the images. An image generator is used to create an image that is a map of the minimum intensity for every pixel. In other words it is an image which shows everything but the particles, such as the wing or supports. This image is subtracted from every image, creating images which ideally only show the particles. For MPIV a horizontal mirror operation is also needed to account for the physical mirror used in those experiments.

A classic PIV algorithm was employed for processing; it used interrogation windows 32 by 32 pixels, Figure 2.7 shows two particle images and the histogram created by the PIV algorithm. A Nyquist grid engine, which creates a grid with 50% overlap was used. This grid engine has low computation time, allowing more images to be captured and analyzed. The correlation engine used was developed by Hart (1998); it only examines the most significant pixels in the interrogation window. This reduces the effects

of low level noise on the vector calculation. A Gaussian peak engine was used which fits a Gaussian curve to the highest pixels, allowing for sub-pixel accuracy when calculating the magnitude and direction of the velocity vector.

After the velocity vectors are calculated, post-processing is used to both validate and condition this vector field. First local vector validation is performed using a median test to determine if any component of a vector is different enough from its neighbors that it could not accurately represent the flow. After these vectors are eliminated they are replaced using a technique based on the local mean which is generated using a 5 by 5 grid centered on the missing vector. Finally a smoothing pass is performed, with each vector being replaced by the Gaussian-weighted mean generated using the 5 by 5 nearest vectors and a smoothing kernel $\sigma = 0.8$. Figure 2.8 includes representative images from each step of image processing.

At this point, the processes for MPIV and SPIV diverge. In MPIV the vector array created in the previous step is mapped onto the object plane using the calibration file, which yields the in-plane components of velocity. In SPIV there are two cameras, designated 1 and 2, which have each yielded an array of two dimensional velocity vectors. Insight combines these vector arrays using the calibration file in order to determine an array of three dimension velocity vectors on the object plane. For all of the experiments, a peak-to-noise ratio larger than 2 was achieved for the vast majority of interrogation windows.

To obtain accurate averaged representations of the vectors , both time and phase averaging were used; 100 images were used for time averaged MPIV, 80 images were

used for phase-averaged MPIV, and 150 for time-averaged SPIV. This averaging further reduced the likelihood of a bad vector being present in the final data. A discussion on the number of images required for time averaging is given in Section 2.5.3 which deals with error analysis.

2.4.4 Volume Reconstruction

Two dimensional arrays of velocity vectors were collected at multiple streamline locations which varied by experiment, but generally extended from 1C (one wing chord) upstream of the follower wing to 2C downstream. These data planes were close enough together that the flow in-between these planes could be accurately interpolated. The two dimensional arrays were combined to form a three dimensional array which allowed for visualization of the flow field as a volume, and, for SPIV, the calculation of the two out-of-plane vorticity components ω_y and ω_z.

2.5 ERROR ANALYSIS

2.5.1 Random Error

Random error encompasses any non-repeatable error which is not due to variations in the flow field. This error can be caused by slight difference in lighting intensity, irregularities in particle densities, electronic noise in the camera circuits, etc. Regardless of the cause of the random error, the effect is always the same, to cause the

same particle to appear slightly different between the two exposures, denoted as frames A and B in Section 2.4.3.

This difference is quantified as the rms error in determining the centroid of the particle image $\sigma_{\Delta X}$. This term is used to calculate the rms error of the velocity measurement $\sigma_u = \sigma_{\Delta X} / (M_0 \Delta t)$, where M_0 is the image magnification and Δt, as previously defined, is the time between exposures. $\sigma_{\Delta X} = c_\tau d_\tau$ where c_τ is a constant dependent on the ability of the analysis procedure to determine the particle displacement between images and d_τ is the diameter of the particle on the image plane. c_τ can be estimated utilizing the displacement of a particle in pixels, which in this case is approximately 3 pixels, yielding a c_τ of between 0.04 and 0.06. The diameter of the particle on the image plane $d_\tau = M_0(1.5\delta z\lambda + d_p^2)$ where δz is the depth of field, the laser wavelength λ = 532 nm, and the particle diameter d_p = 11 μm. $\delta z = 4f^{\#} \lambda (1 + 1/M_0)^2$ where the f-stop $f^{\#} = 8$. Finally, $M_0 = Z_0/z_0$ where the distance from the image plane to the lens is Z_0 = 0.0381 m and the distance from the lens to the object plane z_0 = 1.143 m. Evaluating all of the previously mentioned terms yields an in-plane σ_u = 0.051 to 0.071 of the freestream velocity. These calculations were performed based on the work of Adrian and Westerweel (2011). In the present investigation, this random error is significantly reduced by the use of either phase or time-averaging.

According to Lawson and Wu (1997), the error in the out-of-plane velocity can be calculated as a function of in-plane error and the camera angle. The camera angle used in these experiments is 40° which corresponds to an error ration e_r = 1.05. Therefore the out-of-plane error σ_u = 0.054 to 0.075.

2.5.2 Bias Error

Bias error covers any error which is not random in nature, but is instead systematic. A source of bias error for PIV comes about when the size of the particle on the image plane is small relative to the size of the pixels. Since the PIV technique is limited by the pixel size, it cannot resolve any smaller than that length scale. For these experiments the ratio of the particle image diameter to the pixel pitch d_τ/d_r is approximately 1.75. According to Adrian and Westerweel (2011) this ratio relates to error, and for these experiments the bias error associated with a Gaussian fit is no more than 1%.

Another source of bias error comes from calculating out-of-plane vorticity, which requires the comparison of several nearby velocity vectors. Soria et al. (1995) showed that the distances between these vectors can cause errors which predictably underpredict the vorticity in the core of an Oseen vortex, which is a good approximation of the incident vortices seen in these experiments. Consideration of six velocity vectors along the radius of the vortex, defined as the radial distance from the vortex axis to the maximum tangential velocity, gives a maximum out-of-plane vorticity bias error of 3% along the vortex axis. This bias error decreases linearly as the radial distance from the vortex axis increases.

2.5.3 Phase and Time Averaging Error Reduction

To reduce the random error discussed previously, both phase and time averaging were used. These types of averaging reduce any non-systematic errors that may occur

during experiments. To determine how many averages are needed for the images to converge, a large data set containing 200 images was taken. Averages were then constructed using 20, 40, 60, 80, 100, 120, 140, 160, 180 and 200 images from this set. Figure 2.9 shows how the (color) contours of streamwise vorticity ω_x at different numbers of averages compare to the final (black line) contours constructed with all 200 images. Examining the (color) contours constructed using 20 and 40 images, the contours do not align with the black lines which represent the final case constructed with 200 images. As the number of averages of the (color) contours increases the match between them and the (black) lines improves. By an average of 80 images, the fewest used for averaging in these experiments, there are only very slight differences.

As a further representation of the degree of convergence in relation to the number of images averaged, two different approaches were employed for the magnitude of the inplane velocity over the area of the vortex, by the area considered is a square whose sides are coincident with the lowest level vorticity contour. The first calculation was performed by comparing the velocity at N averaged images to N + 10 averaged images, while the second compared N averaged images to the final image. The percent difference as a function of the number of averages is shown in Figure 2.10. It is evident that for both methods of comparison, the percent difference of the value of velocity drops quickly as the number of averages increases.

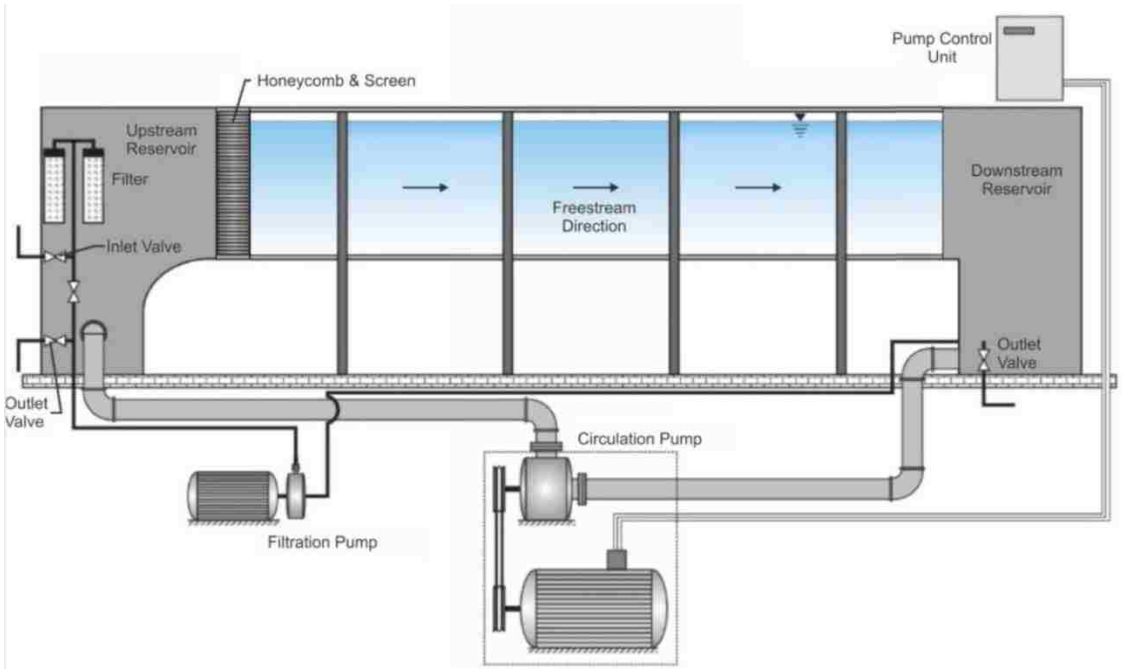

Figure 2.1: Water channel system in Packard Lab room 174.

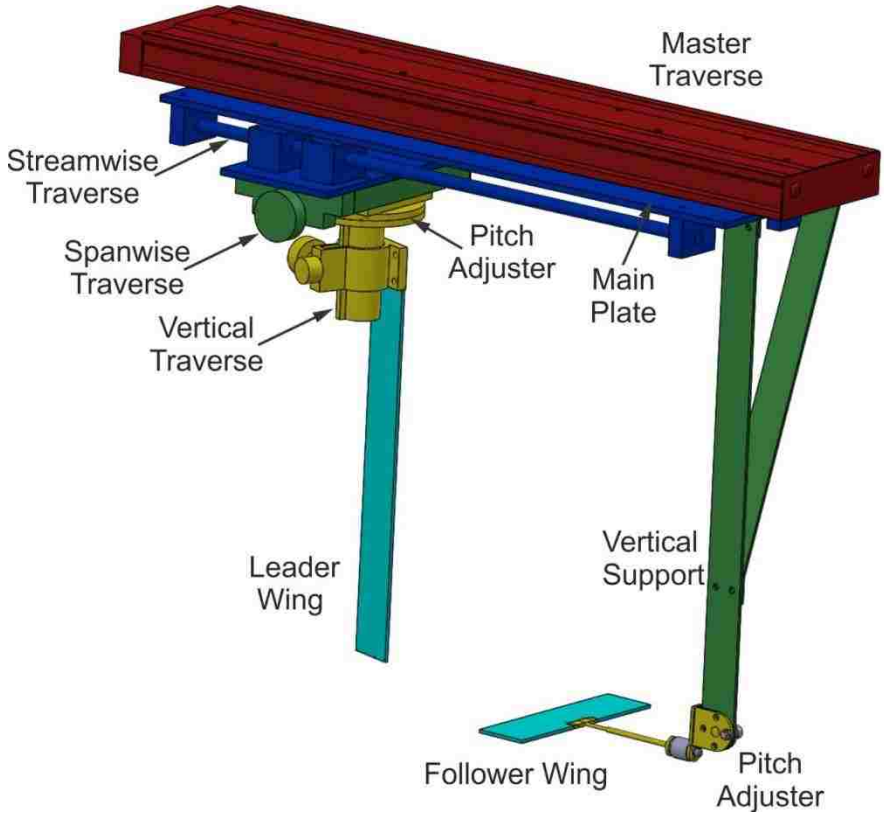

Figure 2.2: Experimental setup for steady vortex-wing interaction experiments.

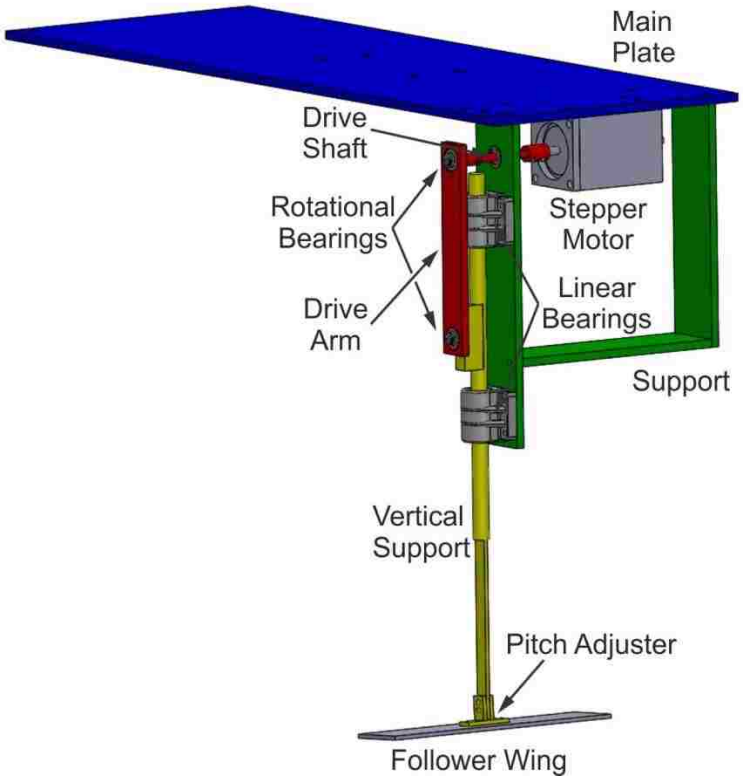

Figure 2.3: Experimental setup for unsteady vortex-wing interaction experiments.

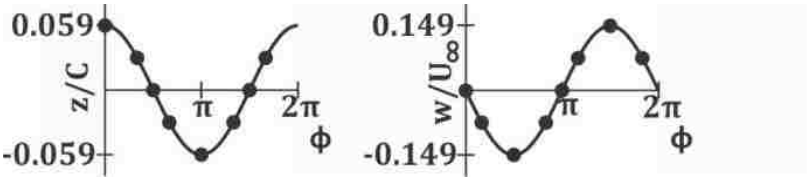

Figure 2.4: Vertical position and velocity of the wing as a function of phase angle for the vortex-oscillating wing experiments.

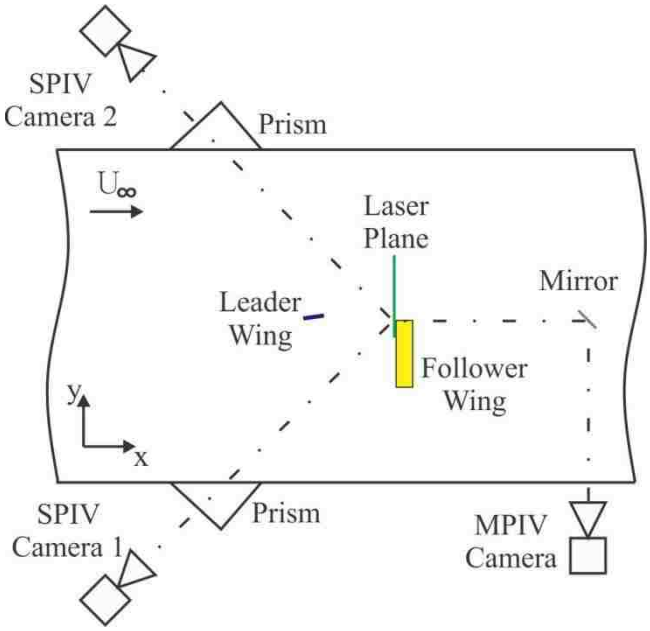

Figure 2.5: Plan view of camera arrangement for monographic PIV (MPIV) and stereographic PIV (SPIV).

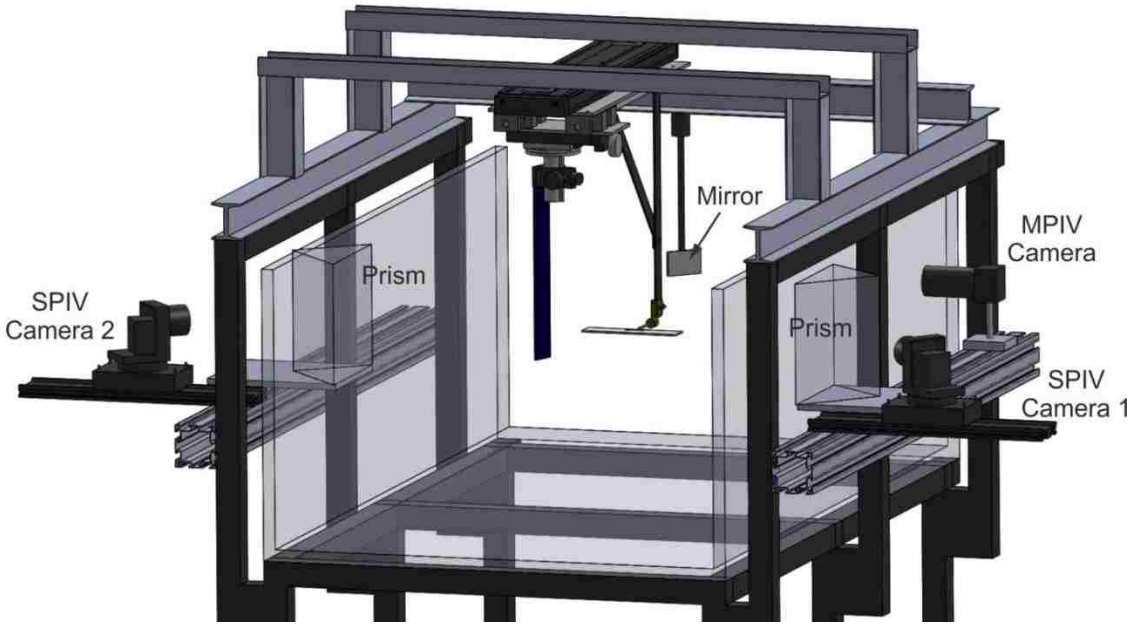

Figure 2.6: Setup of monographic PIV (MPIV) and stereographic PIV (SPIV).

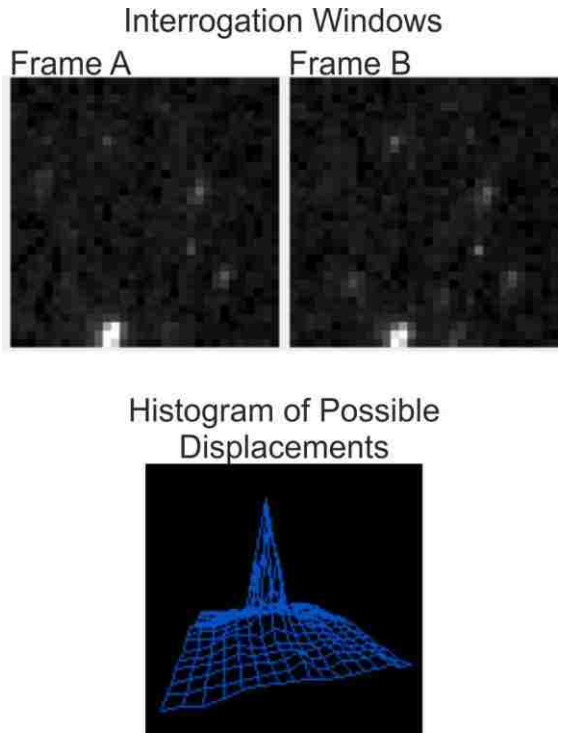

Figure 2.7: Image of interrogation process. The top two images are particle images of the same location window for the two different frames. These images are statistically compared to generate the histogram of possible displacements seen in the bottom image. The highest peak in the histogram indicates the most probable displacement, and therefore the most probable velocity.

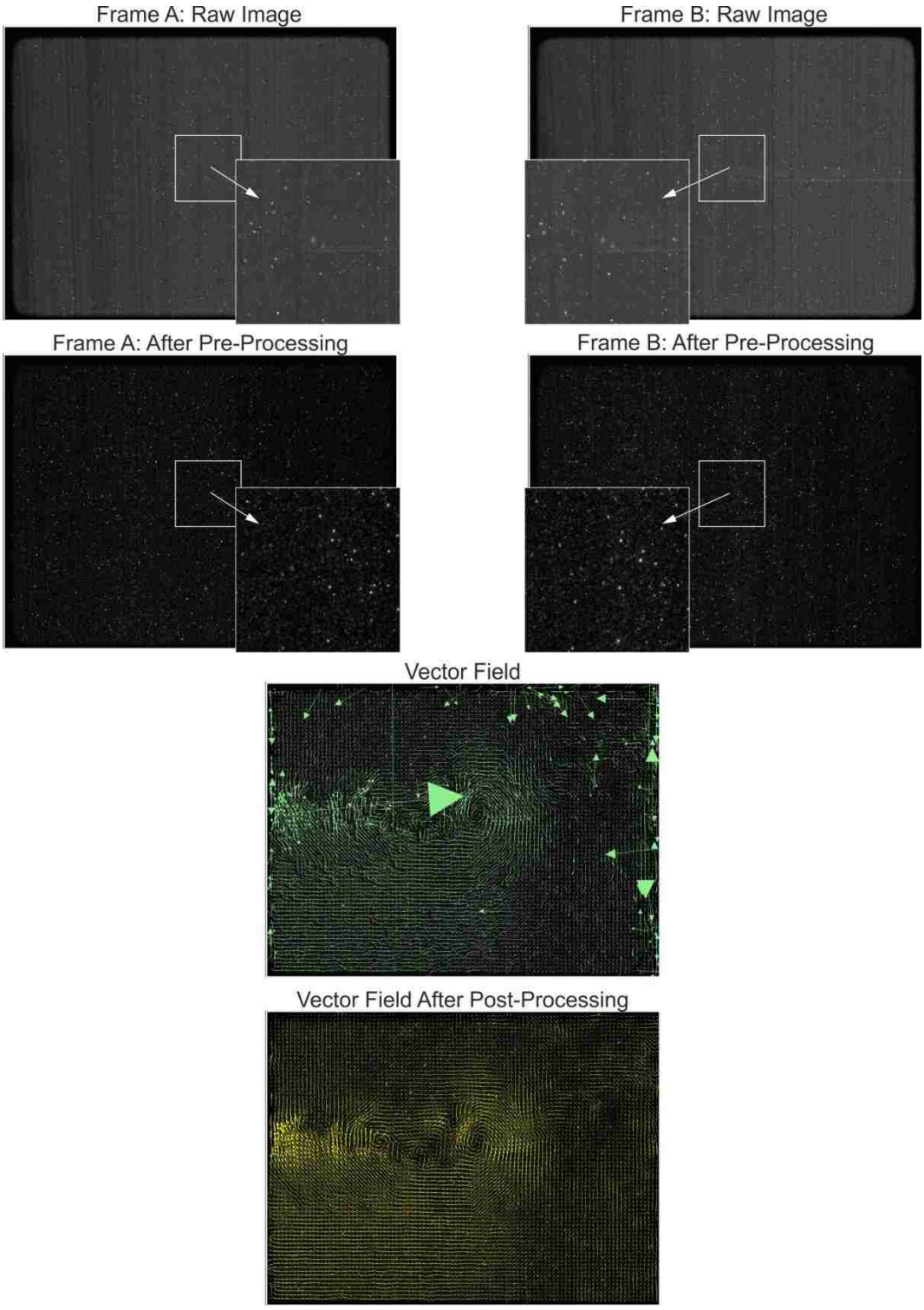

Figure 2.8: Image processing for PIV.

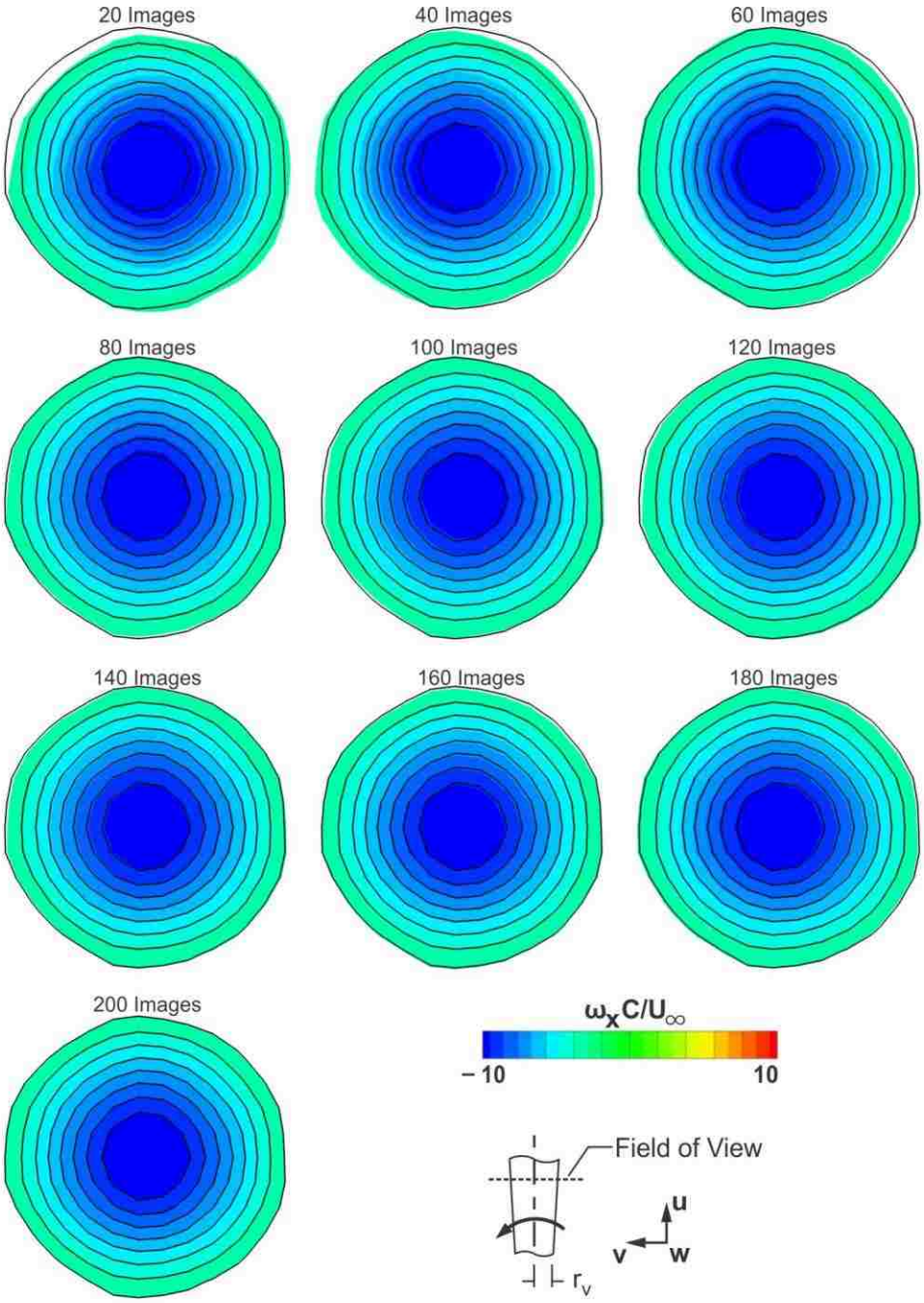

Figure 2.9: Color contours and (black) lines of constant values of streamwise vorticity for a vortex shed from a NACA 0012 airfoil with C = 50.8 mm at a distance of x/C = 5, r/C = 50 from the trailing edge of the wing. The lines of streamwise vorticity were created using 200 averaged images and the color contours of streamwise vorticity were created using increasing numbers of images. The maximum magnitude of vorticity for the average of 200 images was $\omega_x C/U_\infty$ = -11.54, and the largest deviation from this value was for an average of 20 images corresponding to $\omega_x C/U_\infty$ = -12.12.

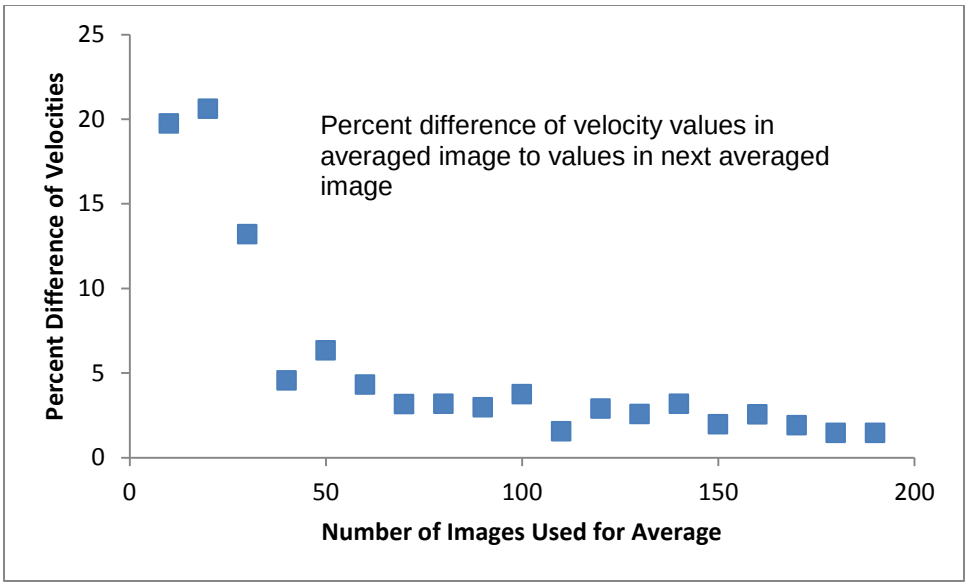

(**a**)

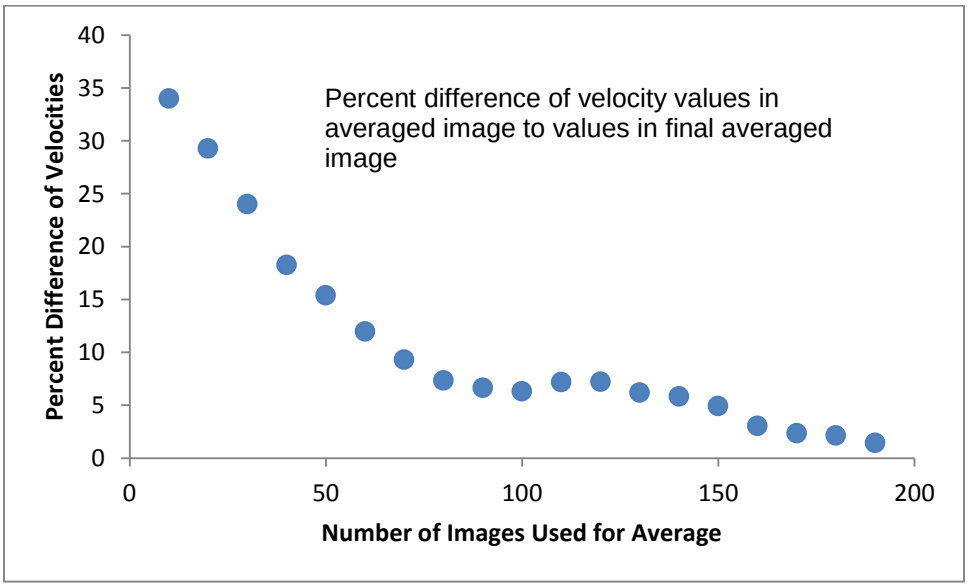

(**b**)

Figure 2.10: Image averaging for a vortex shed from a NACA 0012 airfoil with C = 50.8 mm at a distance of x/C = 5, r/C = 50 from the trailing edge of the wing. (**a)** Comparison of velocity at N averaged images to N + 10 averaged images. (**b)** Comparison of velocity at N averaged images to 200 averaged images.

CHAPTER 3

STRUCTURE OF A STREAMWISE-ORIENTED VORTEX INCIDENT UPON A WING

3.1 OVERVIEW

Interaction between a streamwise-oriented vortex and a fin, blade, or wing has emerged as a critical class of flow-structure interaction, with important consequences for both unsteady and steady loading. Examples include: buffeting of a fin or tail of an aircraft by the vortex originating from an upstream canard; steady and unsteady loading of the downstream blade in a rotating machine arising from the tip vortex generated from an upstream blade; loading of a helicopter rotor due to the tip vortex from a preceding rotor; and alteration of the lift and drag, as well as potential buffeting, of a follower wing due to the streamwise vortex originating from the leader wing in formation flight. This latter type of interaction is not limited to a small number of aircraft and wings of large or moderate scale, but extends to a large number of very small-scale of micro air vehicles in a swarm or flock that may be deployed for atmospheric surveillance (Kroo, 2004). In the following, the essential features of the foregoing interactions are summarized.

The foregoing advances provide a basis for gaining new insight into the internal structure of the vortex incident upon simulated fins, tails, plates and wings, and the manner in which it is altered in upstream regions. In particular, the heretofore unclarified relationships between the deficit of the streamwise velocity, the magnitudes of streamwise and azimuthal vorticity, the upwash and downwash, the root-mean-square of

the velocity and vorticity fluctuations, and the swirl ratio will be addressed in relation to the degree that the tip of the downstream wing penetrates the incident vortex.

3.2 EXPERIMENTAL SYSTEMS AND TECHNIQUES

A free-surface water channel was used for experiments, where the water channel had a test section with a length of 4877 mm, a width of 927 mm, and a depth of 610 mm. The freestream velocity was U_∞ = 158 mm/s, which corresponded to a Reynolds number of 8000 based on the wing chord. The turbulence intensity was 0.3%. The experimental setup is shown in figure 3.1. The leader wing is a squared tip NACA 0012 airfoil which has chord C = 50.8 mm, angle of attack α = 16° and is oriented vertically. This angle of attack was selected to generate a tip vortex having a dimensionless circulation similar to that in the computations of Garmann and Visbal (2014a & 2015a). The follower wing is a clear acrylic flat plate with chord C = 50.8 mm, thickness t = 1.58 mm, span b = 203.2 mm, and angle of attack β = 4°. The streamwise distance between the two wings is Δx = 152.4 mm.

The vertical Δz and spanwise Δy offsets were defined by the trajectory of the tip vortex shed from the leader wing. Preliminary stereo particle image velocimetry (SPIV) images were acquired to determine which values of vertical and spanwise offset led to impingement of the tip vortex from the leader wing on the tip of the follower wing. This location was defined by the leader wing offsets Δy_0 and Δz_0. In this investigation, four

different values of spanwise offset Δy were examined, $\Delta y = \Delta y_0$ + 12.7 mm, Δy_0 + 6.35 mm, Δy_0, and Δy_0 - 31.75 mm, while $\Delta z = \Delta z_0$, i.e., no offset in the vertical direction.

To quantitatively visualize the structure of the vortex, SPIV was employed. It provides all three components of velocity. The flow was seeded with 11 μm hollow metallic coated plastic spheres, which provide 15-20 particle images in the interrogation window of 32 x 32 pixels. To illuminate the spheres, a 3 mm thick laser sheet was produced by a dual-pulsed Nd-YAG operating at 14.29 Hz. Images were acquired from each camera simultaneously, where each had a CCD array of 1600 x 1200 pixels. In this SPIV arrangement, the cameras were placed upstream of the laser plane at a 40° angle from the flow, thereby allowing an unobstructed view of the laser plane. The images from the two cameras were then evaluated using a cross-correlation technique with 50% overlap, yielding 8432 vectors in the field of view. Each pixel was 47.36 μm/px, which corresponds to an interrogation window width of 1515 μm.

Both the in- and out-of-plane uncertainties were calculated using the technique described by Adrian and Westerweel (2011). The RMS random error for the in-plane velocity is between 1.0% and 1.4% of the freestream velocity, furthermore, the RMS random error is between 1.2% and 1.6% of the freestream velocity for the out-of-plane velocity component. For this SPIV setup, the pixel size is large compared to the particle image diameter and therefore the bias error is small in comparison to the RMS random error.

For each experimental configuration, image acquisition was performed at 6.35 mm intervals from 50.8 mm to 6.35 mm upstream of the leading edge of the follower

wing. At each of these locations, 150 images were captured; these images were time-averaged to produce the final images. The flow structure at different streamwise locations was examined by translating the wing system to the desired location in the streamwise direction. The leader wing could move independently from the rest of the system, which allowed examination of the flow at successive spanwise locations of the leader wing. At each location, the individual images on the crossflow planes of the vortex, taken at successive streamwise locations, were combined to provide iso-surface representations of the three-dimensional flow field. These fields contain 67 456 vectors, and allowed calculation of all three components of vorticity.

3.3 DISTORTION OF VORTEX STRUCTURE DUE TO IMPINGEMENT

3.3.1 Initial Structure of Undistorted Vortex

The velocity profiles of the trailing vortex generated from the leader wing, at a location upstream of the region of significant flow distortion as the follower wing is approached, were acquired in absence of the follower wing and are compared in figure 3.2 with previous investigations at Reynolds numbers at least an order of magnitude larger than the present study: Devenport et al (1993), Zheng and Ramaprian (1993); and Inasawa et al (2012). The distribution of normalized azimuthal velocity $u_\theta/(u_\theta)_{\max}$ is indicated in figure 3.2a and normalized axial velocity deficit $(U_\infty\text{-}u)/(U_\infty\text{-}u_{min})$ in figure 3.2b. For the present experiment, the dimensional value of maximum azimuthal velocity is $u_\theta/U_\infty = 0.49$, and the maximum axial velocity deficit is $\Delta u = 0.19$. Moreover, the

vortex Reynolds number $Re_v = \Gamma/\nu$ is 2959. In both figures 3.2a and 3.2b, the solid line corresponds to the theoretical *q*-vortex described by Garmann and Visbal (2015a). This *q*-vortex has its origin in the work of Batchelor (1964). These normalized distributions of azimuthal and axial velocity have a similar form for all cases, over the range of the Reynolds number based on wing chord from 8 000 to 250 000. At the highest value of Re = 530 000, there is discernible departure.

For the present investigation, the swirl ratio q = 3.95, and the value of circulation is Γ/CU_∞ = 0.4. This value of q lies above the value of q = $\sqrt{2}$ corresponding to the onset of azimuthal instabilities (Garmann and Visbal, 2014a & 2015a) according to the criterion of Leibovich and Stewartson (1983).

3.3.2 Velocity Defect and Streamwise Vorticity

Figure 3.3 shows iso surfaces of the streamwise velocity deficit $1 - u/U_\infty$, hereafter referred to as velocity deficit, along the axis of the vortex incident upon the leading edge of the wing. These surfaces of velocity deficit increase in both radius and magnitude as the spanwise impingement location $\Delta y/r_v$ is displaced from outboard to inboard. For all but the outboard case, all levels of iso-surfaces increase in radius near the leading edge of the follower wing.

The plot of figure 3.4 shows the maximum velocity deficit $1 - u/U_\infty$ as a function of distance x'/C upstream of the leading edge of the wing. For the outboard and slightly outboard positions of the incident vortex, $\Delta y/r_v$ = 1.25 and 2.5, along with the case of no follower wing, there is a mild increase of velocity deficit as the leading-edge is

approached. Then, in the immediate vicinity of the leading-edge, at x'/C = 0.125, a decrease occurs. On the other hand, for the aligned and inboard cases, the velocity deficit increases rapidly as the leading-edge is approached. For the case of inboard interaction, the magnitude of the deficit increases by approximately a factor of two from x'/C = 1 to x'/C = 0.125. The form of this variation of velocity deficit is detectably distorted relative to the other three variations; such distortion is associated with onset of a large diameter region of high velocity defect that extends well upstream of the leading edge, as indicated in figure 3.3, as well as relatively large rms values of velocity and vorticity, which will be addressed subsequently. It is evident from these plots of figure 3.4, as well as the images shown in figure 3.3, that the upstream influence of the wing extends at least a distance of one chord C, which corresponds to 5 diameters D_v of the incident vortex in absence of the follower wing.

Figure 3.5 shows iso surfaces of the streamwise vorticity $\omega_x C/U_\infty$. The layout of these images and the designated values of $\Delta y/r_v$ correspond to the images of velocity deficit $1 - u/U_\infty$ in figure 3.3. In accord with the surfaces of velocity deficit given in figure 3.3, the patterns of streamwise vorticity are sensitive to changes in the spanwise location of vortex impingement, again indicating upstream influence of the wing. The maximum value of streamwise vorticity is significantly altered, but unlike the surfaces of velocity deficit given in figure 3.3, the outer radii of the lowest level surfaces do not change significantly with either spanwise offset or streamwise position. However, as the location of vortex impingement moves inboard, the length of the highest level iso-surface of $\omega_x C/U_\infty$ = -15 is attenuated, such that for the inboard interaction ($\Delta y/C$ = -0.625, $\Delta y/r_v$

= -6.25) it exists only in the region well upstream of the leading edge of the wing. In other words, the downstream boundary of the highest level iso-surface of $\omega_x C/U_\infty$ = -15 retreats in the upstream direction for increased inboard displacement of vortex impingement; simultaneously, the diameter of this iso-surface decreases.

Further information related to the radial distribution of the streamwise vorticity can be determined by examining the distribution of circulation within the vortex. Although the total circulation of the vortex remains essentially constant over the range of streamwise locations in the field of view, varying by less than 3%, the radial distribution of the circulation is, of course, not constant. Herein the core of the vortex is defined as having a radius r^* that contains half of the total circulation of the vortex. Calculations show that the magnitude of r^* increases in the streamwise direction by as much as 30% as the leading edge of the wing is approached. Correspondingly, the magnitude of the peak vorticity along the centerline decreases by 29.7%. Taken together with the decrease in the higher levels of axial vorticity indicated in the iso-surfaces of figure 3.5, this observation indicates that the average streamwise vorticity in the core of the vortex of radius r^* decreases, while the average streamwise vorticity outside the core increases, as the vortex develops in the streamwise direction. Therefore, the aforementioned decrease of maximum axial (streamwise) vorticity is due to a redistribution of that vorticity out of the vortex core.

3.3.3 Azimuthal Vorticity

Figure 3.6 shows time-averaged slices of the azimuthal vorticity $\omega_\theta C/U_\infty$, which is dominated by the derivative of streamwise velocity u in the radial direction, $(\partial u/$

$\partial r)C/U_\infty$, relative to the other component of azimuthal vorticity, which is the derivative of the radial velocity in the streamwise direction, $(\partial u_r/\partial x)C/U_\infty$. The highest levels of azimuthal vorticity take the form of well-defined rings which are centered on the axis of the vortex. As the spanwise location of vortex impingement moves from outboard to inboard, both the maximum value of azimuthal vorticity and its outer radius increase. An increase in the magnitude and outer radius of the ring of azimuthal vorticity can also be seen for decreasing values of x'/C, that is, for locations closer to the leading edge of the wing. These trends can be compared with the increase in velocity deficit indicated in figure 3.3. In essence, as x'/C decreases, the maximum values of both velocity deficit and azimuthal vorticity increase.

Garmann & Visbal (2015a) show a helical instability around the perimeter of their incident vortex for streamwise locations where the swirl ratio $q < \sqrt{2}$; this instability is evident in their instantaneous images. As indicated on the images of figure 3.6, the magnitude of the swirl ratio drops below this threshold value for both $\Delta y/r_v = 0$ and -6.25, at $x'/C < 0.5$ and 0.75 respectively. In these regions, azimuthal vorticity has its largest magnitudes, corresponding to the same region as the helical instability observed by Garmann & Visbal (2015a).

3.3.4 Cross-Comparisons of Velocity Defect and Components of Vorticity

Figure 3.7 provides a direct comparison of time-averaged slices of the flow structure for two selected spanwise locations $\Delta y/r_v$, of the incident vortex. Representative inboard ($\Delta y/r_v$ = -6.25) and outboard ($\Delta y/r_v$ = 1.25) interactions are compared. For the inboard interaction, the following alterations are evident relative to the outboard

interaction: enhancement of the magnitude and radial extent of the region of velocity defect $1 - u/U_\infty$; attenuation of the highest levels of streamwise vorticity $\omega_x C/U_\infty$; and enhancement of the magnitude and radial extent of azimuthal vorticity $\omega_\theta C/U_\infty$.

Focusing on the comparison of the cross-sectional cuts of velocity defect and axial vorticity given in figure 3.7, as well as the iso-surfaces of these same parameters given in figures 3.3 and 3.5, it is evident that there is a close relationship between enhancement of the velocity defect and attenuation of the peak value of axial vorticity. A direct, quantitative comparison is given in figure 3.8, which shows superposition of (dark blue line) contours of constant axial vorticity and shaded regions of velocity defect for three impingement locations on a longitudinal cut through the vortex. In all cases, the tip *B* of the moderate level of velocity defect $1 - u/U_\infty$ = 0.3 extends well upstream through the center of the vortex, and immediately downstream of this tip, the width of the region of vorticity defined by the lowest level contour $\omega_x C/U_\infty$ = -15 rapidly decreases and goes to zero at the location *A*. In other words, occurrence of a sufficiently large magnitude of the velocity defect promotes attenuation of high level vorticity along the vortex axis.

The axial vorticity was integrated over the entire cross-section of the vortex at successive streamwise locations along the axis of the vortex, and the magnitude of the circulation was found to be constant within 3%. Herein, the core of the vortex is defined as the inner portion that contains one-half of the total circulation; it has a radius designated as r*. The dashed line on figure 3.8 defines the locus of r*, which increases

over the streamwise extent of the vortex by approximately 33%, 21%, and 10% for the inboard, aligned, and slightly outboard cases respectively.

As indicated in the foregoing, with increasing streamwise distance along the vortex, the defect of axial velocity increases, the magnitude of the maximum value of the axial vorticity decreases, the circulation remains constant, and the radius r^* based on half circulation increases. These changes in the vortex structure can be related to the adverse pressure gradient in the streamwise direction created by the downstream wing. In view of the fact that these parameters change rapidly over a small streamwise distance, a process of rapid distortion occurs, and inviscid effects dominate.

The inviscid theoretical model of Batchelor (1964) provides a guide for interpretation of the foregoing relationships. It focuses on the effect of streamwise pressure gradient, which can be related to the streamwise velocity variation in the inviscid vortex core via Bernoulli's equation. If the pressure in the core increases in the axial direction, corresponding to an adverse pressure gradient, then Batchelor's (1964) theory indicates that the core diameter will increase provided that the circulation remains constant. Therefore, with this condition on circulation, an adverse pressure gradient is associated with both a decrease of axial velocity and a decrease in maximum vorticity, which is in line with the current experimental findings. Moreover, this relationship persists for varying values of offset of the incident vortex relative to the tip of the follower wing, that is, for different rates of deceleration of the vortex core, corresponding to different rates of increase of the velocity defect in the streamwise direction.

3.3.5 Upwash and Downwash

Iso surfaces of (red-brown) upwash and (blue) downwash w/U_∞ are given in figure 3.9. Consider first the case of the outboard interaction ($\Delta y/r_v$ = 2.5). The (red-brown) upwash surfaces show little variation along the axis of the vortex, except in the region close to the leading-edge of the wing, where the peak magnitude and spatial extent (radii) of the highest level surface is enhanced. Moreover, the (tan) surface representing the moderate levels of upwash extend further inboard as the leading edge of the wing is approached, and close to the leading edge these surfaces extend in the spanwise direction along the leading edge of the wing. These trends are due to the upwash component induced by the angle of attack of the wing, which exists in absence of the incident vortex, and has significantly large values close to the leading edge of the wing. That is, this wing-induced upwash enhances the magnitude and spatial extent of the upwash associated with the incident vortex. The foregoing trends for the outboard interaction ($\Delta y/r_v$ = 2.5) persist at successive locations of the incident vortex further inboard, i.e., slightly outboard ($\Delta y/r_v$ = 1.25), aligned ($\Delta y/r_v$ = 0), and inboard ($\Delta y/r_v$ = -6.25) interactions. In fact, there is little difference in the shapes of the upwash surfaces between impingement locations.

Regarding the contours of (blue-green) downwash w/U_∞ for the outboard interaction of figure 3.9, a clear decrease in the peak magnitude and spatial extent of the highest level surface of downwash occurs along the axis of the vortex as the leading-edge of the follower wing is approached. This decrease with streamwise distance along the axis of the vortex is in accord with the increased magnitude of the upwash arising from the angle of attack of the wing. The attenuation of downwash magnitude with streamwise

distance becomes increasingly prevalent at successive inboard locations corresponding to the slightly outboard, aligned and inboard interactions.

Figure 3.10 shows the superposition of: shaded contours of upwash and downwash of the incident vortex; and line contours of the wing-induced upwash in absence of the incident vortex. Both sets of contours are at a location close to the leading edge, $x'/C = 0.125$, for four different spanwise impingement locations. Comparison of the sets of contours at a given position of the incident vortex shows that the spanwise extension of upwash at locations inboard of the vortex axis is at least partially due to the self-induced upwash induced by the follower wing. Furthermore, low levels of the self-induced upwash of the wing are associated with a decrease of the maximum value of downwash of the vortex-wing interaction. The wing-induced upwash is additionally responsible for the increasing counter-clockwise rotation of the upwash and downwash contours around the vortex axis as the streamwise impingement location moves inboard. The highest levels of induced upwash are situated slightly vertically above the axis of the vortex, and when they combine with the incoming vortex, the result is rotated contours.

Figure 3.11 shows the change in the maximum magnitude of both the upwash and downwash for all four values of vortex offset. For the case of the aligned ($\Delta y/r_v = 0$) and inboard ($\Delta y/r_v = -6.25$) positions of the incident vortex, the overall decrease of the peak magnitude of downwash is approximately one third of its initial value. In contrast, the peak upwash velocity shows only small changes in the streamwise direction for all values of spanwise offset of the vortex, except in the immediate vicinity of the leading edge, where there is clearly a rise of the order of one eighth of the approach value.

3.3.6 Swirl Ratio

Changes of the surfaces of velocity deficit $1 - u/U_\infty$, and w/U_∞ described in the preceding figures 3.3 and 3.9 can be related to changes in the swirl ratio q, where $q = \Gamma/(2\pi r \Delta u) \approx 1.567\ u_\theta / \Delta u$ according to Jacquin & Pantano (2002), in which Γ is circulation, r is the vortex radius, Δu is the velocity deficit in the core, and u_θ is the maximum azimuthal velocity. Values of swirl ratio computed from the present experimental data are plotted in figure 3.12 as a function of distance x'/C upstream of the leading edge for the four different values of spanwise offset $\Delta y/r_v$, i.e., the outboard, slightly outboard and aligned positions of the incident vortex, along with the no follower wing case. It is evident that the magnitude of swirl ratio continually decreases up to $x'/C = 0.25$. At locations closer to the leading edge, the magnitude of the swirl ratio rises in the outboard and aligned cases. This rise is largest for the outboard position and smallest for the aligned position of the incident vortex. In accord with the computations of Garmann & Visbal (2015a), this rise is due to acceleration of the core flow in that region. Moreover, the plot of the velocity deficit given in figure 3.4 shows a decrease of velocity deficit as the leading-edge is approached for the outboard and slightly outboard cases and a fairly constant value for the aligned case, in contrast to the continued increase in velocity deficit for the inboard location.

Furthermore, for the aligned and inboard positions of the incident vortex, the decrease of swirl ratio as the leading edge is approached is relatively rapid, and small values of swirl ratio in the range of $1.0 < q < 1.5$ are eventually attained. A horizontal line on this plot defines the magnitude of $q = \sqrt{2}$, which represents the critical value of swirl ratio for the q-vortex according Leibovich & Stewartson (1983), below which azimuthal

instabilities are excited. For both the aligned and inboard positions of the incident vortex, the magnitude of the swirl ratio falls below this critical value for values of $x'/C < 0.5$. From figure 3.12, these small values of swirl ratio correspond to large values of velocity deficit. This region where the values of $q < \sqrt{2}$ correspond to the region of large (dark red) azimuthal vorticity $\omega_\theta C/U_\infty$ is designated in figure 3.6. The occurrence of a helical instability embedded within the turbulent background of the incident vortex can produce enhanced values of time averaged azimuthal vorticity. In the computations of Garmann & Visbal (2015a) the nature of the incident vortex is shown as a laminar *q*-vortex incident upon the leading-edge, for which a helical instability is easily discernible near the leading edge.

3.3.7 Patterns of Instantaneous and RMS Flow Structure

Figure 3.13 shows instantaneous images of streamwise vorticity $\omega_x C/U_\infty$ of the incident vortex at the location $x'/C = 0.125$ immediately upstream of the leading edge for four different impingement locations. At each spanwise location of vortex impingement, the three randomly selected images show variation of the pattern of vorticity. For the outboard case, $\Delta y/r_v = 2.5$, the vortex core is dominated by a single region of high streamwise vorticity for all images acquired at arbitrary instants t_1, t_2, and t_3. Near the outer edge of the vortex there are some irregularities, but the shape remains approximately circular. The slightly outboard case, $\Delta y/r_v = 1.25$, has regions of large streamwise vorticity that are more distorted, and the shape of the vortex is more irregular than at $\Delta y/r_v = 2.5$. The aligned case, $\Delta y/r_v = 0$, is even more irregular, and the core of the vortex is no longer identifiable. However, in all three instantaneous images the high level

of streamwise vorticity is connected to a lower level of streamwise vorticity. For the inboard case, $\Delta y/r_v$ = -6.25, the regions of high streamwise vorticity are separated by regions of very low streamwise vorticity, such that they almost appear to be separate structures. This is most apparent in image t_1, where the vortex has split into three separate regions of high streamwise vorticity.

Figure 3.14 illustrates the effects of the impingement location $\Delta y/r_v$ and the upstream distance x'/C on the root-mean-square of the streamwise velocity u_{rms}/U_∞. In each image, the patterns of velocity vectors V are superposed on the contours of u_{rms}/U_∞, thereby allowing identification of the center of swirl. As the spanwise impingement location moves from outboard to inboard, u_{rms}/U_∞ increases for all upstream positions. Furthermore, as x'/C decreases, the u_{rms}/U_∞ values increase for the aligned and inboard impingement locations. The increase of values of u_{rms}/U_∞ corresponds to the aforementioned increases in the velocity deficit $1 - u/U_\infty$. That is, comparing figures 3.3 and 3.14, it is evident that the patterns of largest u_{rms}/U_∞ occur at the same streamwise location where the magnitude of the velocity deficit is largest, evident for the aligned and inboard interactions. Moreover, the patterns of largest u_{rms}/U_∞ in figure 3.14 correspond to the lowest values of swirl ratio q given in the plot of figure 3.12, in particular, regions where $q < \sqrt{2}$ for the aligned and inboard interactions.

Figure 3.15 illustrates patterns of root-mean-square streamwise vorticity $(\omega_x)_{rms}/(\omega_x)_{max}$ which has been normalized by the local maximum value of the time-averaged streamwise vorticity $(\omega_x)_{max}$. The highest levels of $(\omega_x)_{rms}/(\omega_x)_{max}$ do not occur on the vortex axis; instead they are located in a ring surrounding the axis. Generally

speaking, larger values of $(\omega_x)_{rms}/(\omega_x)_{max}$ tend to occur at smaller values of x'/C and at spanwise locations further inboard. At $x'/C = 0.125$, the increase in magnitude and spatial extent of $(\omega_x)_{rms}/(\omega_x)_{max}$ with successive displacements of the impingement location of the incident vortex in the inboard direction correlates with increasing distortion of the instantaneous images given in figure 3.13. It also corresponds to the aforementioned increases of u_{rms}/U_∞ and velocity deficit given respectively in figures 3.14 and 3.3, as well as associated decreases of swirl ratio given in figure 3.12.

As shown in both figures 3.14 and 3.15, the RMS contours depart from axisymmetry in this region of flow distortion, especially near the leading-edge for the inboard and aligned impingement cases $\Delta y/r_v = 0$ and -6.25. For the type of encounter addressed herein, a nominally axisymmetric incident vortex approaches a planar leading-edge, rather than an axisymmetric leading-edge. This encounter likely induces non-axisymmetric distortions of the turbulent fluctuations and the mean flow in the vicinity of the leading edge.

3.4 CONCLUSIONS

The distortion of a trailing vortex from a leader wing incident upon the tip of a follower wing (flat plate) has been characterized using a stereoscopic technique of particle image velocimetry, thereby providing the flow structure of the incident vortex at locations well upstream of the follower wing for varying degrees of spanwise offset Δy of the incident vortex relative to the tip of the wing designated as outboard ($\Delta y/r_v = 2.5$),

slightly outboard ($\Delta y/r_v$ = 1.25), aligned ($\Delta y/r_v$ = 0), and inboard ($\Delta y/r_v$ = -6.25) of the tip, in which r_v is the radius of the incident vortex.

The influence of the vortex-wing interaction is not simply confined to a localized region in the vicinity of the leading-edge of the follower wing; rather, it can extend a distance upstream of at least one wing chord (approximately five vortex diameters). Moreover, significant upstream influence is evident when the tip of the vortex impinges well outboard of the tip of the follower wing.

The magnitude and radius of the region of streamwise velocity deficit $1 - u/U_\infty$ of the incident vortex are significantly enhanced for the slightly outboard interaction and substantially altered for the aligned and inboard interactions, relative to the outboard interaction.

The value of the velocity deficit increases as the leading edge of the follower wing is approached, except in the domain close to the leading edge, where the velocity deficit either attains a plateau value or decreases. Correspondingly, the radius of the vortex increases while its circulation remains constant; this observation is associated with a potentially large decrease of streamwise vorticity in the vortex core and an increase outside the core. When rapid attenuation of high level vorticity occurs along the vortex axis, it is associated with existence of a sufficiently large magnitude of velocity defect.

The aforementioned enhancement of streamwise velocity deficit, attenuation of maximum streamwise vorticity, and increase of vortex radius are linked to the adverse pressure gradient that exists in the region upstream of the wing. These observations are in

accord with the inviscid theoretical model of Batchelor (1964), whereby the rapid distortion of the vortex structure approaching the wing is associated with dominance of inviscid mechanisms.

These alterations to the vortex structure correspond to a decrease in swirl ratio q; when swirl ratio becomes sufficiently small, in particular in the region approaching the leading edge of the follower wing for the aligned and inboard interactions, a substantial increase in the time-mean azimuthal vorticity $\omega_\theta C/U_\infty$ arises along the outer periphery of the vortex. The largest enhancements of azimuthal vorticity occur when $q < \sqrt{2}$, which is in accord with the theoretical prediction of Leibovich & Stewartson (1983) for small-wavelength instabilities about the vortex, and with the computations of Garmann & Visbal (2014a & 2015a), which show an instantaneous helical instability about the exterior region of the vortex. On the other hand, for the cases of the outboard and slightly outboard interactions of the vortex with the tip of the wing, the swirl ratio q does not reach values below the threshold value $q < \sqrt{2}$, and enhancement of azimuthal vorticity does not occur along the entire streamwise extent of the incident vortex.

The attainment of lower values of swirl ratio q also corresponds to the onset of relatively large values of root-mean-square fluctuations of streamwise vorticity $(\omega_x)_{rms}/(\omega_x)_{max}$ and axial velocity u_{rms}/U_∞ on cross-sectional cuts of the incident vortex. The predominant magnitudes tend to be concentrated in a ring-like region surrounding the central portion of the incident vortex. Moreover, the largest rms magnitudes of these fluctuations are prevalent in the region immediately upstream of the leading edge of the follower wing, and for progressively further inboard locations of the incident vortex. The

corresponding instantaneous structure of the streamwise vorticity $\omega_x C/U_\infty$ on a cross-sectional cut of the vortex, at a location upstream of the leading edge of the follower wing, shows progressively more severe degradation of the coherent structure of the vortex for decreasing values of swirl ratio, i.e., for further inboard locations of the incident vortex.

The foregoing changes of the incident vortex are associated with alterations of the upwash (positive vertical velocity w/U_∞) and downwash (negative w/U_∞). Downwash is attenuated as the leading edge of the follower wing is approached; corresponding values of upwash, however, do not change significantly, except for a mild enhancement in the immediate vicinity of the leading edge. Both of these effects are at least partially due to the self-induced upwash of the follower wing, which exists in absence of the incident vortex. This observation is deduced from comparison of upwash and downwash patterns for cases of an incident vortex and no incident vortex incident upon the follower wing.

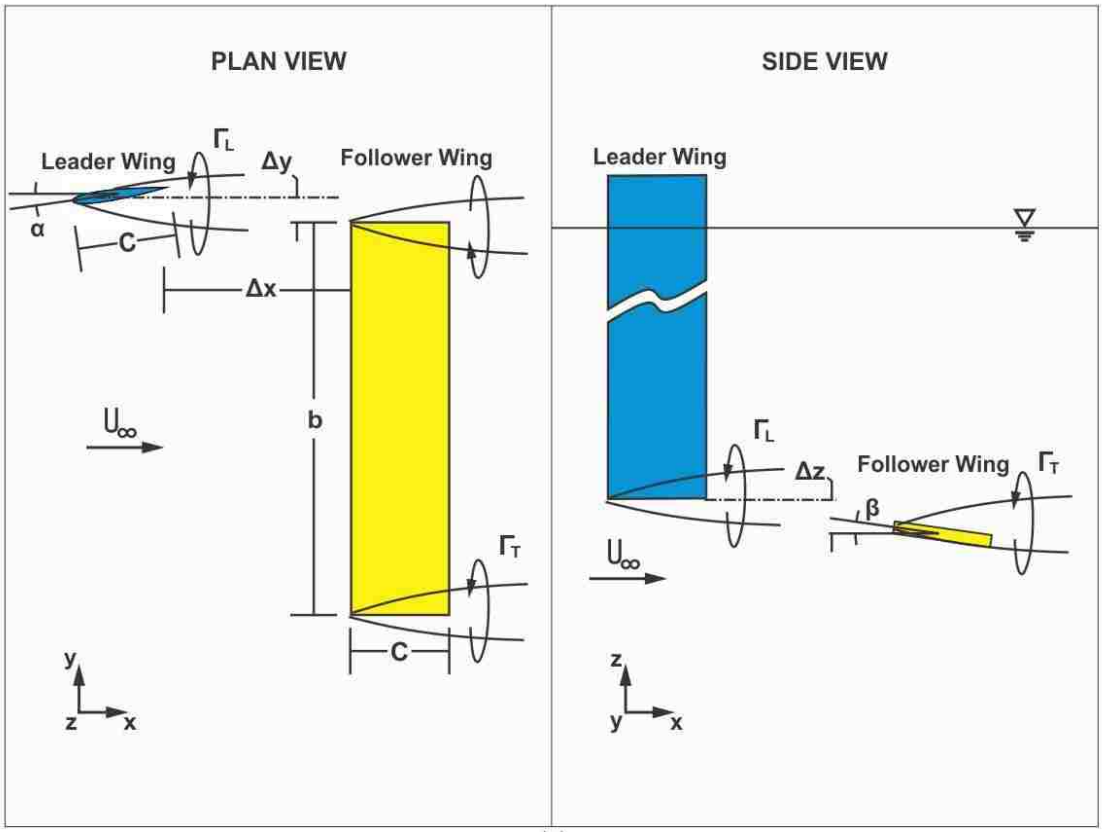

Figure 3.1: Plan and side views of the experimental arrangement.

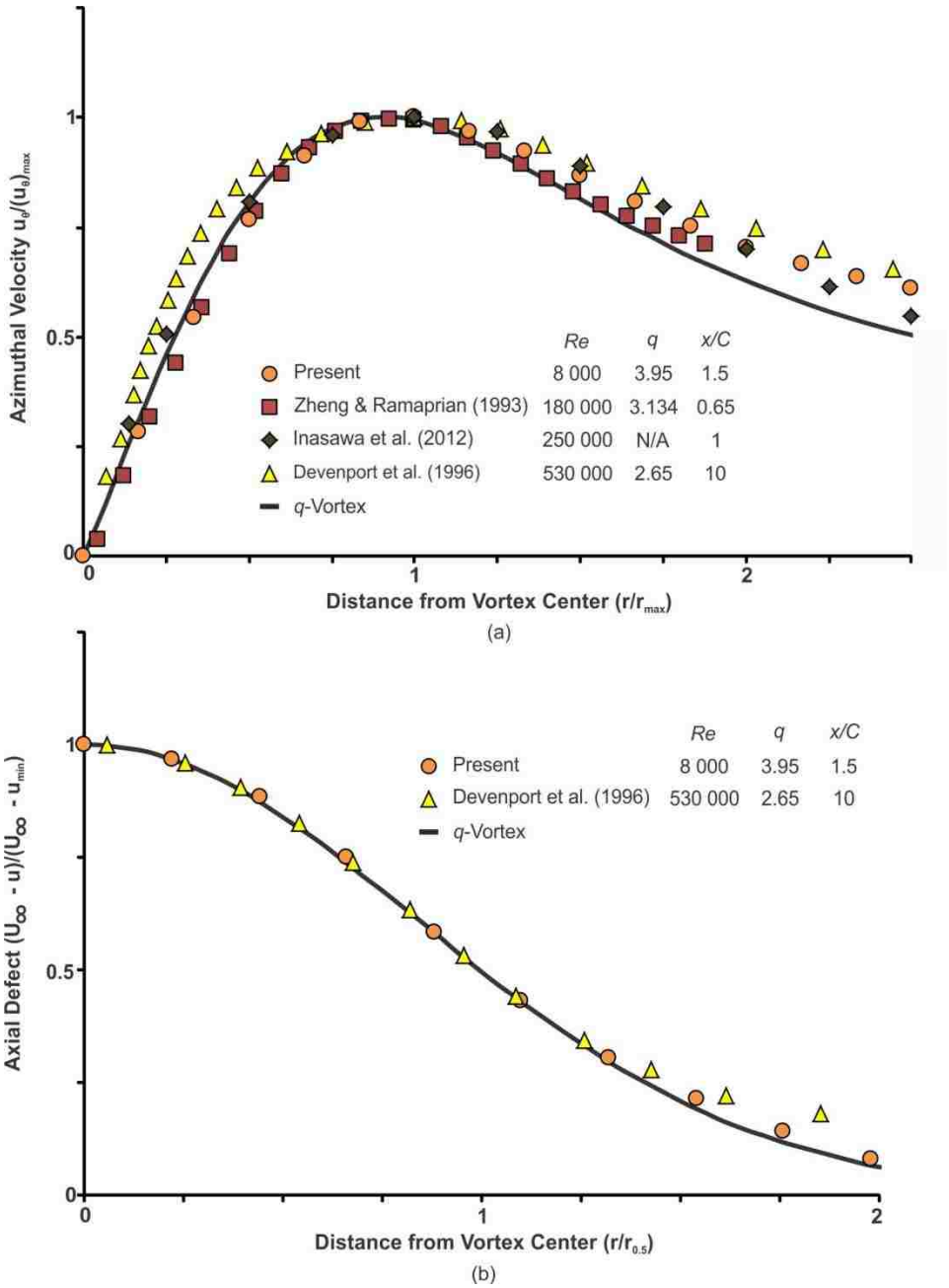

Figure 3.2: (a) Azimuthal velocity $u_\theta/(u_\theta)_{max}$ versus r/r_{max} in which r_{max} is the radial location of the maximum azimuthal velocity $(u_\theta)_{max}$; and (b) Axial velocity deficit $(U_\infty - u)/(U_\infty - u_{min})$ versus $r/r_{0.5}$ where u_{min} is the deficit velocity at the centerline and $r_{0.5}$ is the radius at which the axial velocity deficit is equal to half the maximum deficit. Each profile was created by averaging all available data.

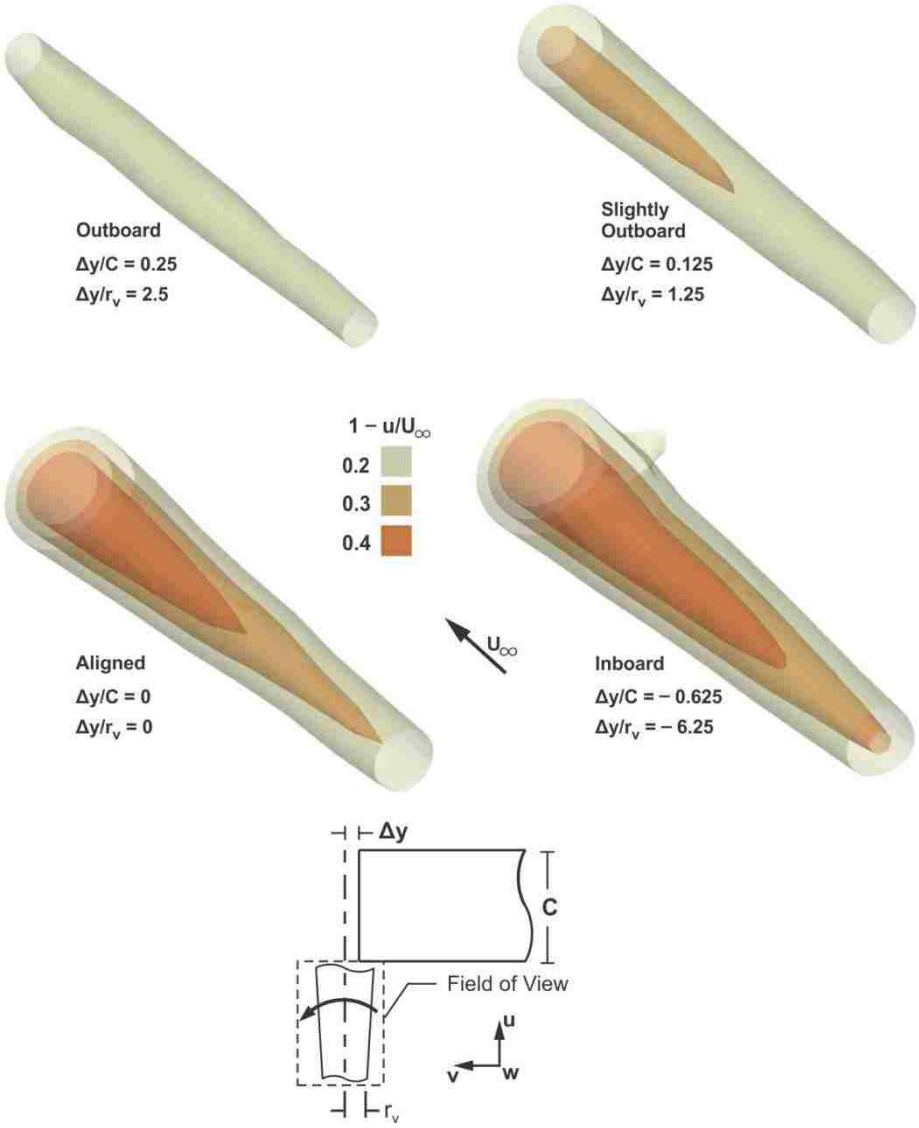

Figure 3.3: Iso-surfaces of streamwise velocity deficit $1 - u/U_\infty$ at four spanwise locations $\Delta y/r_v$ of vortex impingement. The surfaces extend over the streamwise distance from 0.125 C to 1 C upstream of the leading edge of the wing.

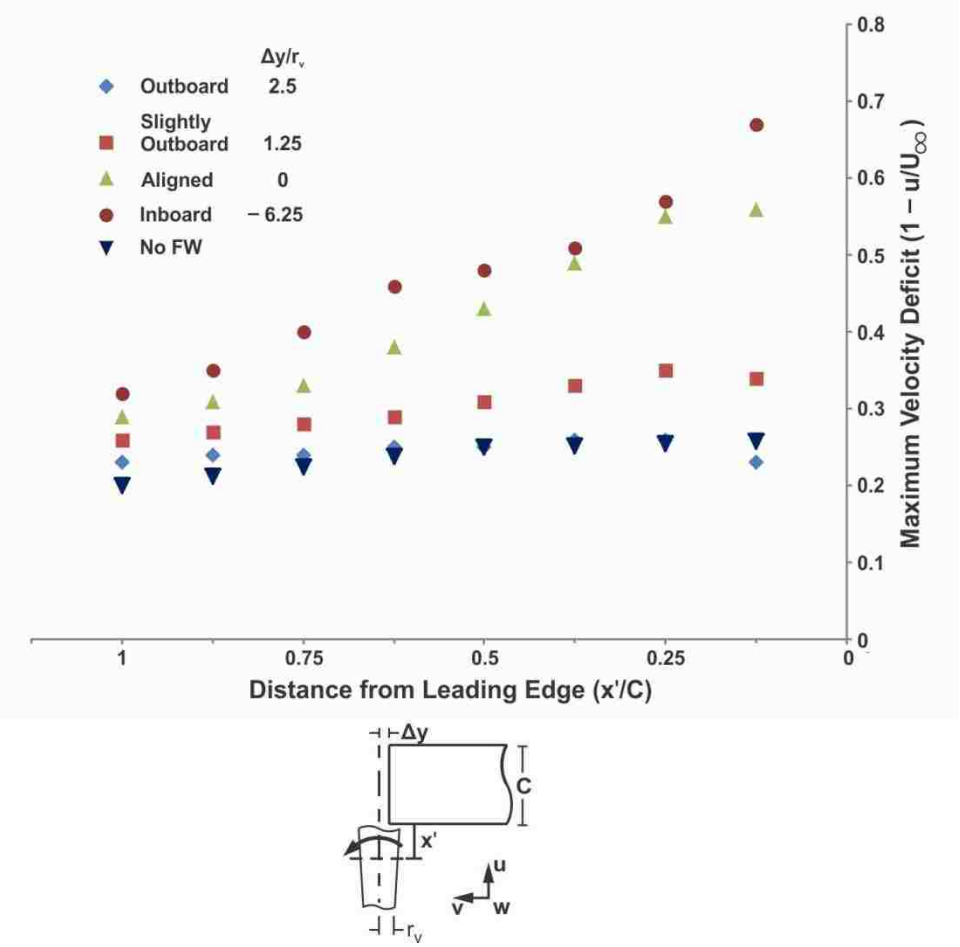

Figure 3.4: Plot of the maximum velocity deficit $1 - u/U_\infty$ along the centerline of the vortex for different spanwise locations $\Delta y/r_v$ of vortex impingement, as well as for the case of no vortex impingement, i.e., in absence of the follower wing. All cases are plotted as a function of streamwise location x'/C upstream of the leading-edge of the wing.

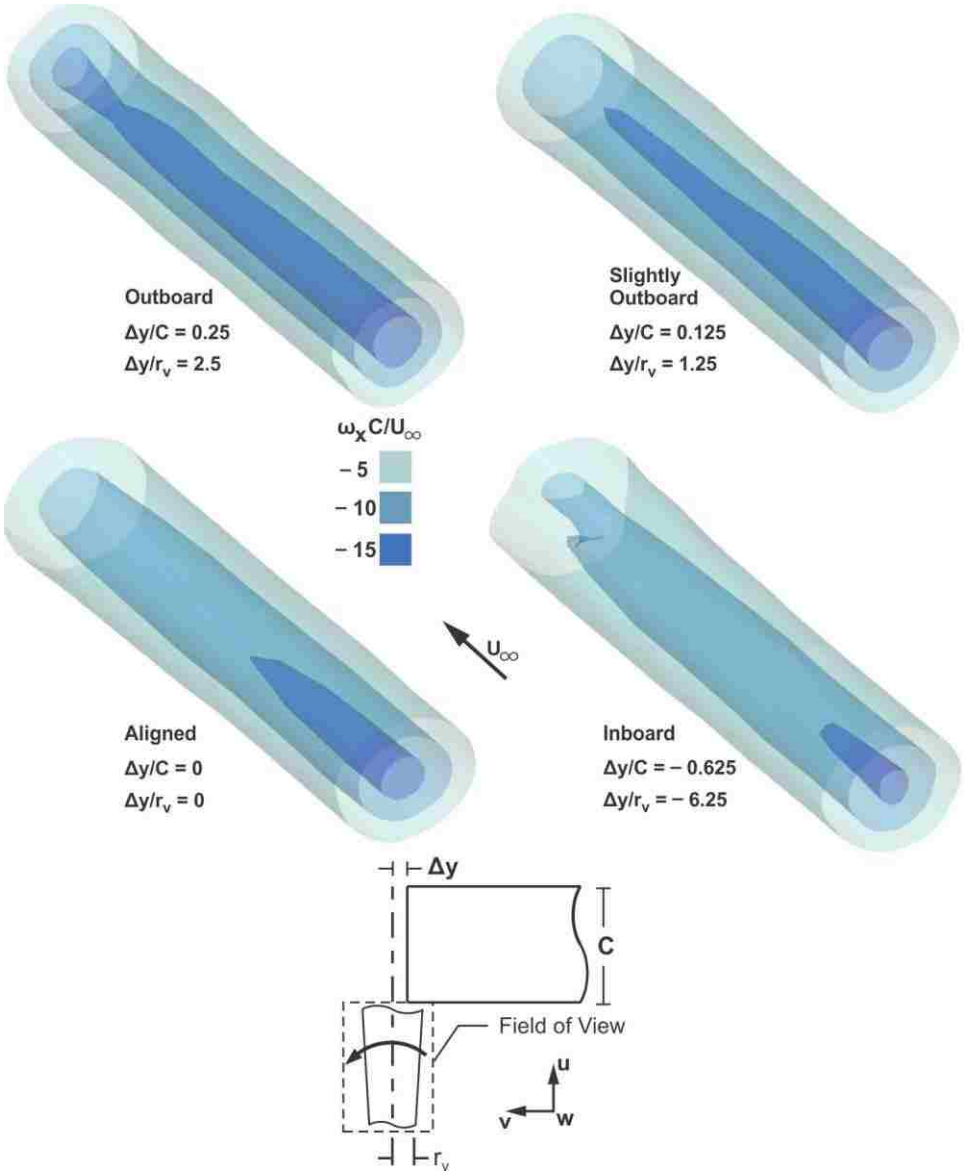

Figure 3.5: Iso-surfaces of streamwise vorticity $\omega_x C/U_\infty$ at four spanwise locations $\Delta y/r_v$ of vortex impingement. The surfaces extend over the streamwise distance from 0.125 C to 1 C upstream of the leading edge of the wing.

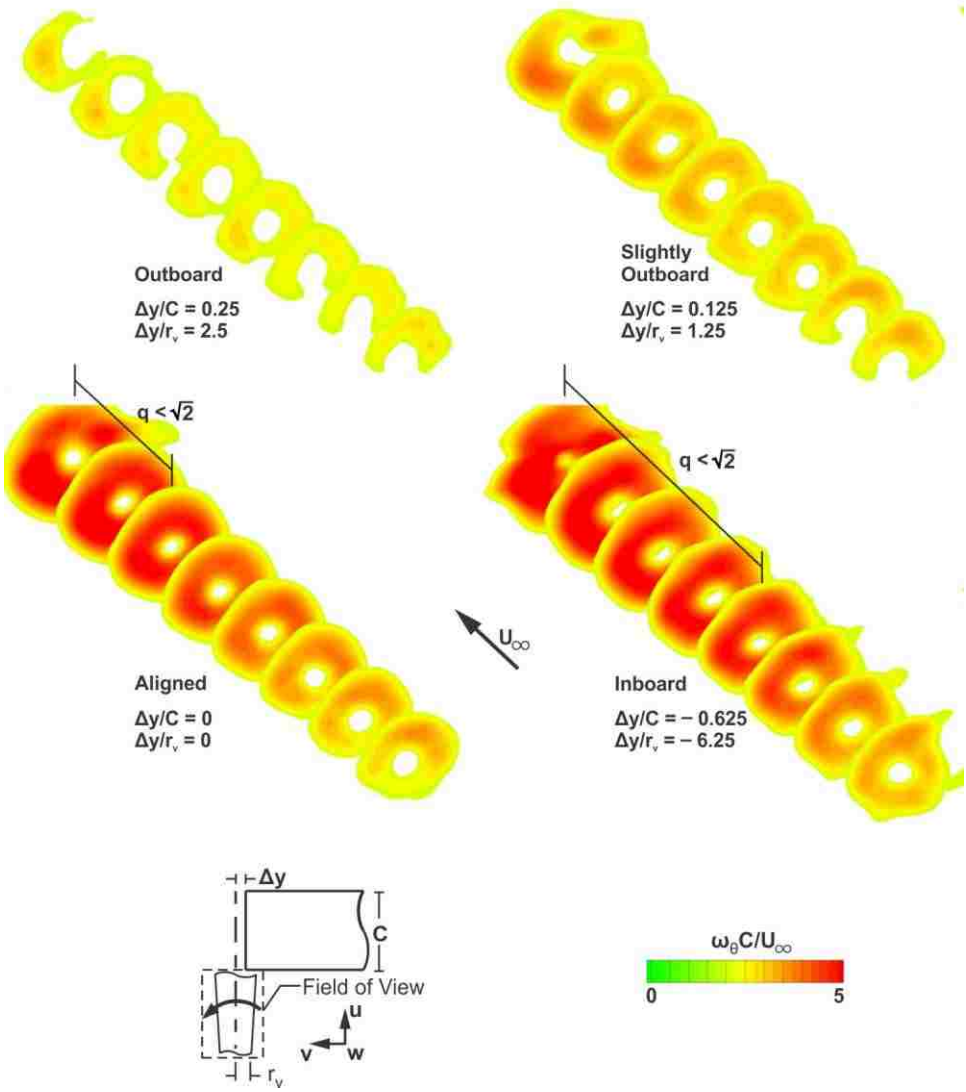

Figure 3.6: Slices of azimuthal vorticity $\omega_\theta C/U_\infty$ at four spanwise locations $\Delta y/r_v$ of vortex impingement. The slices extend over the streamwise distance from 0.125 C to 1 C upstream of the leading edge of the wing.

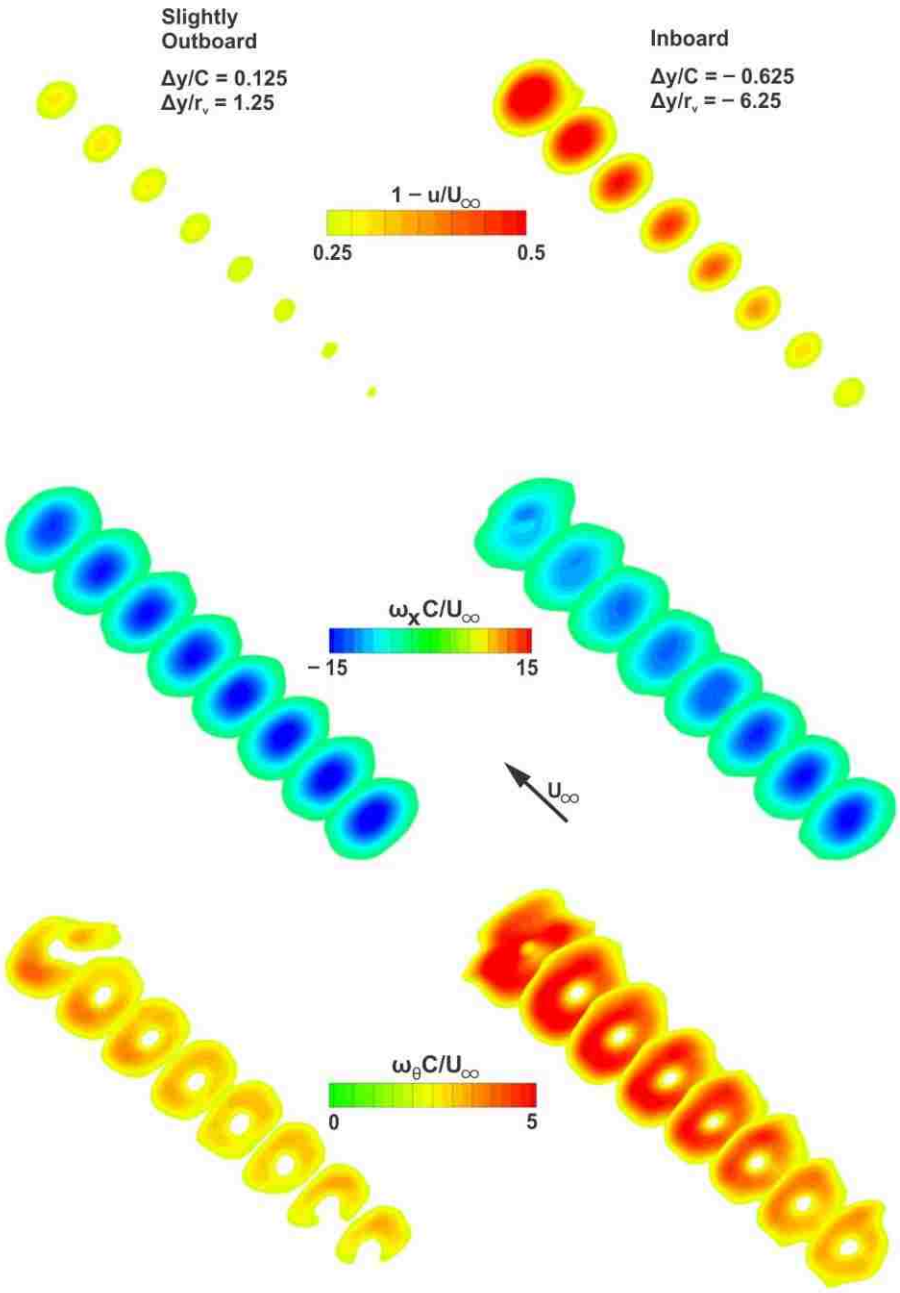

Figure 3.7: Sectional cuts of velocity defect, streamwise vorticity and azimuthal vorticity on streamwise-oriented planes at two different spanwise impingement locations $\Delta y/r_v$. The sectional cuts extend over the streamwise distance from 0.125 C to 1 C upstream of the leading edge of the wing.

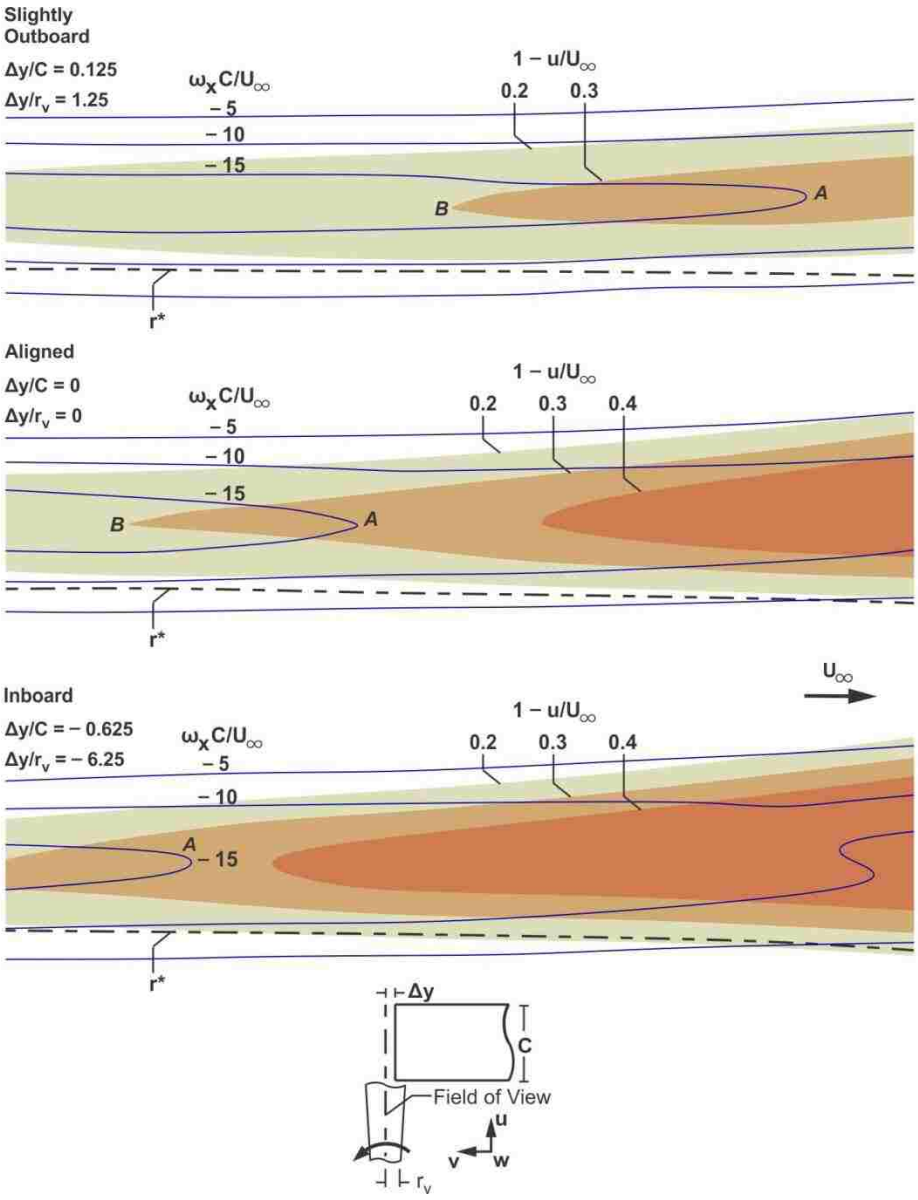

Figure 3.8: Longitudinal (axially-oriented) cuts of streamwise vorticity $\omega_x C/U_\infty$ and streamwise velocity deficit $1 - u/U_\infty$ contours along the axis of the vortex for three different spanwise locations $\Delta y/r_v$ of vortex impingement. Also shown is a dashed line that represents the vortex core radius r*.

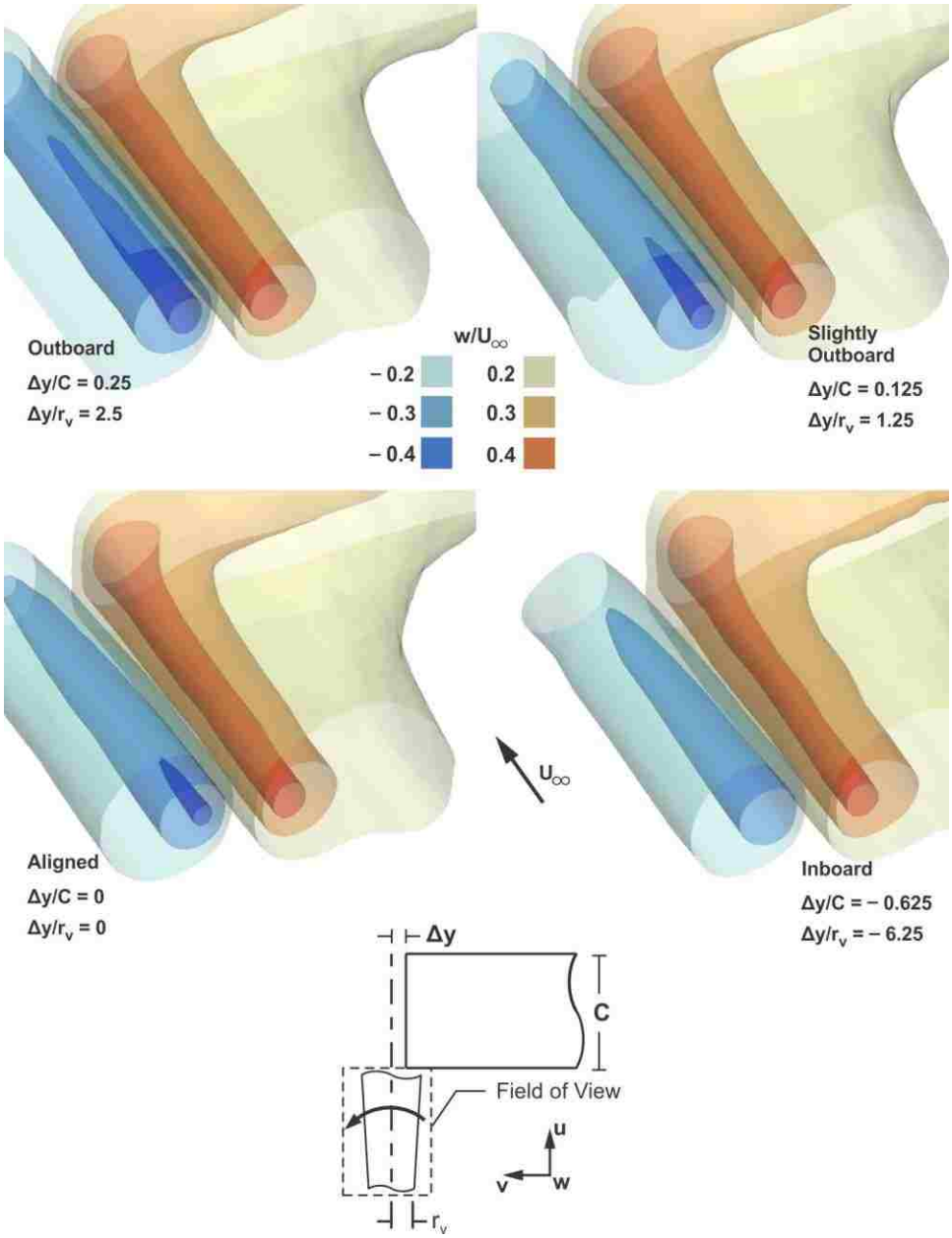

Figure 3.9: Iso-surfaces of upwash and downwash w/U_∞ at four spanwise locations $\Delta y/r_v$ of vortex impingement. The surfaces extend over the streamwise distance from 0.125 C to 1 C upstream of the leading edge of the wing.

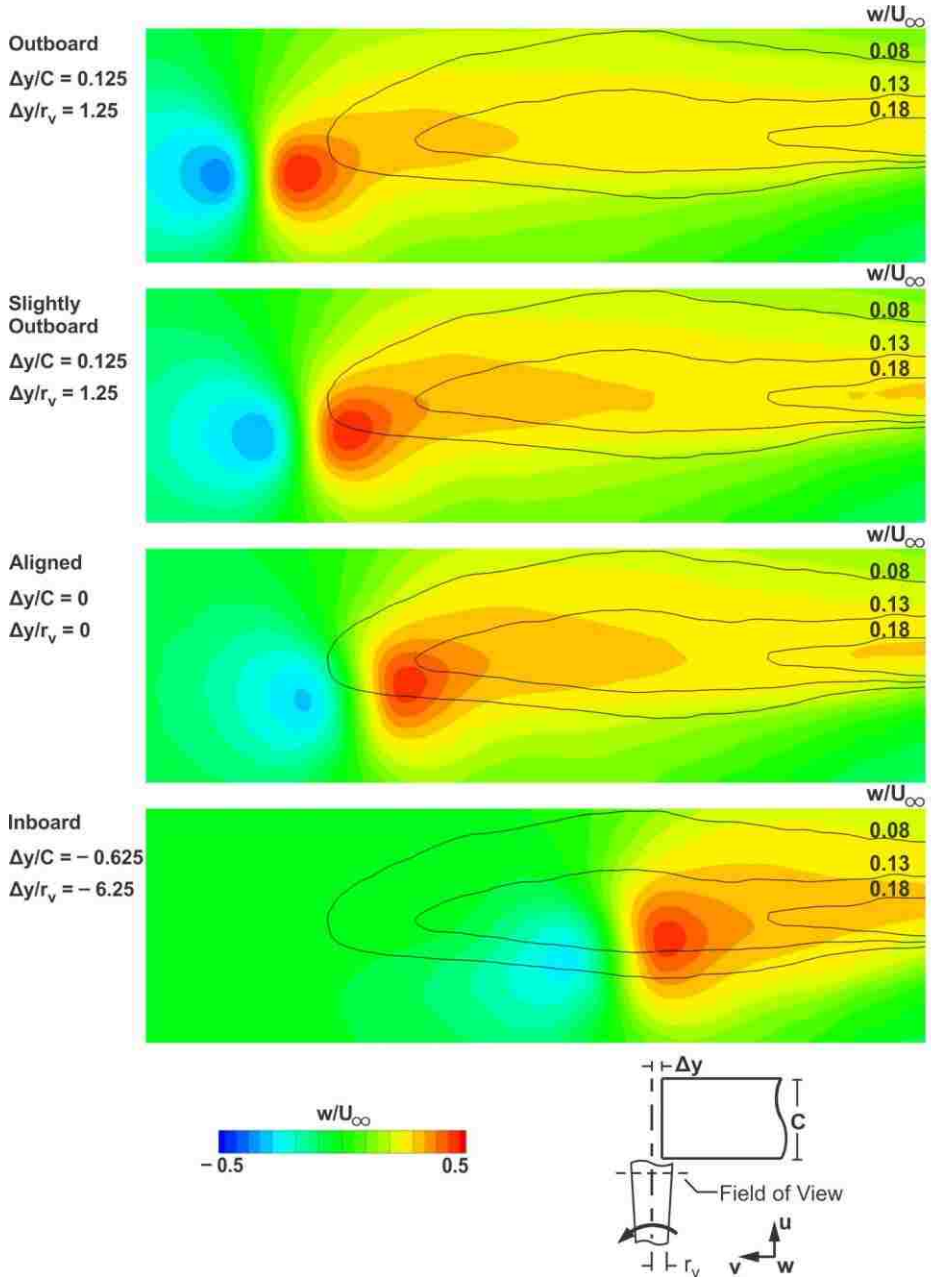

Figure 3.10: Cross-sectional cuts of upwash (positive) and downwash (negative) w/U_∞ for four different spanwise locations $\Delta y/r_v$ of vortex impingement at x'/C = 0.125. These plots also show (black) contour lines of wing-induced upwash w/U_∞ due to the follower wing in absence of the incident vortex.

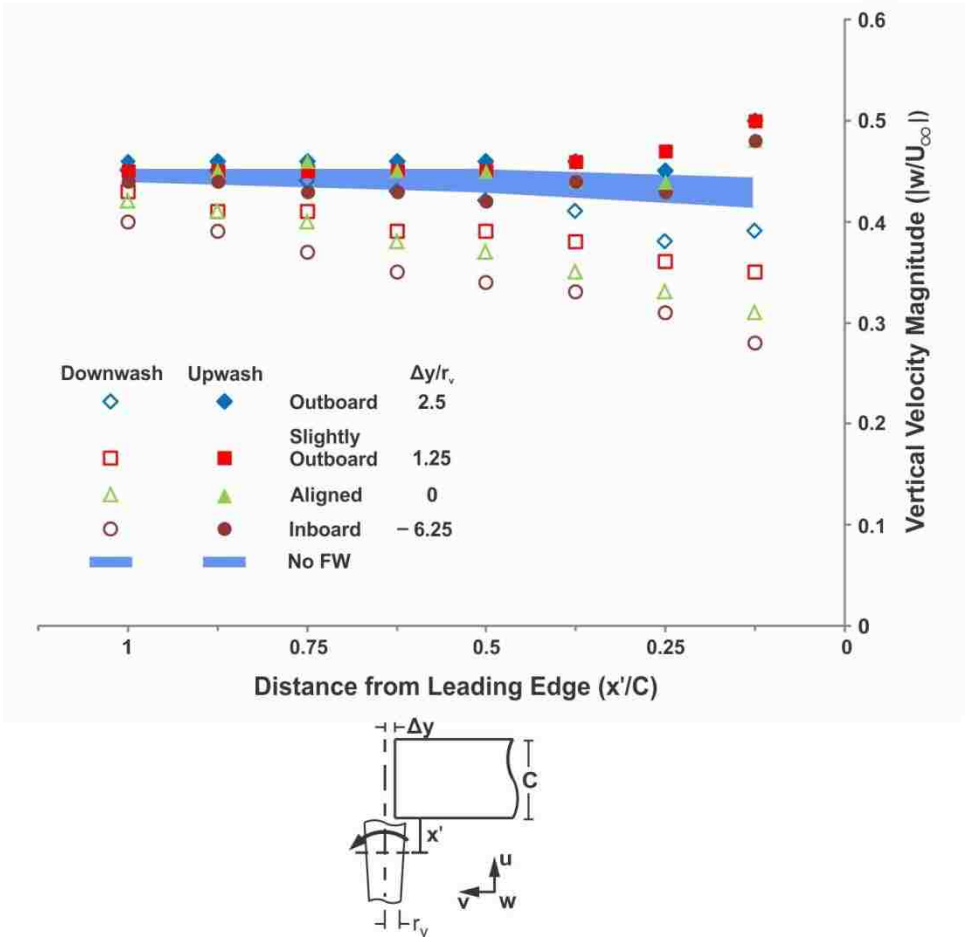

Figure 3.11: Plot of the magnitude of maximum upwash and downwash for different spanwise locations $\Delta y/r_v$ of impingement, as well as the no follower wing case. All cases are plotted as a function of streamwise location x'/C upstream of the leading-edge of the wing. The shaded blue region represents the band of data corresponding to the no follower wing (FW) case.

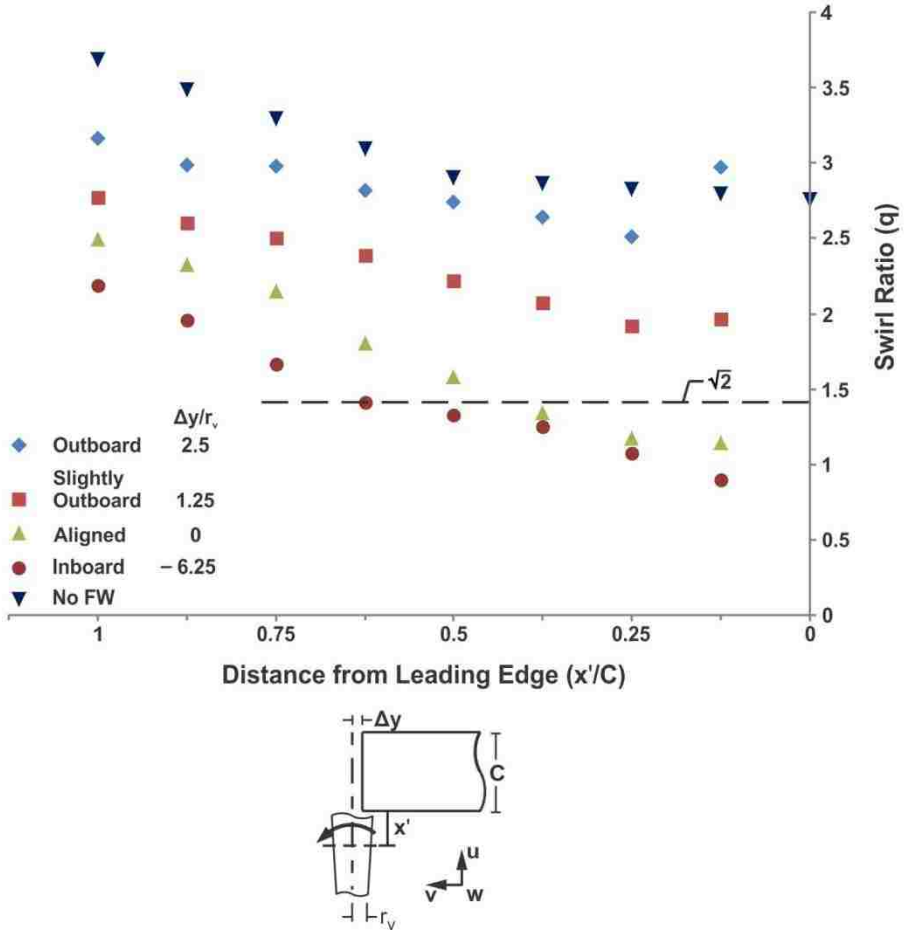

Figure 3.12: Plot of the swirl ratio q for different spanwise locations $\Delta y/r_v$ of impingement, as well as the no follower wing case. All cases are plotted as a function of streamwise location x'/C upstream of the leading-edge of the wing.

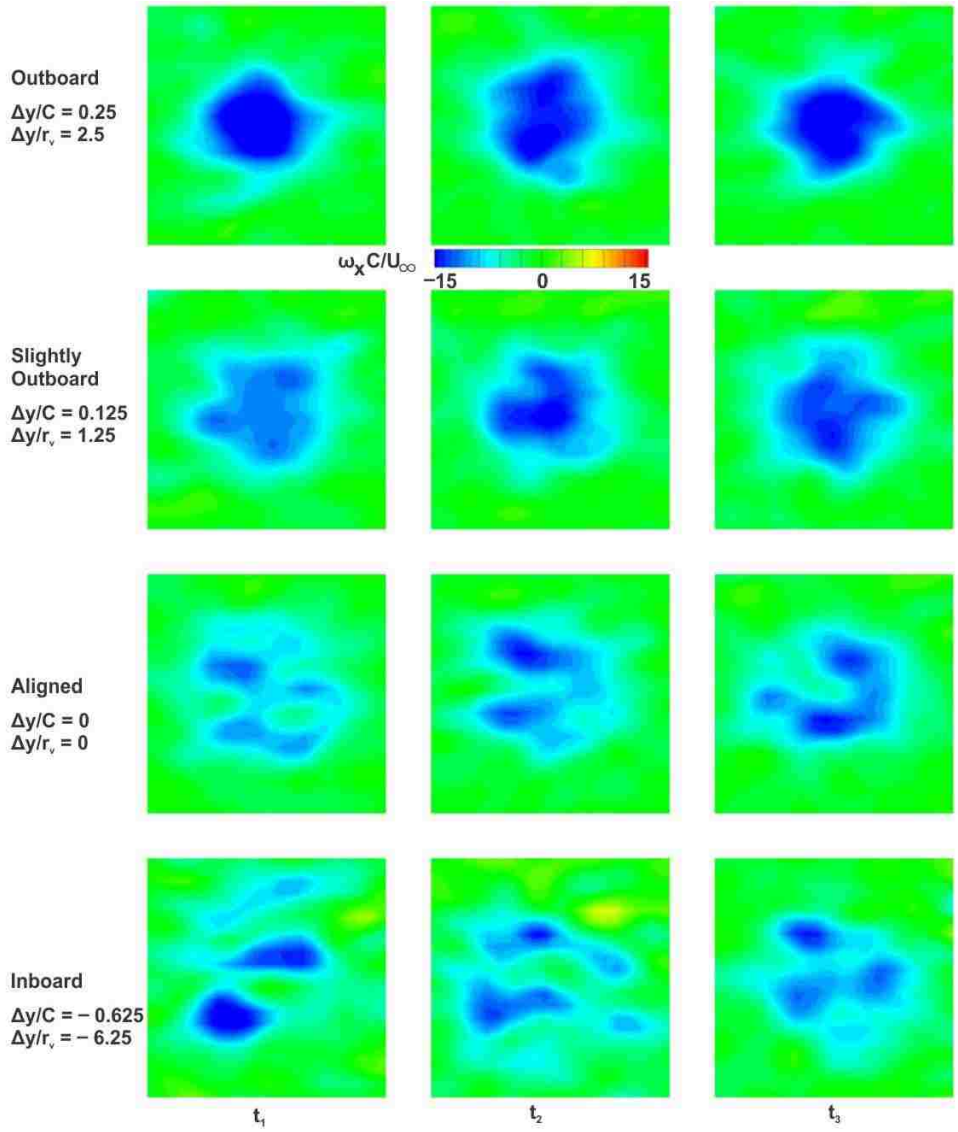

Figure 3.13: Cross-sectional cuts of instantaneous streamwise vorticity $\omega_x C/U_\infty$ on streamwise oriented planes at x'/C = 0.125 C; four different spanwise locations $\Delta y/r_v$ of impingement are shown. The three different images in each row show different instantaneous images.

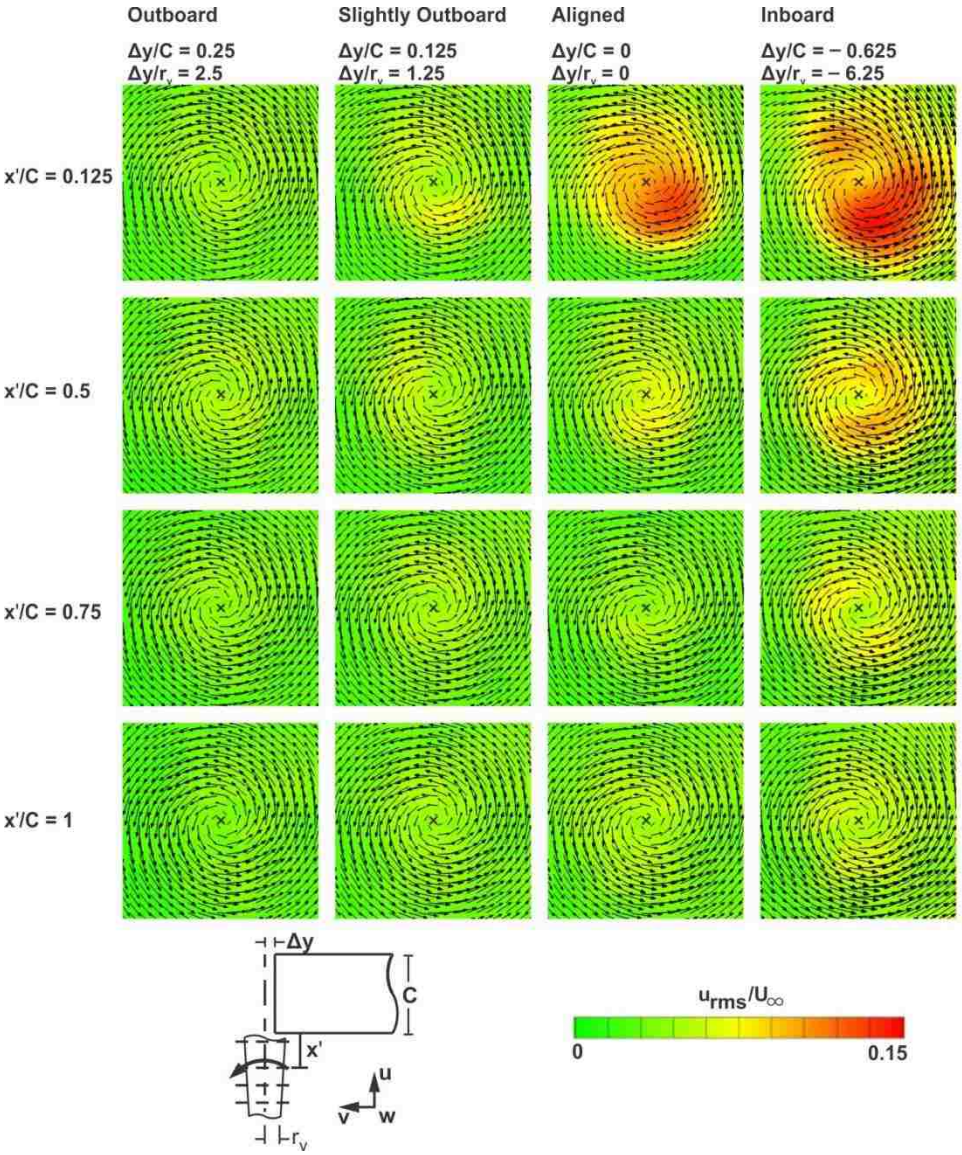

Figure 3.14: Cross-sectional cuts of rms streamwise velocity u_{rms}/U_∞ on streamwise-oriented planes; four different spanwise locations $\Delta y/r_v$ of impingement are shown.

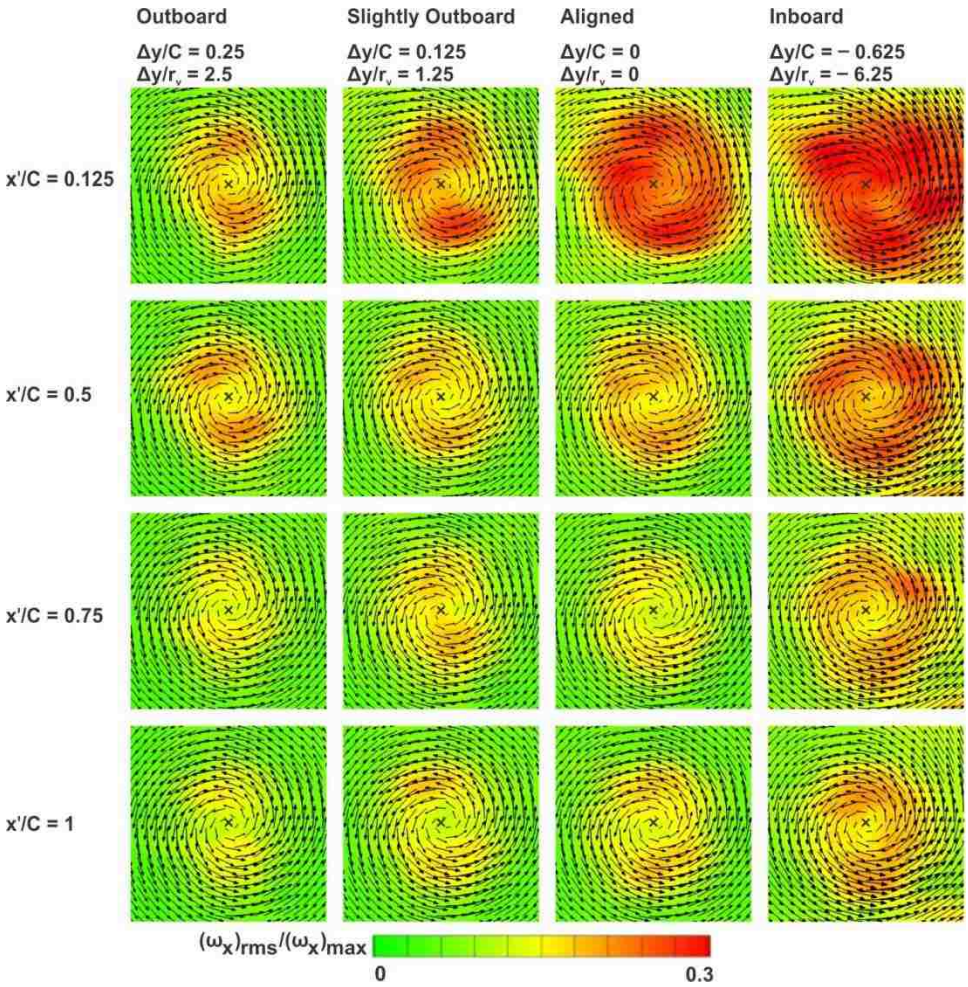

Figure 3.15: Cross-sectional cuts of rms streamwise vorticity $(\omega_x)_{rms}/(\omega_x)_{max}$ on streamwise oriented planes; four different spanwise locations $\Delta y/r_v$ of impingement are shown.

CHAPTER 4

TOPOLOGY OF VORTEX-WING INTERACTION

4.1 OVERVIEW

Recently there has been increased interest in formation flight, which can be represented by the interaction between a streamwise-oriented vortex and a wing. Formation flight has been shown to provide aerodynamic advantages for both biological and man-made fliers. It involves at least two wings, where the follower (downstream) wing is under the influence of the trailing vortex generated from the leader (upstream) wing.

A goal of the present experiments is to determine if generic modes of vortex-wing interaction exist at extreme values of Reynolds number and circulation of the incident vortex. It is hypothesized that the basic classes of interaction will be insensitive to Reynolds number. Irrespective of this hypothesis, however, the results of the present experiments are directly applicable to micro air vehicles, where the Reynolds number is relatively small. A central concept, which has not yet been addressed, is the nature of the streamline topology associated with the basic modes of interaction. The existence and location of critical points of this topology, including foci, bifurcation lines, saddle points, and nodal lines can provide deeper insight into the physics of generation of the basic modes of interaction, including extreme cases of enhancement and attenuation of the tip vortex from the wing. This investigation focuses on these issues and employs a technique of particle image velocimetry to characterize the flow structure.

4.2 EXPERIMENTAL SYSTEM AND TECHNIQUES

Experiments were performed in a free-surface water channel. Its test section was 4877 mm long, 927 mm wide and 610 mm deep. The free stream velocity in the test section was 158 mm/s, giving a value of Reynolds number of 8000 based on the chord of the leader wing. An overview of the experimental arrangement is provided in Figure 4.1. The leader wing is oriented vertically; it is a NACA 0012 airfoil, which has a chord C = 50.8 mm, and an angle of attack α = 16°. The leader wing extends upwards through the free surface. As a consequence, a tip vortex is generated only from the lower wing tip. The follower wing is a clear acrylic flat plate with a chord C = 50.8 mm, thickness t =1.5875 mm, span b = 203.2 mm, and angle of attack β = 4°. The streamwise distance between the two wings is Δx = 152.4 mm.

When the trailing vortex is formed from the tip of the leader wing, it will undergo a given trajectory influenced by induction effects as it approaches the follower wing. It is therefore necessary to offset the position of the tip of the leader wing to achieve the desired interaction with the trailer wing. The displacements Δy_0 and Δz_0 that resulted in a tip vortex impinging directly on the tip of the trailer wing were determined using monoscopic particle image velocimetry (MPIV) data. In this investigation, five different offsets Δy were examined, $\Delta y = \Delta y_0 - 12.7$ mm, $\Delta y_0 - 3.175$ mm, Δy_0, $\Delta y_0 + 3.175$ mm, and $\Delta y_0 + 12.7$ mm, while three different Δz offsets were examined at each value of Δy, $\Delta z = \Delta z_0 - 3.175$ mm, Δz_0, $\Delta z_0 + 3.175$ mm.

MPIV was employed to determine the quantitative structure of the vortices. It provides the two in-plane components of velocity. The flow was seeded with 11 μm hollow metallic coated plastic spheres such that 15-20 particle images were present in the interrogation window of 32 x 32 pixels. To illuminate these particles, a 3 mm thick laser sheet was produced by a dual-pulsed Nd-YAD laser operating at 14.29 Hz. Images were acquired from a camera that had a CCD array of 1600 x 1200 pixels. The image from the camera was then evaluated using a cross-correlation technique with 50% overlap, yielding 7227 vectors in the field of view. Each pixel is 48.8 μm/px, which corresponds to an interrogation window width of 1562 μm.

The in-plane uncertainty was calculated using the technique described in Adrian and Westerweel (2011). The RMS random error for the in-plane velocity is between 5.1% and 7.2% of the freestream velocity. For this MPIV setup, the pixel size is large compared to the particle image diameter and therefore the bias error is small in comparison to the RMS random error.

For each experimental configuration, image acquisition was performed at 6.35 mm intervals from a location 12.7 mm upstream of the leading edge of the follower wing to 12.7 mm downstream of its trailing edge. At each of these locations, 100 images were captured; they were then time-averaged to produce the final images. Based on convergence tests, an average of 100 images was found to be sufficient to represent the time-averaged flow, with the maximum values of spanwise velocity, upwash, and streamwise vorticity being within 3% of the converged values.

The flow structure at different streamwise locations was examined by translating the wing system to the desired location in the streamwise direction. The leader wing could move independently from the rest of the system, which allowed examination of the flow at successive spanwise locations of the leader wing.

4.3 MODES OF VORTEX-WING INTERACTIONS: COMPUTATIONS AND EXPERIMENTS

Variation of the offset of the incident vortex relative to the tip of the follower wing generates a number of modes of vortex-wing interaction. These modes are described in the following.

4.3.1 Vertically-Oriented Vortex Dipole

Figure 4.2 compares the computations of Garmann and Visbal (2015a) with the present experiments; a schematic of this interaction is given in Figure 4.1. The inception of the tip (red) vortex, which is enhanced by the upwash induced by the incident (blue) vortex, occurs for both computations and experiments at $x'/C = 0.25$ and increases in scale with streamwise distance x'/C along the chord of the wing. Simultaneously, the incident vortex is distorted at increasing values of x'/C. That is, its left side is flattened and its overall shape is elongated in the vertical direction due to interaction with the induced tip vortex. The vortex dipole formed by the incident vortex and the induced tip vortex rises vertically above the tip of the wing at successive values of x'/C. In the wake

of the trailer wing, at x'/C = 1.25, the vortex dipole is remarkably preserved, and the levels of streamwise vorticity $\omega_x C/U_\infty$ are not significantly altered.

4.3.2 Inclined Vortex Dipole

Figure 4.3 displays both the computations of Barnes et al. (2015a) and the present experiments. At the leading edge of the wing x'/C = 0 the vertical position of the incident vortex is slightly above the surface of the wing. Similar to the interaction shown in Figure 4.2, the initial formation of the tip vortex is evident at x'/C = 0.25. At successively larger values of x'/C, the induced tip vortex shows an increase in scale while it forms a dipole with the incident vortex. Due to the fact that the incident vortex is located above the tip vortex, the vortex dipole translates upwards and inboard, that is, its trajectory is inclined with respect to the surface of the plate. During this process, elongation of the shape of the incident vortex occurs due to its interaction with the tip vortex. Downstream of the trailing edge, at x'/C = 1.25, both vortices of the vortex dipole retain their overall forms and levels of streamwise vorticity $\omega_x C/U_\infty$.

4.3.3 Nested Vortex System Transforming into a Vortex Dipole

Figure 4.4 shows comparison of experiments with computations of Garmann and Visbal (2015a) for the case where the incident (blue) vortex is aligned with the tip of the wing. The structure of the incident vortex is distorted at x'/C = 0 as it encounters the tip of the wing. At x'/C = 0.25, formation of the tip (red) vortex is nested within the incident vortex. At successively larger values of x'/C, the tip vortex grows in scale and initiates departure from the tip region. Simultaneously, the incident vortex moves upward and

inboard, in accord with the self-induced motion of the incident vortex-tip vortex dipole along an inclined trajectory with respect to the surface of the plate. In the wake of the plate, at x'/C = 1.25, the vorticity levels of the tip and incident vortices are significantly attenuated, in contrast to the foregoing cases of vortex dipole development indicated in Figures 2 and 3, where the incident vortex was located significantly outboard of the tip of the wing.

4.3.4 Inboard-Directed Vortex Dipole

In Figure 4.5, which represents the computations of Barnes et al. (2015a) in comparison with the present experiments, the incident (blue) vortex is nearly aligned with the tip of the wing and located slightly above it. At x'/C = 0.25, a concentrated (red) vorticity layer is generated along the upper surface of the wing; it is located beneath the concentration of (blue) vorticity associated with the incident vortex. From x'/C = 0.5 to 1.0, the incident (blue) vortex moves over the cluster of vorticity from the tip, while continuing to move inboard from the tip. Simultaneously, the computations indicate an identifiable, small concentration of (red) vorticity along the surface of the plate, whereas the experiments indicate a layer of elevated (red) vorticity along the plate beneath the incident vortex as it translates inboard. At x'/C = 1.25, the levels of (blue) vorticity in the incident vortex and the (red) vortex/vorticity layer from the tip are significantly degraded relative to the values at the trailing edge x'/C = 1.0.

4.3.5 Inboard-Directed Incident Vortex

Figure 4.6 shows the case of vortex-plate interaction where the incident vortex is slightly inboard and above the tip of the wing. The computations of Barnes et al. (2015a) are shown together with the present experiments. Downstream of the leading edge, at x'/C = 0.25, and along the upper surface of the wing, the cluster of vorticity takes an elongated form that extends well inboard of the tip of the wing for both computations and experiments. Over the region extending from x'/C = 0.5 to 1.0, the vorticity level of the (blue) cluster of vorticity decreases as it translates inboard from the tip. This translation is due to a ground effect whereby coexistence of the indicated vortex and its image within the plate induces motion along the plate.

The formation of a tip vortex is suppressed in contrast to the enhanced formation of the tip vortex indicated in Figures 2 and 3. The onset of a small scale vortex in the computations is likely due to: the significantly smaller circulation of the incident vortex of the computations compared to experiments, $\Gamma_v/(CU_\infty)$ = 0.105 and 0.503 respectively; and the fact that the incident vortex in the experiments is closer to the tip than in computations. In the wake, at x'/C = 1.25, remnants of the incident vortex are almost nonexistent, and only a small-scale tip vortex exists in the computations.

4.4 STREAMLINE TOPOLOGY OF VORTEX-WING INTERACTIONS

The patterns of vorticity concentrations described in the foregoing define the basic modes of vortex-wing interaction. In order to provide a further physical basis for interpretation of these modes, streamline topology is employed. This approach, which

employs experimental imaging, provides a means for describing the compatibility between coexisting, adjacent regions of complex flow patterns in relation to the types and locations of critical points. In the following, representative modes of vortex-wing interaction are described using this topological approach. Some critical points such as half-saddle points are not addressed here for the purpose of clarity.

4.4.1 Structure in absence of incident vortex

Figure 4.7 shows patterns of time-averaged streamlines superimposed on colored contours of streamwise vorticity $\omega_x C/U_\infty$ for the case of a free trailer wing, i.e., a wing in absence of an incident vortex. Images are shown at locations extending from upstream of the leading edge of the wing (plate) to the near wake, i.e., from x'/C = -0.25 to x'/C = 1.25. At each value of x'/C, the patterns of vorticity contours are indicated separately in the inset.

Near the leading edge at x'/C = -0.25 and x'/C = 0 the upstream influence of the trailer wing on the incoming flow is evident. This is manifested as a region of upwash directly upstream of the leader wing, which is bounded on the outboard side by a bifurcation line BL_b^+. Just past the leading edge at x'/C = 0.25, a new bifurcation line BL_a^+ occurs; it is associated with the flow wrapping around the wing tip. Furthermore, the first traces of the tip vortex can be seen as the small region of positive (red) vorticity near the wing tip.

Further along the chord of the wing, from x'/C = 0.5 to x'/C = 1, the tip vortex shows a stable focus, which is labeled F_c. Spiral foci, both stable and unstable, are

associated with axial velocity in the core, according to Perry and Chong (1990). The size and shape of this vortex do not change significantly over this region, which is in stark contrast to the evolution of the tip vortex seen in Figure 4.8. While BL_b^+ is still present outboard of the wing, BL_a^+ is not. Downstream of the trailing edge at x'/C = 1.25 the tip vortex has separated from the wing and is now surrounded by an unstable limit cycle, otherwise known as a positive closed bifurcation line, which feeds BL_b^+.

4.4.2 Vertically-Oriented Vortex Dipole

Figure 4.8 shows patterns of time-averaged streamlines superimposed on colored contours of streamwise vorticity $\omega_x C/U_\infty$ at locations extending from upstream of the leading edge of the plate to the near wake, i.e., from x'/C = -0.25 to x'/C = 1.25. At each value of x'/C, the patterns of vorticity contours are indicated separately in the inset.

At x'/C = -0.25 and x'/C = 0, it is evident that the incident vortex is located outboard of the tip of the plate, and has a well-defined focus F_a; streamlines spiral either outward from, or inward towards, F_a. These spiral patterns are associated with the existence of an axial velocity component and either contraction or stretching of the vortex. Such spiral patterns are embedded within limit cycles of the streamlines. The limit cycle present in this case is unstable, similar to the limit cycle addressed in section *4.4.1 Free Trailer Wing*. Moreover, the nature of the axial flow for this vortex is known from the previously performed experiments of McKenna, Bross, and Rockwell (2016), which showed that the incident vortex has a velocity defect in the core for all spanwise impingement locations upstream of the leading edge of the trailer wing. Streamline patterns shown for other types of interaction in subsequent figures have the same

conceptual interpretation as in the foregoing, regarding a stable or unstable focus and limit cycle(s).

Downstream of the leading-edge, at x'/C = 0.25, separation from the tip of the plate yields a positive (red) vorticity concentration that is associated with a pattern of streamlines that reattach to the upper surface of the plate. Inboard of this location, a small negative (blue) vorticity cluster is associated with a focus F_b. To account for existence of the upwash (upward-oriented streamlines) above the plate, and for that fact that the vortices associated with foci F_a and F_b involve clockwise-oriented swirling streamlines, saddle point SP_a exists between them. Beneath the plate, another saddle point SP_b exists; it allows compatibility between: the downwash beneath the plate; the upwash associated with the incident vortex; and the flow from the region below the plate into the feeding sheet of the tip (red) vortex.

At x'/C = 0.5, the positive (red) vorticity concentration near the tip, originally evident at x'/C = 0.25, has developed into a vortex with focus F_c. Focus F_a of the incident vortex forms a dipole with F_c, thereby propelling F_a and F_c upwards, and creating the bifurcation line BL_a^+ originating from the accelerated flow through the dipole, i.e., the flow between F_a and F_c. This accelerated region of the flow has a maximum velocity that corresponds to 159% of the maximum azimuthal velocity of the incident vortex in the absence of the trailer wing (plate). The saddle point SP_b still exists beneath the plate and is displaced downwards away from the plate.

At x'/C = 0.75 and 1, the vortex involving F_c continues to develop, and detaches from the (orange-red) feeding sheet at the tip of the plate. The vortex dipole associated

with the foci F_a and F_c moves further upward. Simultaneously, the bifurcation line BL_a^+ is deflected upwards.

In the near wake, at x'/C = 1.25, the overall structure of the dipole associated with the major vorticity concentrations is preserved. The concentrations continue to be identified with the foci F_a and F_c. Separation from the trailing corner of the tip of the plate has, however generated a distorted limit cycle streamline on the inboard side of the vortex associated with the focus F_c. Moreover, the saddle point SP_b beneath the vortex dipole persists.

4.4.3 Inboard-Directed Vortex Dipole

In Figure 4.9, the center of the incident vortex approaching the wing is slightly displaced from its tip in the outboard direction, as evident by the location of the focus F_a at the streamwise position x'/C = -0.25 upstream of the leading edge of the wing and x'/C = 0 at the leading edge. Moreover, at these locations, a positive bifurcation line BL_a^+ arises from distortion of the incident vortex in presence of the tip of the wing.

At x'/C = 0.25, the flow structure replicates the major critical points indicated for the case of outboard interaction in Figure 4.8: foci F_a and F_b, and saddle point SP_a. The foci F_a and F_b are, however, much closer together than for the case of outboard interaction in Figure 4.8. In addition, the region of streamline separation and reattachment at the tip of the edge associated with the positive (red) vorticity concentration now has a detectable focus F_c at its center, and the bifurcation line BL_a^+ emerges from densely packed streamlines surrounding the incident vortex. An important

feature of this topology, in comparison with the pattern at the streamwise location in Figure 4.8, is the abrupt upward displacement of the focus F_a at x'/C = 0.25. This new position of F_a represents the genesis of the inclined vortex dipole, which develops at larger values of streamwise distance x'/C.

Images at larger values of streamwise distance x'/C = 0.5 to 1 indicate further development of the inclined vortex dipole as it moves away from the tip of the wing along a trajectory at an angle of approximate 45° with respect to the wing surface. During this process, the saddle point SP_a and a nodal line N_a evident at x'/C = 0.5 give way to a bifurcation line BL_b^+ at x'/C = 0.75 and 1.0. Moreover, a new saddle point SP_b at x'/C = 0.5 and 0.75 allows compatibility between: the downwash beneath the plate; the flow into the feeding sheet of the vortex formed from the tip of the wing; and the flow through the center of the dipole.

At x'/C = 1.0, departure of the positive (red) vorticity concentration identified by the focus F_c away from the tip of the wing is associated with disappearance of the saddle point SP_b beneath the tip. A new positive cluster of positive vorticity has formed near the tip. To allow compatibly between the streamlines associated with this cluster and the focus F_c, a new saddle point SPc is formed.

In the wake of the plate at x'/C = 1.25, all of the critical points of the flow topology defined at the trailing edge x'/C = 1.0 are preserved, and the saddle point SP_c has rotated clockwise by approximately 90°. Moreover, comparison with the vorticity concentrations in the images shown in the inserts at x'/C = 1.0 and 1.25 indicate that they are also generally preserved, with some attenuation of higher levels.

4.4.4 Inboard-Directed Vortex

Figure 4.10 shows the case of a slightly inboard interaction of the incident vortex with the leading-edge of the plate. That is, the center of the vortex is located just inboard of the tip of the plate and slightly above its leading-edge, such that the major share of vorticity $\omega_x C/U_\infty$ is on the upper side of the plate, as indicated at streamwise locations upstream of and at the leading-edge of the plate, x'/C = -0.25 and 0.

At x'/C = 0.25, a single focus F_a exists on the upper side of the plate, which is associated with the cluster of negative (blue) vorticity. The direction of swirl is in the clockwise direction, in accord with the incident vortex and the swirl exists both in the region above and below the surface of the plate. At the tip of the plate, a saddle point SP_a exists. In fact, this saddle point persists for larger streamwise distances along the plate of x'/C = 0.5, 0.75 and 1.0. As shown particularly clearly at x'/C = 0.5 and 0.75, a small-scale separation bubble, defined by the region of the separation and reattachment streamline in the immediate vicinity of the tip, occurs to the left of the saddle point. On the other hand, to the right of the saddle point, the streamlines pass about the region of the tip relatively undistorted to the region beneath the plate. For the limiting location at the trailing edge of the plate, i.e., at x'/C = 1.0, the saddle point rotates clockwise by approximately 90° such that it is located beneath the tip of the plate. This preservation of the small-scale separation-reattachment region at the tip of the plate in conjunction with the saddle point indicates that there is no formation of a tip vortex in contrast to the cases of the outboard and slightly outboard interactions of the incident vortex with the plate indicated in Figures 8 and 9. A complementary interpretation of lack of formation of a tip

vortex is as follows. The downwash of the streamlines in the immediate vicinity of the tip of the plate overwhelms the naturally occurring upwash due to angle of attack and thereby the tendency to form a tip vortex.

A further observation associated with this slightly inboard interaction is as follows. The well-defined focus F_a that exists at $x'/C = 0.25$ is not identifiable at larger values of x'/C. This is due to the fact that the peak level of negative (blue) vorticity is attenuated at larger values of x'/C, and thereby cannot induce a localized region of swirl relative to the large-scale overall swirl associated with the original incident vortex, which is preserved over all locations up to the trailing edge at $x'/C = 1.0$.

Although this slightly inboard interaction does not induce an enhanced tip vortex, in contrast to the cases of the outboard and slightly outboard interactions of Figures 8 and 9, it does yield a layer of high level positive (red) vorticity along the upper surface of plate, this layer of positive vorticity is in accord with the streamlines directed from right to left, that is, from the tip to inboard locations along the surface of the plate.

In the wake of the plate, that is, at $x'/C = 1.25$, the saddle point SP_a is still identifiable. In addition, a focus F_b occurs; it is apparently associated with the shedding process from the trailing edge of the tip of the plate

4.5 CONCLUSIONS

The impingement of a trailing vortex upon a wing has been characterized using a technique of particle image velocimetry. The present experiments are employed in conjunction with high fidelity computations at the Air Force Research Laboratory to classify the basic modes of vortex-wing interaction. The predominant parameter that dictates the mode of interaction is the dimensionless location of the incident vortex relative to the tip of the wing. Substantial differences in the values of dimensionless circulation and Reynolds number of the incident vortex between computations and experiments yield the same mode of interaction so long as the dimensionless position of the incident vortex is matched.

The central focus of this investigation is to define the streamline topology for generic modes of interaction. The patterns of streamlines and the associated critical points, including foci, saddle points, bifurcation lines and nodal lines, provide insight into the physics of the interaction and genesis of the various types of interaction modes. When the incident vortex is located outboard of the tip of the wing, it forms a dipole with the enhanced vortex generated from the wing tip. This dipole involves a region of accelerated flow between the two vortices, which manifests as a bifurcation line that exists above and parallel to the plate. Saddle points above and below the tip of the plate allow complex, localized patterns of the flow to coexist.

Substantially different streamline topology occurs if the incident vortex is located inboard of the wing tip. In this case, a portion of the incident vortex moves above the surface of the plate; it is initially identified with a focus which does not persist with increasing distance along the chord due to rapid attenuation of higher levels of vorticity.

Moreover, the streamline topology above and below the tip of the plate is greatly simplified, with absence of any saddle points, relative to the aforementioned case where the incident vortex is located outboard of the tip of the wing. At the tip of the wing, a separation bubble defined by separation-reattachment streamlines encloses only low level vorticity. Immediately adjacent to this bubble at the tip, a saddle point occurs. This separation bubble-saddle point system is remarkably invariant with increasing chordwise distance along the wing. This means that onset of a separation line at the tip does not occur and thereby formation of a tip vortex does not develop. This type of topology is compatible with the downwash that occurs immediately outboard of the saddle point.

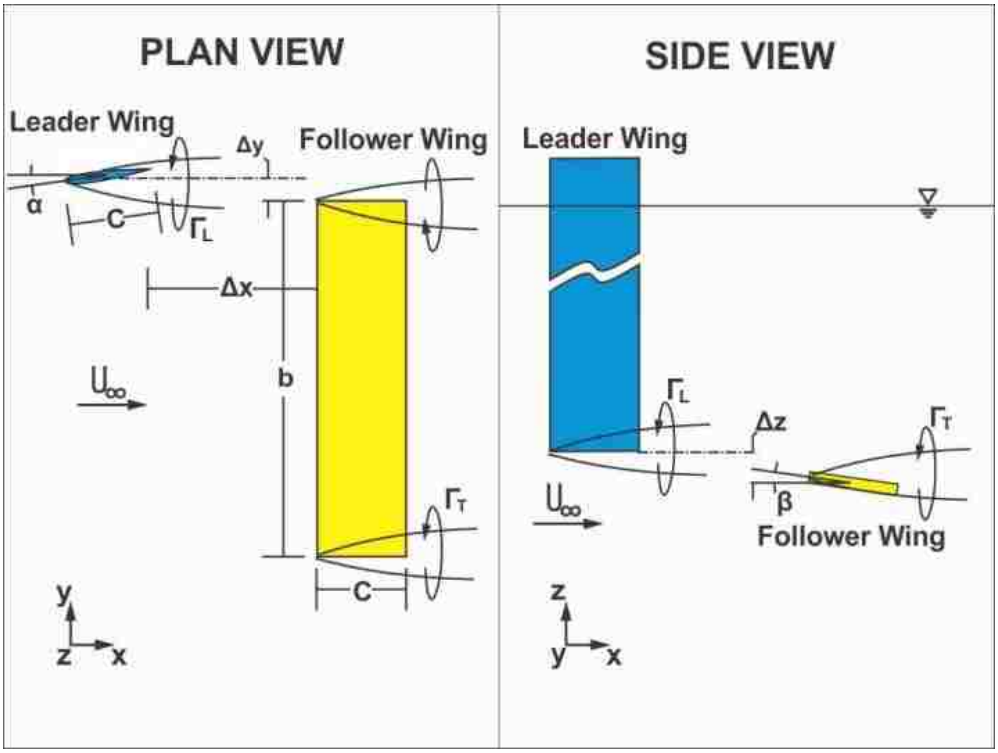

Figure 4.1: Plan and side views of the experimental arrangement

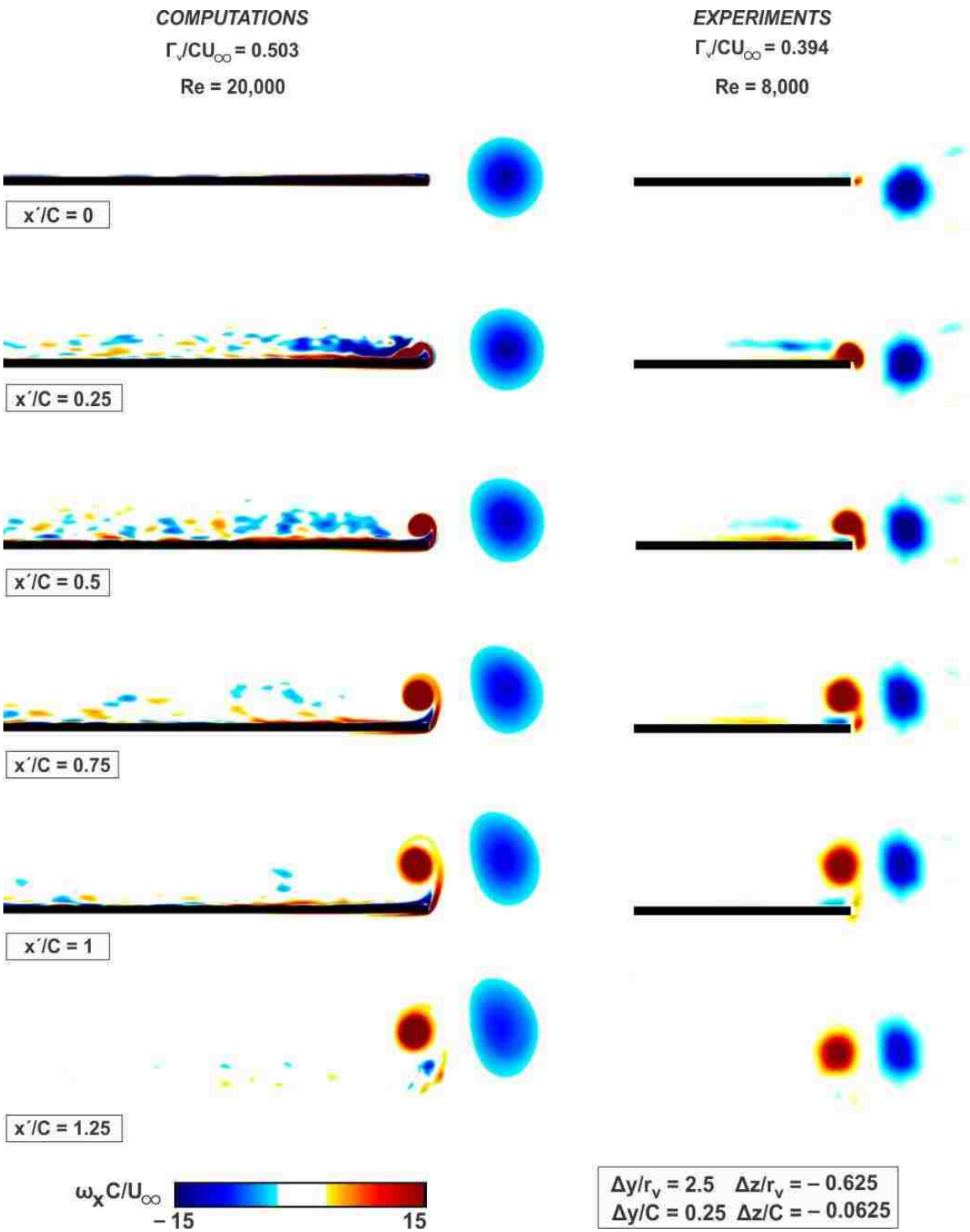

Figure 4.2: Comparison of streamwise vorticity from computations of Garmann and Visbal (2015a) ($\Gamma_v/(CU_\infty)$ = 0.503; Re = 20,000) and present experiments ($\Gamma_v/(CU_\infty)$ = 0.394; Re = 8,000) for the outboard interaction of an incident vortex with a plate. Images of Garmann et al (2015a) are after images appearing in Garmann, D. J. and Visbal, M. R. 2015a Interactions of a streamwise-oriented vortex with a finite wing. *Journal of Fluid Mechanics* 767, 782-810. Courtesy of Cambridge University Press

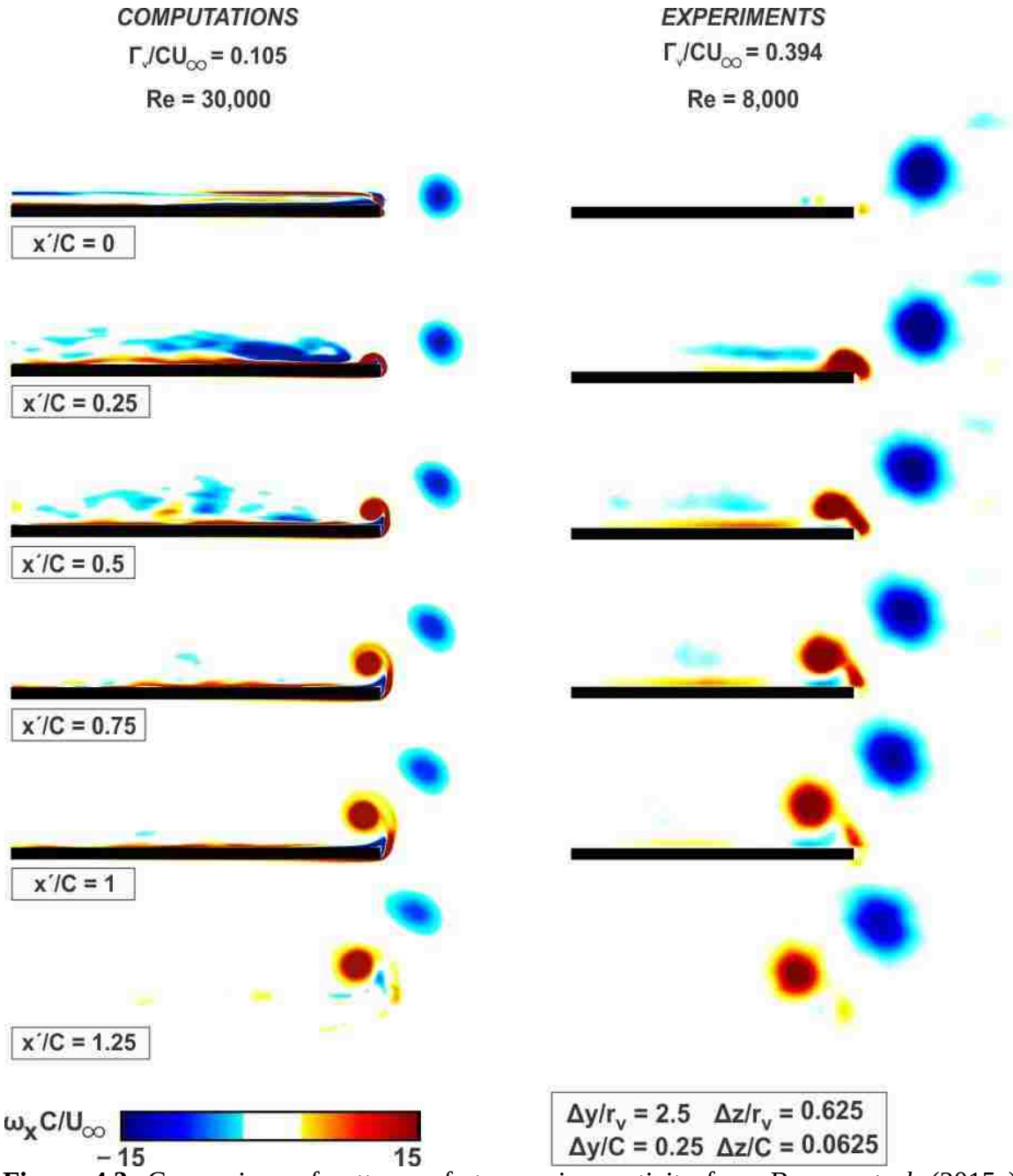

Figure 4.3: Comparison of patterns of streamwise vorticity from Barnes *et al.* (2015a) ($\Gamma_v/(CU_\infty)$ = 0.105; Re = 30,000) and present experiments ($\Gamma_v/(CU_\infty)$ = 0.394; Re = 8,000) patterns correspond to outboard interaction of an incident vortex with a plate. Images after Barnes et al (2015a) are reproduced with permission from Barnes, C. J., Visbal, M. R. & Gordnier, R. E. 2015a Analysis of streamwise-oriented vortex interactions for two wings in close proximity. Phys. Fluids 27 (015103). Copyright 2014, AIP Publishing LLC

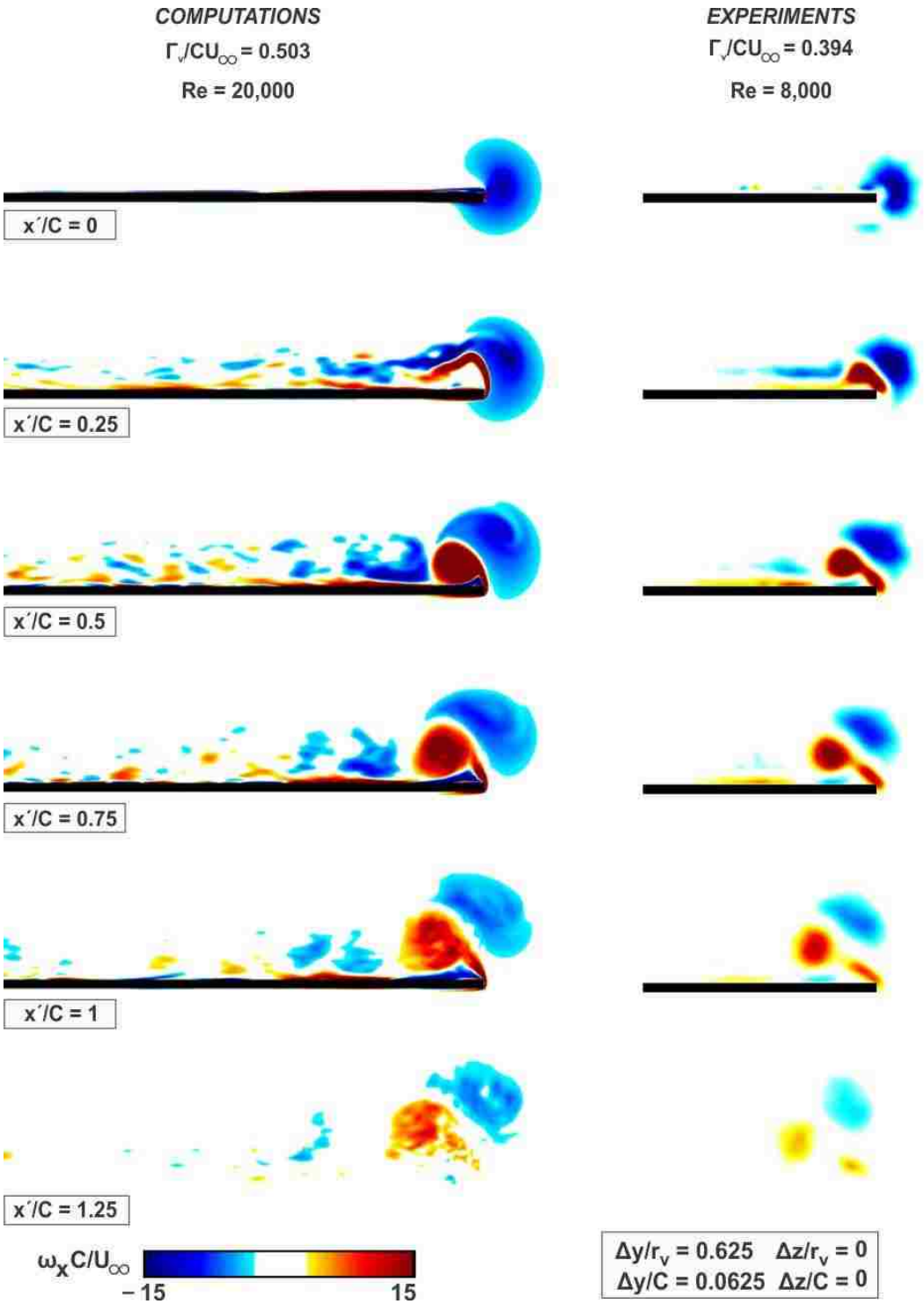

Figure 4.4: Comparison of streamwise vorticity from computations of Garmann and Visbal (2015a) ($\Gamma_v/(CU_\infty)$ = 0.503; Re = 20,000) and present experiments ($\Gamma_v/(CU_\infty)$ = 0.394; Re = 8,000) for the aligned interaction of an incident vortex with a plate. Images of Garmann et al (2015) are after images appearing in Garmann, D. J. and Visbal, M. R. 2015a Interactions of a streamwise-oriented vortex with a finite wing. *Journal of Fluid Mechanics* 767, 782-810. Courtesy of Cambridge University Press.

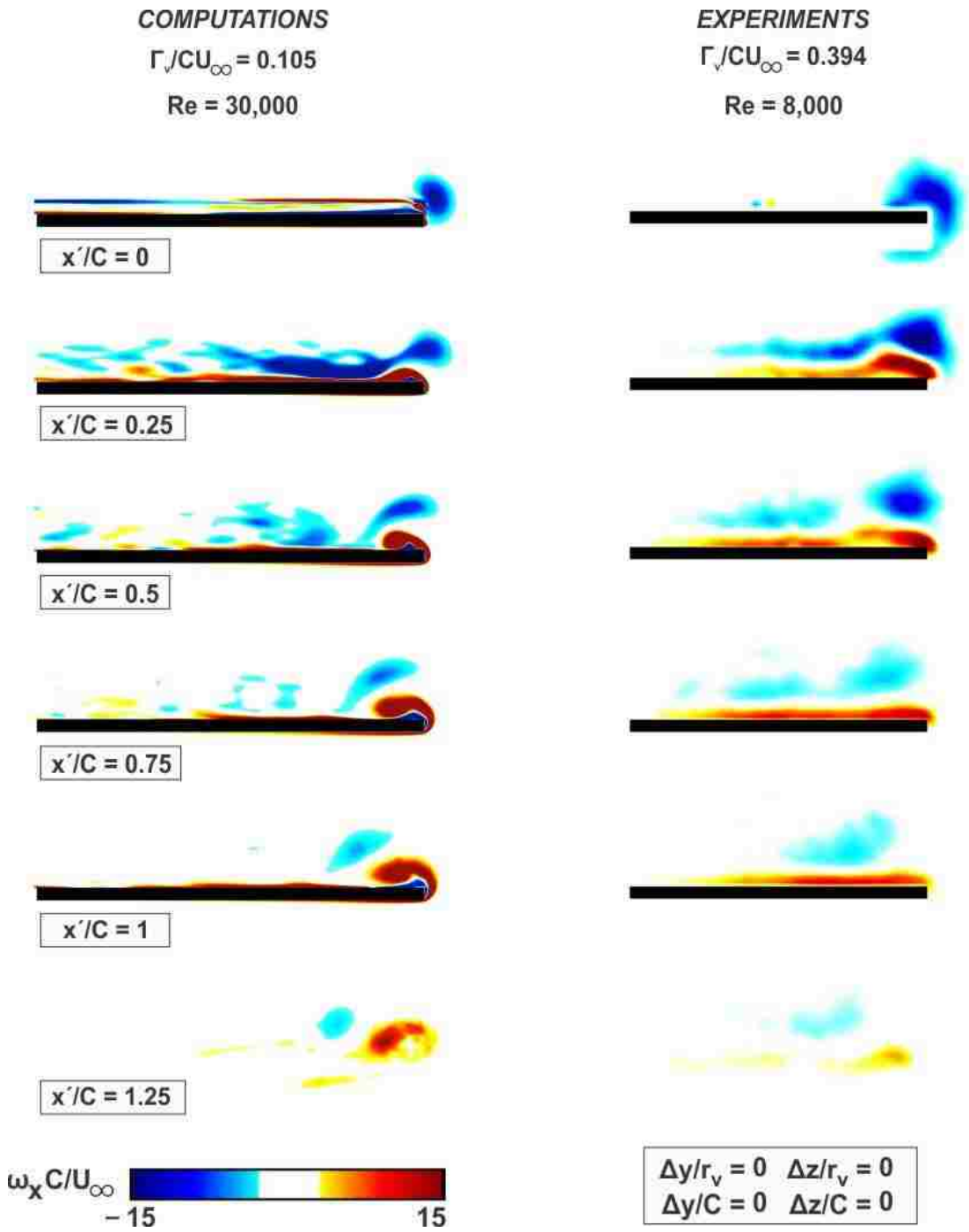

Figure 4.5: Comparison of patterns of streamwise vorticity from Barnes *et al.* (2015a) ($\Gamma_v/(CU_\infty)$ = 0.105; Re = 30,000) and present experiments ($\Gamma_v/(CU_\infty)$ = 0.394; Re = 8,000) patterns correspond to aligned interaction of an incident vortex with a plate. Images after Barnes et al (2015a) are reproduced with permission from Barnes, C. J., Visbal, M. R. & Gordnier, R. E. 2015a Analysis of streamwise-oriented vortex interactions for two wings in close proximity. Phys. Fluids 27 (015103). Copyright 2014, AIP Publishing LLC

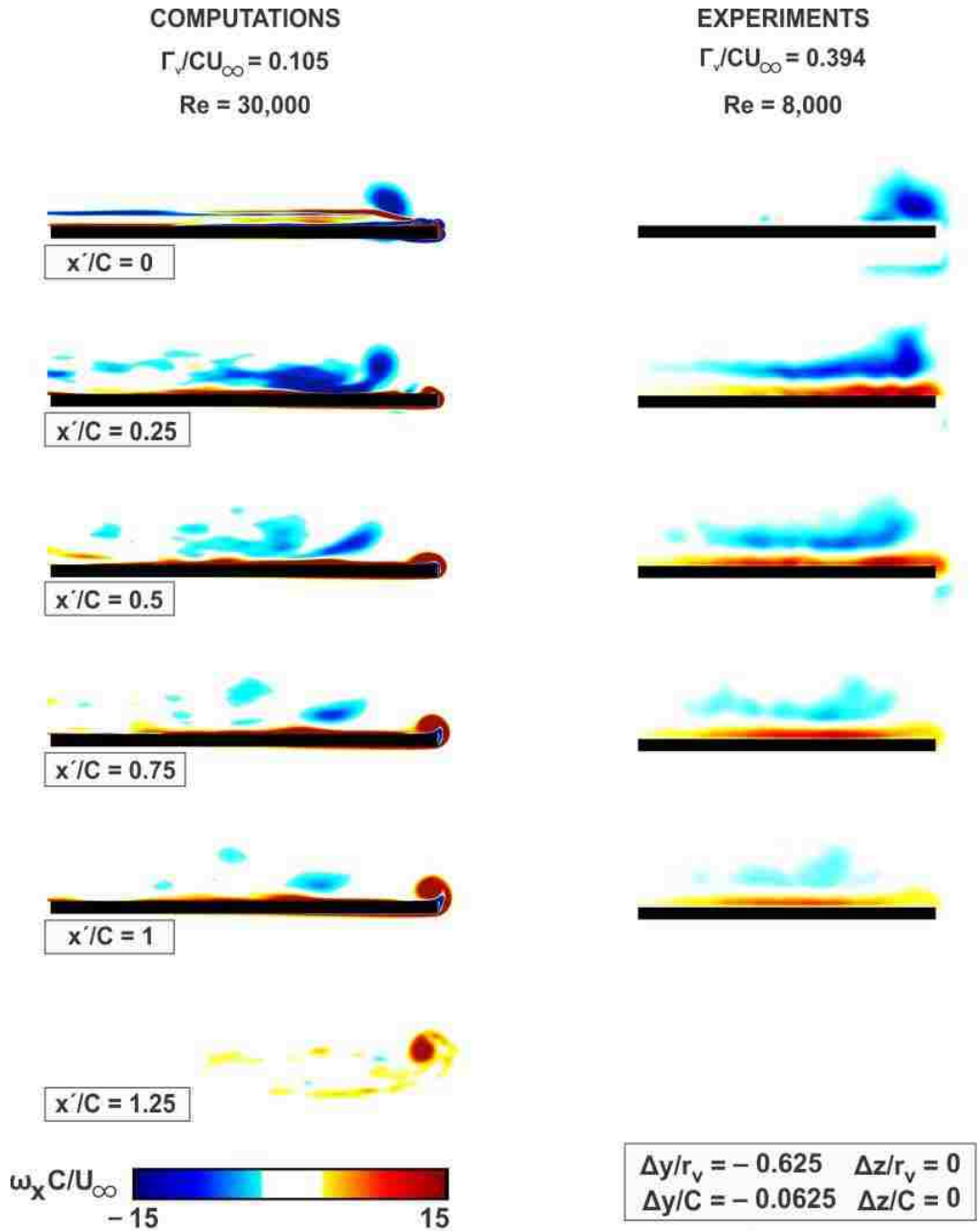

Figure 4.6: Comparison of patterns of streamwise vorticity from Barnes *et al.* (2015a) ($\Gamma_v/(CU_\infty)$ = 0.105; Re = 30,000) and present experiments ($\Gamma_v/(CU_\infty)$ = 0.394; Re = 8,000) patterns correspond to inboard interaction of an incident vortex with a plate. Images after Barnes et al (2015a) are reproduced with permission from Barnes, C. J., Visbal, M. R. & Gordnier, R. E. 2015a Analysis of streamwise-oriented vortex interactions for two wings in close proximity. Phys. Fluids 27 (015103). Copyright 2014, AIP Publishing LLC

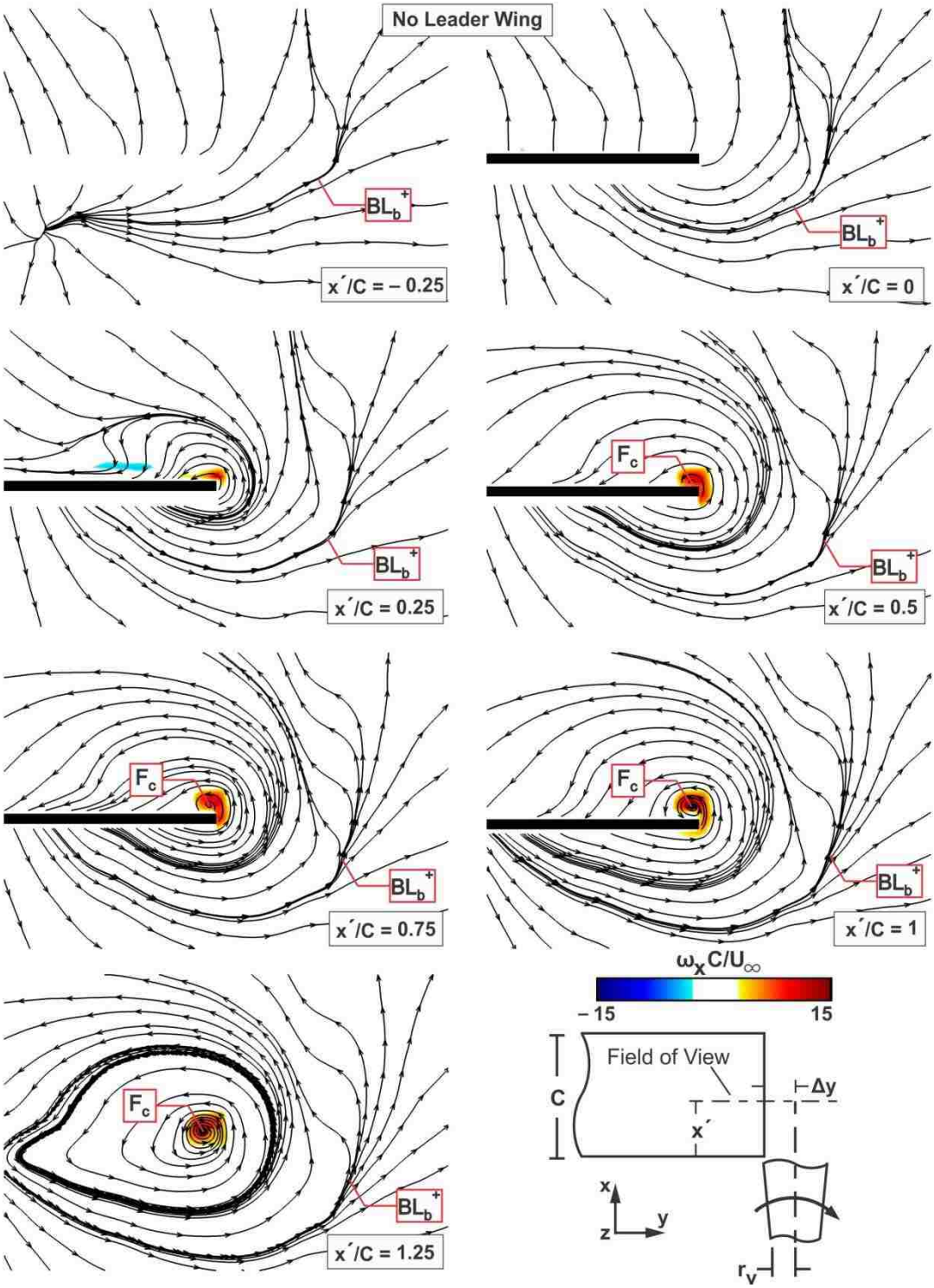

Figure 4.7: Experimental patterns of time-averaged streamlines superimposed on streamwise vorticity $\omega_x C/U_\infty$ contours located on streamwise oriented planes

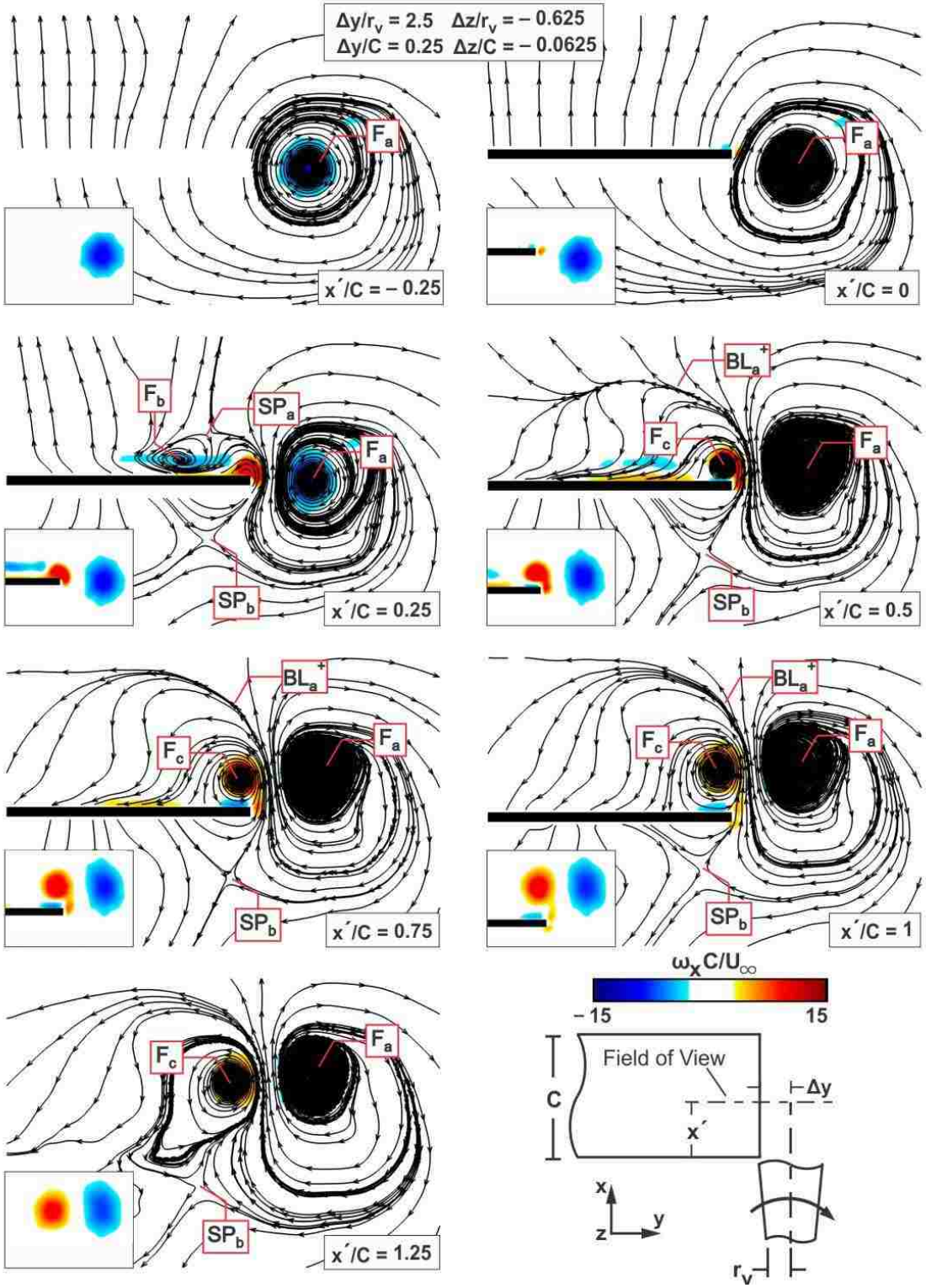

Figure 4.8: Experimental patterns of time-averaged streamlines superimposed on streamwise vorticity $\omega_x C/U_\infty$ contours located on streamwise oriented planes

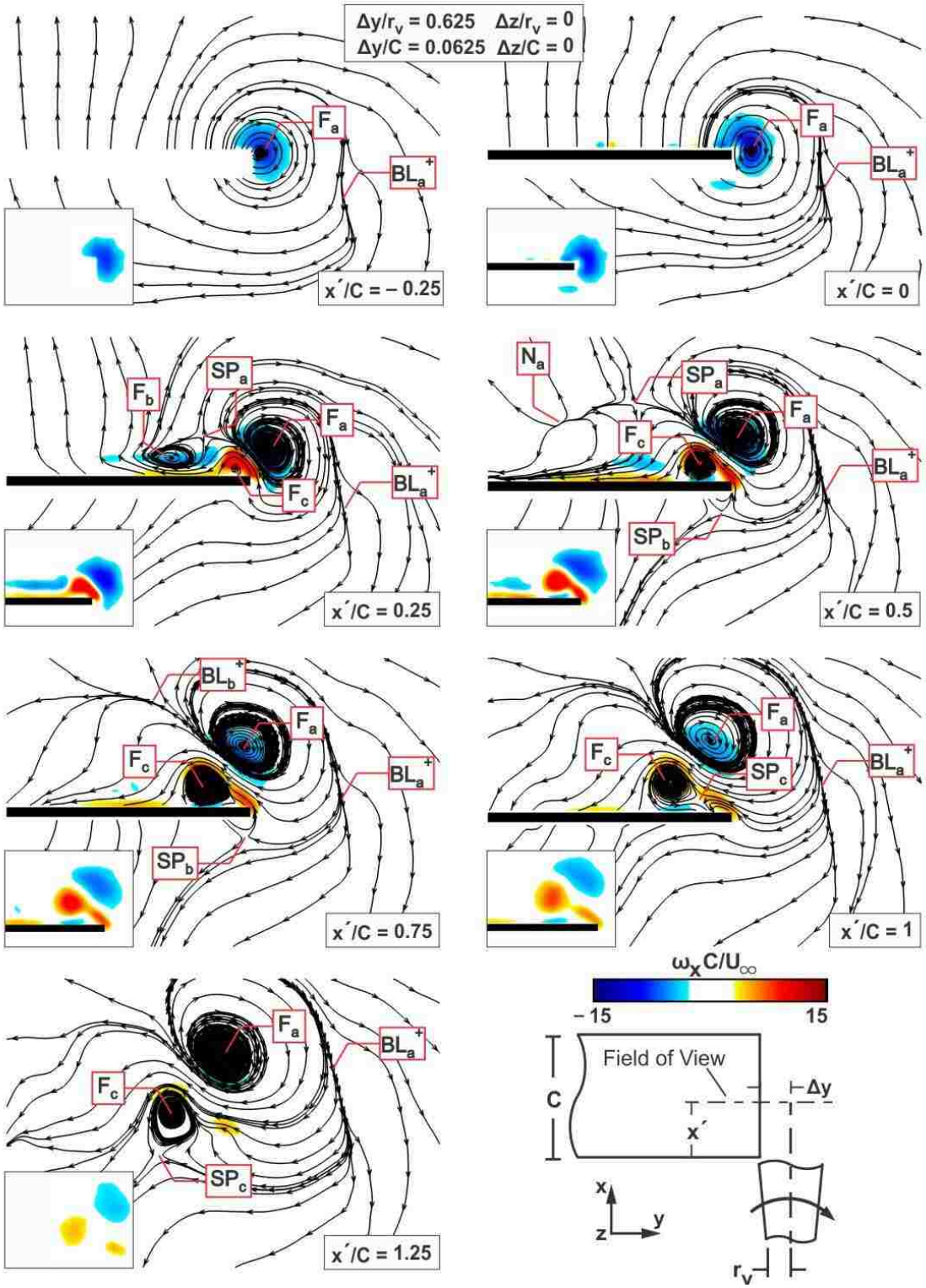

Figure 4.9: Experimental patterns of time-averaged streamlines superimposed on streamwise vorticity $\omega_x C/U_\infty$ contours located on streamwise oriented planes.

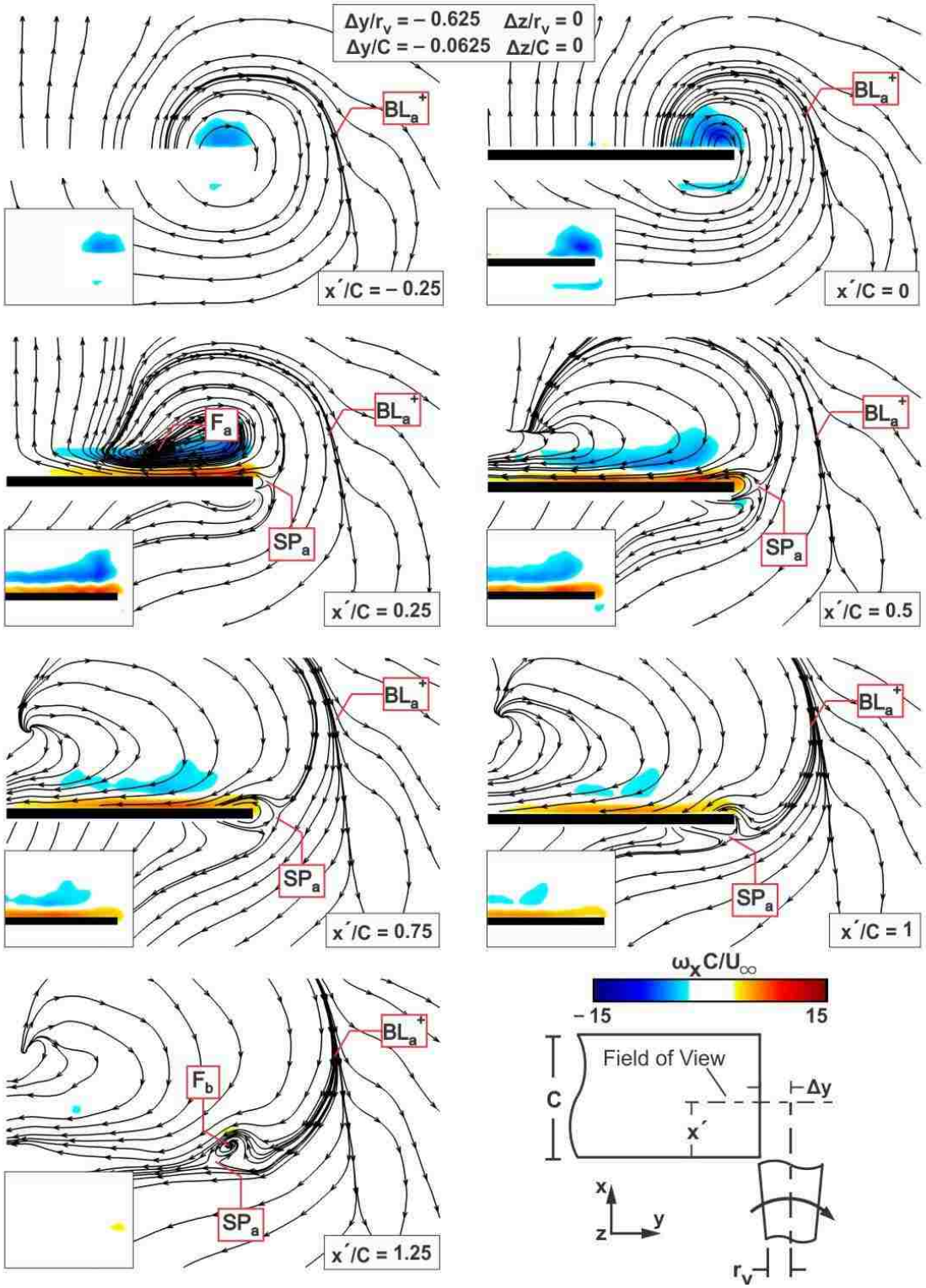

Figure 4.10: Experimental patterns of time-averaged streamlines superimposed on streamwise vorticity $\omega_x C/U_\infty$ contours located on streamwise oriented planes.

CHAPTER 5

INTERACTION OF A TRAILING VORTEX WITH AN OSCILLATING WING

5.1 OVERVIEW

Interactions between vortices and bodies and the associated unsteady loading have been reviewed by Rockwell (1998). One class of interaction involves an incident vortex with its axis oriented in the streamwise direction. Applications include vortices incident upon the wing of a trailing aircraft in formation flight, the fin or tail of an aircraft, and blading in turbomachinery. While the interaction with a stationary wing has been examined extensively, relatively little attention has been devoted to the case of a trailing vortex impinging on an oscillation wing. Investigation into an oscillating wing would reveal the underlying flow physics in applications where wings were bending or flapping, both of these cases are common in formation flight.

The focus of this investigation is on the physics of interaction of an incident vortex with an oscillating wing, in particular the unexplored effect of outboard displacement of the vortex from the tip of the wing. It is anticipated that the nature of this interaction will vary during the oscillation cycle of the wing. More specifically, variations of the trajectory of the incident vortex, potential shedding of vorticity from the tip of the wing, and net upwash and downwash outboard of the wing tip are anticipated during the oscillation cycle. The interrelationship between these features will be pursued.

5.2 EXPERIMENTAL SYSTEMS AND TECHNIQUES

A free-surface water channel was employed in the present experiments; it had a test section length of 4877 mm, a width of 927 mm, and a depth of 610 mm. The freestream turbulence intensity was 0.3%, and the freestream velocity was U_∞ = 158 mm/s, which corresponded to a Reynolds number of 8000 based on the wing chord. The experimental setup is shown in figure 5.1(a). The vortex generator (blue) is a squared tip NACA 0012 airfoil which has chord C = 50.8 mm, angle of attack α = 8° and is oriented vertically. The wing (yellow) is a clear acrylic flat plate with chord C = 50.8 mm, thickness t = 3.175 mm, span b = 203.2 mm, and angle of attack β = 0°. The streamwise separation between the two wings is held constant in these experiments at Δx = 254 mm.

The vertical Δz and spanwise Δy offsets relative to the tip of the wing were defined by the trajectory of the vortex shed from the vortex generator. Preliminary mono particle image velocimetry (MPIV) images were acquired to determine which values of vertical and spanwise offset led to impingement of the tip vortex from the vortex generator on the tip of the wing. This location was defined by the vortex generator offsets Δy_0 and Δz_0. In this investigation, four different values of spanwise offset Δy were examined, $\Delta y = \Delta y_0$ + 19.05 mm, Δy_0 + 12.7 mm, Δy_0 + 6.35 mm, and Δy_0, while $\Delta z = \Delta z_0$, i.e., no offset in the vertical direction.

To allow precise movement of the components of the experimental arrangement during experiments, a motion control system was used. It involved two Compumotor stepper motors interfaced with National Instruments P70530 micro-stepper drives, a National Instruments PCI-7344 4-card, and a UMI-7764 indexer box. Oscillation of the

vertical position of the wing was achieved by applying a constant angular velocity to a wheel which had an off-center hole and was connected to the wing via an arm. This connection translated the rotational motion of the wheel into z sinusoidal perturbation in the heaving mode, which had an amplitude A = 6 mm and a frequency f = 2.5 Hz. Figure 5.1(b) depicts the position and velocity of the wing during the heaving cycle.

Monoscopic particle image velocimetry (MPIV) was employed to determine the quantitative structure of the vortices, which provides the two in-plane components of velocity. The flow was seeded with 11 μm hollow metallic coated plastic spheres such that 15-20 particle images were present in the interrogation window of 32 x 32 pixels. To illuminate these particles, a 3 mm thick laser sheet was produced by a dual-pulsed Nd-YAD laser operating at 10 Hz, which allowed eight images to be captured during each heaving cycle. Images were acquired with a camera that had a CCD array of 1600 x 1200 pixels. The image from the camera was then evaluated using a cross-correlation technique with 50% overlap, yielding 7227 vectors in the field of view. Each pixel is 52.04 μm/px, which corresponds to an interrogation window width of 1665.28 μm.

The in-plane uncertainty was calculated using the technique described in Adrian and Westerweel (2011). The RMS random error for the in-plane velocity is between 5.1% and 7.2% of the freestream velocity. For this MPIV setup, the pixel size is large compared to the particle image diameter and therefore the bias error associated with the uncertainty in the location of a particle is small in comparison to the RMS random error. Another source of bias error comes from calculating out-of-plane vorticity, which requires the comparison of several nearby velocity vectors. Soria et al. (1995) showed

that the distances between these vectors can cause errors that deterministically underpredict the vorticity in the core of an Oseen vortex, which is a reasonable approximation of the incident vortex of the present experiments. Consideration of six velocity vectors along the radius of the vortex, defined as the radial distance from the vortex axis to the maximum tangential velocity, gives a maximum out-of-plane vorticity bias error of 3% along the vortex axis. This bias error decreases linearly as the radial distance from the vortex axis increases.

For each experimental configuration, image acquisition was performed at intervals of 12.7 mm intervals extending from a location 25.4 mm upstream of the leading edge of the wing to 50.8 mm downstream of its trailing edge. At each location, 640 images were captured, which corresponded to 80 images per phase. These images were then phase-averaged, a process performed by averaging every image at a certain phase, to produce the final images. Based on convergence tests, an average of 80 images was found to be sufficient to represent the phase-averaged flow, with the maximum values of spanwise velocity, upwash, and streamwise vorticity being within 4% of the converged values.

The flow structure at different streamwise locations was examined by translating the wing system to the desired position. The vortex generator could move independently from the rest of the system, which allowed investigation of different locations of vortex impingement upon the trailer wing.

5.3 SIMULTANEOUS EFFECTS OF WING MOTION AND INCIDENT VORTEX ON FLOW STRUCTURE

5.3.1 Patterns of Streamwise Vorticity

Figure 2 shows contours of streamwise vorticity ω_x at the half-chord location along the wing. The vertical displacement z_w and velocity w_w of the wing are indicated in the diagrams at the bottom of the layout. The downstroke z_w occurs from $\phi = 0$ to π, and the upstroke from π to 2π. The vertical velocity w_w of the wing is $w_w = 0$ at its extreme positions, $\phi = 0$ and π. Moreover, the maximum positive velocity occurs at $\phi = 3\pi/2$ while maximum negative velocity is at $\phi = \pi/2$.

For the case where the incident vortex is located furthest outboard, $\Delta y/C = 0.375$, shown in the left column of images of figure 5.2, the shape of the incident vortex, comprised of negative (blue) vorticity, is relatively unchanged over the full cycle of motion of the wing. On the other hand, for the vortex formed from the tip of the edge, comprised of positive (red) vorticity, its existence is evident only over a portion of the oscillation cycle of the wing. As the downstroke begins, at $\phi = \pi/4$, the tip velocity has a significant negative value; a small region of (red) vorticity is apparent at the tip of the wing. This scale of the tip vortex increases as the negative (downward) velocity of the wing increases, reaching its largest size at $\phi = \pi/2$ and $3\pi/4$. At the extreme position of the downstroke, the region of vorticity associated with the tip vortex decreases in scale. The upstroke immediately follows at $\phi = 5\pi/4$, where there is only a very small region of

positive vorticity above the surface of the wing. For the remainder of the rising motion of the wing, there is no positive vorticity present in the field of view.

The same general trend as in the foregoing, with several distinctive differences, occurs for the vortex offset $\Delta y/C = 0.25$ shown in the second column of images of figure 5.2. In this case, the incident (blue) vortex becomes slightly distorted as the (red) tip vortex increases in scale and strength. The shape of the vortex goes from circular to oblong, over the range of phase angle from $\phi = 0$ to π, whereby the top of the incident vortex leans towards the tip vortex. As will be shown subsequently, this distortion is associated with a dipole involving the two vortices. The close proximity of the incident vortex to the tip of the wing has an effect on the structure of the tip vortex, which has increased in scale and strength (defined as higher vorticity values, darker red) at all phases, relative to the outboard case shown in the first column of images.

For the incident vortex at an offset of $\Delta y/C = 0.125$, represented in the third column of images of figure 5.2, the shape and position of the incident vortex experiences large variations with phase angle of the wing motion. This observation is due to the close proximity of the incident vortex to the wing.

Finally, for the extreme case where the incident vortex is nominally aligned with the tip of the wing, $\Delta y/C = 0$, corresponding to the images in the fourth column of figure 5.2, the incident (blue) vortex is not detectable from $\phi = \pi/4$ to $3\pi/4$. For this range of phase angle, it impinges directly on the tip of the wing, whereas outside this range of phase angle, the trajectory of the incident vortex is deflected away from the tip of the wing. Furthermore, a well-defined (red) tip vortex does not form at the wing tip. The only

positive vorticity is in the form of a small layer of low level (yellow) vorticity that wraps around the tip; it remains adjacent to the surface of the wing from $\phi = \pi/2$ to $5\pi/4$.

The effect of offset $\Delta y/C$ of the incident vortex on the maximum value of positive (red) streamwise vorticity $(\omega_x)_{max}$ is as follows. At $\Delta y/C$ = 0.375, 0.25, and 0.125, the respective values are $(\omega_x)_{max}$ = 18.24, 22.60, and 18.32. That is, as the impingement location of the vortex moves inboard, the maximum value of vorticity initially increases, then decreases until the tip vortex is eliminated entirely at $\Delta y/C$ =0 corresponding to the aligned interaction. This maximum value $(\omega_x)_{max}$ is not achieved at $\phi = \pi/2$, where the wing has its maximum negative velocity w_w, but instead at $\phi = 3\pi/4$. That is, the tip vortex continues to increase in strength despite the deceleration of the wing, resulting in a phase lag between the occurrence of maximum vorticity of the tip vortex and the motion of the wing.

5.3.2 Overview of Flow Structure

Figure 5.3 compares: contours of upwash w (upper row of images); and streamlines superimposed on contours of streamwise vorticity ω_x (lower row). The offset of the incident vortex is at its furthest outboard location $\Delta y/C$ = 0.375, and the images correspond to the two phase angles $\phi = \pi/2$ to $3\pi/2$ during the oscillation cycle. These values of ϕ represent the largest magnitudes of wing velocity w_w, in the negative (downward) and positive (upward) directions respectively.

The images corresponding to the phase angle $\phi = \pi/2$ in the left column in figure 5.3 show three distinct regions of vertical velocity. A small region of (blue) downwash is

located furthest inboard, a large region of upwash (red-yellow) extends from the wing tip outwards, and an additional region of downwash is located furthest outboard. These contours can be physically interpreted with the aid of the corresponding streamlines in figure 5.3. The closely spaced streamlines near the tip of the wing indicate that the flow is accelerated in that region. This observation is due to the combined effect of the upwash induced by the downward velocity of the wing and the upwash induced by the incident vortex. These components combine to form the elongated (red-yellow) region of net upwash indicated in figure 5.3. The two regions of (blue) net downwash are associated with the inboard portion of the forming tip vortex and the outboard portion of the incident vortex.

Next, consider the images corresponding to the phase angle $\phi = 3\pi/2$ in the right column of figure 5.3. The differences between these contours of (red-yellow) upwash and the previously discussed contours at $\phi = \pi/2$ are stark. The present contours show a region of upwash that has smaller magnitude and scale than the upwash at $\phi = \pi/2$ and the nearby region of (blue) downwash at $\phi = 3\pi/2$. Comparing the outboard region of (blue) downwash at $\phi = \pi/2$ and $3\pi/2$, it has increased in size at $\phi = 3\pi/2$. The streamlines reveal that the upward motion of the wing, represented by positive w_w, induces a component of downwash, and thereby results in a decrease of the net (red-yellow) upwash and net (blue) downwash outboard of the tip. In essence, the wing-induced downwash is counter to the upwash induced by the incident vortex, which is the origin of the foregoing changes.

Comparison of the patterns of streamline topology superposed on patterns of vorticity in figure 5.3, shows dramatic differences at $\phi = \pi/2$ and $3\pi/2$, corresponding respectively to maximum negative and positive velocities of the wing. That is, the patterns at maximum negative and positive values of wing velocity are not simply mirror images of each other. They are fundamentally different, with well-defined shedding of vorticity from the tip of the wing and formation of a dipole system of vorticity and streamline topology at the maximum negative velocity of the wing. At the maximum positive velocity of the wing, none of these major features are present. These differences are particularly remarkable in view of the fact that the vertical displacement and maximum magnitude of velocity of the oscillating wing are only 6% of the wing chord and 6% of the freestream velocity respectively; that is, the effect of the wing oscillation or perturbation is greatly magnified in terms of the consequences for streamline topology and formation of a tip vortex.

5.3.3 Patterns of Upwash and Downwash

Large offset of incident vortex Figure 5.4 shows color contours of (red) upwash and (blue) downwash for the case where the incident vortex is displaced furthest in the outboard direction from the tip of the wing, i.e., $\Delta y/C = 0.375$. Contours of black solid lines and dashed lines superposed on the color contours represent respectively upwash and downwash in absence of the incident vortex.

The red-yellow contours of upwash indicate that the largest values occur at the phase angles $\phi = \pi/2$ and $3\pi/4$. At these values of ϕ, there are two primary contributions to the net value of upwash: the upwash indicated by the contours of solid lines arising

from downward velocity of the tip of the wing; and upwash induced by the incident vortex. These contributions are separated spatially over the range of phase angles from $\phi = \pi/4$ to π, where there are two local maxima of upwash. The local maximum near the wing is mostly due to the downward velocity of the tip, while the maximum located further outboard is due to the upwash of the incident vortex. On the other hand, the yellow-orange contours at values of $\phi = 3\pi/2$, $7\pi/4$, and 0 represent relatively small values of net upwash, which are due to the counteracting effects of: the downwash due to the upward velocity of the tip indicated by the black dashed line contours; and the upwash due to the incident vortex.

The magnitude and scale of the (blue) contours of downwash also undergo changes during the oscillation cycle of the wing. They are large when substantial downwash arises from the motion of the wing, as represented by the dashed line contours at values of $\phi = 3\pi/2$, $7\pi/4$, and 0.

Moderate offset of incident vortex Figure 5.5 shows images corresponding to the incident vortex located closer to the tip of the wing, that is, the dimensionless displacement of the vortex axis is $\Delta y/C = 0.25$. The entire pattern of (red-yellow) upwash and (blue) downwash is shifted closer to the tip of the wing relative to the pattern shown in figure 5.4. Furthermore, the pattern of upwash is contracted substantially in the spanwise direction, and the two local maxima of the upwash contours evident over the range of phase angles from $\phi = \pi/4$ to π in the image layout of figure 5.4 have now merged. Moreover, the corresponding concentrations of (red) vorticity shed from the tip

of the wing have a larger scale than those in figure 5.4, indicating a larger value of circulation.

Small offset of incident vortex Figure 5.6 shows that when the incident vortex is located even closer to the tip of the wing, $\Delta y/C = 0.125$, as represented by the images of figure 5.6, the patterns of (red) upwash take on a distinctly different form, namely a narrow cluster that eventually rises above the tip and decreases in magnitude at larger values of phase angle. The patterns of (red) upwash and (blue) downwash form a dipole-like combination at most values of phase angle ϕ.

A further point is that the magnitudes of regions of (blue) downwash are greatly diminished from those given in figure 5.5. In fact, at $\phi = 3\pi/4$ there are no contours of downwash outboard of the wing tip. Apparently the magnitude of the upwash induced in this region by the wing motion is sufficient to cancel the downwash associated with the incident vortex.

Effect of vortex offset on interrelationship between upwash and vorticity. Figure 5.7 shows line contours of upwash superimposed on color contours of vorticity for the four values of offset of the incident vortex. At the offset $\Delta y/C = 0.375$, the spanwise extent of the upwash extends from the incident (blue) vortex towards the shed (red-yellow) vortex during the downstroke from $\phi = \pi/4$ to π, in order to conjoin the two regions of upwash. During the upstroke, extending from $\phi = 5\pi/4$ to 0, this process is reversed, until the only remaining region of upwash is that associated with the incident vortex. Similar patterns are evident for the vortex offset $\Delta y/C = 0.25$. In this case, the two

vortices are close enough that the upwash region extends towards the wing except at values of phase where the wing has a large value of positive (upward) velocity, i.e., $\phi = 3\pi/2$ and $7\pi/4$.

When the incident vortex is offset a small distance from the tip, $\Delta y/C = 0.125$, there is no meaningful distinction between the two regions of upwash. The compressed nature of the dipole causes the line contours to be very closely spaced, representing a large rise in velocity over a short distance. The inclined nature of the dipole is also apparent in this case, with the contours of upwash wrapping around the tip of the wing.

The maximum value of upwash increases at $\Delta y/C = 0.375$ relative to $\Delta y/C = 0.25$, but then decreases from $\Delta y/C = 0.25$ to 0. This observation correlates with changes of the maximum value of streamwise vorticity ω_x with $\Delta y/C$ in figure 5.2. As previously indicated, there is essentially no upwash for the aligned interaction case, $\Delta y/C = 0$.

5.3.4 Patterns of Upwash and Spanwise Velocity

Figure 5.8 shows (black) line contours of upwash *w* superimposed on color contours of spanwise velocity *v* for $\phi = 3\pi/4$. For the outboard location $\Delta y/C = 0.375$ of the incident vortex, there are well defined regions of positive (yellow) and negative (blue) spanwise velocity well outboard of the tip, which are associated with the incident vortex. Near the wing tip there is a small region of positive spanwise velocity beneath the tip, and a region of negative positive velocity above the tip. In short, fluid moves around the wing tip, from the bottom to the top surface.

At $\Delta y/C$ = 0.25, the two regions of negative spanwise velocity have merged into one, which extends from above the wing to well outboard of the tip. This is due to the close proximity of the incident vortex to the tip, as well as the slight incline of the vortex dipole, which is clearly visible in figure 5.2. Further inboard, at $\Delta y/C$ = 0.125, the magnitude of negative spanwise velocity has increased, and there is no longer a region of positive spanwise velocity above the tip. Correspondingly, the incident vortex is above the surface of the wing and forms a dipole with the vortex shed from the tip of the wing (see patterns of vorticity in figure 5.2). Associated with this dipole is an inboard-directed jet evident in figure 5.8. For the aligned case, $\Delta y/C$ = 0, there is lack of a vortex dipole (compare pattern of vorticity in Figure 5.2) and only a region of negative (dark blue) spanwise velocity, which represents a horizontal, inboard-directed jet along the upper surface of the wing.

5.3.5 Patterns of Streamline Topology

Figure 5.9 shows streamlines superimposed on color contours of vorticity at the phase angle $\phi = \pi/2$ during the oscillation cycle of the wing. The smaller image at the center of the layout corresponds to the case of no incident vortex, that is, the oscillating wing in absence of an incident vortex. The four larger images represent varying degrees of offset $\Delta y/C$ of the centerline of the incident vortex relative to the tip of the oscillating wing. Images in the inset of each streamline pattern show the patterns of vorticity.

At $\phi = \pi/2$ the wing is undergoing its maximum negative velocity, w_w, as indicated in the schematic at the bottom of the figure layout. For the case of no incident vortex this negative (downward) velocity of the wing is associated with upwash outboard

of the wing tip. Moreover, in the immediate vicinity of the wing tip, a focus F_c exists; it is associated with generation of positive (yellow) vorticity caused by the motion of the wing.

In presence of the incident vortex, displaced from the tip of the wing by distances of $\Delta y/C$ = 0.375, 0.25 and 0.125, focus F_c still occurs immediately adjacent to the tip. Another focus F_b is located above the surface of the wing for $\Delta y/C$ = 0.25 and 0.125; this focus is associated with the tip vortex. The (red) positive vorticity concentration surrounding focus F_b is connected to a positive vorticity feeding sheet which extends around the tip of the wing. Between the (blue) incident vortex and the tip of the wing, the spacing between streamlines is small indicating a region of large velocity for all values of $\Delta y/C$; this is due to the vortex dipole. The accelerated flow is mostly upwash for $\Delta y/C$ = 0.375, but as the dipole inclines at values of offset $\Delta y/C$ = 0.25 and 0.125, the flow is also accelerated in the spanwise direction. A further topological critical point, evident at values of vortex offset of $\Delta y/C$ = 0.25 and 0.125, is the saddle point SP_a, which allows compatibility between different regions of the streamline patterns.

On the other hand, for the case where the incident vortex is aligned with the tip of the wing, $\Delta y/C$ = 0, no residual (blue) regions of vorticity are evident. However F_c and SP_a are still present. Focus F_c is associated with a low level (yellow) layer of vorticity extending from the tip, and SP_a allows for compatibility between this vorticity and the downwash outside of the tip.

Figure 5.10 shows the streamline topology at a phase angle of $\phi = 3\pi/4$, that is, immediately following attainment of the maximum negative velocity of the wing. For

values of vortex offset relative to the tip of the wing of Δy/C = 0.375, 0.25 and 0.125, the vortex dipole, which is indicated by the spiral patterns of streamlines having F_a and F_b as their foci, have rotated in the counterclockwise direction, relative to their positions in figure 5.9. Moreover, the saddle points SP_a and SP_b also rotate in the same direction.

For the case where the incident vortex is aligned with the tip of the edge, $\Delta y/C$ = 0, the streamlines passing through the saddle point SP_a provide boundaries of the region within which the focus F_c of the tip vortex occurs.

Taking an overview of the general features of the patterns of streamline topology at $\Delta y/C$ = 0.375, 0.25 and 0.125 in both figures 9 and 10, in comparison with the image for the case of no incident vortex, it is apparent that presence of the incident vortex dramatically enhances the magnitude and scale of the tip vortex, thereby giving rise to a dipole vortex system involving the tip vortex and the incident vortex. As a consequence, the incident vortex is displaced significantly in the vertical direction with decreasing values of $\Delta y/C$ until, at the smallest value, it is positioned well above the tip of the wing. All of these features become undetectable and irrelevant when the incident vortex is nominally aligned with the tip of the wing; its coherence is lost.

Figure 5.11 is at the value of phase angle $\phi = 5\pi/4$, and as indicated in the schematic at the bottom of the image layout, this phase corresponds to the upstroke of the wing and the wing velocity w_w is nearly at its maximum positive value. Focus F_a still exists for all positive values of vortex offset $\Delta y/C$. It is now present in the extreme case where the incident vortex is nominally aligned, $\Delta y/C$ = 0, with the tip of the wing. In fact, in this case, the incident vortex is well above the surface of the wing. Moreover, for all

values of $\Delta y/C$, a single saddle point SP_c exists above, and well inboard of, the tip of the wing. This saddle point is at the interface between the flow regions dominated by the incident vortex and the inboard focus F_d. The pronounced concentrations of (red) positive vorticity shed from the tip of the wing have degenerated both in magnitude and scale relative to earlier values of phase angle during the oscillation cycle. At $\Delta y/C = 0$, the yellow layer of vorticity along the surface of the wing is due to the induced boundary layer, which involves flow from right to left along the upper surface.

Figure 5.12 represents attainment of the maximum positive (upward) velocity w_w of the wing at the value of phase angle $\phi = 3\pi/2$. For the case of no incident vortex, represented by the small image at the center of the layout of figure 5.12, a well-defined concentration of (blue) negative vorticity is shed from the tip of the wing and focus F_e is associated with this negative concentration. Furthermore, in the region immediately outboard of the tip of the wing, the induced velocity is in the downward direction, i.e., downwash occurs. In presence of the incident vortex, the integrity of the associated (blue) region of negative vorticity is maintained for all values of vortex offset $\Delta y/C$. It is coincident with the focus F_a of the swirling streamline pattern. For decreasing values of offset $\Delta y/C = 0.375$, 0.25 and 0.125, the center of the incident vortex was further above the tip of the wing and at $\Delta y/C = 0$, it remains above the tip. No saddle points exist in all images. A well-defined positive bifurcation line BL_a is formed above the surface of the wing except at the largest value of incident vortex offset of $\Delta y/C = 0.375$. Furthermore, there is no formation of a red positive tip vortex for all values of $\Delta y/C$ due to the

counteracting effects of downwash that is induced outboard of the tip of the wing and upwash induced by the incident vortex.

Comparison of the patterns of streamline topology and the associated concentrations of vorticity for the case where the wing has its maximum negative velocity in figure 5.9 and its maximum positive velocity in figure 5.12 shows dramatic differences. That is, the patterns at maximum negative and positive velocity are not simply mirror images of each other. They are fundamentally different, with well-defined shedding of vorticity from the tip of the wing and formation of a dipole system of vorticity and streamline topology at the maximum negative velocity of the wing. At the maximum positive velocity of the wing, none of these major features are present. Furthermore, at the maximum negative velocity of the wing, when there is zero offset between the incident vortex and the tip of the wing, its coherence is destroyed and the incident vortex has no apparent consequence for the shedding of vorticity from the tip of the wing. Conversely, at the maximum positive velocity of the wing, the incident vortex maintains its integrity and is displaced well above the tip of the wing. This small oscillation results in effects in the flow field which are greatly enhanced relative to its magnitude.

5.3.6 Volume Representations of Vorticity and Upwash

Figures 13 through 16 show volume reconstructions of the entire flow field surrounding the wing. These images extend from half a chord upstream of the wing (the bottom-most slice) to a chord downstream of the trailing edge (the upper-most slice).

Figure 5.13 shows slices of streamwise vorticity ω_x for the largest offset $\Delta y/C$ = 0.375 of the incident vortex from the tip of the wing. The incident vortex composed of negative (blue) vorticity is evident on the left side of each frame. In agreement with figure 5.2, at x'/C = 0.5, the position of the incident vortex does not vary significantly during motion of the wing. Conversely, the tip vortex undergoes formation and shedding over the wing oscillation cycle. During the downstroke, the scale and magnitude of (red) vorticity vary with both phase and streamwise position along the chord. Overall, the images of figure 5.13 indicate that the physics indicated in figure 5.2 at the mid-chord actually extend over the entire chord of the wing.

Figure 5.14 shows four pairs of images that directly compare net (red-yellow) upwash immediately outboard of the tip of the wing and formation and shedding of (red) axial vorticity ω_x from the tip at four values of phase angle ϕ of the oscillating wing. At $\phi = 0$ there is little positive vorticity along the chord of the wing, and an examination of the upwash reveals that only lower level (orange-yellow) concentrations exists in this region. The wing reaches its maximum negative velocity at $\phi = \pi/2$ and, at this stage, the tip vortex has formed along the chord of the wing. This vortex arises from the correspondingly high levels of upwash that are now present between the incident vortex and the wing. As phase angle ϕ continues to increase, the patterns of large and small upwash move along the tip of the wing into its wake and, correspondingly, the concentrations of shed vorticity shed from the tip are convected downstream as well. This process repeats itself with every oscillation cycle of the wing.

Figure 5.15 shows slices of streamwise vorticity for the limiting case where the axis of the incident vortex is aligned with the tip of the wing i.e., $\Delta y/C = 0$. Keep in mind that the amplitude of the wing motion is only 6% of its chord, that is, $z_w/C = 0.06$. During the downstroke the wing moves low enough such that the majority of the vortex moves over the upper surface of the wing. This can be seen in the third slice downstream at $x'/C = 0$ from $\phi = 0$ to $3\pi/4$. From $\phi = \pi$ to $5\pi/4$ this negative (blue) vorticity associated with the tip vortex moves in the downstream direction along the upper surface of the wing. The upward motion of the wing, which began during these values of ϕ, moves the wing progressively higher towards the incident vortex. As the vertical distance between the wing and the incident vortex decreases, the strength of the interaction between the vortex and its mirror image vortex inside the surface of the wing increases. This interaction moves the incident vortex outboard to the tip, where the upward motion of the plate draws it around the tip. By $\phi = 7\pi/4$, this vorticity is split by the wing, and any remaining vorticity near the trailing edge of the wing is shed. Such vorticity is evident in the wake during the first several phases from $\phi = 0$ to $3\pi/4$. This volume reconstruction again shows that the trends apparent at the half chord extend over the entire chordwise extent of the wing. That is, the incident vortex moves above the upper surface of the wing when the wing is at its lowest position, and is eliminated due to direct interaction with the wing during its upstroke.

The region of positive (red-yellow) vorticity along the surface of the wing also varies during the oscillation cycle. It has the largest extent when the wing has large

negative velocity w_v. While these are the same values of phase where the tip vortex had its largest spatial extent at other values of $\Delta y/C$, a tip vortex does not form in this case.

Figure 5.16 shows patterns of upwash corresponding to figure 5.15 ($\Delta y/C$ = 0). This volume reconstruction represents slices of upwash and downwash near the wing for the aligned incident vortex. Focusing on the region of (blue) downwash, it first diminishes, then disappears along the chord of the wing during the downstroke until $\phi = \pi$. Subsequently, during the upstroke, the downwash increases in magnitude and scale. For the images corresponding to the largest offset of the incident vortex, given in figure 5.14, the upwash associated with the incident vortex is directly outboard of the tip, and it combines with the flow moving around the tip caused by the motion of the wing. In the present case the location of the incident vortex causes its downwash to be positioned directly outboard of the tip. Therefore, the magnitude of the downwash outboard of the tip decreases during the downstroke and increases during the upstroke.

5.4. CONCLUSIONS

Modes of incident vortex-oscillating wing interaction may be defined as follows: (i) the trajectory of the incident vortex is largely unaltered when its impingement location is displaced a distance $\Delta y/C$ = 0.375 outboard of the tip of the wing, in which C is the chord of the wing; (ii) its trajectory is substantially altered, with deviations in both the spanwise and surface normal directions to the wing, when the impingement location is in the range $\Delta y/C$ = 0.25 or 0.125; and (iii) its trajectory undergoes changes in spanwise

position over part of the oscillation cycle and disintegration over the remaining portion of the cycle when it is nominally aligned with the tip of the wing, i.e., $\Delta y/C = 0$.

For all of the foregoing modes, shedding of positive vorticity and formation of a vortex from the tip of the oscillating wing occurs only over a portion of the oscillation cycle. The maximum vorticity and circulation of the shed vortex occurs for the mode (ii) interaction of the incident vortex. In fact, for this mode, the trajectory of the incident vortex is closely linked to the formation of the tip vortex. On the other hand, for mode (iii), where direct encounter of the incident vortex with the tip occurs over a portion of the oscillation cycle, only very low level shedding of vorticity occurs from the tip.

The magnitude and scale of the vorticity shed from the tip of the wing is dictated by the magnitude of the upwash immediately outboard of the tip of the wing. This upwash is due to two contributions: the upwash arising from the small amplitude motion of the wing; and the upwash induced by the incident vortex. These two contributions may be either mutually reinforcing or counteracting, depending on the phase angle of the wing motion. As a consequence, the magnitude and scale of the net upwash immediately outboard of the wing tip can vary substantially during the oscillation cycle. Large magnitude positive vorticity is shed when the tip velocity of the wing is negative. This observation arises from the fact that the induced upwash immediately outboard of the wing tip is positive when the tip velocity is negative, thereby reinforcing the upwash induced by the incident vortex, giving a large magnitude of net upwash and maximum strength of the shed vorticity/vortex from the tip.

The magnitude and scale of the foregoing patterns of upwash are influenced by the offset of the incident vortex from the wing tip. As the offset is decreased, the magnitude and scale of the vorticity shed from the tip of the wing initially increases, then decreases until the limiting case of no shed vorticity when the vortex is aligned with the tip of the wing. This trend can be interpreted in terms of distinctive forms of upwash patterns in relation to the vorticity concentrations of the incident and shed vortices.

Further outboard from the tip of the wing, a region of downwash is induced by the incident vortex. Moreover, a component of downwash is induced during part of the oscillation cycle of the wing. As a consequence, the net downwash in this outboard region is either reinforced or attenuated due to the same physical reasoning as in the foregoing for the net upwash closer to the tip of the wing. This observation has implications for loading on a trailer wing in formation flight.

All of the foregoing features of net upwash and downwash, as well as vorticity shed from the tip of the wing, can be interpreted in terms of streamline topology. Such topology defines the patterns of streamlines in terms of critical points such as foci and saddle points, and allows interpretation of the origins of regions of large upwash and downwash in terms of neighboring regions of the flow field. It is been demonstrated that even though the tip velocity of the wing is relatively small in relation to the freestream velocity, radically different streamline topology occurs at, for example, the maximum positive velocity of the tip in comparison with the maximum negative velocity, i.e., such patterns are not simply symmetrical about the wing.

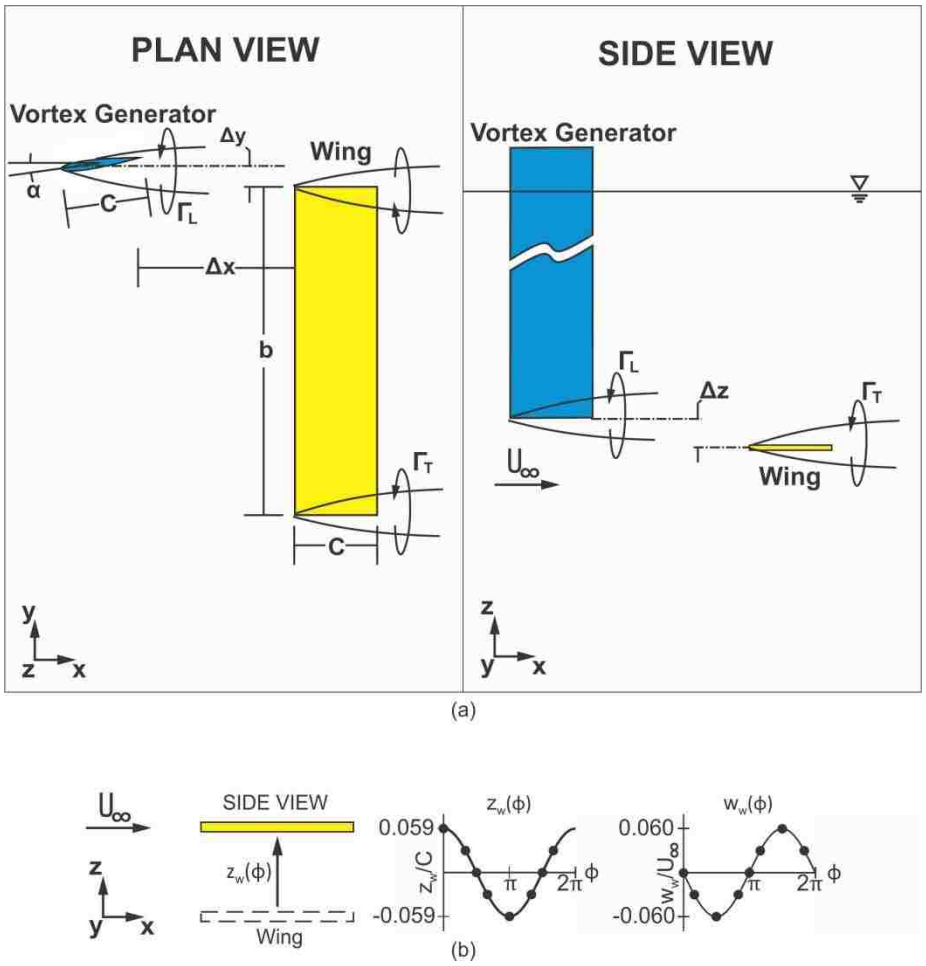

Figure 5.1: (a) Plan and side views of the experimental arrangement. (b) Velocity and position of the wing over the oscillation cycle.

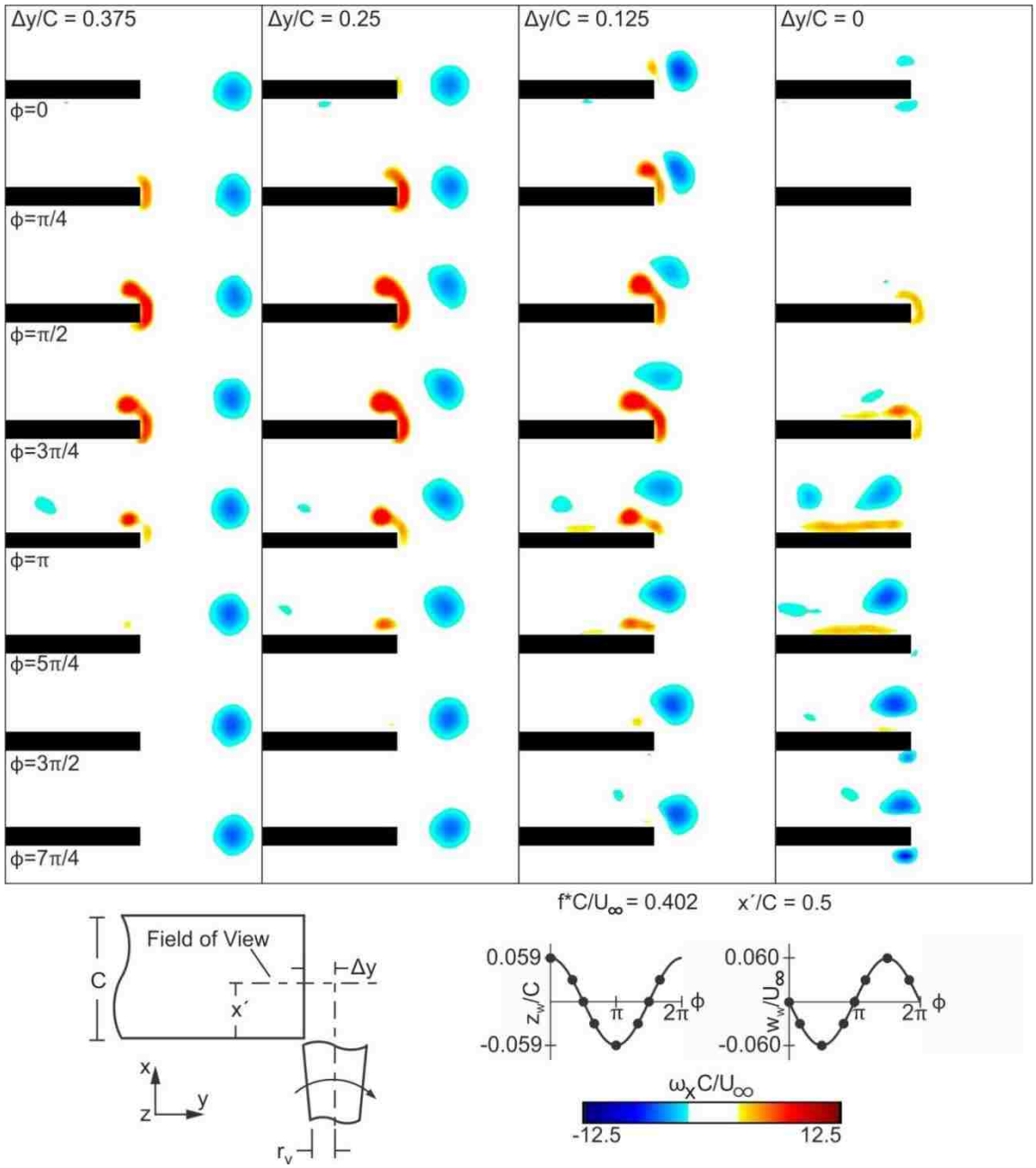

Figure 5.2: Comparison of contours of streamwise vorticity at *x'/C* = 0.5 for four impingement locations (columns) and different phase angles (rows).

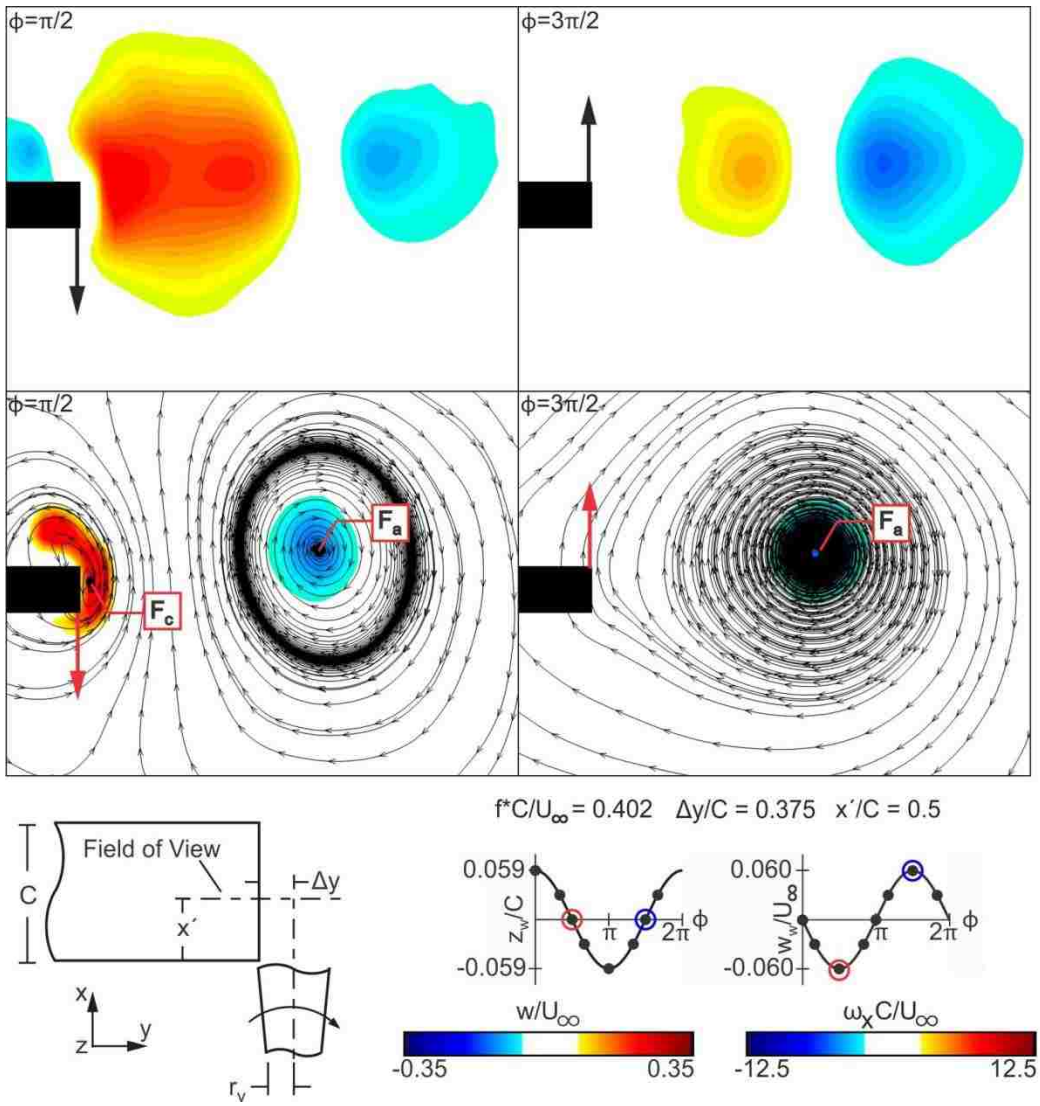

Figure 5.3: Comparison of contours of upwash and streamline topology superimposed on contours of streamwise vorticity for the outboard most impingement case across two phases.

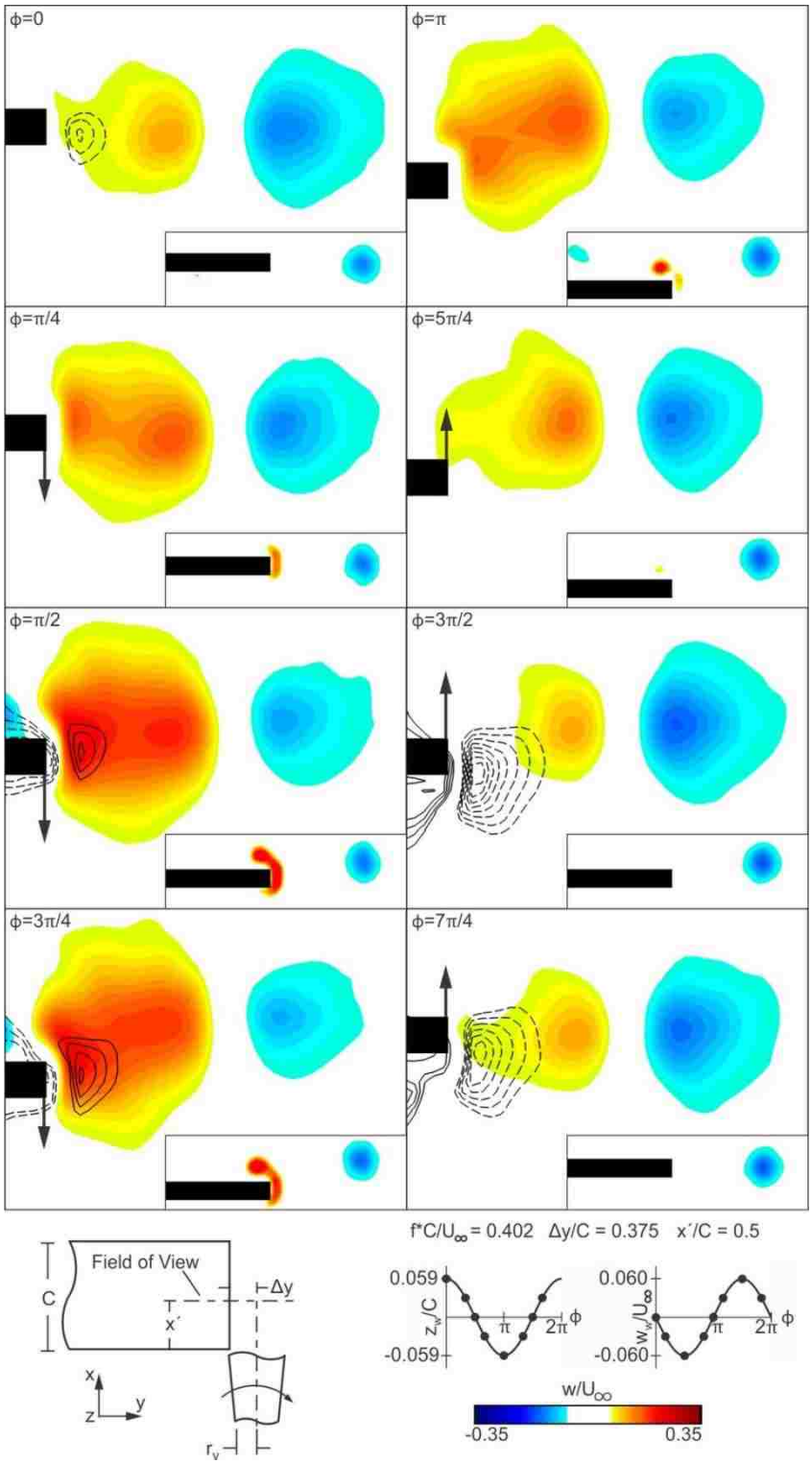

Figure 5.4: Comparison of line contours of upwash (solid) and downwash (dashed) for the case of no incident vortex with color contours of upwash for the largest outboard displacement of the incident vortex $\Delta y/C$ = 0.375. Inlays of streamwise vorticity are visible in the bottom right corner of each image.

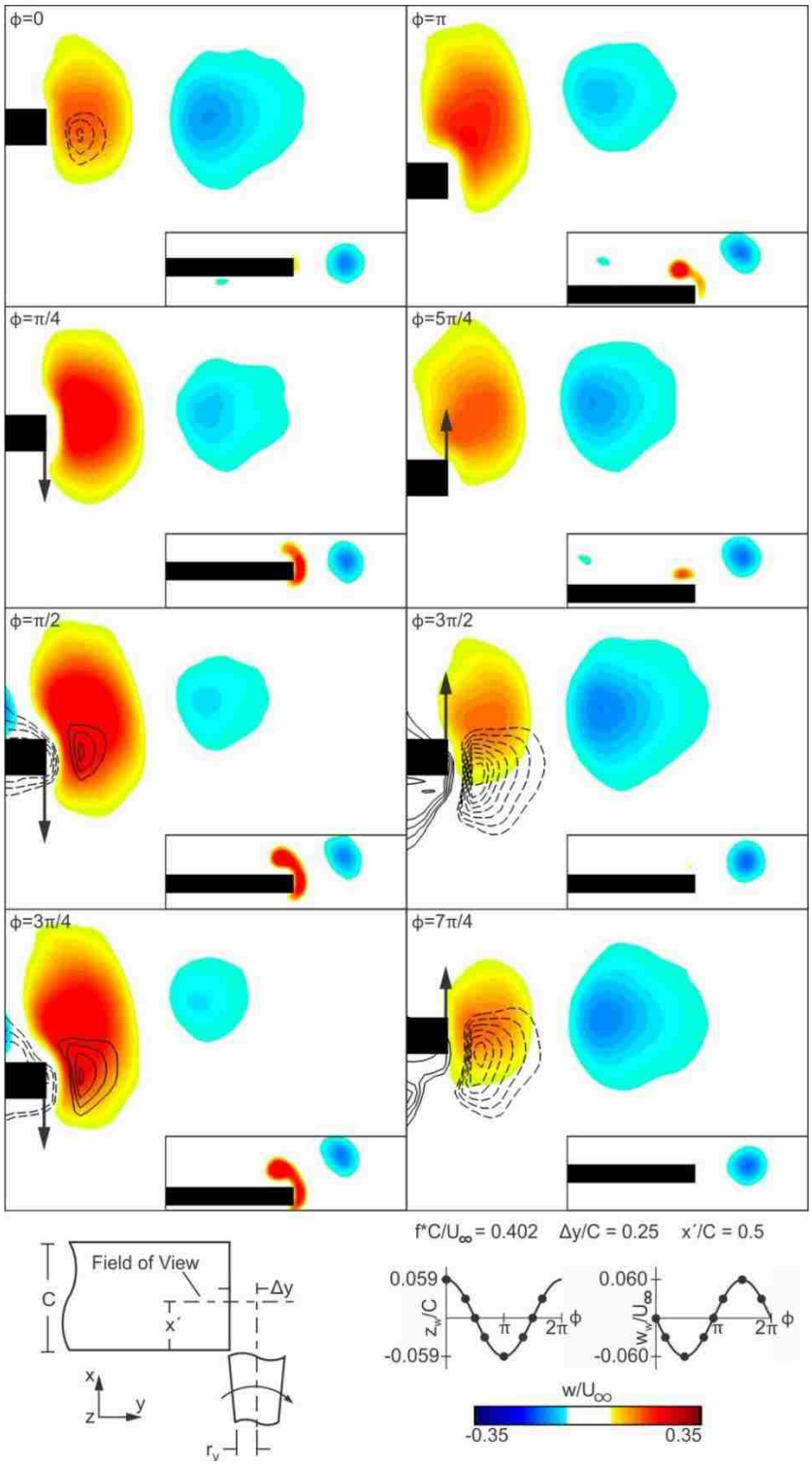

Figure 5.5: Comparison of line contours of upwash (solid) and downwash (dashed) for the case of no incident vortex with color contours of upwash for the outboard displacement of the incident vortex $\Delta y/C = 0.25$. Inlays of streamwise vorticity are visible in the bottom right corner of each image.

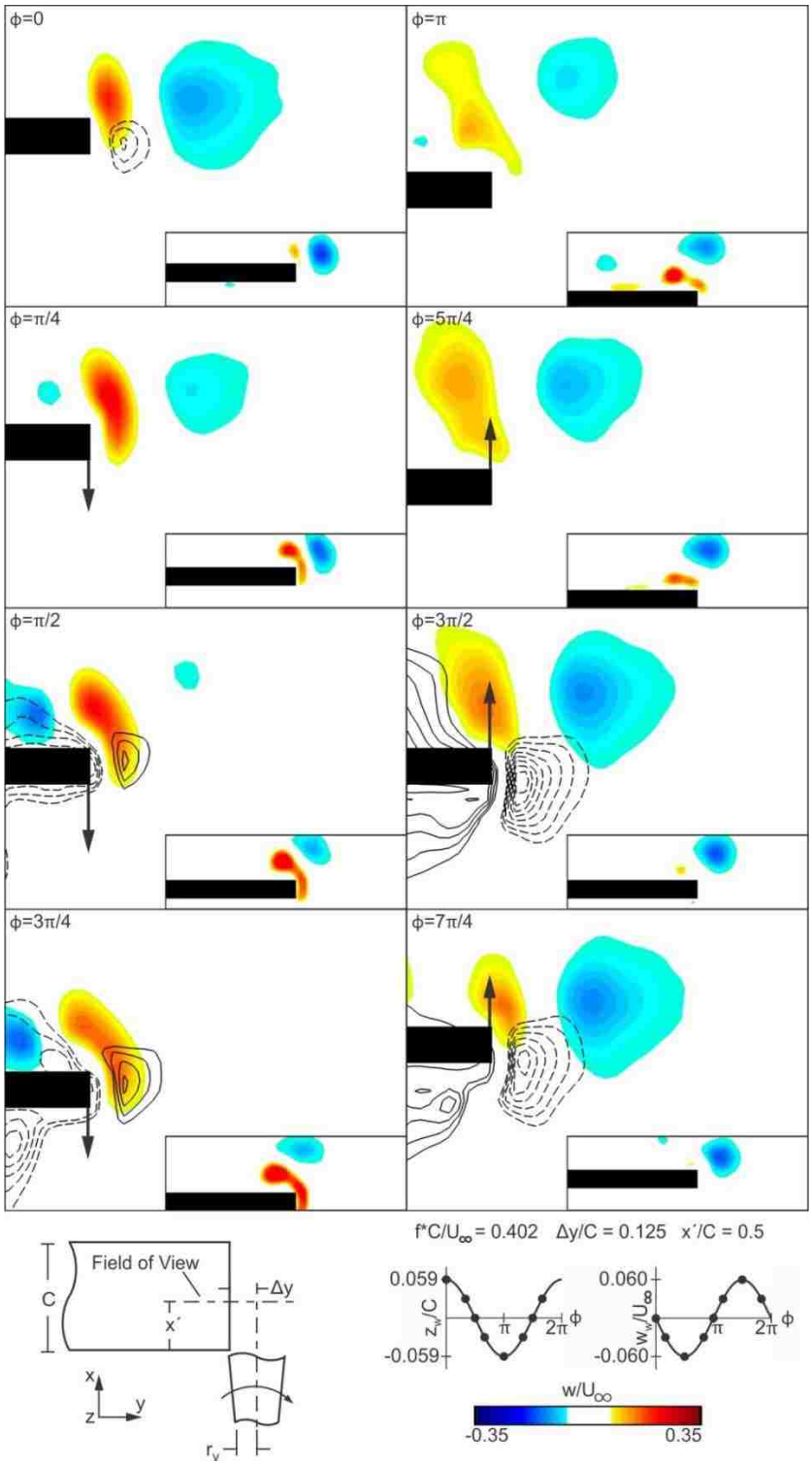

Figure 5.6: Comparison of line contours of upwash (solid) and downwash (dashed) for the case of no incident vortex with color contours of upwash for small outboard displacement of the incident vortex $\Delta y/C$ = 0.125. Inlays of streamwise vorticity are visible in the bottom right corner of each image.

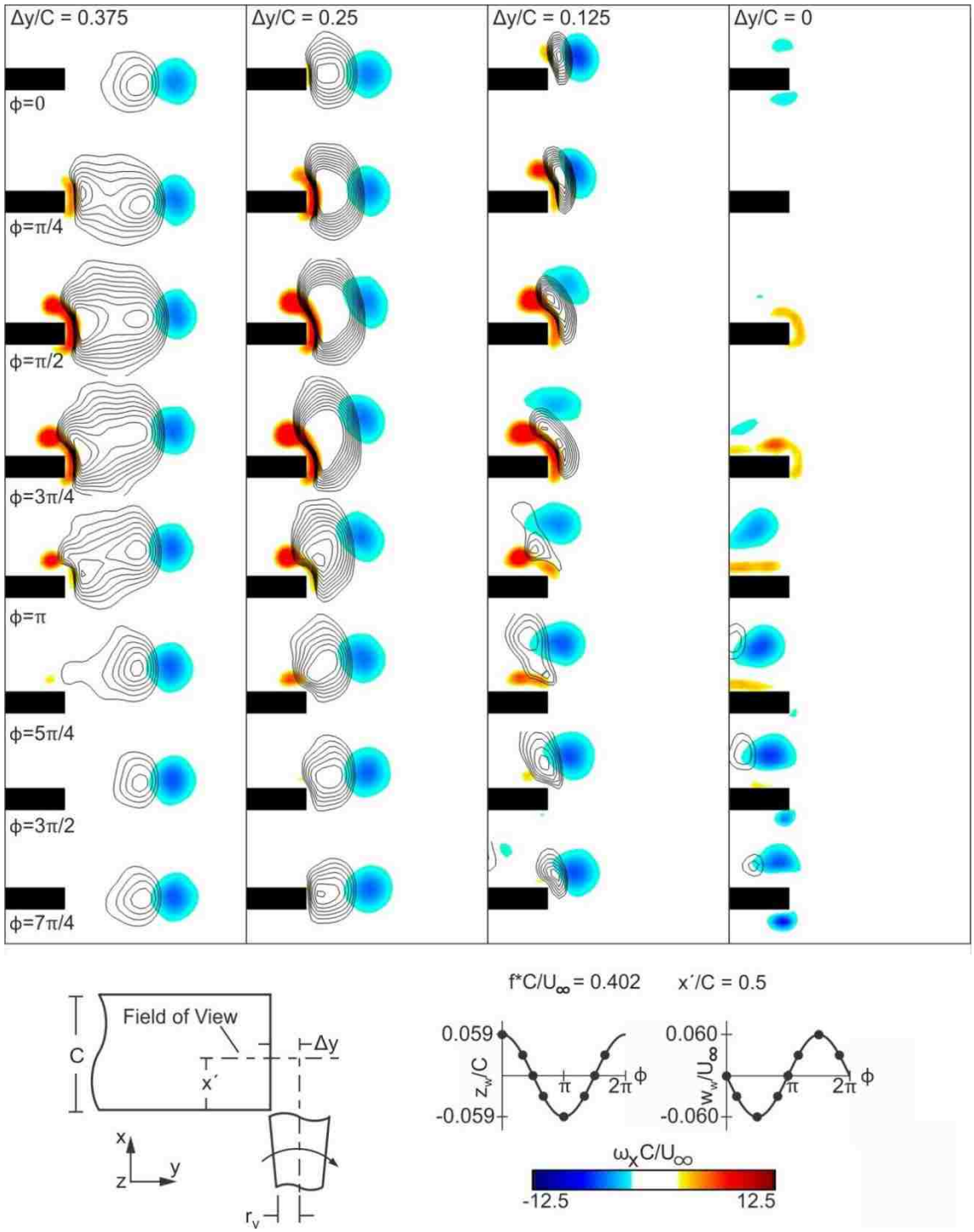

Figure 5.7: Comparison of line contours of upwash with color contours of streamwise vorticity at *x'/C* = 0.5 for four impingement locations (columns) and different phase angles (rows).

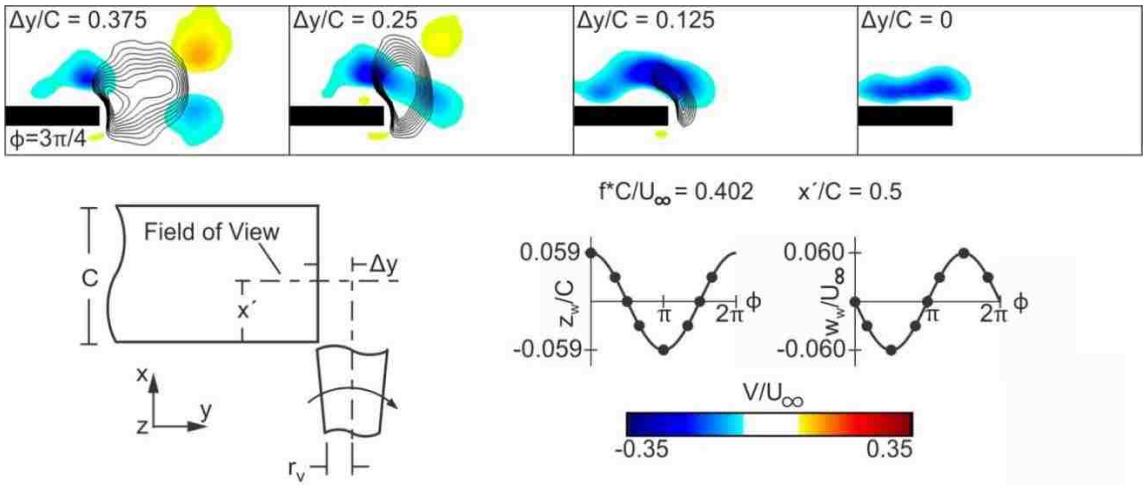

Figure 5.8: Comparison of line contours of upwash with color contours of spanwise velocity at $x'/C = 0.5$ for four impingement locations at $\phi = 3\pi/4$.

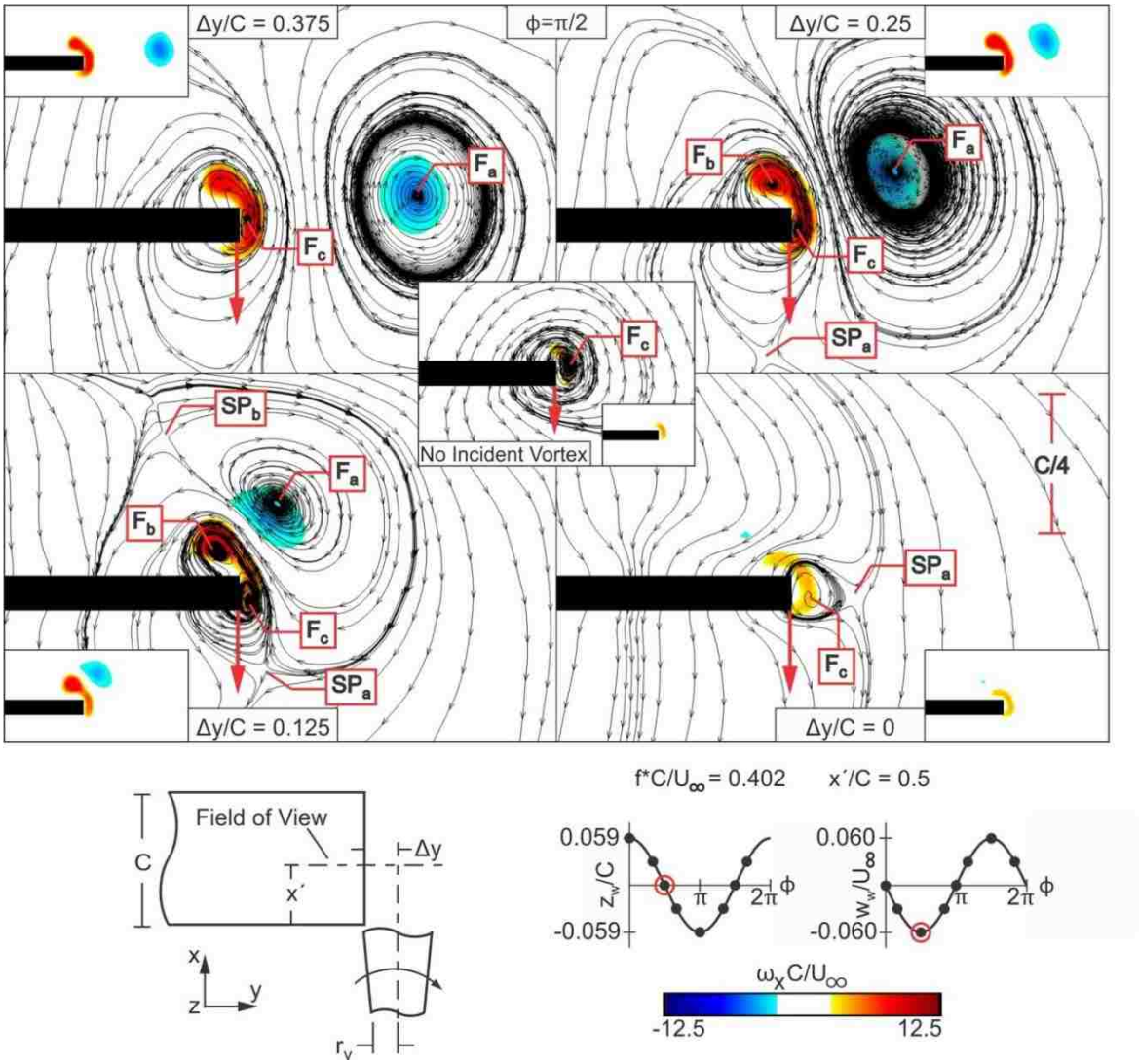

Figure 5.9: Experimental patterns of time-averaged streamlines superimposed on streamwise vorticity $\omega_x C/U_\infty$ contours for four different offsets $\Delta y/C$ of the incident vortex. Also shown is the case of no incident vortex.

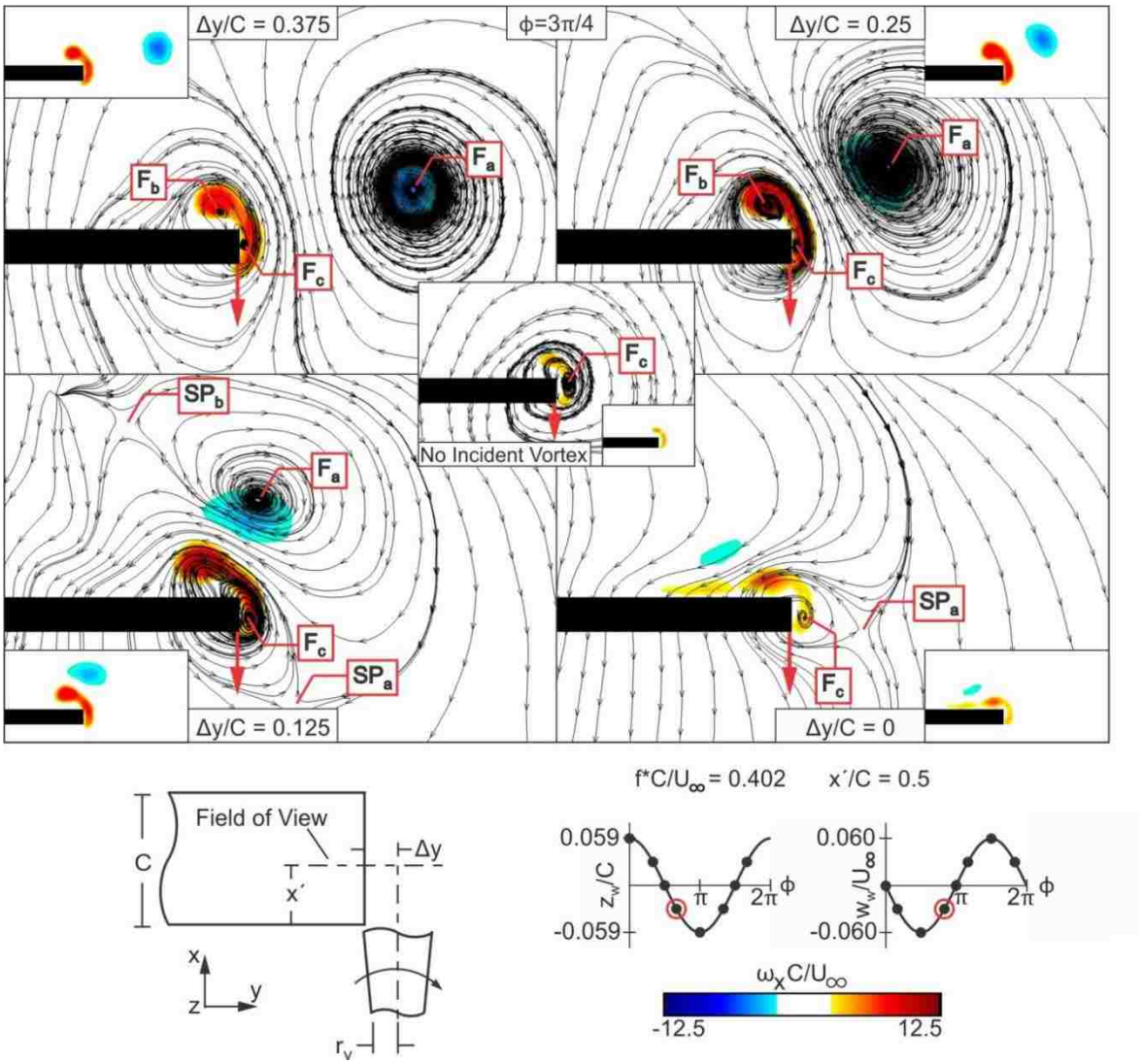

Figure 5.10: Experimental patterns of time-averaged streamlines superimposed on streamwise vorticity $\omega_x C/U_\infty$ contours for four different offsets $\Delta y/C$ of the incident vortex. Also shown is the case of no incident vortex.

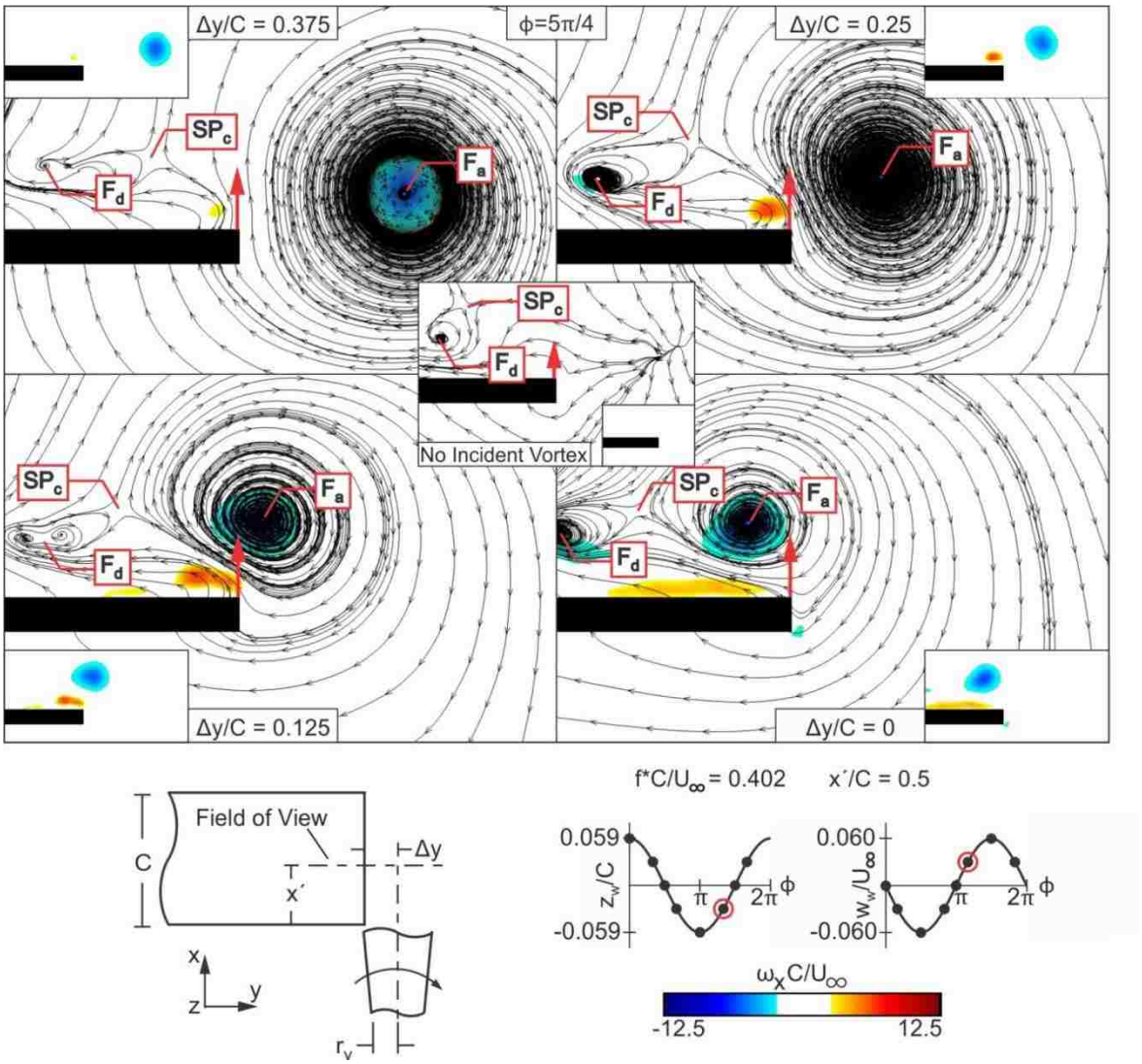

Figure 5.11: Experimental patterns of time-averaged streamlines superimposed on streamwise vorticity $\omega_x C/U_\infty$ contours for four different offsets $\Delta y/C$ of the incident vortex. Also shown is the case of no incident vortex.

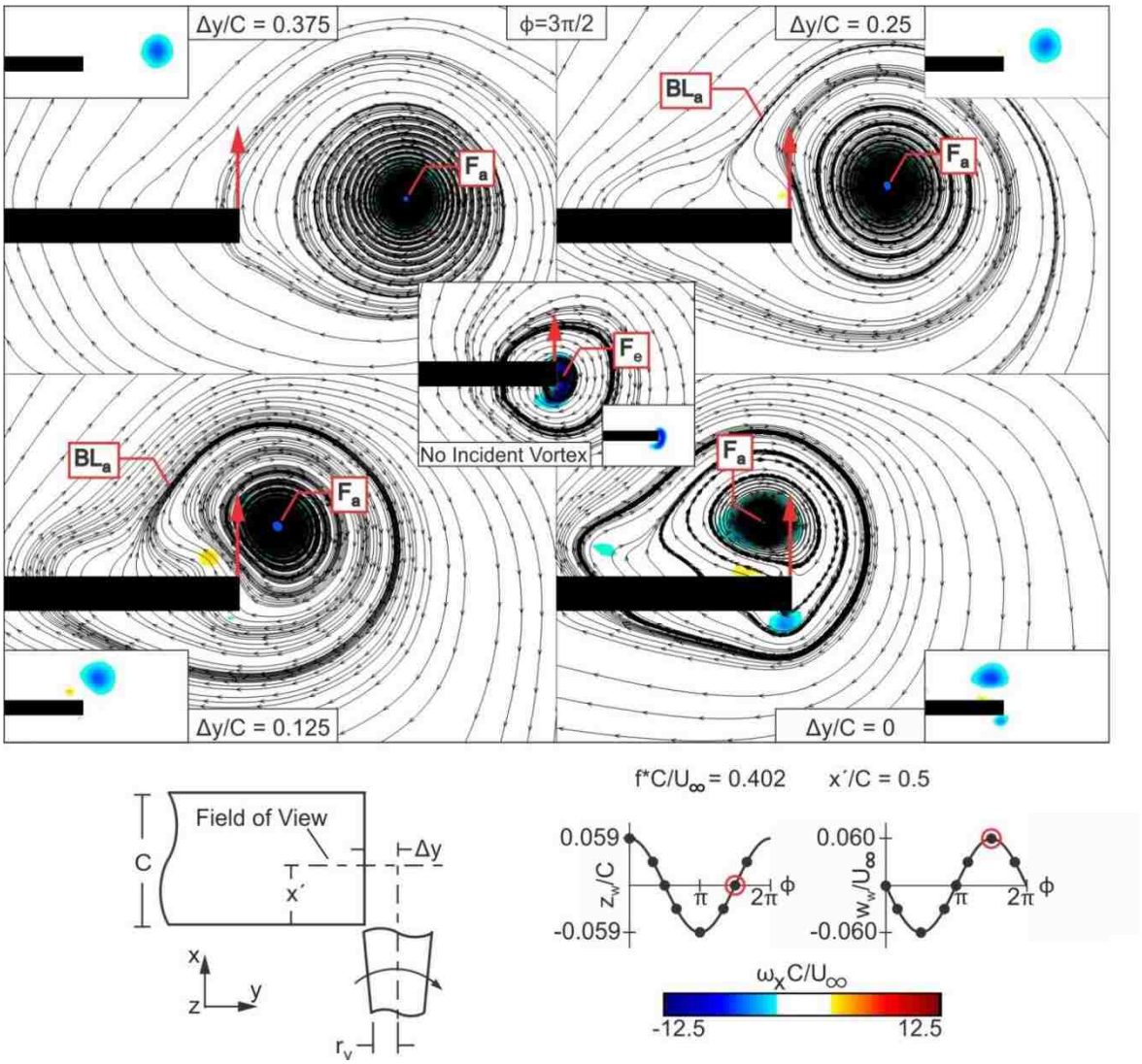

Figure 5.12: Experimental patterns of time-averaged streamlines superimposed on streamwise vorticity $\omega_x C/U_\infty$ contours for four different offsets $\Delta y/C$ of the incident vortex. Also shown is the case of no incident vortex.

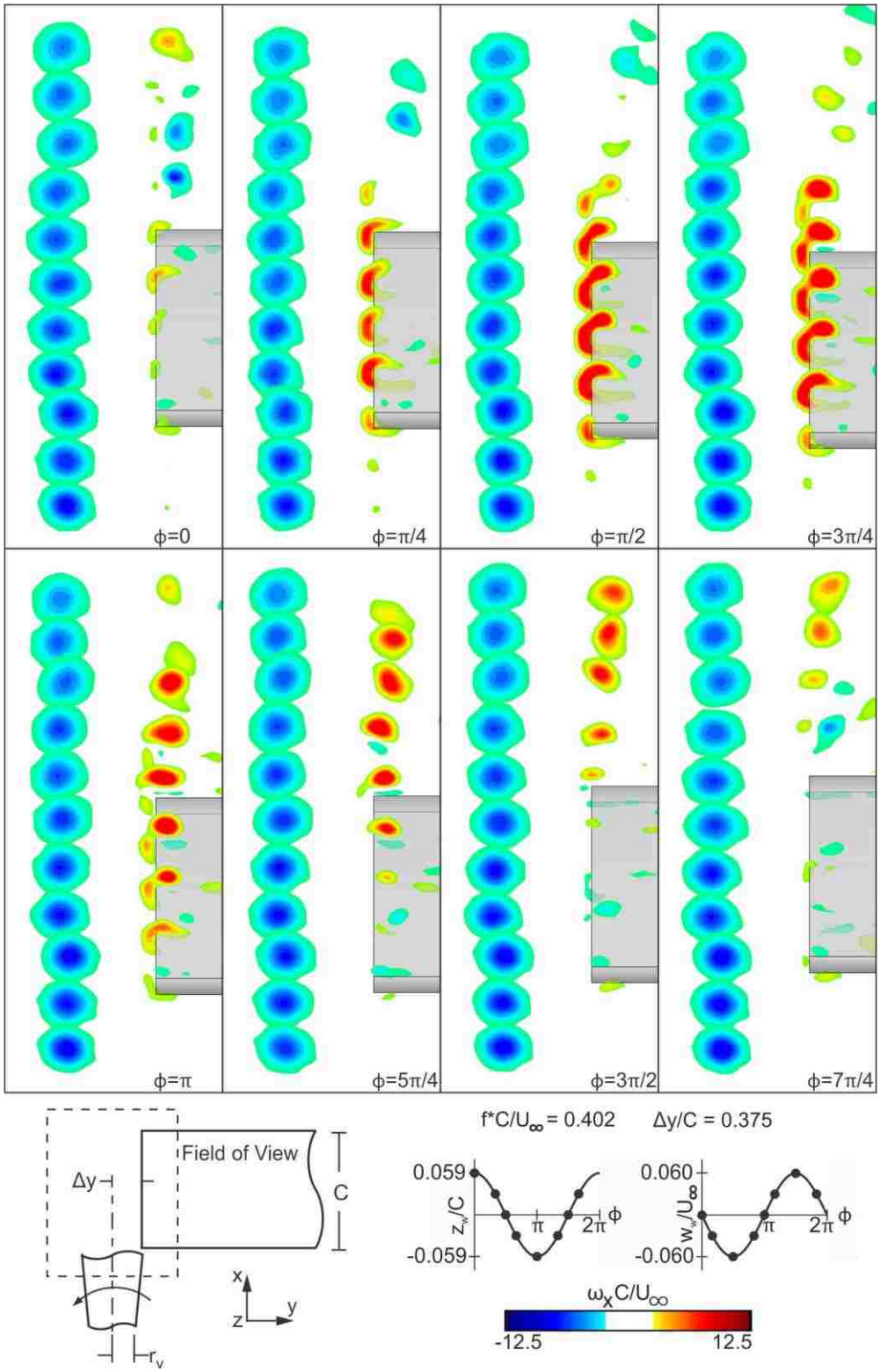

Figure 5.13: Slices of streamwise vorticity for the largest outboard displacement of the incident vortex $\Delta y/C$ = 0.375 for different phase angles. The slices extend over the streamwise distance from x'/C = -0.5 to 2.

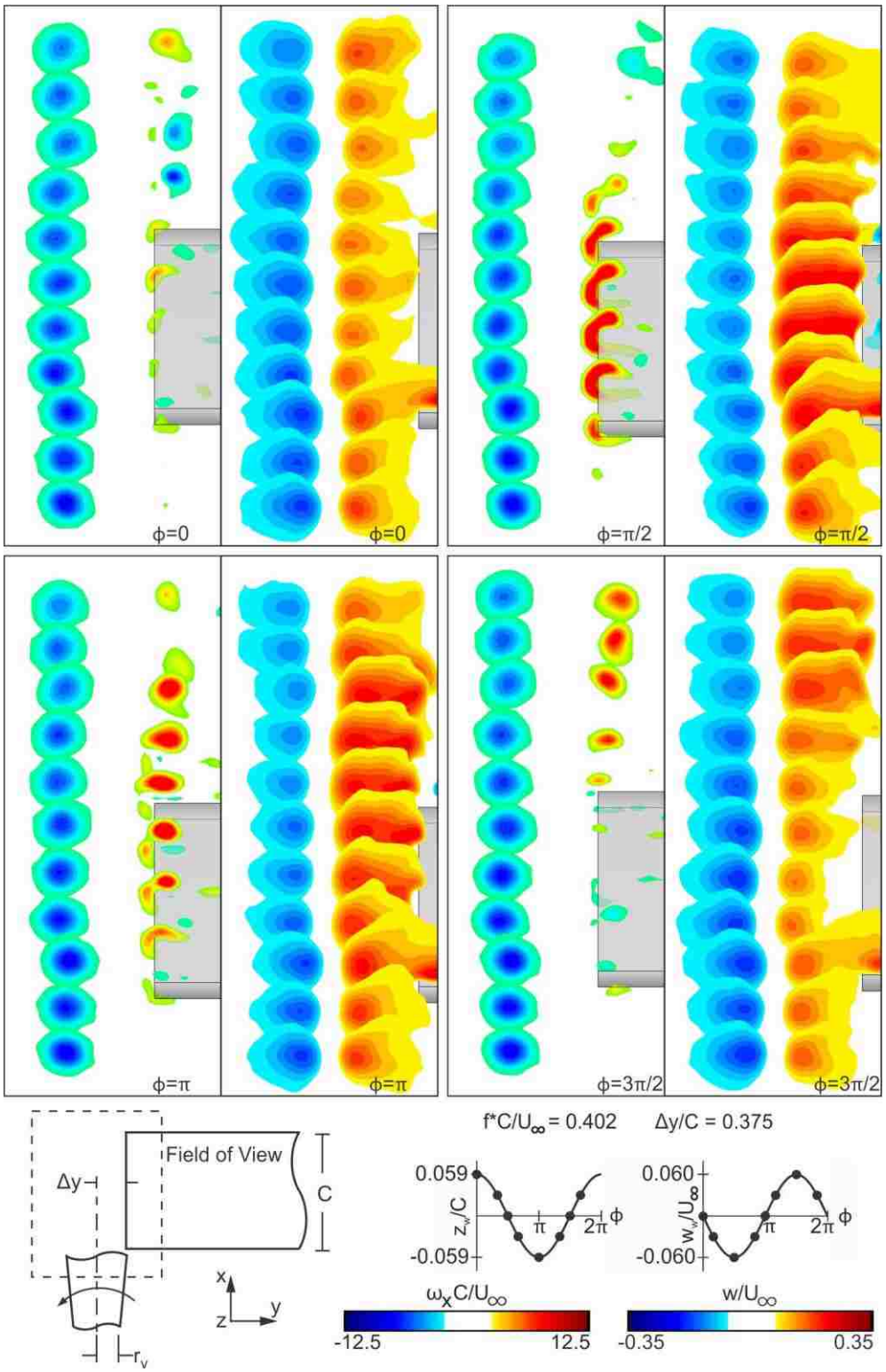

Figure 5.14: Slices of streamwise vorticity compared with slices of upwash for the largest outboard displacement of the incident vortex $\Delta y/C$ = 0.375, for indicated phase angles. The slices extend over the streamwise distance from x'/C = -0.5 to 2.

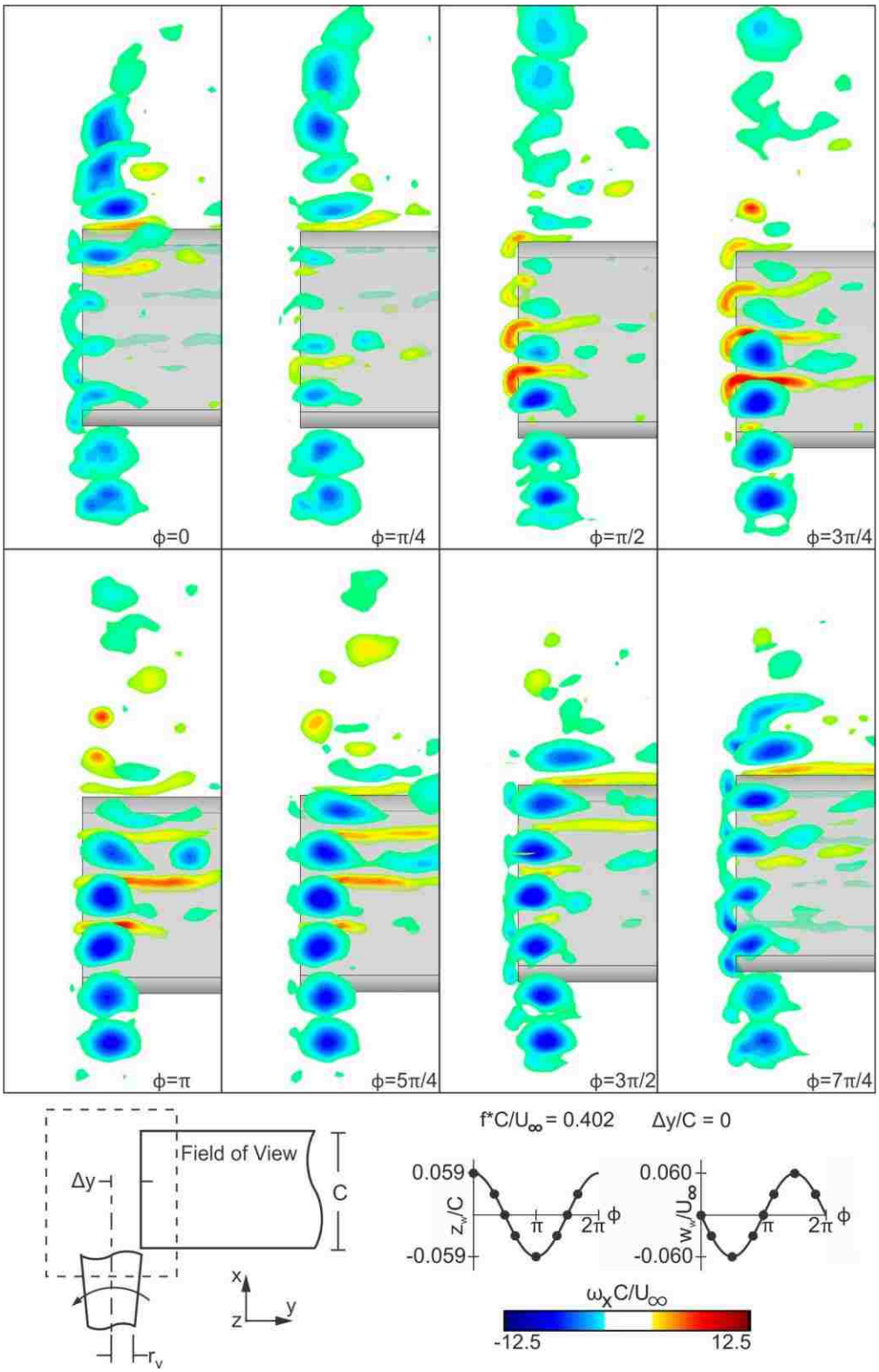

Figure 5.15: Slices of streamwise vorticity for the aligned impingement case $\Delta y/C = 0$ for different phase angles. The slices extend over the streamwise distance from $x'/C = -0.5$ to 2.

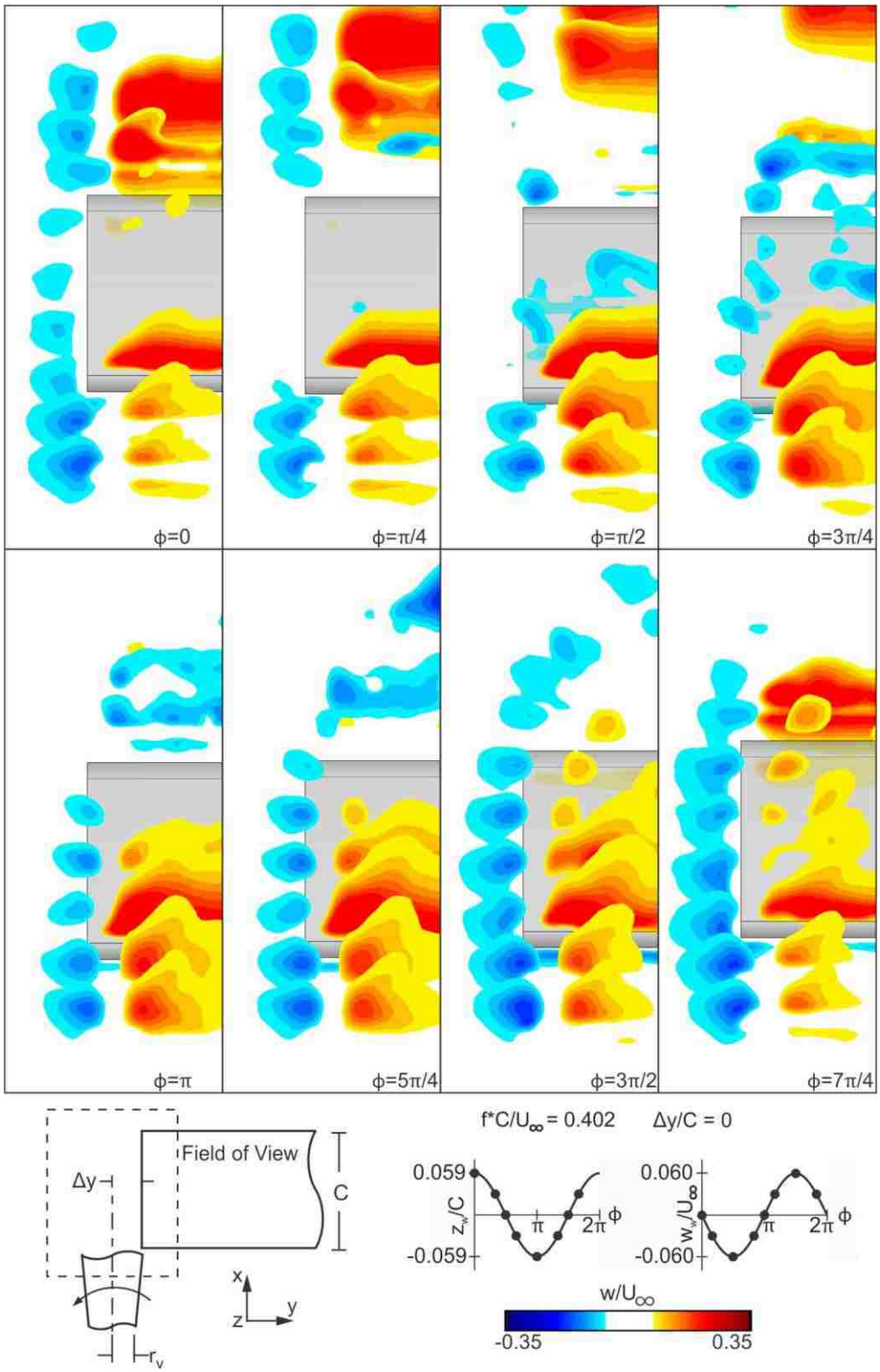

Figure 5.16: Slices of upwash for the aligned impingement case $\Delta y/C = 0$ for different phase angles. The slices extend over the streamwise distance from $x'/C = -0.5$ to 2.

CHAPTER 6

CONCLUSIONS AND RECOMMENDATIONS

6.1 CONCLUSIONS

This investigation focused on vortex-wing interaction with application to formation flight of aircraft, helicopter rotors, and turbomachinery blades. Experiments were performed using a system that was custom designed and built in-house. It gave precise control of the position of the leader wing that generated a trailing vortex and the position and harmonic motion of the downstream (follower) wing. Quantitative data acquisition using both monoscopic and stereoscopic particle image velocimetry (PIV) was employed to determine both phase-averaged and time-averaged sectional and volumetric patterns of a variety of flow parameters, including velocity components, vorticity components, swirl ratio, and streamlines.

A nominally steady vortex impinging upon a stationary wing and a wing undergoing controlled oscillation of small amplitude was characterized. The flow structure was determined over the region extending from upstream of the leading edge of the wing into its wake. Common features that were pursued include the structure of the incident vortex, the vortex formed from the tip of the wing, the dipole formed by these two vortices, and the streamline topology involving a number of critical points in the flow including foci, saddle points, and bifurcation lines. While detailed remarks are given at the ends of each of the preceding chapters, summaries of the most important findings are given below.

6.1.1 *Structure of a streamwise-oriented vortex incident upon a wing*

The distortion of a vortex impinging upon a wing (flat plate) has been characterized using a stereoscopic technique of particle image velocimetry, thereby providing the flow structure of the incident vortex at locations well upstream of the wing for varying degrees of spanwise offset of the vortex relative to the tip of the wing. The influence of the vortex-wing interaction is not simply confined to a localized region in the vicinity of the leading-edge; rather, it can extend a distance upstream of at least one wing chord (approximately five vortex diameters). Significant upstream influence is evident when the tip of the vortex impinges well outboard of the tip of the wing.

The upstream influence of the wing on the incident vortex is dependent on the vortex offset, but, in general, the following trends are evident for successive streamwise locations approaching the leading edge: an increase in the magnitude and radius of the streamwise velocity deficit; a transport of streamwise vorticity away from the axis of the vortex; an increase in azimuthal vorticity, which is directly related to a decrease in swirl ratio; an increase of root-mean-square fluctuation of streamwise vorticity; and attenuation of the downwash associated with the incident vortex.

The aforementioned enhancement of streamwise velocity deficit, attenuation of maximum streamwise vorticity, and increase of vortex radius are linked to the adverse pressure gradient that exists in the region upstream of the wing. The largest enhancements of azimuthal vorticity occur for the inboard and aligned cases when the swirl ratio decreases below a critical value, which is in accord with the theoretical prediction of Leibovich & Stewartson (1983) for small-wavelength instabilities about the

vortex. On the other hand, for the cases of the outboard and slightly outboard interactions of the vortex with the tip of the wing, the swirl ratio does not reach values below this threshold, and enhancement of azimuthal vorticity does not occur along the entire streamwise extent of the incident vortex.

6.1.2 *Topology of vortex-wing interactions*

The predominant parameter that dictates the mode of vortex-wing interaction is the dimensionless location of the incident vortex relative to the tip of the wing. Even though the values of dimensionless circulation and Reynolds number of the incident vortex are substantially different for computations and experiments, the mode of interaction is the same so long as the dimensionless position of the incident vortex is matched.

The streamline topology of these modes of interaction indicates that when the incident vortex is located outboard of the tip of the wing, it forms a dipole with the enhanced vortex generated from the wing tip. This dipole involves a region of accelerated flow between the two vortices, which manifests as a bifurcation line that exists above and parallel to the plate. Saddle points above and below the tip of the plate allow complex, localized patterns of the flow to coexist. Substantially different streamline topology occurs if the incident vortex is located inboard of the wing tip, with the most noticeable result being lack of a forming vortex. In this case, a portion of the incident vortex moves above the surface of the plate; it is initially identified with a focus that does not persist with increasing distance along the chord due to rapid attenuation of higher levels of vorticity. At the tip of the wing, a separation bubble defined by separation-reattachment

streamlines encloses only low level vorticity. Immediately adjacent to this bubble at the tip, a saddle point occurs. This separation bubble-saddle point system is remarkably invariant with increasing chordwise distance along the wing. This means that onset of a separation line at the tip does not occur and thereby formation of a tip vortex does not develop.

6.1.3 *Interaction of a trailing vortex with an oscillating wing*

For the case of an incident vortex located outboard of the tip of an oscillating wing, the distortion of the incident vortex and the generation of a vortex from the tip of the oscillating wing depend not only on the offset of the incident vortex relative to the tip, but also on the phase of the wing motion during its oscillation cycle. If the incident vortex is located far outboard of the wing, no distortion occurs, a slightly enhanced region of upwash arises outboard of the tip of the wing, and a vortex forms at the tip during its downstroke. If, however, the incident vortex is located closer to the wing, its trajectory and form are distorted, and a greatly enhanced region of upwash occurs outboard of the wing tip; a tip vortex having larger circulation, is present over a longer portion of the oscillation cycle. If the vortex impinges directly onto the wing tip, the motion of the wing attenuates the coherence of the incident vortex during part of the oscillation, such that no enhanced upwash is present outboard of the tip, and no tip vortex is present.

The foregoing modes can be interpreted in the context of the enhanced region of upwash between the incident vortex and the tip of the wing. This enhancement is created by the combined effect of the flow that wraps around the wing tip during its oscillation

and the upwash associated with the incident vortex. During the downstroke of the wing tip, upwash is created, and it is enhanced by the upwash associated with the incident vortex. This additive effect enhances the formation of the vortex that forms from the tip of the wing. During the upstroke, the flow wraps down around the tip of the wing and counteracts the upwash of the incident vortex. As a consequence, during this part of the oscillation cycle of the wing a vortex is not formed from its tip. Furthermore, the streamline topology and the associated critical points are remarkably different for the cases where the wing-induced upwash adds to, or detracts from, the upwash of the incident vortex.

6.2 RECOMMENDATIONS

This investigation has provided insight into the basic physics of vortex-wing interaction, and thereby provided the foundation for further studies. Taking into consideration the present findings, it is possible to define the following unclarified/uninvestigated aspects of vortex-wing interaction:

The present study has employed a wing in the form of a flat plate at very small or zero angle of attack. To account for the range of conditions encountered in practical applications, implementation of an actual airfoil of defined shape and camber, at angles of attack up to and including the onset of separation and stall, would be a productive path. The degree to which the incident vortex can enhance the tip vortex of the wing is a central issue. That is, by changing the circulation of the naturally-occurring vortex from

the tip of the wing through variations of angle of attack, one could gain insight into the enhancement of circulation of the tip vortex that is attainable in relation to its naturally occurring state.

The wing used in the present experiments is made of acrylic, a material which is functionally rigid under small loading. Both biological fliers and aircraft have wings which flex in the presence of extreme or unsteady loading. This aspect of flight could be modeled by changing the material of the wing to one that is more flexible. It has been shown herein that the location of vortex impingement on the wing dictates which mode of vortex interaction will occur; therefore any displacement of the location of the wing tip during bending will have drastic effects on the flow field.

In biological formation flight, both flapping and gliding are utilized to maintain the individual fliers in formation. While the present experiments involve a downstream wing capable of flapping (oscillatory) motion, the addition of an oscillating incident vortex would allow examination of realistic formation flight configurations of biological fliers. The present study shows that oscillations of the trailer wing greatly affect the circulation of the tip vortex, and it is expected that an oscillating incident vortex would have similar effects. Further experiments could address the effects of phase difference between the flapping wings, with the potential of explaining why some birds regulate this phase difference.

In the present experiments, unsteadiness of the flow around the wing was identified by variations of patterns of streamlines and velocity contours, as well as root-mean-square values of vorticity and velocity. These representations indicated that the

wing was undergoing unsteady loading for many of the experimental vortex-wing interactions investigated herein. Simultaneous force and flow measurements would clarify how fluctuations in certain unsteady flow features, such as the tip vortex from an oscillating wing, affects the loading on the wing.

REFERENCES

ADRIAN, R. J. & WESTERWEEL, J. 2011, Particle Image Velocimetry. Cambridge University Press, 2011.

BANGASH, Z. A., SANCHEZ, R.P., AHMED, A. & KHAN, M.J. 2006 Aerodynamics of Formation Flight. J. Aircraft 43 (4), 907-912.

BARNES, C. J., VISBAL, M. R. & GORDNIER, R. E. 2014a Investigation of aeroelastic effects in streamwise-oriented vortex/wing interactions. AIAA Paper 2014-1281. AIAA.

BARNES, C. J., VISBAL, M. R. & GORDNIER, R. E. 2014b Numerical simulations of streamwise-oriented vortex/ flexible wing interaction. AIAA Paper 2014-2313. AIAA.

BARNES, C. J., VISBAL, M. R. & GORDNIER, R. E. 2015a Analysis of streamwise-oriented vortex interactions for two wings in close proximity. Phys. Fluids 27 (015103).

BARNES, C. J., VISBAL, M. R. & GORDNIER, R. E. 2015b Effect of bending oscillations on a streamwise-oriented vortex interaction. AIAA Paper 2015-3303. AIAA.

BATCHELOR, G. 1964 Axial flow in trailing line vortices. J. Fluid Mech. 20 (4), 645–658.

BLAKE, W.B. & GINGRAS, D.R. 2004 Comparison of Predicted and Measured Formation Flight Interference Effect. J. Aircraft 41 (2), 201-207.

CEBECI, T. 2013 Analysis of turbulent flows with computer programs. Elsevier Ltd. 2013.

CHANG, J. W. & PARK, S. O. 2000 Measurements in the tip vortex roll-up region of an oscillating wing. AIAA J. 38(6), 1092-1095.

DAWES, W. N., 1994 A numerical study of the interaction of a transonic compressor rotor overtip leakage vortex with the following stator blade row. Gas Turbine and Aeroengine Congress and Exposition. June.

DEVENPORT, W. J., RIFE, M. C., LIAPIS, S. I. & FOLLIN, G. J. 1993 The structure and development of a wing-tip vortex. J. Fluid Mech. 312, 67-106.

DOLIGALSKI, T. L., SMITH, C. R. & WALKER, J. D. A. 1994 Vortex interactions with walls. Annu. Rev. Fluid Mech. 26, 573–616.

GARMANN, D. J. & VISBAL, M. R. 2014a Interactions of a streamwise-oriented vortex with a wing. AIAA Paper 2014-1282. AIAA.

GARMANN, D. J. & VISBAL, M. R. 2014b Unsteady interactions of a wandering streamwise-oriented vortex with a wing. AIAA Paper 2014-2105. AIAA.

GARMANN, D. J. & VISBAL, M. R. 2015a Interactions of a streamwise-oriented vortex with a finite wing. J. Fluid Mech. 767, 782-810.

GARMANN, D. J. & VISBAL, M. R. 2015b Streamwise-oriented vortex interactions with a NACA0012 wing. AIAA Paper 2015-1066. AIAA.

GARMANN, D. J. & VISBAL, M. R. 2015c Transient encounters of a NACA0012 wing with a streamwise-oriented vortex. AIAA Paper 2015-3073. AIAA.

GARMANN, D. J. & VISBAL, M. R. 2016a Unsteady evolution of the tip vortex on a stationary and oscillating naca0012 wing. AIAA Paper 2016-0328. AIAA.

GARMANN, D. J. & VISBAL, M. R. 2016b Further investigations of the tip vortex on an oscillating naca0012 wing. AIAA Paper 2016-4343, AIAA.
GORDNIER, R. E. & VISBAL, M. R. 1999 Numerical simulation of the impingement of a streamwise vortex on a plate. Int. J. of Computational Fluid Dynamics 12(1) 49-66.
GURSUL, I. & XIE, W. 2001 Interaction of vortex breakdown with an oscillating fin. AIAA J. 39(3), 438-446.
HAINSWORTH, F. R. 1987 Precision and dynamics of positioning by Canada geese flying in formation. J. Exp. Biol. 128, 445-462.
HART, D. P. 1998 High-speed PIV analysis using compressed image correlation. Journal of Fluids Engineering 130, 463-470.
HUMMEL, D. 1983 Aerodynamic aspects of formation flight in birds. J. Theor. Biol. 104 (3), 321–347.
HUMMEL, D. 1995 Formation flight as an energy-saving mechanism. Isr. J. Zool. 41 (3), 261–278.
INASAWA, A., MORI, F. & ASAI, M. 2012 Detailed observations of interactions of wingtip vortices in close-formation flight. J. Aircraft 49 (1), 206–213.
JACQUIN, L. & PANTANO, C. 2002 on the persistence of trailing vortices. J. Fluid Mech. 471, 159-168.
KAO, D. L. AHMAD, J. U. HOLST, T. L. & ALLAN, B. G. 2013 Visualization and analysis of vortex features in helicopter rotor wakes. AIAA 2013-1162.
KLESS, J., AFTOSMIS, M. J., NING, S. A. & NEMEC, M. 2013 Inviscid analysis of extended-formation flight. AIAA J. 51 (7), 1703–1715.
KROO, I. 2004 Innovations in Aeronautics AIAA 2004-0001.
LAWSON, N. J. & WU, J. 1997 Three-dimensional particle image velocimetry: experimental error analysis of a digital angular stereoscopic system. Measurement Science and Technology 8, 1455-1464.
LEIBOVICH, S. & STEWARTSON, K. 1983 A sufficient condition for the instability of columnar vortices. J. Fluid Mech. 126, 335–356.
MASKEW, B. 1974 Formation flying benefits based on vortex lattice calculations. NASA Contractor Report NASA-CR-151974 Ames Research Center.
McKENNA, C. K., BROSS, M., & ROCKWELL, D. 2017 Structure of a streamwise-oriented vortex incident upon a wing. J. Fluid Mech. 816, 306-330.
McKENNA, C. K, & ROCKWELL, D. 2016 Topology of vortex-wing interactions. Exp Fluids 57:161.
MOSES, R. W. 1997 Active vertical tail buffeting alleviation on a twin-tail fighter configuration in a wind tunnel. NTRS 20040110392.
NING, S. A., FLANZER, T. C. & KROO, I. M. 2011 Aerodynamic performance of extended formation flight. J. Aircraft 48 (3), 855-865.
PATEL, M. H. & HANCOCK, G. J. 1974 Some experimental results of the effect of a streamwise vortex on a two-dimensional wing. Aeronautical Journal 78, 151-155.
PERRY, A. E. & CHONG M. S. 1990 Interpretation of flow visualization. University of Melbourne.
PORTUGAL, S. J., HUBEL, T. Y., FRITZ, J., HEESE, S., TROBE, D., VOELKL, B., HAILES, S., WILSON, A. M. & USHERWOOD, J.R. 2014 Upwash exploitation

and downwash avoidance by flap phasing in ibis formation flight. Nature. 399-404.
RAFFEL, M. (2000) Investigation of helicopter rotor blade tip vortices in wind tunnels and in flight. DLR Institute of Aerodynamics and Flow Technology, Gottingen.
RAFFEL, M., STEELHORST, U. & WILLERT, C. 1998 Vortical flow structures at a helicopter rotor model measured by LDV and PIV. Aeronaut. J. 102 (1014), 221–227.
RAMAPRIAN, B. R. & Zheng, Y. 1998 Near field of the tip vortex behing an oscillating rectangular wing. AIAA J. 36(7), 1263-1269.
ROCKWELL, D. 1998 Vortex–body interactions. Annu. Rev. Fluid Mech. 30, 199–229.
SCHLICHTING, H. 1951 Saving of power in formation flying. Navy Department Report 239, April.
SCHLIENGER, J., KALFAS, A. I. & ABHARI, R. S. 2005 Vortex-Wake-Blade Interaction in a Shrouded Axial Turbine. J. of Turbo. 127, 699-707.
SLOTNICK, J. P., CLARK, R. W., FRIEDMAN, D. M., YADLIN, Y., YEH, D. T., CARR, J. E., CZECH M. J. & BIENIAWSKI, S. W. 2014 Computational Aerodynamic Analysis for the Formation Flight for Aerodynamic Benefit Program. AIAA Paper 2014-1458. AIAA.
SORIA, J. & FOURAS, A. 1995 Accuracy of out-of-plane vorticity component measurement using in-plane velocity vector field measurements. Twelfth Australasian Fluid Mechanics Conference.
THOMAS, C. 2001 Autonomous Formation Flight program. Photo Number: EC01-0328-3.
WAGNER, G., JACQUES, D., BLAKE, B. & PACHER, M. 2002 Flight test results of close formation flight for fuel savings. AIAA paper 2002-4490.
WENTZ, W. H. 1987 Vortex-fine interaction on a fighter aircraft. 5th Applied Aerodynamics Conference.
WEIMERSKIRCH, H., MARTIN, J., CLERQUIN, Y., ALEXANDRE, P. & JIRASKOVA, S. Energy saving in flight formation. Nature. 413, 697-698.
WIDNALL, S. 1970 Helicopter noise due to blade-vortex interaction. J. Aco. Soc. of America 50(1) 354-365.
WITTMER, K. S. & DEVENPORT, W. J. 1999 Effects of perpendicular blade-vortex interaction, part1: turbulence structure and development. AIAA J. 37 (7) 805-812.
WOLFE, S., LIN, J. C. & ROCKWELL, D. 1995 Buffeting at the leading-edge of a flat plate due to a streamwise vortex: flow structure and surface pressure loading. J. of Fluids and Structures 9 359-370.
YU, Y. H., GMELIN, B., SPLETTSTOESSER, W., PHILIPPE, J. J., PRIEUR, J. & BROOKS, T. F. 1997 Reduction of helicopter blade-vortex interaction noise by active rotor control technology. Prog. Aerospace Sci. 33, 647-687.
ZHENG, Y. & RAMAPRIAN, B. R. 1993 An experimental study of wing tip vortex in the near wake of a rectangular wing. U.S. Army Research Office Report No. MME-TF-93-1.

APPENDIX A

SUPPLEMENT TO CHAPTER 2: MONOSCOPIC PIV WITH A MIRROR

In section 2.4.1, which discussed the optical arrangement for monoscopic PIV, it was stated that the inclusion of a mirror located downstream of the experiments would not affect the results. The following figures indicate that this is indeed the case.

Figure A.1 shows contours of streamwise velocity u/U_∞ of a tip vortex three chords after it was formed. These six contours show different streamwise positions of the mirror x_m, which is defined as the distance of the mirror from the interrogation plane. At x_m = 1C the minimum axial velocity u/U_∞ is lower than any other case, and the extent of each contour level is at its largest. As x_m increases the u/U_∞ contours converge to the no mirror case, achieving convergence by x_m = 6C.

Figure A.2 demonstrates the effects that a downstream mirror can have on the streamwise vorticity $\omega_x C/U_\infty$ of a tip vortex. It is immediately apparent that the differences in contours between the values of mirror offset x_m are significantly smaller than the differences seen in Figure A.1 for the streamwise velocity u/U_∞. Once again these contours are well converged by x_m = 6C.

These two figures both exhibit a similar trend in terms of the variation of the flow structure as a result of mirror location x_m. While the flow structure is significantly altered for cases in which $x_m < 4$, the structures converge to that of the no mirror case for locations greater than six chords. For these locations, the influence of the mirror is small enough that it no longer affects the flow field in a discernable way. Therefore, a mirror

location eight chords downstream of the laser plane, as it was in all monoscopic PIV experiments, does not influence the imaging.

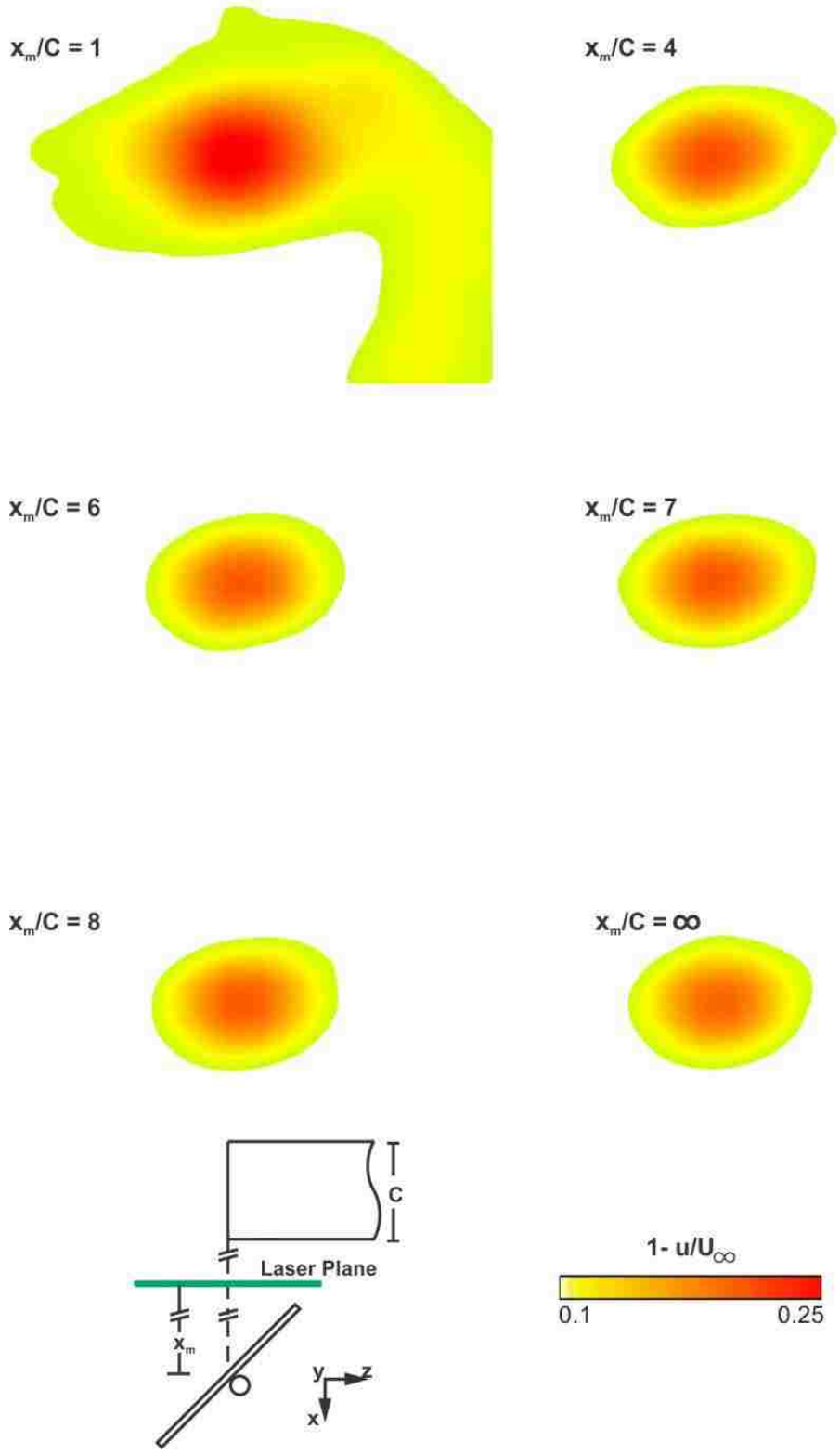

Figure A.1: Cross-sectional cuts of streamwise velocity u/U_∞ on streamwise oriented planes three chords (3C) behind the trailing edge of the leader wing; six different mirror locations x_m are shown.

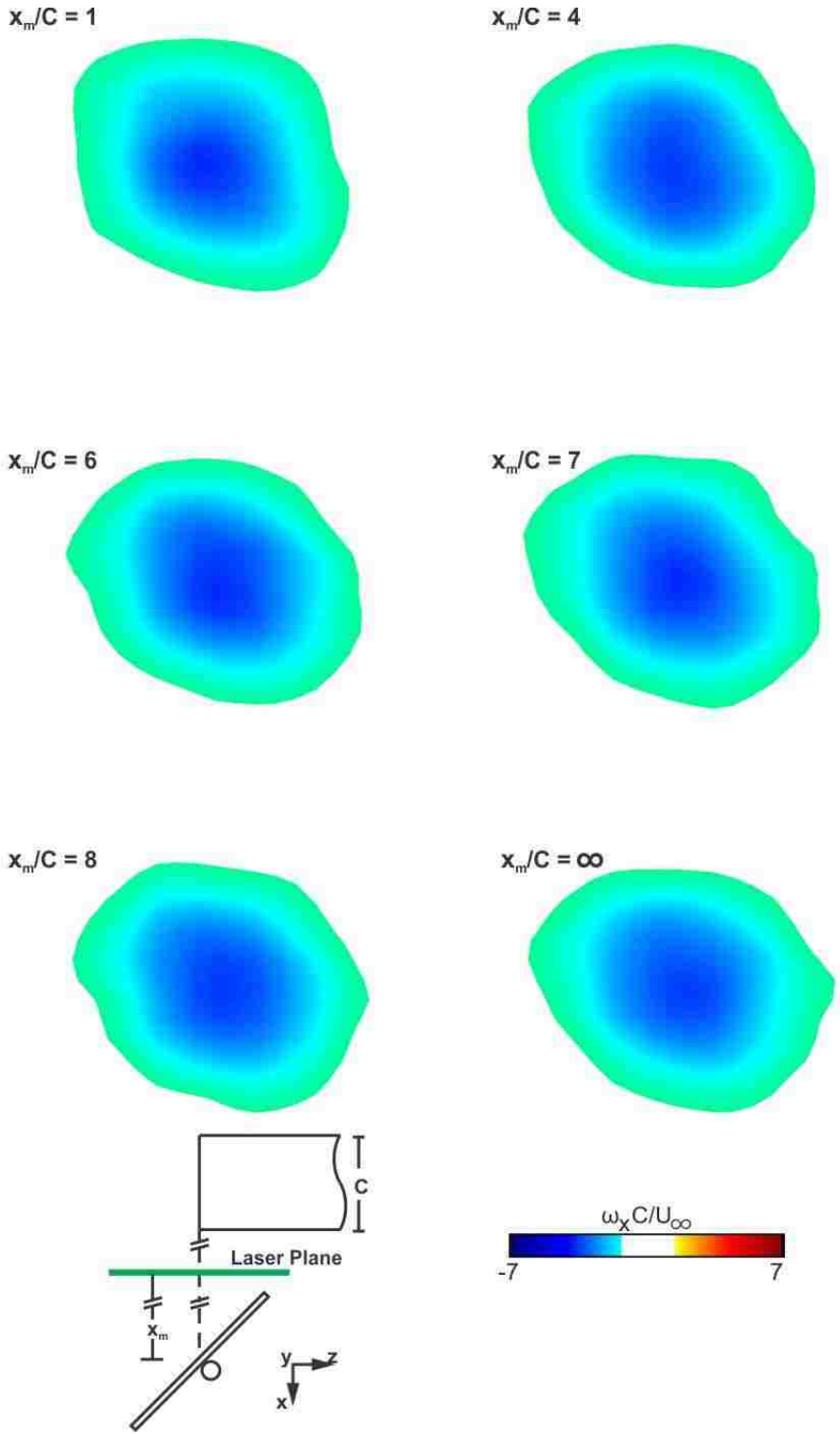

Figure A.2: Cross-sectional cuts of streamwise vorticity $\omega_x C/U_\infty$ on streamwise oriented planes three chords (3C) behind the trailing edge of the leader wing; six different mirror locations x_m are shown.

APPENDIX B

SUPPLEMENT TO CHAPTER 4: VOLUME TOPOLOGY OF VORTEX-WING INTERACTION

Appendix B is an extention of chapter 3, which deals with the flow structure along the chord of a wing which is subjected to impingement of an incident vortex. Chapter 3 addresses contours of streamwise vorticity $\omega_x C/U_\infty$ and plots of streamline topology for several locations of vortex impingement. This supplementary section covers several more impingement locations in detail, including volumetric representations of streamwise vorticity, vertical velocity, and spanwise velocity.

B.1 VERTICALLY AND INCLINED VORTEX DIPOLE

Figures B.1 and B.2 display sectional slices amd iso-surfaces of streamwise vorticity $\omega_x C/U_\infty$ for the largest outboard location of the incident vortex $\Delta y/r_v = 2.5$. For all values of vertical offset $\Delta z/r_v$ both the incident vortex (blue-green) and the tip vortex (red-yellow) are present; furthermore, these vortices form a dipole as they move along the chord of the wing. For increasing values of $\Delta z/r_v$, the vortex dipole system is deflected increasingly inboard, until at the maximum value of $\Delta z/r_v = 1.25$, this deflection is very distinct. An examination of the iso-surfaces reveals that the highest vorticity (dark blue) contour decreases in radius with downstream position until it is no longer persent in the flow. This results in a tip vortex having a larger magnitude streamwise vorticity then the incident vortex.

Sectional cuts and iso-surfaces of vertical velocity w/U_∞ are indicated in figures B.3 and B.4 respectively, which have the same layout as figure B.1. The upwash (red-yellow) is in two distinct regions: along the leading edge; and just outside the tip. Near the leading edge, the upwash is associated with the angle of attack of the wing, and enhanced by the upwash of the incident vortex. The region outside the wing tip is a combination of the upwash from the incident vortex and the tip vortex corresponding to the flow accelerated by the vortex dipole. Regions of downwash (blue-green) are visible both inboard and outboard of the upwash near the tip. These regions correspond respectively to the downwash of the tip vortex and the downwash of the incident vortex. The iso-surfaces reveal that while the outboard most region of downwash decreases in magnitude, evident from the decreasing radius of the surfaces, the region of upwash increases.

Sectional cuts of contours of spanwise velocity v/U_∞ are indicated in figure B.5, with the corresponding iso-surfaces being shown in B.6. The incident vortex involves the spanwise velocity dipole, located outboard of the wing tip, while the tip vortex is associated with the dipole near the tip. This organization is most distinct in the $\Delta z/r_v$ = -1.25 case, but as $\Delta z/r_v$ increases, the two inboard motion components (blue-green) merge together. This is due to the tilt in the vortex dipole angle discussed previously. As the dipole tilts, the jet that forms at its center rotates from vertical towards the plate; this results in a jet which accelerates flow in both the vertical and horizontal directions.

B.2 SUPRESSION OF TIP VORTEX VIA DIRECT IMPINGEMENT

Contour slices and iso-surfaces of streamwise vorticity $\omega_x C/U_\infty$ for the aligned $\Delta y/r_v = 0$, interaction are indicated in figures B.7 and B.8. In all cases, the formation of the tip vortex is suppressed in comparison to the outboard $\Delta y/r_v = 2.5$ cases seen in figure B.1. For $\Delta z/r_v = -1.25$ and 0, the incoming vortex bifurcates at the leading edge of the plate. This causes negative (blue-green) vorticity to be present on both the pressure and suction surfaces of the wing.

For $\Delta z/r_v = -1.25$ the negative region of $\omega_x C/U_\infty$ beneath the plate begins to move around the tip. After this occurs, it is in close proximity to the positive vorticity (red-yellow) tip vortex which is beginning to form. This close proximity causes both regions of vorticity to lose strength moving downstream. On the top of the plate, the negative vorticity associated with the incident vortex flattens out and moves inboard. This motion is induction caused by the interaction between the vortex and its mirror image vortex inside the plate. In this region there is a thin layer of positive vorticity between the negative vorticity and the plate.

Similar to the offset $\Delta z/r_v = -1.25$, the $\Delta z/r_v = 0$ case shows the incident vortex bifurcating at the leading edge of the plate. In this case a larger portion of the vorticity is present on the upper surface of the plate. Once again the portion of the vortex beneath the plate moves towards the forming tip vortex. Above the plate, the incident vortex again moves inboard with a similar mechanism as was described in the $\Delta z/r_v = -1.25$ case.

In the final case of $\Delta z/r_v = 1.25$ the incident vortex is entirely above the plate. At this location, the tip vortex is still suppressed. The negative vorticity above the plate again moves inboard for the same reasons discussed previously.

The iso-surfaces in figure B.8 reveal that the higher level surfaces of streamwise vorticity $\omega_x C/U_\infty$ change drastically between vertical impingement locations $\Delta z/r_v$. As $\Delta z/r_v$ increases the extent of these surfaces increase as well; at $\Delta z/r_v$ = -1.25 the highest magnitude contour is not present anywhere in the flow, but at $\Delta z/r_v$ = 1.25 it extends over the surface of the plate. This is in stark contrast to the outboard impingement case $\Delta y/r_v$ = 2.5 where the highest level contour essentially identical for all $\Delta z/r_v$. Slices and iso-surfaces of the vertical velocity w/U_∞ for the case where the incident vortex is aligned with the tip of the wing are indicated in figures B.9 and B.10. The large region of upwash seen near the leading edge for the outboard interactions, figures B.3 and B.4, is again present in these images. For the aligned interaction, this upwash does not extend all the way to the tip as was seen for the outboard interactions. This is due to the incident vortex moving inboard, eliminating the increased upwash at the tip. In all cases, a region of downwash moves from the tip near the leading edge to further inboard at the trailing edge. This matches the motion of the vortices seen in figures B.7 and B.8. As $\Delta z/r_v$ increases, the strength of the downwash region increases, which again matches the observations of the strength of the incident vortex in figures B.7 and B.8. At $\Delta z/r_v$ = -1.25 there is a small region of downwash beneath the plate which corresponds to the larger portion of the vortex beneath the plate. While there is little upwash above the plate for the vertically aligned case, $\Delta z/r_v$ = 0, there is a significant portion for the above case, $\Delta z/r_v$ = 1.25. This is due to the larger portion of the vortex above the plate at this location.

Figures B.11 and B.12 shows slices and iso-surfaces of spanwise velocity v/U_∞ for the interaction case where the incident vortex is aligned with the tip of the wing. For

all cases a layer of fluid with inboard motion is located directly above the surface of the wing, and outboard flow is present further above the wing near the tip. The magnitude and extent of both these regions increases as $\Delta z/r_v$ increases. This is due to larger portions of the incident vortex present above the plate. For $\Delta z/r_v$ = -1.25 a small region of fluid with inboard motion is also present under the plate near the leading edge. This region is due to the bifurcation of the incident vortex leaving a larger portion of the vortex beneath the plate. There is also a small portion of outboard flow near the tip, which shows flow move from the pressure to suction sides of the wing.

B.3 SUPRESSION OF TIP VORTEX VIA INBOARD IMPINGEMENT

Volumetric representations of streamwise vorticity $\omega_x C/U_\infty$ for the inboard interactions at $\Delta y/r_v$ = -2.5 are presented in figures B.13 and B.14. Above the surface of the plate the flow is similar to what was seen for the aligned case $\Delta y/r_v$ = 0 in figure B.7. A portion of the incident vortex shifts inboard as the streamwise distance from the leading edge increases; this motion is due to induction effects. Beneath this portion of the incident vortex is a layer of positive vorticity, which is again similar to what was seen in the case of aligned interaction. As $\Delta z/r_v$ increases, the magnitude and extent of both of these regions increase, due to a larger portion of the incident vortex located above the surface of the wing.

Figures B.15 and B.16 show slices and iso-surfaces of vertical velocity w/U_∞ for the inboard interactions at $\Delta z/r_v$ = -1.25, 0, and 1.25. As was seen in both the outboard

and aligned interactions, there is a large region of upwash near the leading edge. This region does not extend as close to the tip as for the aligned interaction, which is due to the further inboard location of the incident vortex. A region of downwash is also present above the wing for all cases. As $\Delta z/r_v$ increases the magnitude and extent of these contours also increases, which is due to the increasing distance between the incident vortex and the wing. At $\Delta z/r_v$ = -1.25 mirrored structures can also be seen beneath the wing, that is, a region of downwash near the tip, and a smaller region of upwash inboard of it. This illustrates the reduced effective angle of attack near the wing tip due to the inboard location of the incident vortex.

Slices and iso-surfaces of spanwise velocity w/U_∞ are indicated in figures B.17 and B.18 respectively for all inboard interactions $\Delta y/r_v$ = -2.5. As with the streamwise vorticity there are many similarities between the inboard and aligned interactions. Once again there is a layer of flow moving inboard, located above the surface of the plate. There is also a region of outboard flow further above the plate which is strongest near the leading edge. As $\Delta z/r_v$ increases, the magnitude and extent of both of these regions also increases; this is due to a larger portion of the incident vortex located above the surface of the wing. For $\Delta z/r_v$ = -1.25, mirrored structures can also be seen beneath the wing, these structures are composed of a layer of outboard flow near the surface and a region of inboard flow beneath it. This observation is due to the comparatively larger portion of the vortex being beneath the plate.

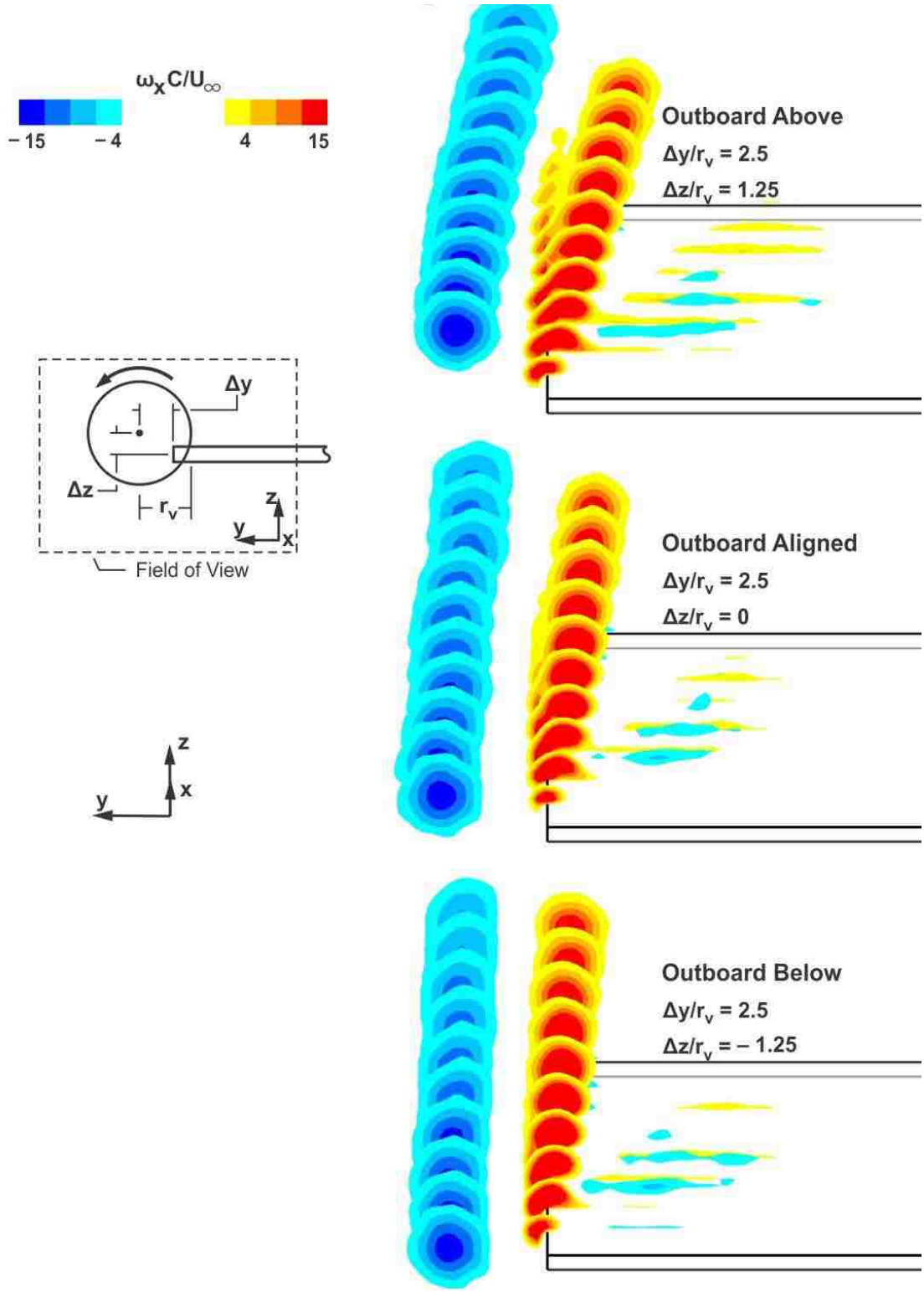

Figure B.1: Slices of streamwise vorticity $\omega_x C/U_\infty$ at three vertical locations $\Delta z/r_v$ of vortex impingement for $\Delta y/r_v = 2.5$. The slices extend over the streamwise distance from 0.125 C to 1.25 C downstream of the leading edge of the wing.

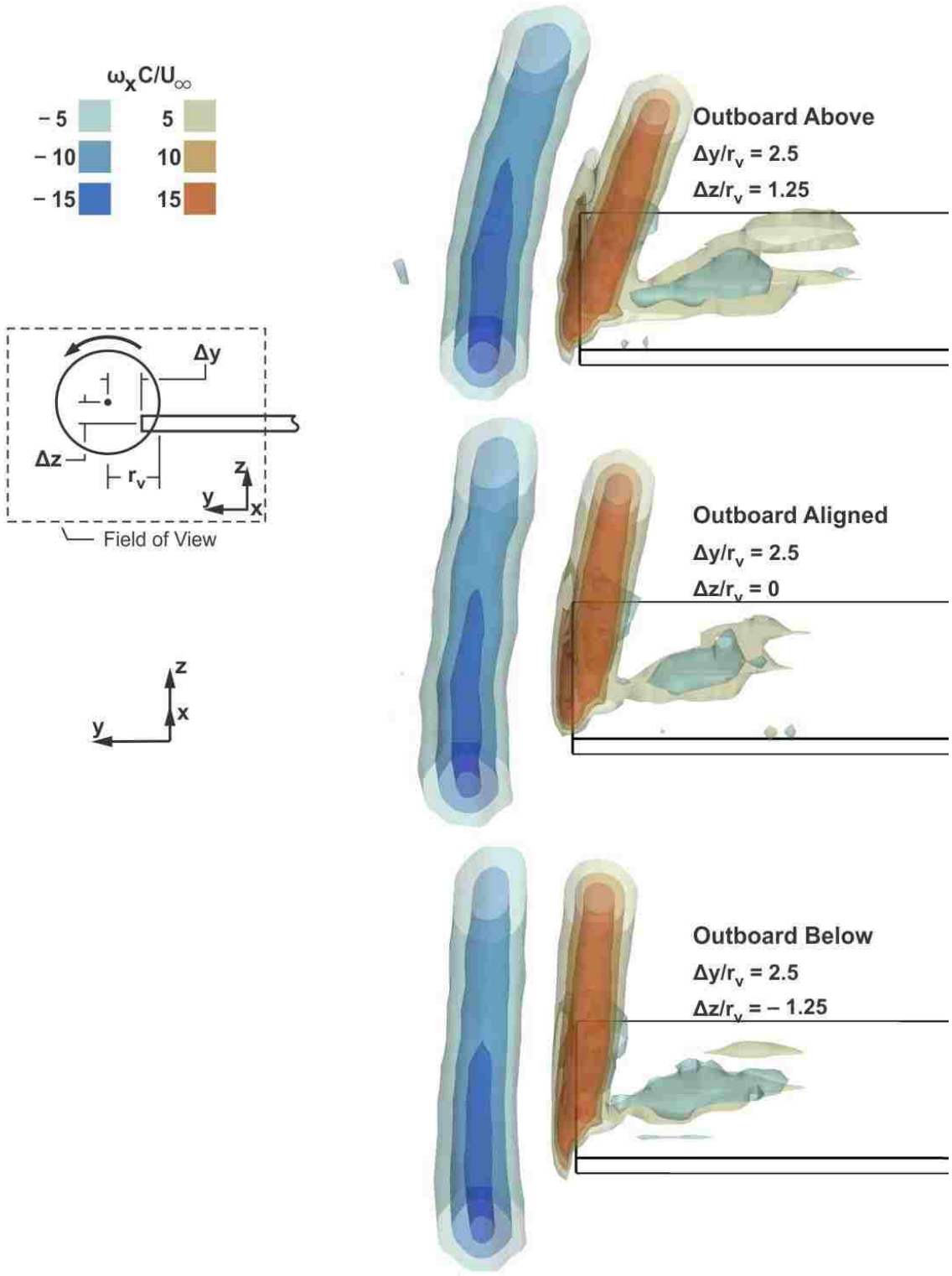

Figure B.2: Iso-surfaces of streamwise vorticity $\omega_x C/U_\infty$ at three vertical locations $\Delta z/r_v$ of vortex impingement for $\Delta y/r_v = 2.5$. The surfaces extend over the streamwise distance from 0.25 C upstream to 1.25 C downstream of the leading edge of the wing.

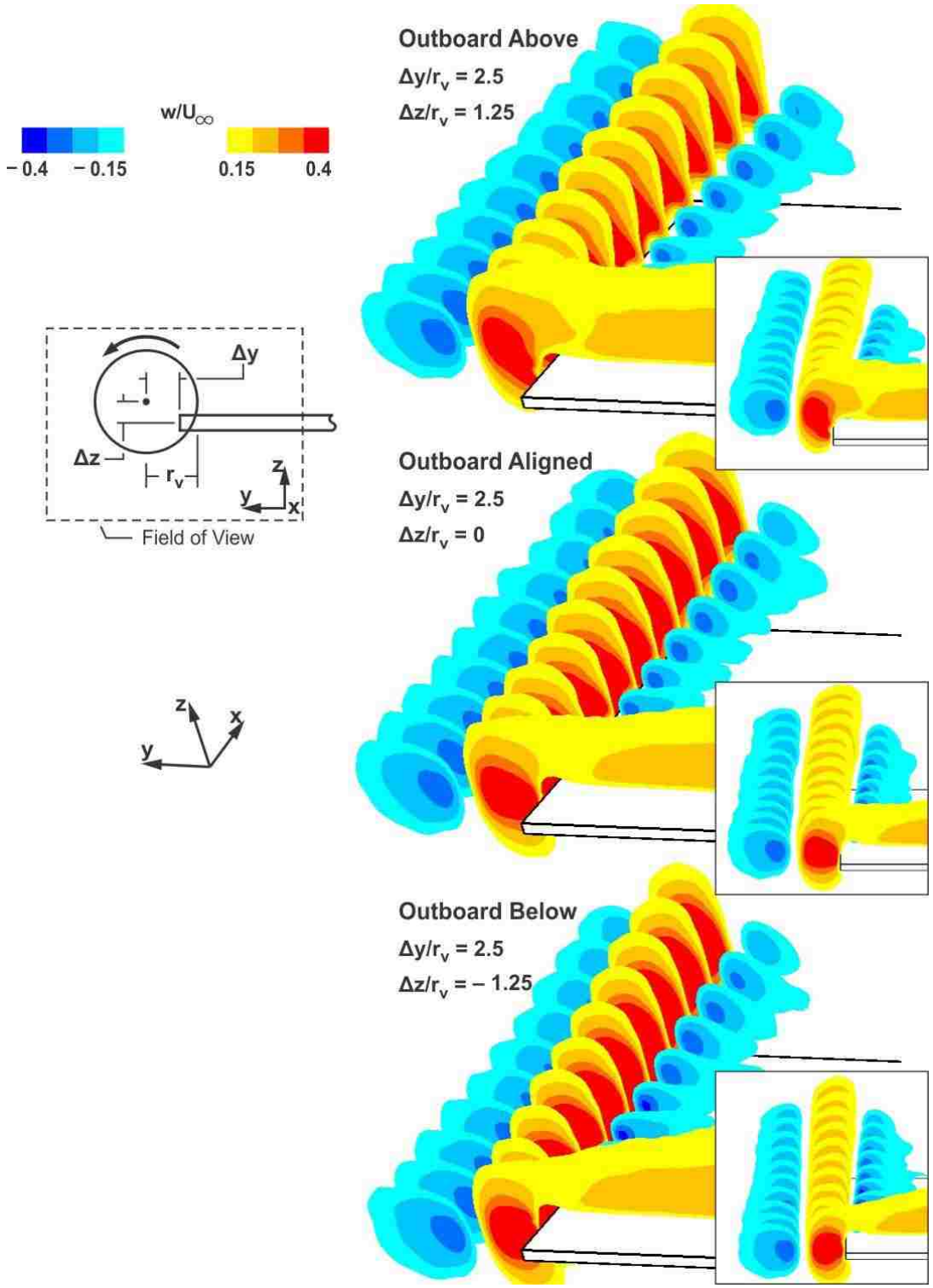

Figure B.3: Slices of vertical velocity w/U_∞ at three vertical locations $\Delta z/r_v$ of vortex impingement for $\Delta y/r_v = 2.5$. The slices extend over the streamwise distance from 0.125 C to 1.25 C downstream of the leading edge of the wing.

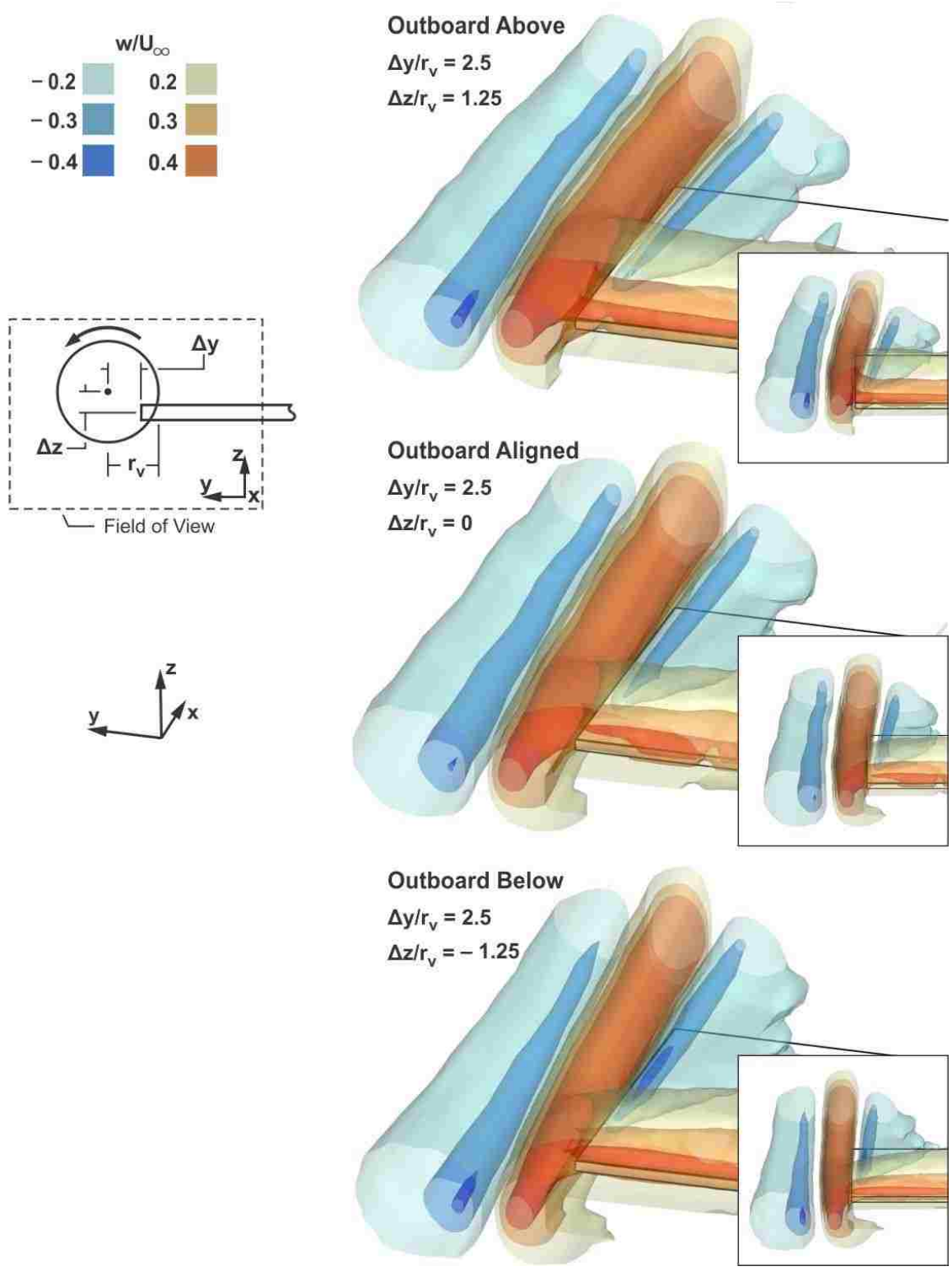

Figure B.4: Iso-surfaces of vertical velocity w/U_∞ at three vertical locations $\Delta z/r_v$ of vortex impingement for $\Delta y/r_v$ = 2.5. The surfaces extend over the streamwise distance from 0.25 C upstream to 1.25 C downstream of the leading edge of the wing.

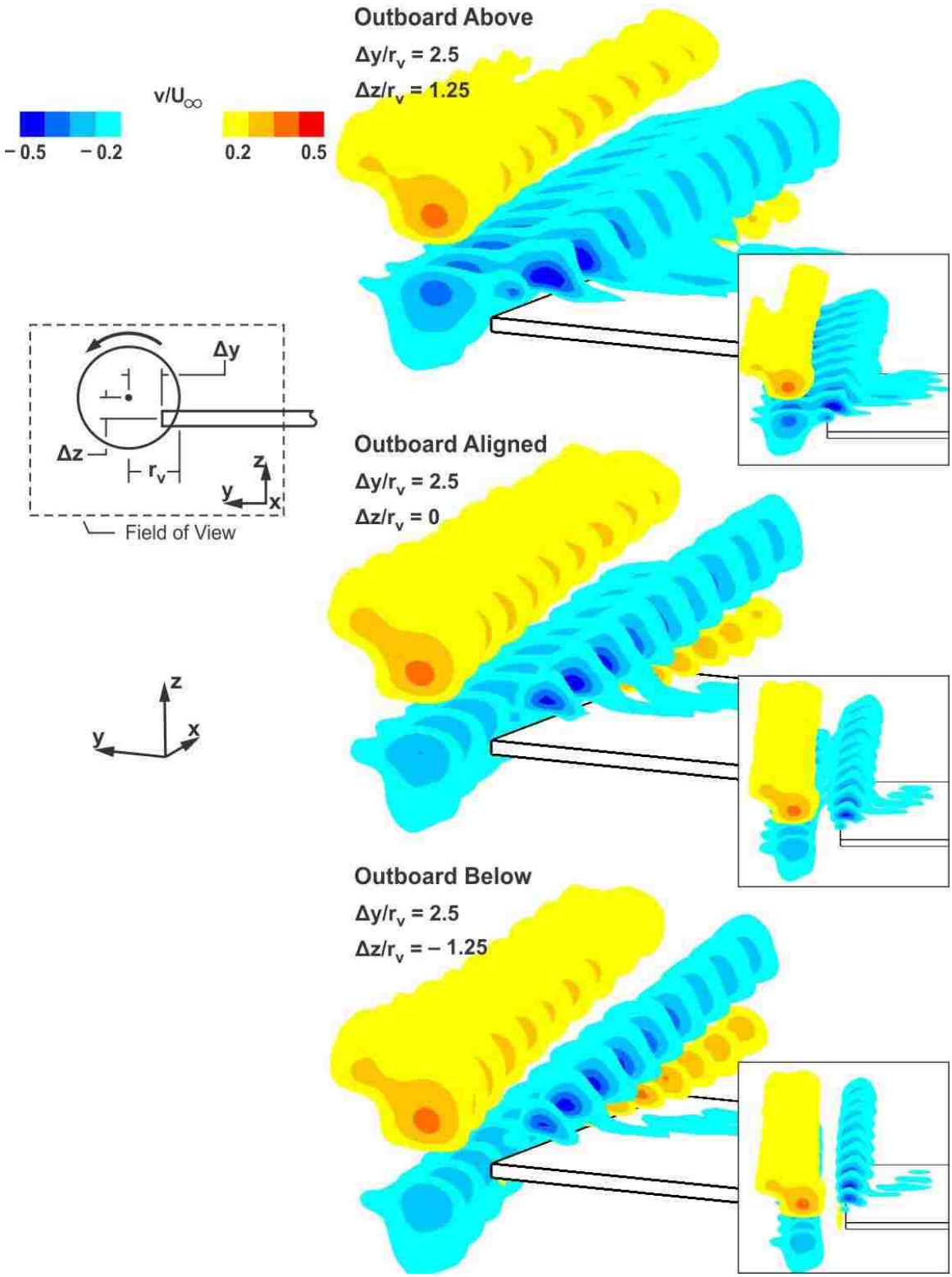

Figure B.5: Slices of spanwise velocity v/U_∞ at three vertical locations $\Delta z/r_v$ of vortex impingement for $\Delta y/r_v = 2.5$. The slices extend over the streamwise distance from 0.125 C to 1.25 C downstream of the leading edge of the wing.

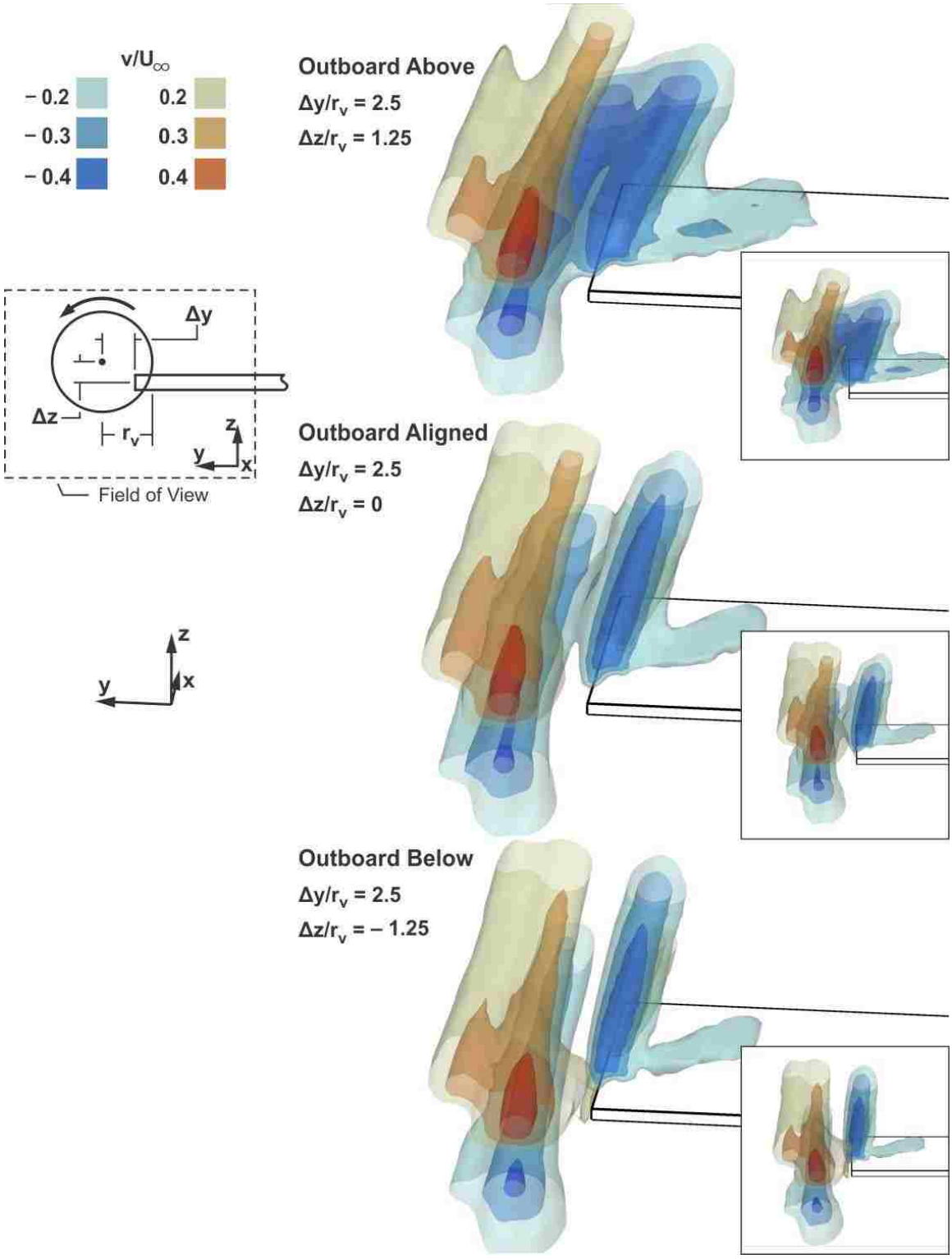

Figure B.6: Iso-surfaces of spanwise velocity v/U_∞ at three vertical locations $\Delta z/r_v$ of vortex impingement for $\Delta y/r_v$ = 2.5. The surfaces extend over the streamwise distance from 0.25 C upstream to 1.25 C downstream of the leading edge of the wing.

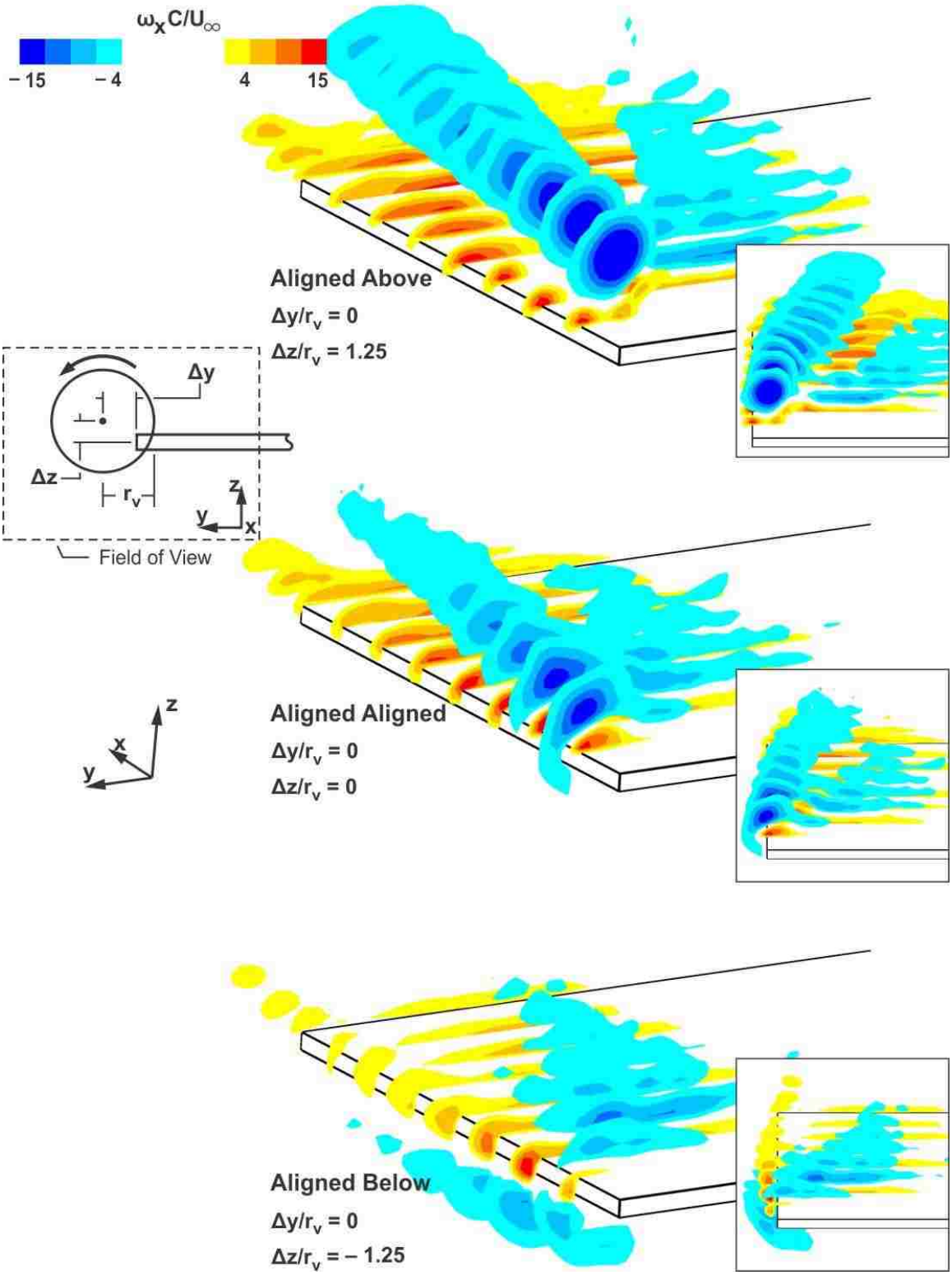

Figure B.7: Slices of streamwise vorticity $\omega_x C/U_\infty$ at three vertical locations $\Delta z/r_v$ of vortex impingement for $\Delta y/r_v = 0$. The slices extend over the streamwise distance from 0.125 C to 1.25 C downstream of the leading edge of the wing.

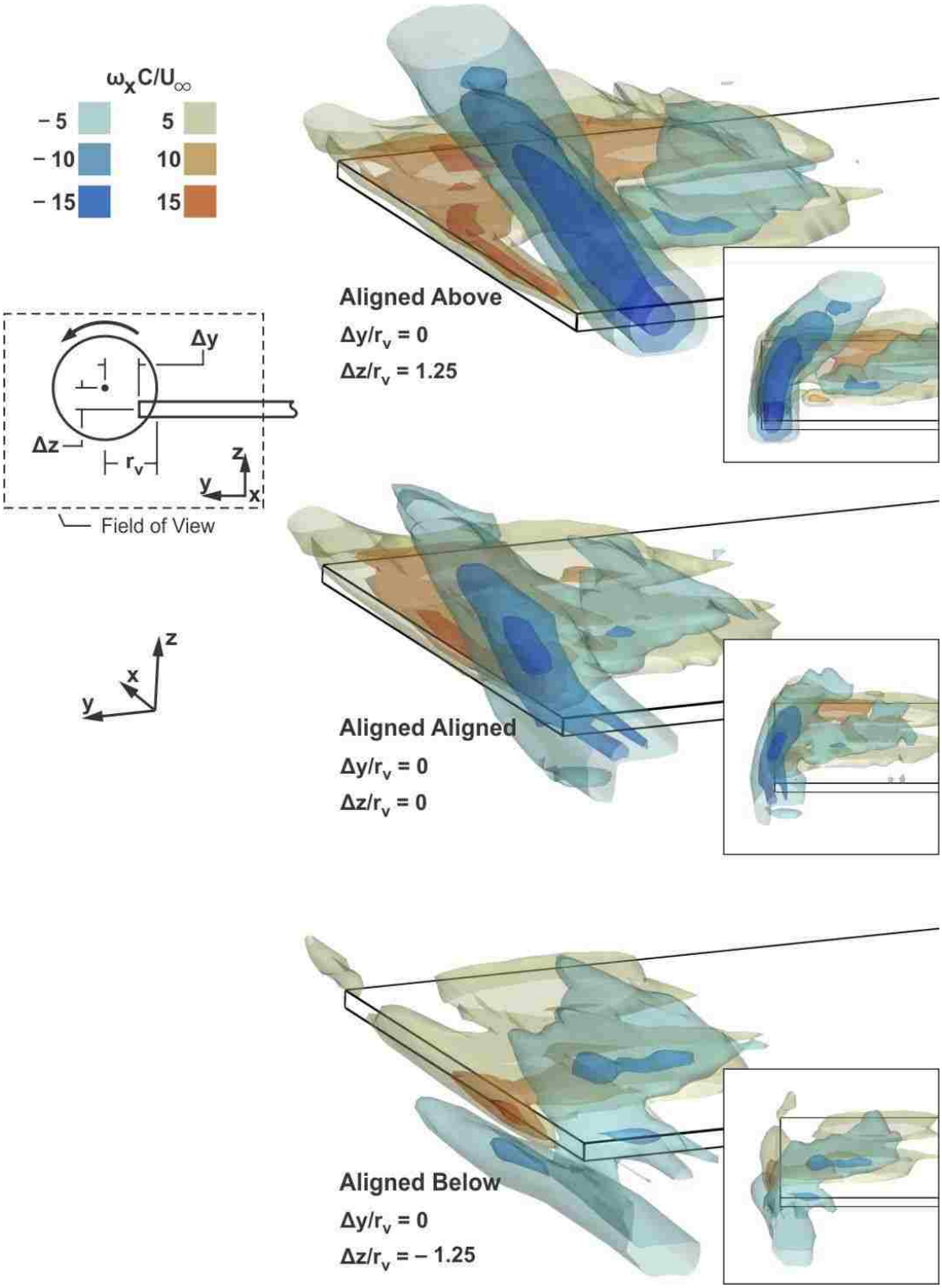

Figure B.8: Iso-surfaces of streamwise vorticity $\omega_x C/U_\infty$ at three vertical locations $\Delta z/r_v$ of vortex impingement for $\Delta y/r_v = 0$. The surfaces extend over the streamwise distance from 0.25 C upstream to 1.25 C downstream of the leading edge of the wing.

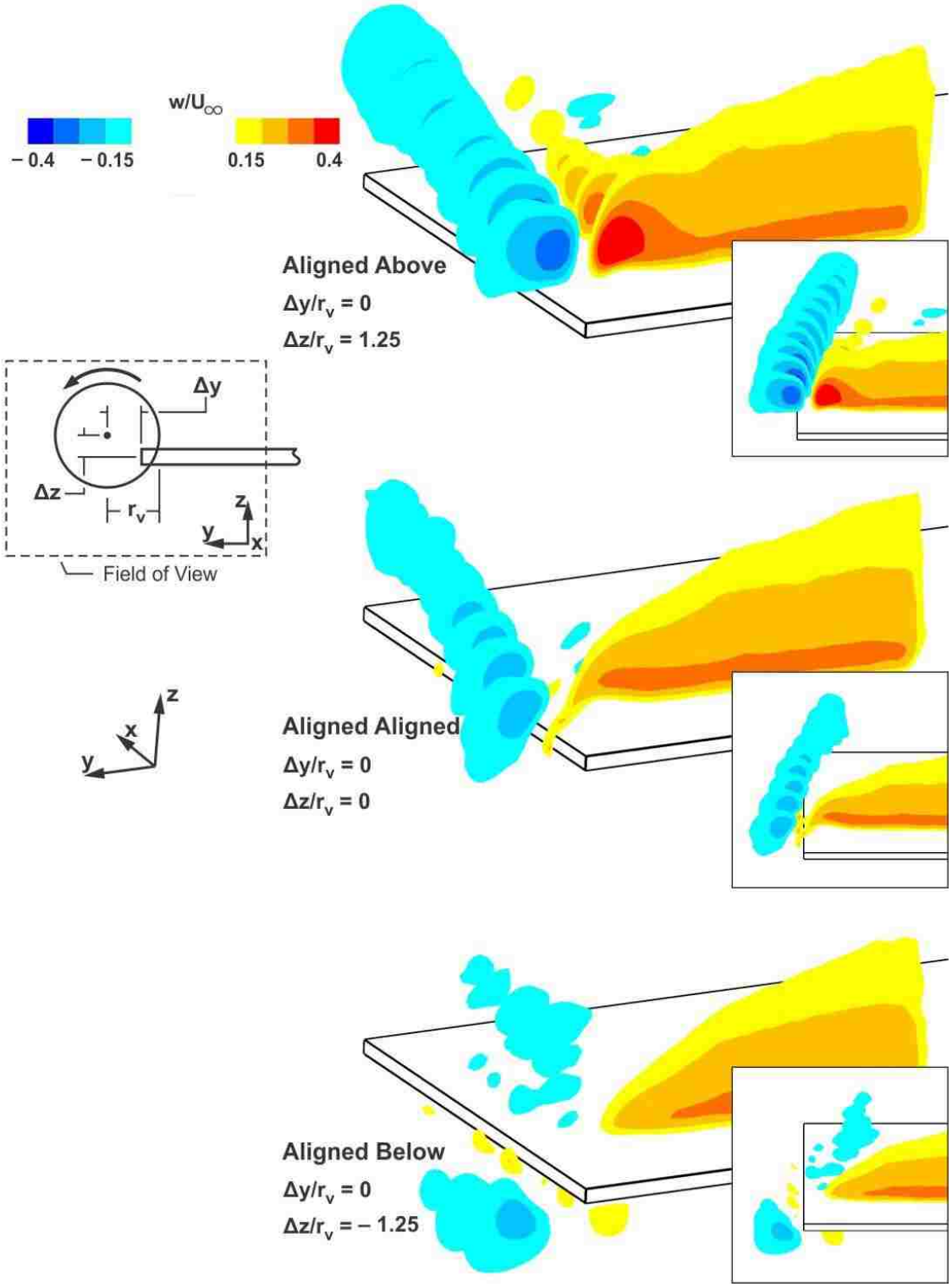

Figure B.9: Slices of vertical velocity w/U_∞ at three vertical locations $\Delta z/r_v$ of vortex impingement for $\Delta y/r_v = 0$. The slices extend over the streamwise distance from 0.125 C to 1.25 C downstream of the leading edge of the wing.

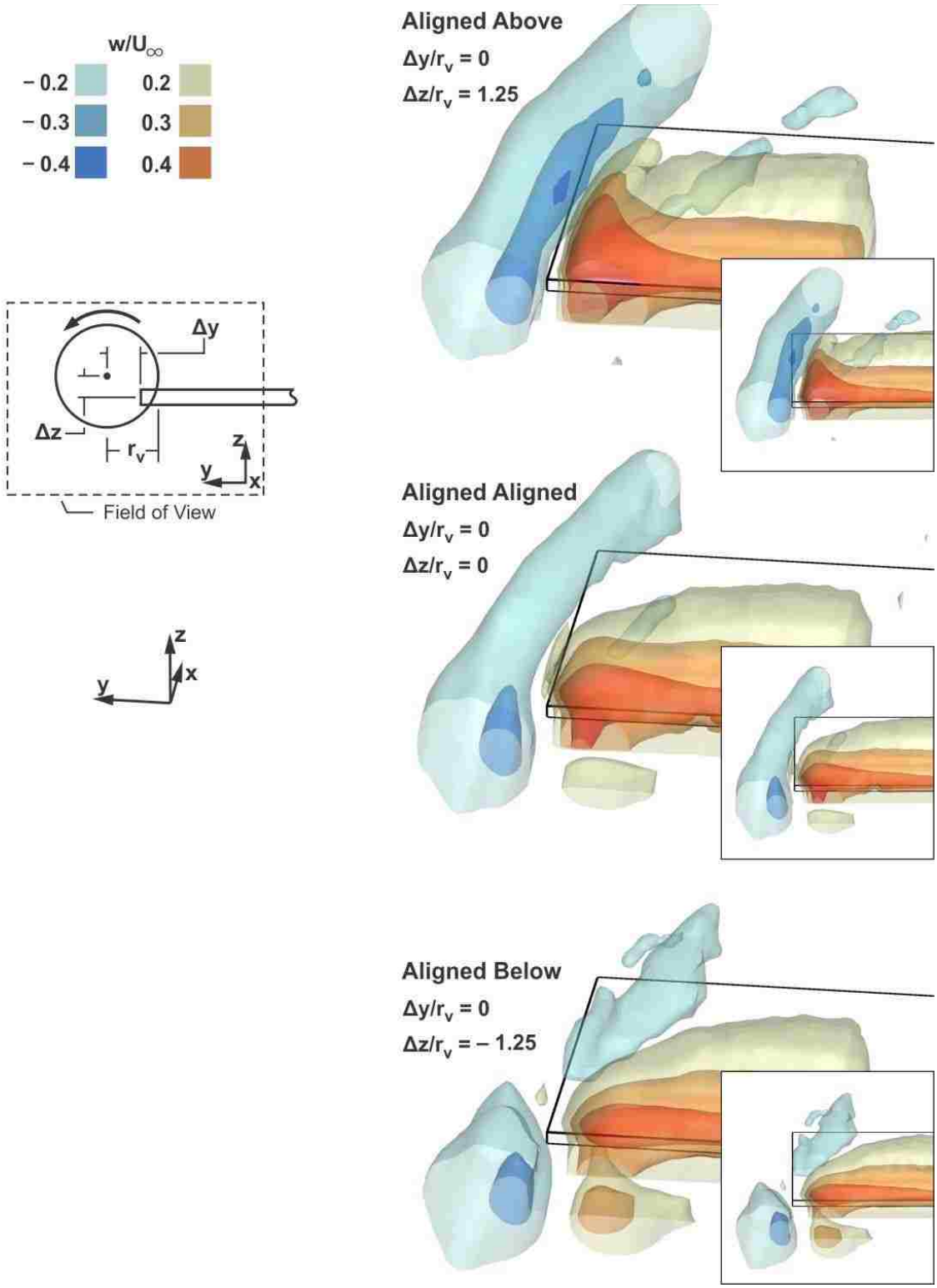

Figure B.10: Iso-surfaces of vertical velocity w/U_∞ at three vertical locations $\Delta z/r_v$ of vortex impingement for $\Delta y/r_v = 0$. The surfaces extend over the streamwise distance from 0.25 C upstream to 1.25 C downstream of the leading edge of the wing.

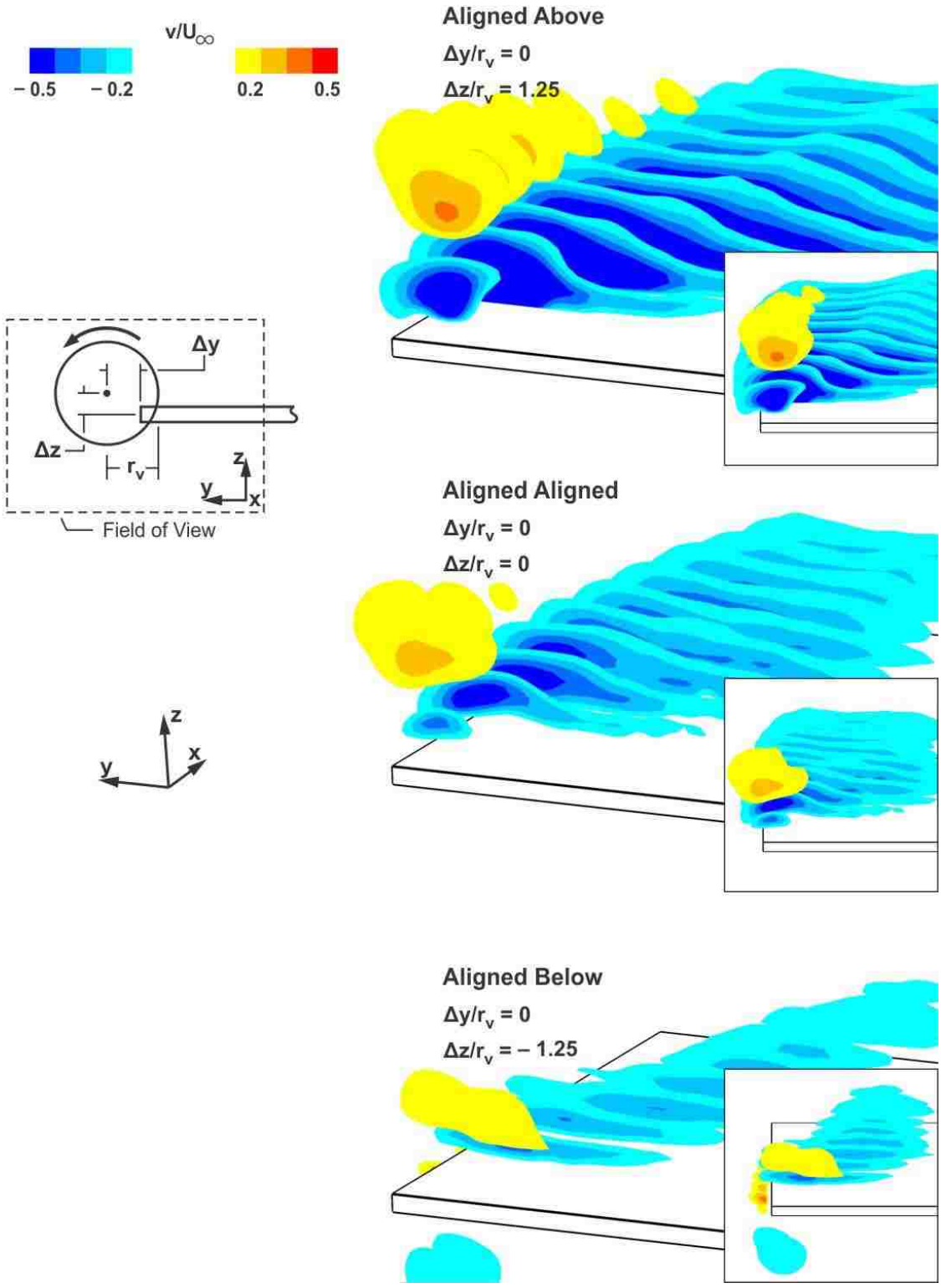

Figure B.11: Slices of spanwise velocity v/U_∞ at three vertical locations $\Delta z/r_v$ of vortex impingement for $\Delta y/r_v = 0$. The slices extend over the streamwise distance from 0.125 C to 1.25 C downstream of the leading edge of the wing.

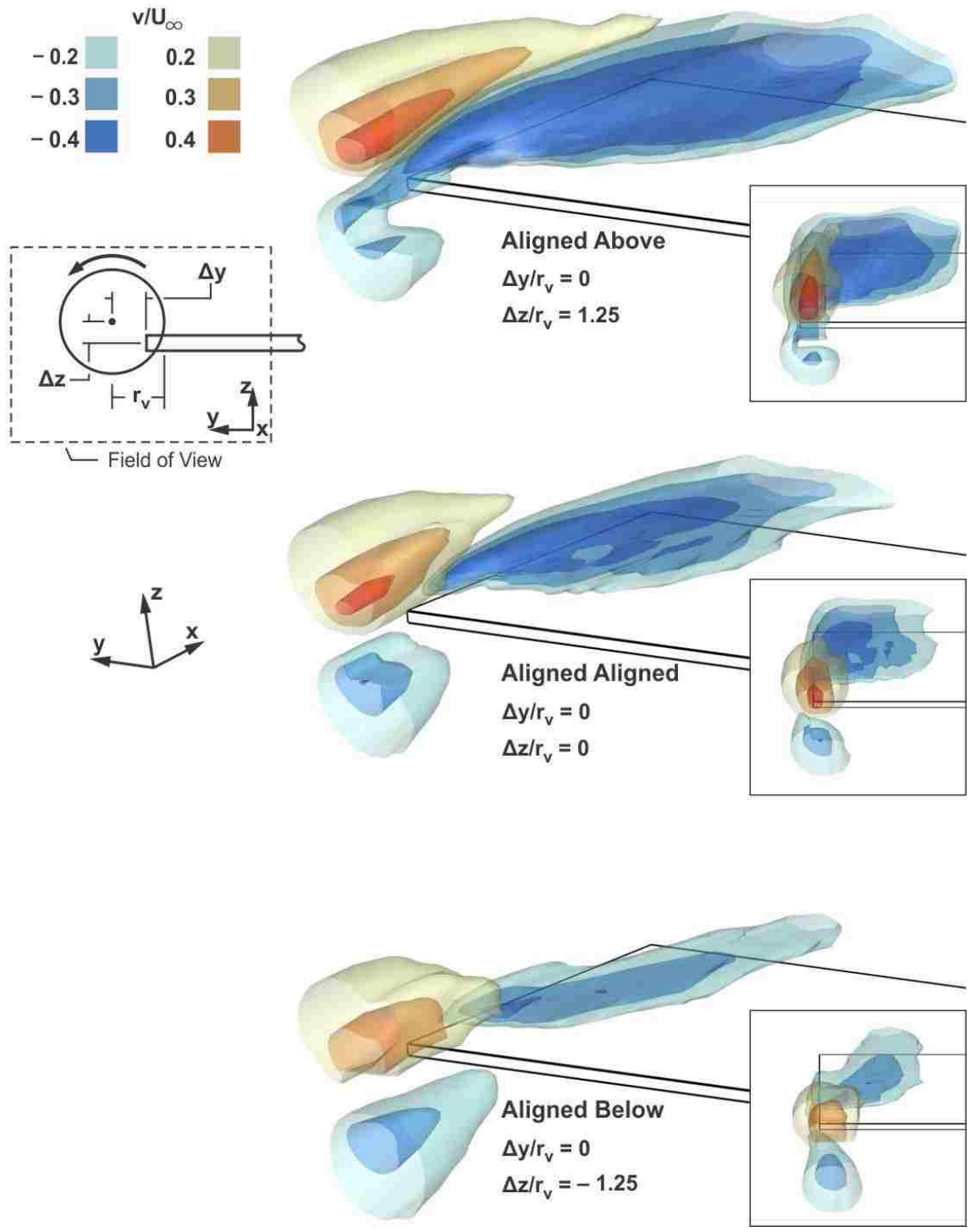

Figure B.12: Iso-surfaces of spanwise velocity v/U_∞ at three vertical locations $\Delta z/r_v$ of vortex impingement for $\Delta y/r_v = 0$. The surfaces extend over the streamwise distance from 0.25 C upstream to 1.25 C downstream of the leading edge of the wing.

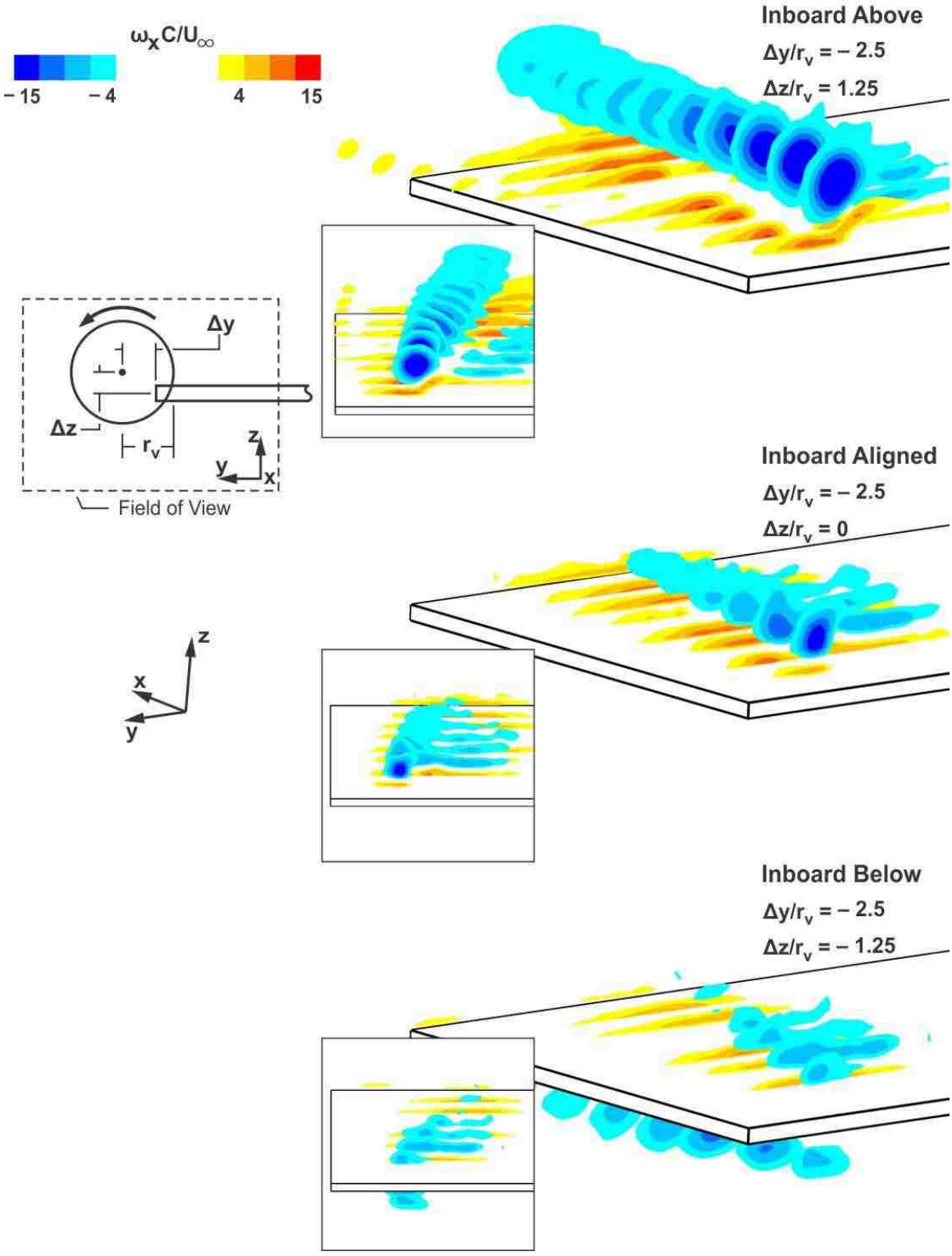

Figure B.13: Slices of streamwise vorticity $\omega_x C/U_\infty$ at three vertical locations $\Delta z/r_v$ of vortex impingement for $\Delta y/r_v$ = -2.5. The slices extend over the streamwise distance from 0.125 C to 1.25 C downstream of the leading edge of the wing.

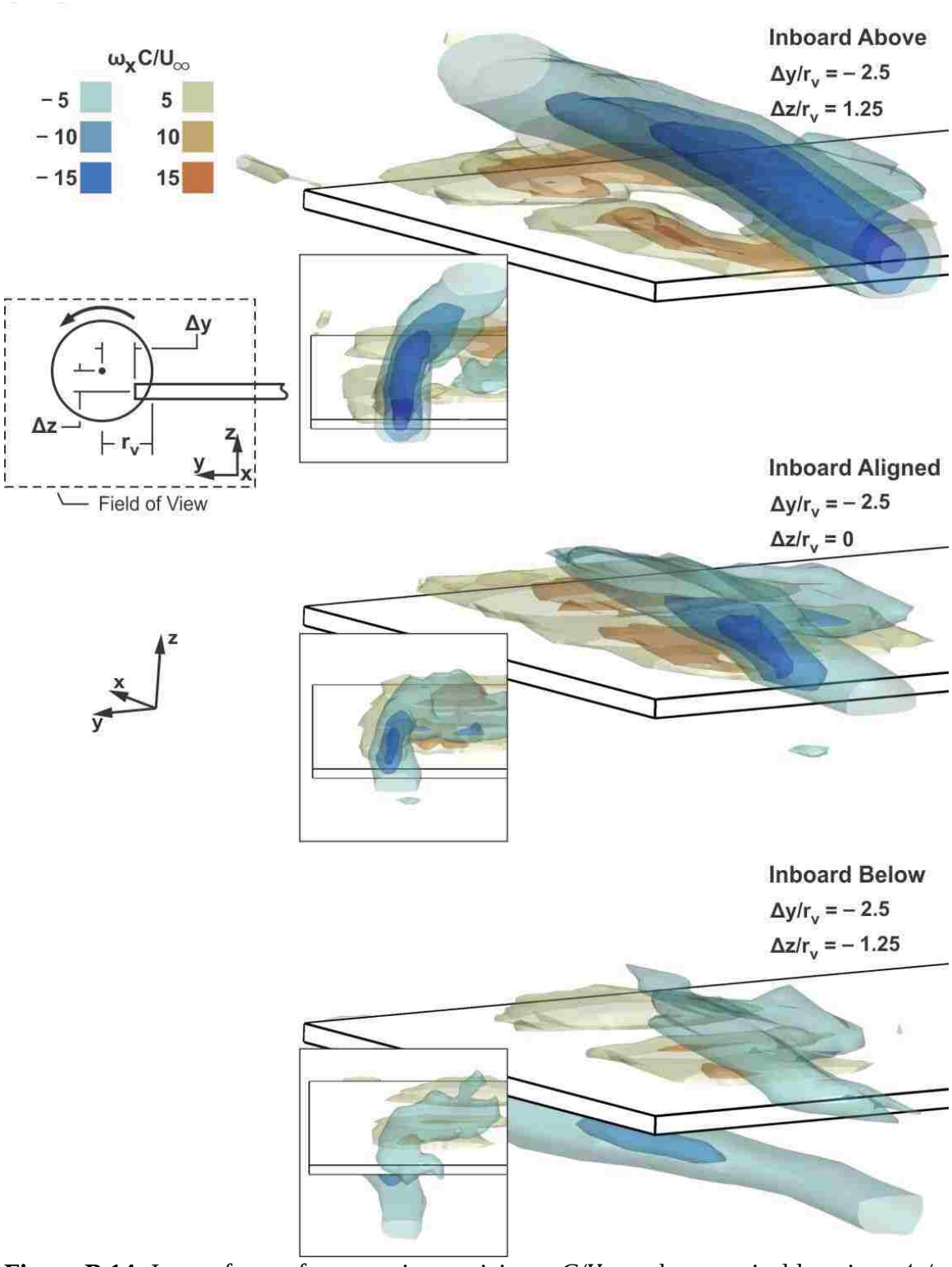

Figure B.14: Iso-surfaces of streamwise vorticity $\omega_x C/U_\infty$ at three vertical locations $\Delta z/r_v$ of vortex impingement for $\Delta y/r_v$ = -2.5. The surfaces extend over the streamwise distance from 0.25 C upstream to 1.25 C downstream of the leading edge of the wing.

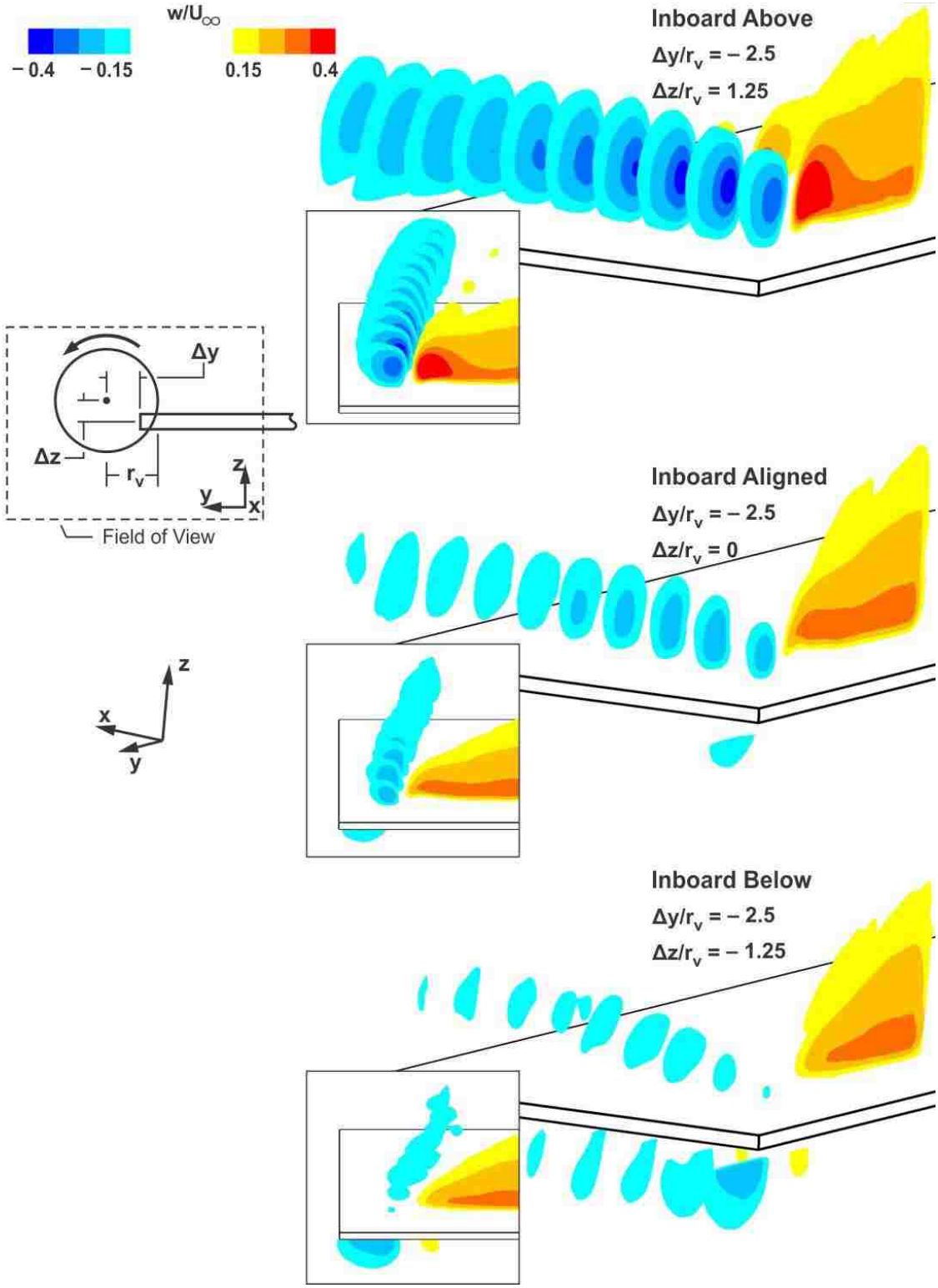

Figure B.15: Slices of vertical velocity w/U_∞ at three vertical locations $\Delta z/r_v$ of vortex impingement for $\Delta y/r_v$ = -2.5. The slices extend over the streamwise distance from 0.125 C to 1.25 C downstream of the leading edge of the wing.

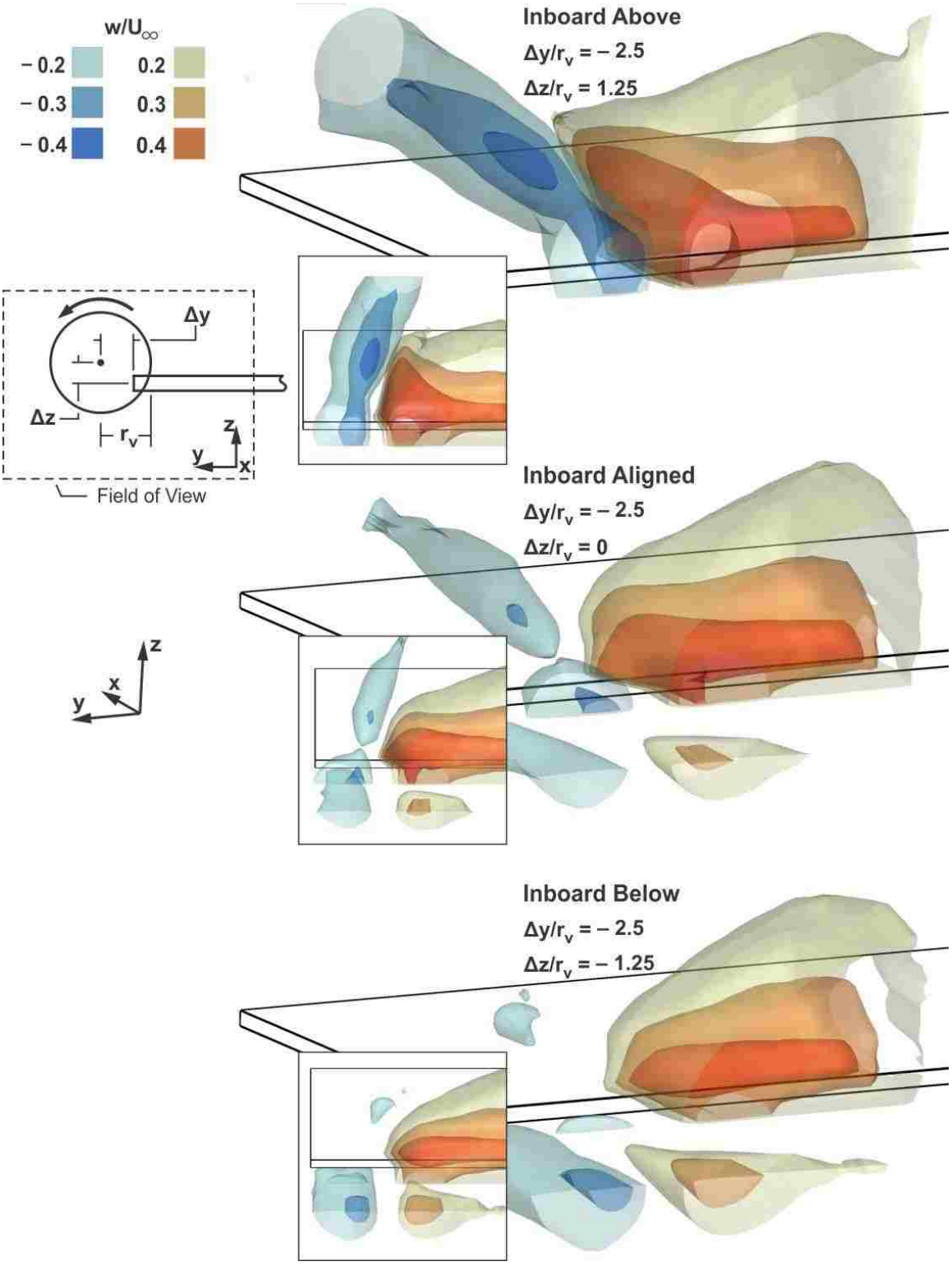

Figure B.16: Iso-surfaces of vertical velocity w/U_∞ at three vertical locations $\Delta z/r_v$ of vortex impingement for $\Delta y/r_v$ = -2.5. The surfaces extend over the streamwise distance from 0.25 C upstream to 1.25 C downstream of the leading edge of the wing.

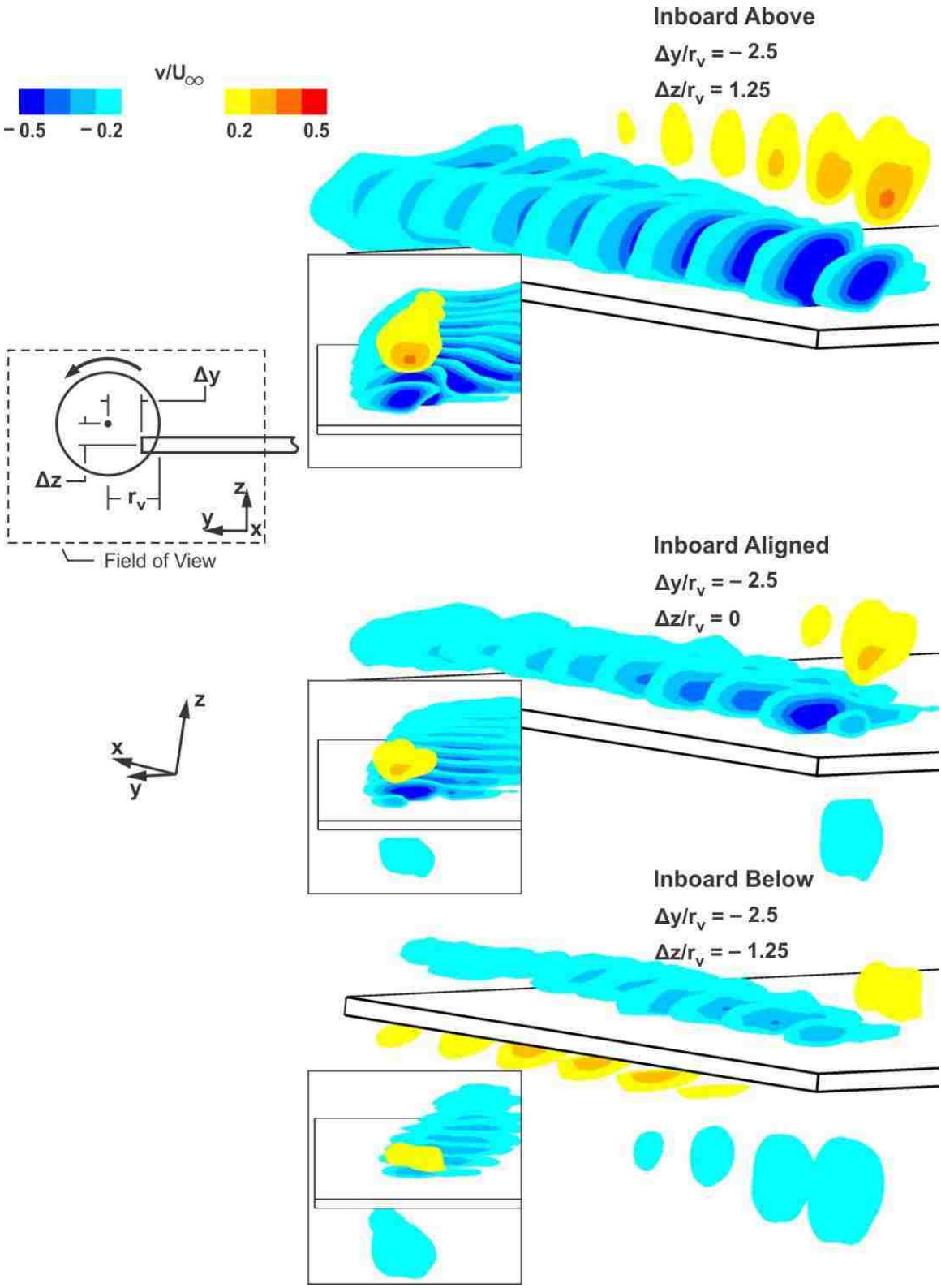

Figure B.17: Slices of spanwise velocity v/U_∞ at three vertical locations $\Delta z/r_v$ of vortex impingement for $\Delta y/r_v$ = -2.5. The slices extend over the streamwise distance from 0.125 C to 1.25 C downstream of the leading edge of the wing.

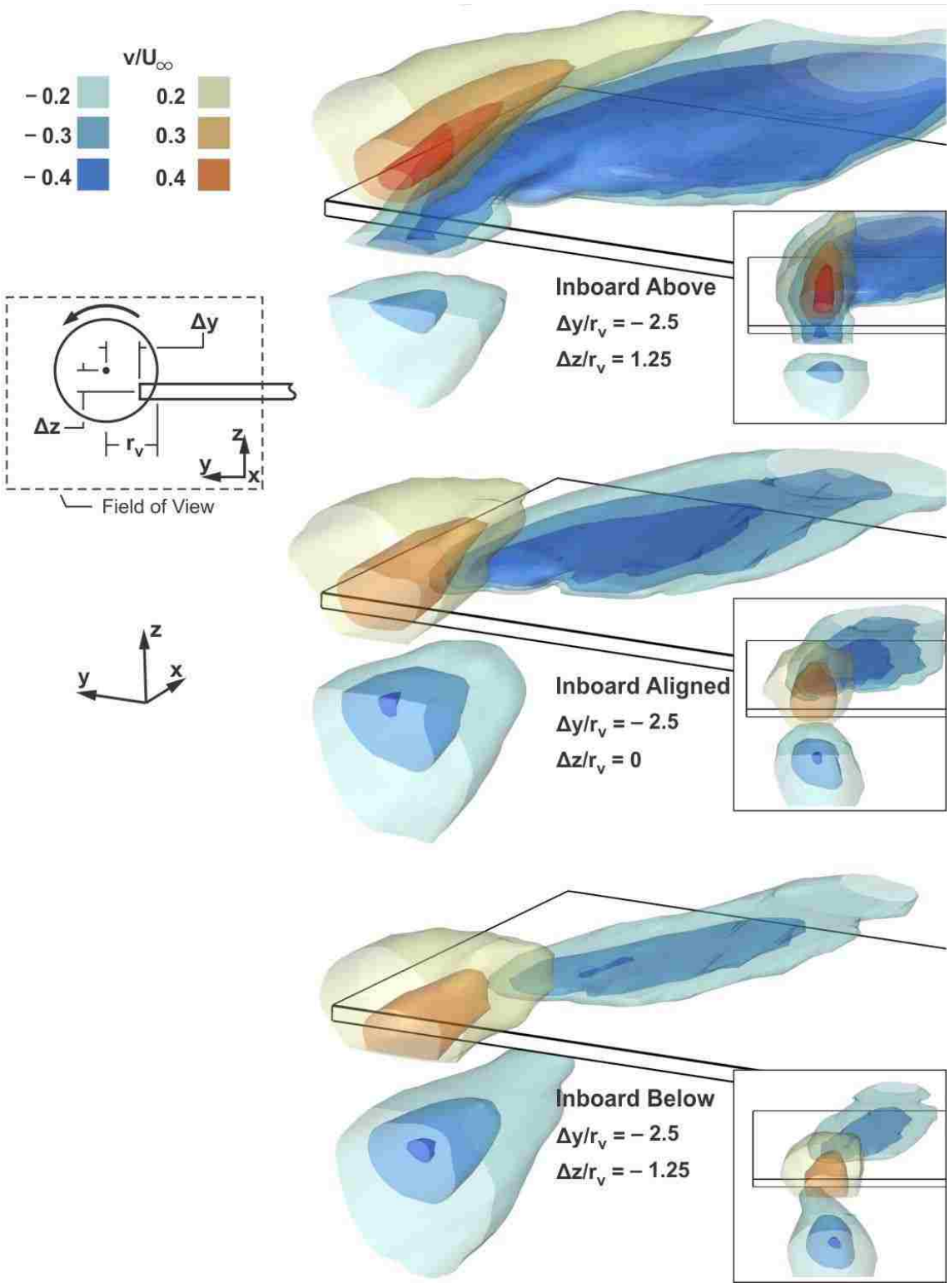

Figure B.18: Iso-surfaces of spanwise velocity v/U_∞ at three vertical locations $\Delta z/r_v$ of vortex impingement for $\Delta y/r_v$ = -2.5. The surfaces extend over the streamwise distance from 0.25 C upstream to 1.25 C downstream of the leading edge of the wing.

APPENDIX C

SUPPLEMENT TO CHAPTER 4: TURBULENT KINETIC ENERGY OF MODES OF VORTEX-WING INTERACTIONS- COMPUTATIONS AND EXPERIMENTS

In section 4.3, comparisons of contours of streamwise vorticity $\omega_x C/U_\infty$ were shown between the computations of Garmann and Visbal (2015a) and the present experiments. Appendix C continues these comparisons by analyzing the similarity and differences in contours of turbulent kinetic energy *T*.

In this section, levels of turbulent kinetic energy *T* are primarily used to identify the separation zone on the wing, and any change in the stability of the vortices. Adjusted in-plane turbulent kinetic energy *T** is used for the experiments, and is defined as $T^* = \frac{1}{2}(\overline{w'^2} + \overline{v'^2} + .5 * \overline{w'^2 + v'^2})$. Since the out-of-plane velocity was not recorded, the out-of-plane velocity fluctuation was estimated using the in-plane velocity fluctuations according to Cebeci (2013). The experiments also show higher levels of turbulent kinetic energy in the incident vortex, which is a byproduct of the vortex generation method.

For the outboard interaction shown in figure C.1, increased levels of *T* can be seen above the surface of the plate from x'/C = 0.25 to 1. These levels are associated with the separated region of the suction surface of the wing. In both cases the highest *T* levels in the separated region occur at x'/C = 0.5. In addition, the boundary of the separated region near the tip moves inboard as the tip vortex develops, and increased levels of *T* can be seen in the core of the tip vortex.

Figure C.2 shows the comparison for the aligned interaction case, which again features a separation region inboard of the tip. This region is present on the wing from x'/C = 0.25 to 1, and has its largest values of T at x'/C = 0.5. From x'/C = 0.5 to 1, the T levels of both the incident and tip vortices increase, with these vortices having a region of lower T between themselves and the separated region.

The comparison of the T levels for the inboard interaction is shown in Figure C.3. In this case there are two different separated regions which are defined by the position of the incident vortex. Inboard of the incident vortex, there is a separated region above the plate which is similar to those seen in both the outboard and aligned interaction cases. Outboard of the impingement location, a separation region is actually present below the surface of the plate. Along the chord of the wing, the T levels of the separation region above the plate are higher than those of the separation region below it.

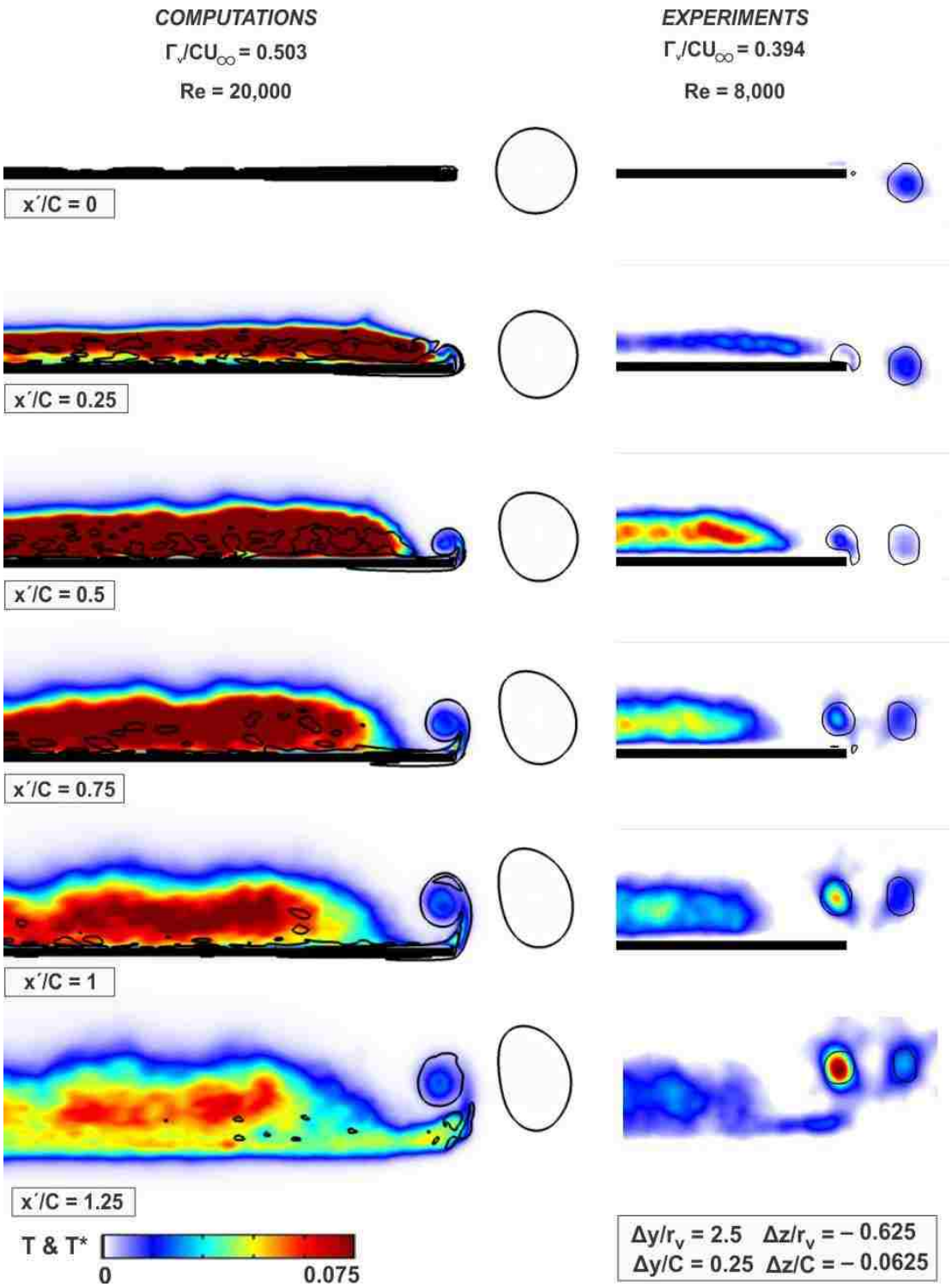

Figure C.1: Comparison of turbulent kinetic energy from computations of Garmann *et al.* (2015a) ($\Gamma_v/(CU_\infty)$ = 0.503; Re = 20,000) and present experiments ($\Gamma_v/(CU_\infty)$ = 0.394; Re = 8,000) for the outboard interaction of an incident vortex with a plate. T* was calculated by estimating the value of the out-of-plane fluctuation $\overline{u'^2}$ by $\overline{u'^2} = \frac{1}{2}(\overline{v'^2} + \overline{w'^2})$ according to Cebeci (2013).

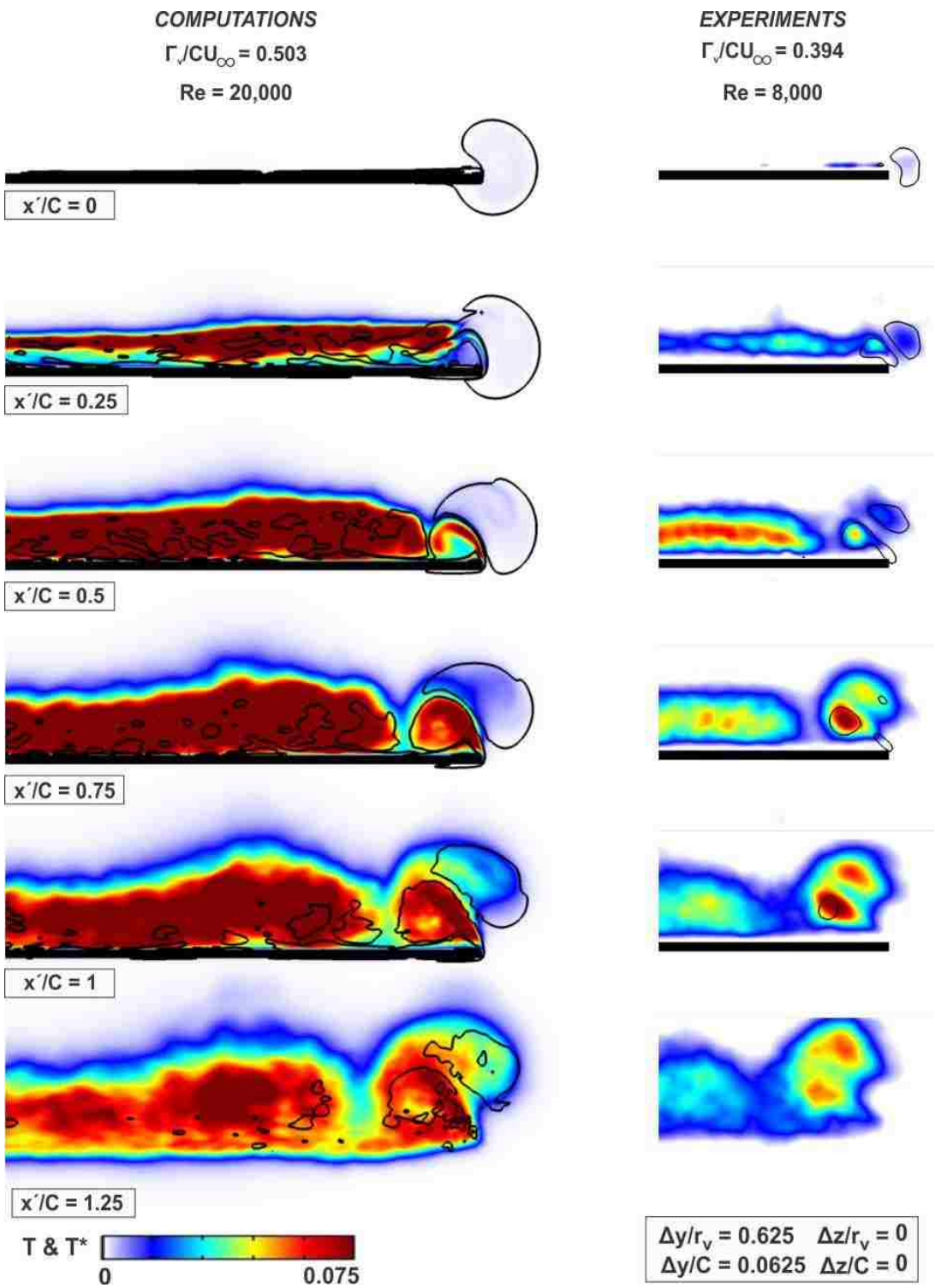

Figure C.2: Comparison of turbulent kinetic energy from computations of Garmann *et al.* (2015a) ($\Gamma_v/(CU_\infty)$ = 0.503; Re = 20,000) and present experiments ($\Gamma_v/(CU_\infty)$ = 0.394; Re = 8,000) for the aligned interaction of an incident vortex with a plate. T* was calculated by estimating the value of the out-of-plane fluctuation $\overline{u'^2}$ by $\overline{u'^2} = \frac{1}{2}(\overline{v'^2} + \overline{w'^2})$ according to Cebeci (2013).

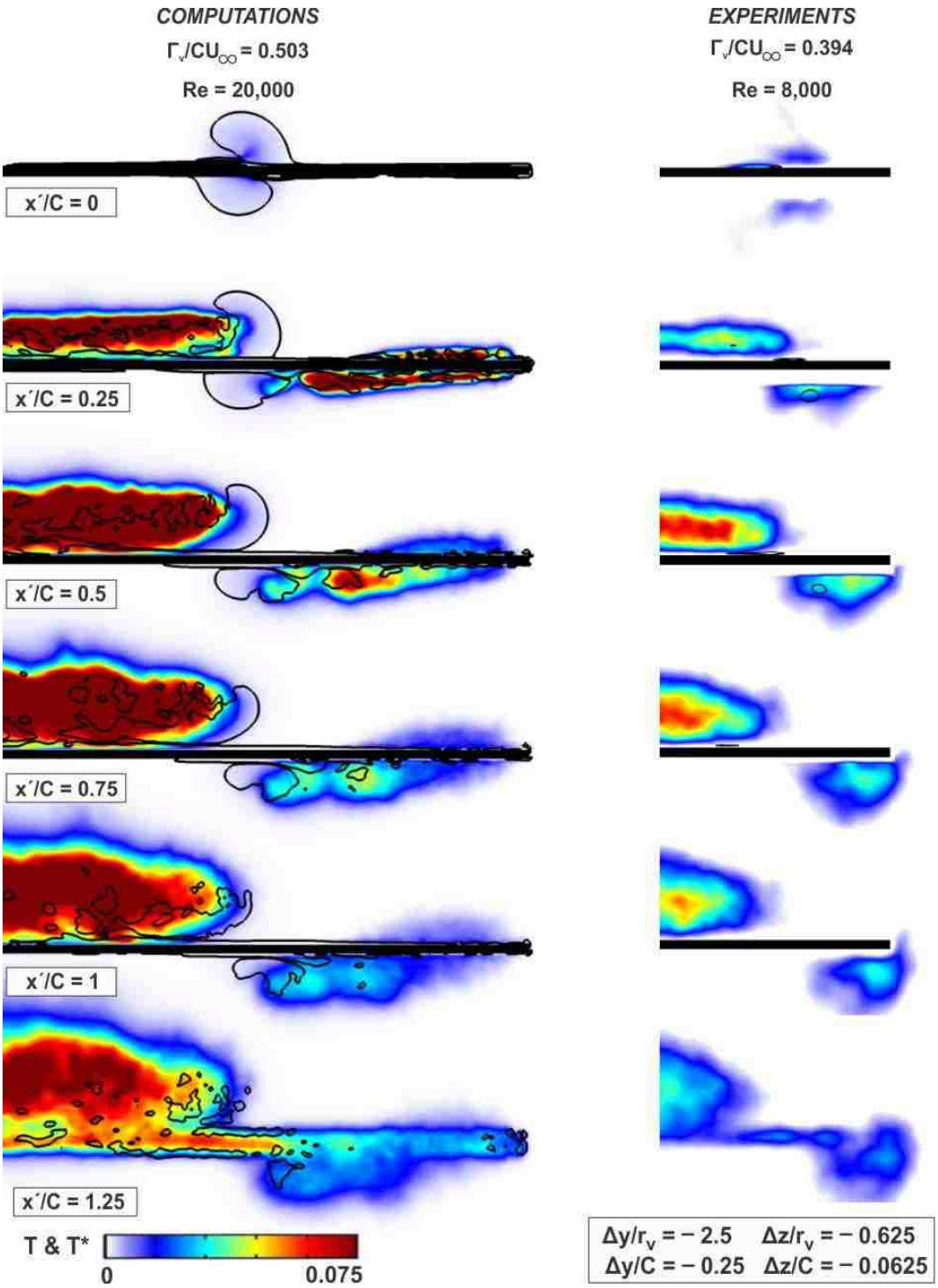

Figure C.3: Comparison of turbulent kinetic energy from computations of Garmann *et al.* (2015a) ($\Gamma_v/(CU_\infty)$ = 0.503; Re = 20,000) and present experiments ($\Gamma_v/(CU_\infty)$ = 0.394; Re = 8,000) for the inboard interaction of an incident vortex with a plate. T* was calculated by estimating the value of the out-of-plane fluctuation $\overline{u'^2}$ by $\overline{u'^2} = \frac{1}{2}(\overline{v'^2} + \overline{w'^2})$ according to Cebeci (2013).

APPENDIX D

SUPPLEMENT TO CHAPTER 5: PHASE LAG DURING THE INTERACTION OF A TRAILING VORTEX WITH AN OSCILLATING WING

This appendix addresses how the signals associated with the maximum upwash and maximum streamwise vorticity lag the wing motion at all streamwise locations. For these images, a phase lag $\phi_L = 0$ means that the peak of the signal occurs at the same phase as the maximum negative velocity of the wing w_w which occurs at $\phi = \pi/2$. A positive value of ϕ_L corresponds to the signal peak occurring after $\phi = \pi/2$, so if $\phi_L = \pi$, the signal has its peak at $\phi = 3\pi/2$.

Figure D.1 shows how the phase lags ϕ_L change for the offset of the incident vortex of $\Delta y/C = 0.375$. Near the leading edge, at $x'/C = 0.25$, the phase lag is small, with the maximum values of upwash and streamwise vorticity occurring soon after the wing has achieved its maximum negative velocity. Further downstream, the phase lag increases for both the upwash and the maximum streamwise vorticity of the incident vortex. From $x'/C = 0.5$ to 1.5 the occurrence of maximum vorticity lags slightly behind the upwash, creating a phase gap between them, but they match up again further into the wake. Over a distance less than two chords of the wing, both signals have fallen π behind the motion of the wing, from being in phase with the maximum negative velocity w_w at $x'/C = 0.25$, to being in phase with the maximum positive velocity at $x'/C = 0$.

The phase lag ϕ_L at $\Delta y/C = 0.25$ is shown in figure D.2. This shows trends similar to those at $\Delta y/C = 0.375$ in figure D.1, although the phase gap between the upwash and

maximum vorticity of the tip vortex has increased over the streamwise region x'/C = 0.5 to 1.5. This increase is caused by ϕ_L for the maximum upwash at x'/C = 0.5 being slightly smaller than at x'/C = 0.25.

This decrease in lag is significantly more pronounced in figure D.3, which shows the lag for $\Delta y/C$ = 0.125; in this case ϕ_L for the maximum upwash is negative, meaning that the velocity signal of the wing lags behind that of the maximum upwash. At the trailing edge, x'/C = 1, ϕ_L for the maximum upwash once again becomes positive, approaching ϕ_L for the maximum vorticity as was seen in the other two cases. Phase lag ϕ_L for the maximum vorticity follows a trend similar to that at $\Delta y/C$ = 0.375 and $\Delta y/C$ = 0.25.

These figures show that the region of upwash outboard of the wing and the formation of the tip vortex on the wing are linked to the velocity of the wing, but they are not phase locked to it. In fact, from inception of the tip vortex, its oscillation in strength, represented by maximum vorticity, lags behind the velocity of the wing, with ϕ_L increasing in size with downstream location. The same is true of the maximum upwash, although it does exhibit interesting behavior along the chord of the wing. In the wake, the two values of ϕ_L approach one another, which is caused by the two vortices dominating the flow at these locations. If the wing motion does not influence the flow, the two values of ϕ_L become equal, which is due to the maximum upwash no longer being enhanced by the motion of the wing.

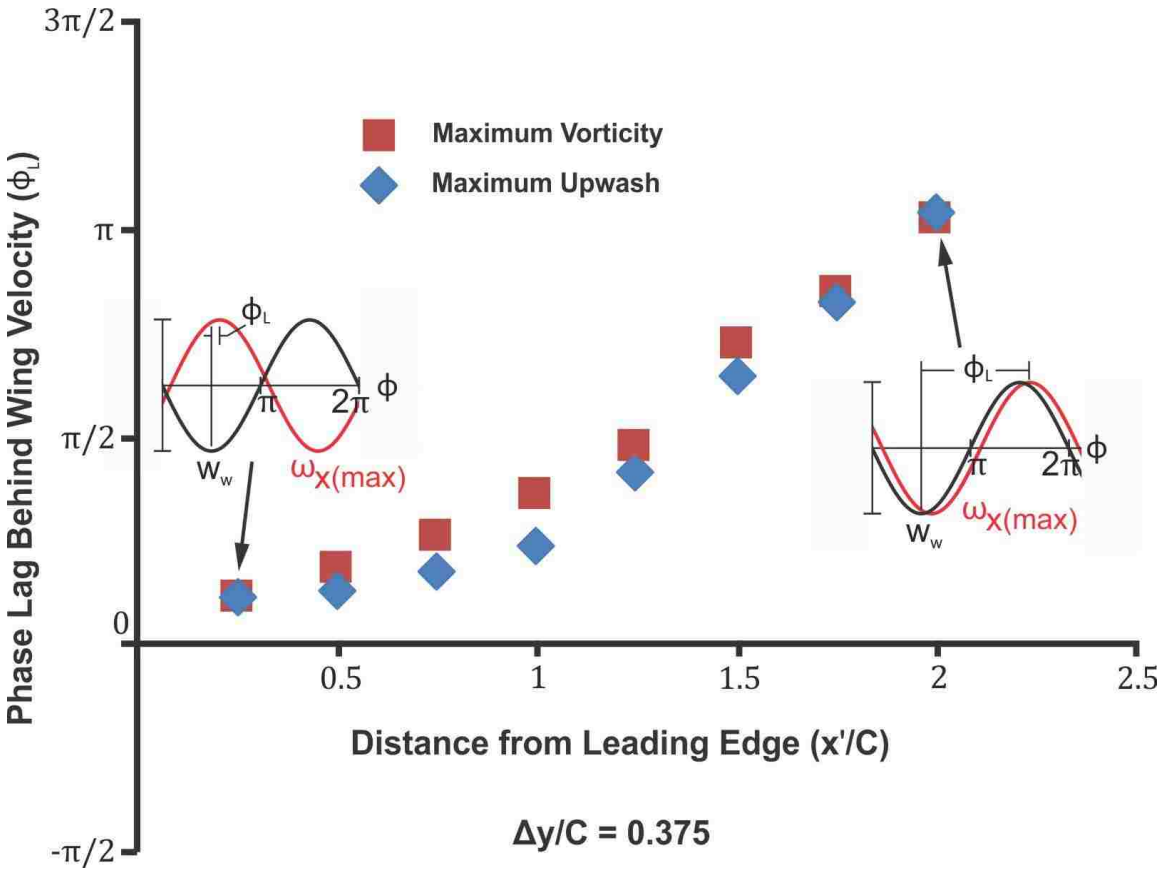

Figure D.1: Phase lags at successive streamwise locations. The red squares are the phase lags between the maximum upwash and the motion of the wing, and the blue diamonds are the phase lags between the maximum streamwise vorticity (associated with the tip vortex) and the motion of the wing.

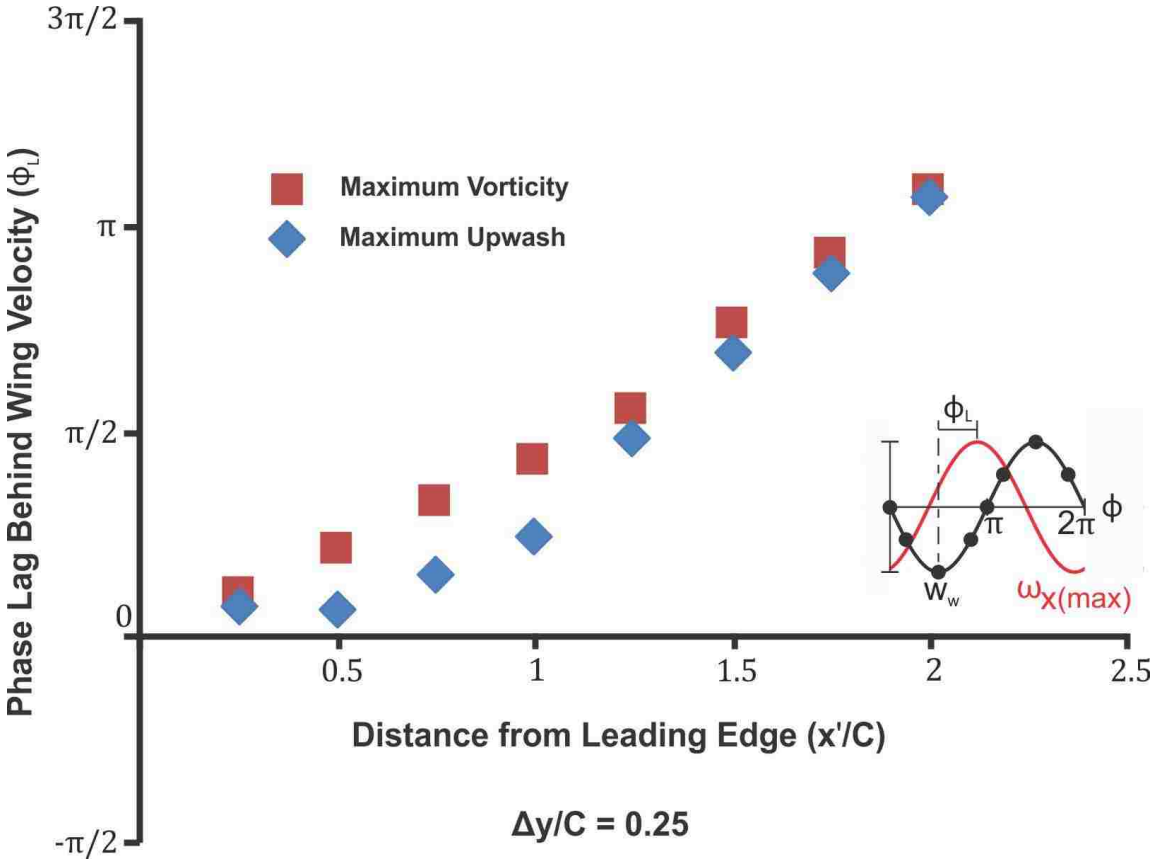

Figure D.2: Phase lags at successive streamwise locations. The red squares are the phase lags between the maximum upwash and the motion of the wing, and the blue diamonds are the phase lags between the maximum streamwise vorticity (associated with the tip vortex) and the motion of the wing.

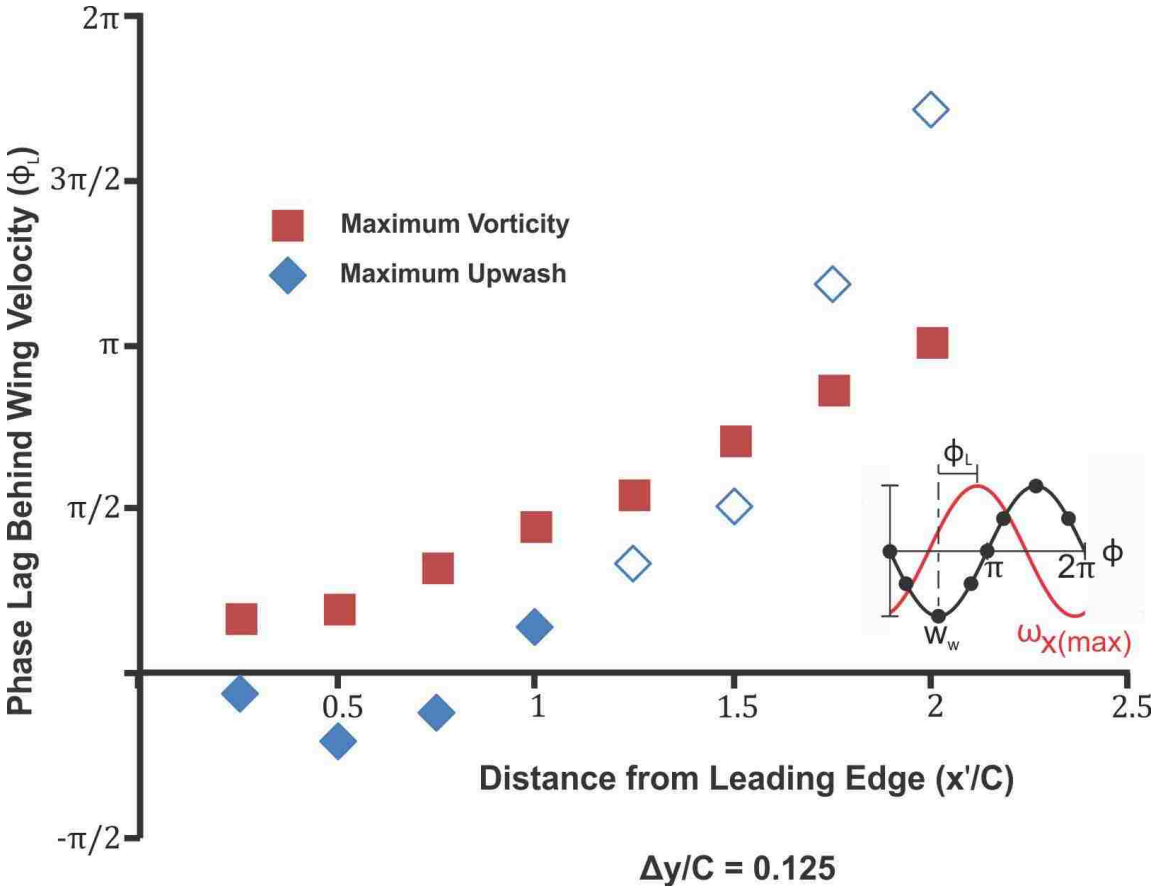

Figure D.3: Phase lags at successive streamwise locations. The red squares are the phase lags between the maximum upwash and the motion of the wing, and the blue diamonds are the phase lags between the maximum streamwise vorticity (associated with the tip vortex) and the motion of the wing. The empty diamonds represent where the coherence is below 0.9.

Vita

Author Christopher Kyle McKenna was born to Walter and Barbara McKenna in Allentown, Pennsylvania on October 22nd, 1989. In May 2012 he graduated with honors from the Mechanical Engineering Department of Lafayette College, where he received his Bachelor of Science degree. He then joined the Mechanical Engineering and Mechanics Department of Lehigh University in August 2012 to pursue his Ph.D. degree. During his doctoral study at Lehigh University, he worked both as a research and teaching assistant under the supervision of Paul B. Reinhold Professor Donald Rockwell. As a result of the research conducted during the doctoral program, several technical talks have been given, and the author has published the following articles:

McKENNA, C. K., BROSS, M., & ROCKWELL, D. 2017 Structure of a streamwise-oriented vortex incident upon a wing. J. Fluid Mech. 816, 306-330.
McKENNA, C. K, & ROCKWELL, D. 2016 Topology of vortex-wing interactions. Exp Fluids 57:161.